

Dust variability and provenance in the Pacific and Atlantic sectors of the Southern Ocean

Kumulative Dissertation zur Erlangung des akademischen Grades
eines Doktors der Naturwissenschaften

Doctor rerum naturalium

Dr. rer. nat.

am Fachbereich Geowissenschaften
der Universität Bremen

vorgelegt von

Marc Wengler

Bremen, Mai 2018

Gutachter: Prof. Dr. Ralf Tiedemann

Gutachterin: Prof. Dr. Gesine Mollenhauer

Erklärung

Ich versichere, dass

1. die Dissertation ohne unerlaubte fremde Hilfe angefertigt wurde,
2. keine anderen als die von mir angegebenen Quellen und Hilfsmittel benutzt wurden und
3. die den benutzten Werken wörtlich oder inhaltlich entnommenen Stellen als solche kenntlich gemacht wurden.

Bremen, 24.05.2018

Marc Wengler

Acknowledgements

First of all, I would like to thank my supervisor Frank Lamy for giving me the opportunity to work on the topic of atmospheric dust and its impact on the climate system, for his ongoing support and several interesting and helpful discussions. Your enthusiasm for this topic always motivated me. I am grateful for the experiences I have had and the people I have met during the past few years.

I want to thank Ralf Tiedemann for the supervision and the helpful support during the last years. Moreover, I want to thank Ralf Tiedemann for reviewing this thesis.

A special thank goes to Gesine Mollenhauer, who additionally reviewed this thesis. Furthermore, I want to thank all the members of my thesis committee.

Additionally, I want to thank Walter Geibert, Oliver Esper and Gerhard Kuhn for several helpful and interesting discussions. Your advices were always valuable.

Rita Fröhlking-Teichert and Susanne Wiebe, without your great support in the lab, this dissertation would not have been possible. The conversations with you were always encouraging.

Thomas Ronge and Johannes Ullermann, my first office mates at the AWI. Sharing an office with you was great and your help, in particular when I started at the AWI, was priceless. Furthermore, I want to thank Thomas Ronge and Jenny Roberts for numerous helpful discussions.

I want to thank Gisela Winckler for giving me the opportunity to work at the Lamont-Doherty Earth Observatory, for the valuable discussions and for the support.

Additionally, I like to thank Katharina Pahnke for the collaboration with the ICBM in Oldenburg. In particular, I would like to emphasize Torben Struve, Philipp Böning and Martina Schulz for your help in the lab and during the mass spectrometric analysis.

I am grateful to my parents for always believing in me. Finally, I want to thank my wife Johanna. I am really grateful for your endless support and your patience.

Abstract

The effect of dust on the global climate results from processes in the atmosphere and in the ocean. On the one hand, dust in the atmosphere scatters or absorbs incoming sunlight (a direct influence on climate) or modifies cloud properties (an indirect influence on climate). On the other hand, dust can stimulate the marine productivity by supplying iron to the ocean (iron fertilization). Increased dust fluxes, especially during glacial periods, may have enhanced the marine productivity in the Southern Ocean, which was likely responsible for an atmospheric CO₂ reduction of ~40 ppmv. Subsequently, the Southern Ocean is a crucial component of the global climate system.

Analyzing marine dust records deposited downwind of the major Southern Hemisphere dust source areas provides valuable information on paleoclimate changes in source areas characteristics (e.g. aridity, precipitation, wind) and within the dust transporting winds. Based on these analyses, this dissertation aims to contribute to a better understanding of paleoclimate changes inferred from the dust variability of marine dust records from the Southern Ocean.

To achieve this goal, four manuscripts are presented in chapters 3, 4, 5 and 6, which each utilizes different methodical approaches. A comprehensive set of sediment surface samples and sediment cores from the Pacific and Atlantic sectors of the Southern Ocean was used to conduct dust provenance, grain size and biomarker analyses.

Manuscript one (chapter 3) presents the first combined lithogenic flux and dust provenance analysis extracted from sediment surface samples from the Pacific sector of the Southern Ocean, which allows to better understand Holocene dust variability. The lowest lithogenic fluxes detected in open ocean surface sediments are interpreted as solely derived from atmospheric dust. The provenance analysis reveals that sources in central and southeast Australia dominate the dust supply to the Pacific sector of the Southern Ocean during the Holocene.

The second manuscript (chapter 4) aims to identify dust fluctuations over glacial-interglacial timescales. Grain size analysis were performed on two sediment cores located in the Pacific and Atlantic sectors of the Southern Ocean, respectively. The results reveal opposing grain size patterns with coarser glacial grain sizes in the Pacific sector compared to finer glacial grain sizes in the Atlantic sector. Additional iron and lithogenic flux records provide consistent results for both sectors with increased glacial values indicating that more dust was available in potential source areas. The inconsistent grain size patterns are the result of different responses

to glacial climate conditions in the source areas coupled with variations within the Southern Westerly Winds favoring or hampering the erosion of coarse dust particles.

A biomarker perspective on different terrigenous and marine proxies (dust, productivity and sea surface temperature) from the polar and subpolar zones of the Pacific sector of Southern Ocean is given in the third manuscript (chapter 5). Reconstructed sea surface temperatures reveal modern summer temperatures confirming that the analyzed surface samples are representative for the Holocene. The results inferred from n-alkanes and brGDGTs (organic tracers for terrigenous material) clearly reveal that the samples located in the open ocean were solely derived from atmospheric dust.

In the fourth manuscript (chapter 6), the Drake Passage throughflow is reconstructed using the sortable silt mean grain size as proxy for changes in bottom current speed. The results illustrate a substantial glacial throughflow reduction, which is consistent with a decrease of the Southern Westerly Winds core zone over Patagonia. The weakened winds reduce, in addition to other factors (e.g. sea ice), the strength of the Antarctic Circumpolar Current, which in turn affects the bottom current speed. The Southern Westerly Winds are the main dust transport medium in the Southern Hemisphere, so that changes within this wind belt can affect the long-range dust transport.

Ultimately, this thesis advances the understanding of the Southern Ocean dust variability with implications for paleoclimate reconstructions and clearly illustrates the versatile application of dust analyses in paleoclimate studies. The combination of different methods, the large spatial coverage and the temporal resolution of the surface samples and sediment cores used provide a unique dataset for the Southern Ocean.

Zusammenfassung

Die Beeinflussung des globalen Klimas durch Staub resultiert aus Prozessen in der Atmosphäre und im Ozean. Zum einen kann Staub in der Atmosphäre eintreffendes Sonnenlicht verteilen oder absorbieren (direkter Einfluss auf das Klima) oder aber die Eigenschaften von Wolken beeinflussen (indirekter Einfluss auf das Klima). Zum anderen kann der Eintrag von Staub in den Ozean die marine Produktivität durch die Zufuhr von Eisen anregen (Eisendüngung). Im Südozean haben erhöhte Staubflüsse besonders während glazialer Perioden die marine Produktivität erhöht und somit wahrscheinlich zu einer Reduzierung des atmosphärischen CO₂ von ~40 ppmv beigetragen. Folglich kann der Südozean als eine zentrale Komponente des globalen Klimasystems bezeichnet werden.

Durch die Analyse mariner Staubablagerungen, die in Hauptwindrichtung der potentiellen Quellregionen abgelagert wurden, können wichtige Informationen über paläoklimatische Veränderungen in den Quellregionen (zum Beispiel Trockenheit, Niederschlag und Wind) und innerhalb der staubtransportierenden Winde gewonnen werden. Basierend auf solchen Analysen soll diese Dissertation zu einem besseren Verständnis der Staubvariabilität im Südozean beitragen, um paläoklimatische Veränderungen nachvollziehen zu können.

Um dieses Ziel zu erreichen, werden in dieser Dissertation vier Manuskripte in den Kapiteln 3, 4, 5 und 6, von denen jedes einzelne einen anderen methodischen Ansatz bietet, vorgestellt. Eine umfassende Zusammenstellung von sedimentären Oberflächenproben und Sedimentkernen aus den pazifischen und atlantischen Sektoren des Südozeans wurde verwendet, um Staubprovenienz-, Korngrößen- und Biomarkeranalysen durchzuführen.

Manuskript eins (Kapitel 3) zeigt die erste kombinierte Analyse von lithogenen Flüssen und Staubprovenienz, durchgeführt an sedimentären Oberflächenproben aus dem pazifischen Sektor des Südozeans, um die Staubvariabilität des Holozäns besser zu verstehen. Die niedrigsten lithogenen Flüsse wurden im offenen Ozean gemessen und stammen ausschließlich von Staub. Die durchgeführte Staubprovenienzanalyse zeigt, dass Zentral- und Südostaustralien den Staubeintrag in den pazifischen Sektor des Südozeans während des Holozäns dominiert haben.

Das zweite Manuskript (Kapitel 4) zielt darauf ab, Staubfluktuationen über glaziale-interglaziale Zeitskalen zu identifizieren. Dazu wurden Korngrößenanalysen an zwei Sedimentkernen aus den pazifischen und atlantischen Sektoren des Südozeans durchgeführt, die zwei gegensätzliche Korngrößenmuster zeigen. Während glazialer Perioden kann der pazifische Sektor durch gröbere Korngrößen charakterisiert werden, während feinere

Korngrößen im atlantischen Sektor dominieren. Zusätzliche Messungen von Eisen- und lithogenen Flüssen zeigen für beide Sektoren einheitliche Ergebnisse mit erhöhten Werten in den Glazialen. Diese deuten auf eine erhöhte Verfügbarkeit von Staub in den potentiellen Quellregionen während glazialer Perioden hin. Die nicht einheitlichen Korngrößenmuster sind das Ergebnis unterschiedlicher Reaktionen auf glaziale Klimabedingungen der Quellregionen verbunden mit Variationen innerhalb der südlichen Westwinde, die die Erosion grober Staubpartikel entweder erlaubt oder verhindert haben.

Eine Biomarkeranalyse von verschiedenen terrigenen und marinen Indikatoren (Staub, Produktivität, Ozeanoberflächentemperaturen) aus den polaren und subpolaren Zonen des pazifischen Sektors des Südozeans ist Inhalt des dritten Manuskriptes (Kapitel 5). Eine Rekonstruktion von Oberflächenwassertemperaturen zeigt moderne Sommertemperaturen und bestätigt, dass die analysierten Oberflächenproben das Holozän repräsentieren. Die gewonnenen Ergebnisse von n-alkanen und brGDGT Analysen (organische Indikatoren für terrigenen Eintrag) zeigen, dass die Proben im offenen Ozean auf eine Staubherkunft deuten.

Im vierten Manuskript wird der Durchfluss durch die Drake Passage mit Hilfe der durchschnittlichen Korngröße des „sortable silt“ rekonstruiert, um Änderungen innerhalb der Bodenströmungen zu identifizieren. Die Ergebnisse zeigen eine substantielle Abnahme des Durchflusses in glazialen Perioden, die mit einer Abnahme der Kernzone der südlichen Westwinde übereinstimmt. Die abgeschwächten Winde reduzieren, neben anderen Faktoren (zum Beispiel Meereis), die Stärke des antarktischen Zirkumpolarstroms und beeinflussen somit die Bodenströmungen. Da die südlichen Westwinde das hauptsächliche Transportmedium für Staub in der Südhemisphäre sind, können Änderungen innerhalb dieses Windsystems den Staubtransport beeinflussen.

Schließlich kann diese Dissertation zu einem besseren Verständnis der Staubvariabilität im Südozean hinsichtlich paläoklimatischer Rekonstruktionen beitragen und zeigt ebenfalls die vielseitige Anwendbarkeit von Staub als Indikator für paläoklimatische Änderungen. Die Kombination von verschiedenen Methoden, die große räumliche Abdeckung und die zeitliche Auflösung der verwendeten Oberflächenproben und Sedimentkernen verdeutlichen die Aussagekraft der Daten und bieten gleichzeitig einen einzigartigen Datensatz für den Südozean.

List of abbreviations

| | |
|-------------------------------|---|
| ACC | Antarctic Circumpolar Current |
| APF | Antarctic Polar Front |
| AZ | Antarctic Zone |
| brGDGTs | Branched Glycerol Dialkyl Glycerol Tetraethers |
| EDC | EPICA (European Project for Ice Coring in Antarctica) ice core drilled at Dome C in East Antarctica |
| Fe | Iron |
| G/IG | Glacial-Interglacial |
| HNLC | High-Nutrient Low-Chlorophyll |
| IODP | International Ocean Discovery Program |
| ICP-MS | Inductively Coupled Plasma Mass Spectrometry |
| La | Lanthanum |
| LGM | Last Glacial Maximum |
| Lu | Lutetium |
| MOC | Meridional Overturning Circulation |
| Nd | Neodymium |
| Pb | Lead |
| PFZ | Polar Frontal Zone |
| PSA(s) | Potential source area(s) |
| REE | Rare Earth Elements |
| SACCF | Southern Antarctic Circumpolar Current Front |
| SAF | Subantarctic Front |
| SAZ | Subantarctic Zone |
| Sm | Samarium |
| SO | Southern Ocean |
| Sr | Strontium |
| STF | Subtropical Front |
| SWW | Southern Westerly Winds |
| Th | Thorium |
| U | Uranium |
| $^{230}\text{Th}_{\text{xs}}$ | ^{230}Th -Thorium excess |

| | |
|--|------------|
| ACKNOWLEDGEMENTS..... | I |
| ABSTRACT | II |
| ZUSAMMENFASSUNG..... | IV |
| LIST OF ABBREVIATIONS | VI |
| 1 INTRODUCTION | |
| 1.1 THE SOUTHERN OCEAN | 1 |
| 1.1.2 <i>Southern Hemisphere climate variability and the role of the Southern Ocean</i> | 4 |
| 1.2 ATMOSPHERIC DUST – A POWERFUL TOOL FOR PALEOCLIMATE RECONSTRUCTIONS..... | 8 |
| 1.2.1 <i>Dust erosion, emission, transport and deposition in the Southern Hemisphere</i> | 8 |
| 1.2.2 <i>Atmospheric dust and its impact on the Southern Hemisphere climate</i> | 11 |
| 1.3 MOTIVATION AND OBJECTIVES OF THE THESIS | 16 |
| 1.4 AUTHORS CONTRIBUTION | 19 |
| 2 SEDIMENT MATERIAL AND METHODOLOGY | |
| 2.1 SEDIMENT MATERIAL..... | 22 |
| 2.2 METHODOLOGY..... | 23 |
| 2.2.1 <i>²³⁰Th-normalized fluxes as tracer for dust input</i> | 23 |
| 2.2.2 <i>Radiogenic isotopes and rare earth elements as tracers for dust provenance</i> | 24 |
| 2.2.3 <i>Grain size analysis as tracer for the past dust variability</i> | 27 |
| 3 A GEOCHEMICAL APPROACH TO RECONSTRUCT MODERN SOUTH PACIFIC DUST FLUXES AND POTENTIAL DUST SOURCE AREAS..... | 29 |
| 4 OPPOSING DUST GRAIN SIZE CHANGES IN THE PACIFIC AND ATLANTIC SECTORS OF THE SOUTHERN OCEAN DURING THE LAST 260 KYR..... | 55 |
| 5 A BIOMARKER PERSPECTIVE ON DUST, PRODUCTIVITY, AND SEA SURFACE TEMPERATURE IN THE PACIFIC SECTOR OF THE SOUTHERN OCEAN..... | 82 |
| 6 GLACIAL REDUCTION AND MILLENNIAL-SCALE VARIATIONS IN DRAKE PASSAGE THROUGHFLOW | 120 |
| 7 CONCLUSIONS AND PERSPECTIVES | |
| 7.1 MAIN CONCLUSIONS | 150 |
| 7.2 PERSPECTIVES | 153 |
| REFERENCES..... | 155 |
| DATA HANDLING..... | 181 |

1 Introduction

1.1 The Southern Ocean

The main study areas of this thesis are the Pacific and Atlantic sectors of the Southern Ocean (SO) with a particular focus on the Pacific sector. In the following, the main oceanographic features of the study areas are described.

The SO is the most important connection between the Pacific, Atlantic and Indian Oceans. It completely encircles the Antarctic continent and is not interrupted by continental land masses (Fig. 1.1) (Talley et al., 2011). The southern boundary of the SO is marked by the Antarctic continent, whereas the definition of the northern limit can vary. The Antarctic Treaty defines 60°S as the political northern boundary of the SO (Talley et al., 2011). From an oceanographic perspective, the SO well extends north of 60°S, where the northernmost limit of the Antarctic Circumpolar Current (ACC) defines the northern boundary of the SO (Fig. 1.1) (Talley et al., 2011). The most widely used definition suggests that the SO ends at ~30°S and therefore comprises all important SO features in each of its ocean basins (Pacific, Atlantic and Indian Oceans) (Fig. 1.1) (Talley et al., 2011).

Located in the SO, the ACC is the world's largest current system. With an estimated length of ~24,000 km it continuously flows eastward and completely encircles the Antarctic continent (Fig. 1.1) (Orsi et al., 1995). It extends through the whole water column from the surface ocean to the seafloor and transports 130-150 Sv ($1 \text{ Sv} = 10^6 \text{ m}^3/\text{s}$) as revealed by measurements across the Drake Passage (e.g. Cunningham et al., 2003; Renault et al., 2011). The dimension of the ACC is well defined along its path through the SO, with the Subantarctic Front (SAF) and the Southern Antarctic Circumpolar Front (SACCF) defining its northern and southern limits, respectively (Fig. 1.1) (Orsi et al., 1995; Carter et al., 2008). The circumpolar flow of the ACC is affected by the continental landmasses of southern South America and Antarctica because parts of these landmasses (southernmost Patagonia and the Antarctic Peninsula) form the ~800 km wide Drake Passage. While flowing through the Drake Passage, the ACC is restricted to its narrowest extend (Lamy et al., 2015). Additionally, the SO bottom topography influences the flow path, for example the Campbell Plateau (off southeastern New Zealand) and the Falkland Plateau (off southeastern southern South America) act as major constrictions to the flow (Fig. 1.1) (Orsi et al., 1995; Carter et al., 2008). As part of the ACC, three eastward flowing and seasonally varying oceanographic fronts can be identified from north to south (Subantarctic Front; SAF, Antarctic Polar Front; APF, Southern Antarctic Circumpolar Current Front;

SACCF) (Orsi et al., 1995; Renault et al., 2011; Koenig et al., 2014). These ACC frontal systems are characterized by a strong eastward flow and strongly sloping isopycnals in the water column as well as by changes in water properties (e.g. salinity and temperature) (Carter et al., 2008; Talley et al., 2011). The general eastward flow is predominantly controlled by the strong Southern Westerly Winds (SWW) (Allison et al., 2010, and references therein). A substantial glacial decrease of the northernmost ACC flow in the Drake Passage is understood to have occurred in response to a glacial reduction in the core of the SWW (Lamy et al., 2010; Kohfeld et al., 2013; Lamy et al., 2015). However, the wind stress imparting eastward momentum in the ACC is partially counterbalanced by bottom stress driven pressure differences at oceanic ridges leading to a reduction in flow speed (Johnson and Bryden, 1989). However, the exact coupling of the SWW and the ACC intensity is not yet fully understood and model dependent (e.g. Allison et al., 2010; Hogg, 2010; Völker and Köhler, 2013).

The regions between the fronts are referred to as the Subantarctic Zone (SAZ; located north of the SAF), the Polar Frontal Zone (PFZ, located between the SAF and APF) and the Antarctic Zone (AZ; located between the APF and SACCF) (Fig. 1.1). The flow within these regions is eddy dominated without any preferred flow direction (Talley et al., 2011).

Although the ACC flow dominates the large-scale circulation in the SO, the cyclonic circulation of the Weddell and Ross gyres, located south of the ACC, are also crucial components of the SO circulation system as they are considered to be responsible for the formation of the densest waters in the SO (Orsi et al., 1995; Talley et al., 2011). The Weddell Gyre is located in the Atlantic sector of the SO and extends to $\sim 20^{\circ}\text{E}$ and is bounded to the west by a northward flowing boundary current along the Antarctic Peninsula. Its northern limit is marked by the Scotia Ridge (Fig. 1.1) (Orsi et al., 1993). The Ross Gyre of the Pacific sector of the SO extends from $\sim 155^{\circ}\text{E}$ to $\sim 145^{\circ}\text{W}$, whereas its northern limit is strongly associated with the topography of the Pacific-Antarctic Ridge (Fig. 1.1) (Reid, 1986).

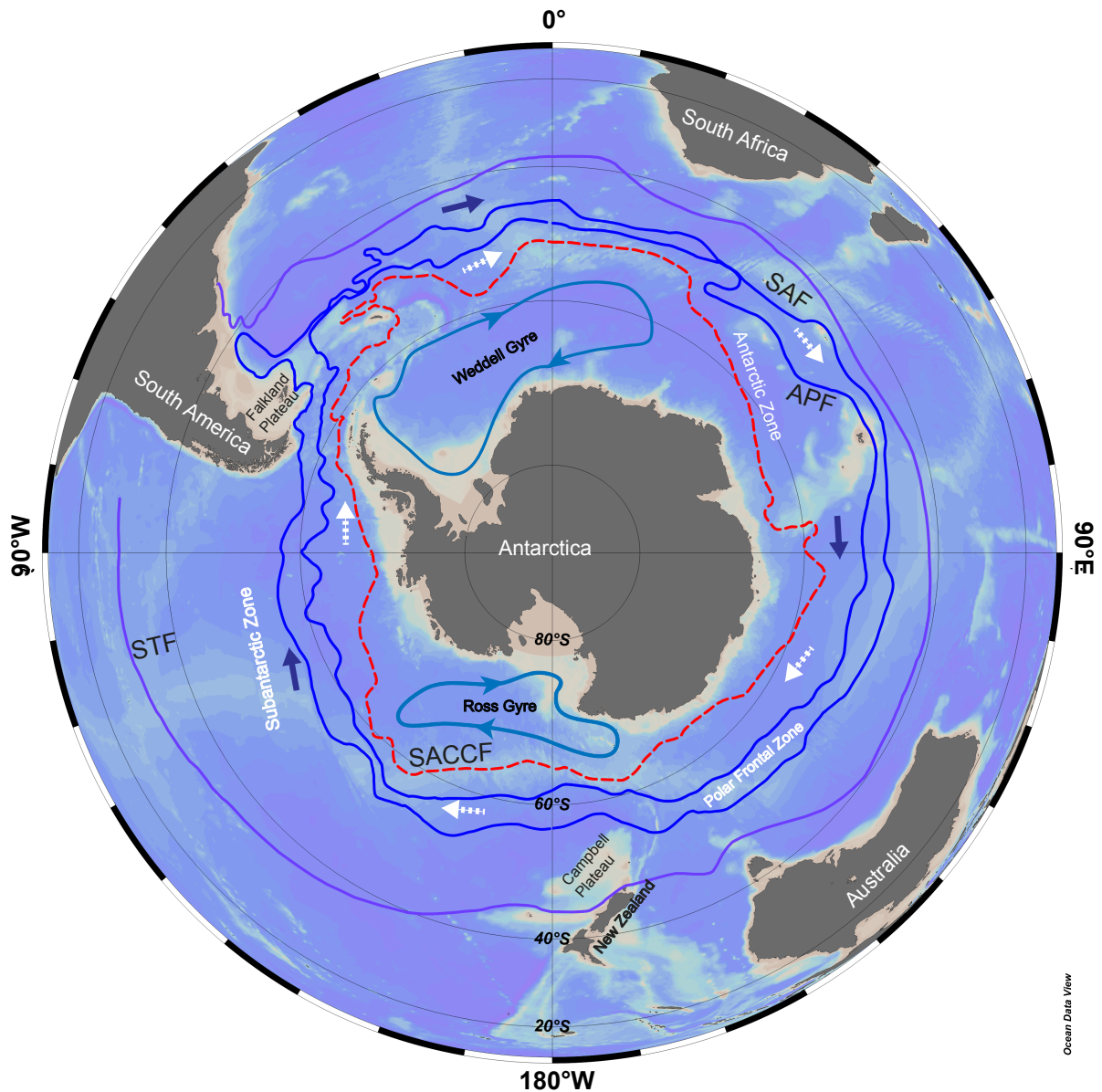


Figure 1.1: Overview map of the entire Southern Ocean. Colored lines refer to mean positions of major front systems (Orsi et al., 1995). STF: Subtropical Front, SAF: Subantarctic Front, APF: Antarctic Polar Front. SACCF: Southern Antarctic Circumpolar Current Front. Dark blue arrows indicate the direction of the SWW. White dashed arrows show the flow direction of the ACC. The map was generated using the Ocean Data View software (Schlitzer, 2015).

1.1.2 Southern Hemisphere climate variability and the role of the Southern Ocean

Approximately 800,000 years of Southern Hemisphere climate history is trapped in Antarctic ice cores (e.g. Jouzel et al., 2007; Lambert et al., 2008; Lüthi et al., 2008). The climate signal extracted from the composition of air sealed in Antarctic ice reveals a strong correlation between atmospheric CO₂ and Antarctic temperature records over the last eight glacial-interglacial (G/IG) cycles (Fig. 1.2) (Jouzel et al., 2007; Lüthi et al., 2008). Atmospheric CO₂ records illustrate a distinct G/IG pattern, with maximum CO₂ values of ~280 to ~300 ppmv (parts per million by volume) during interglacial periods compared to minimum atmospheric CO₂ concentrations during glacial periods (~180 to ~200 ppmv). This is accompanied by synchronous changes in Antarctic temperature, with increased (interglacial) and decreased (glacial) temperatures, respectively (Fig. 1.2) (Jouzel et al., 2007; Lüthi et al., 2008). The driving mechanisms of the coupled G/IG atmospheric CO₂-temperature fluctuations are not yet fully understood, but the interior ocean (which contains about 60 times more carbon than the atmosphere (Broecker, 1982)) is thought to be important for carbon storage. Several mechanisms that mediate the flux of carbon between the interior ocean and the atmosphere have been proposed. These include variations in sea ice cover, changes within the SWW, SO water mass stratification and biochemical processes (linked to variations in atmospheric dust input). Most likely, a combination of all these processes regulates the CO₂-temperature relationship (Sigman and Boyle, 2000; Martínez-García et al., 2009; Ronge et al., 2016).

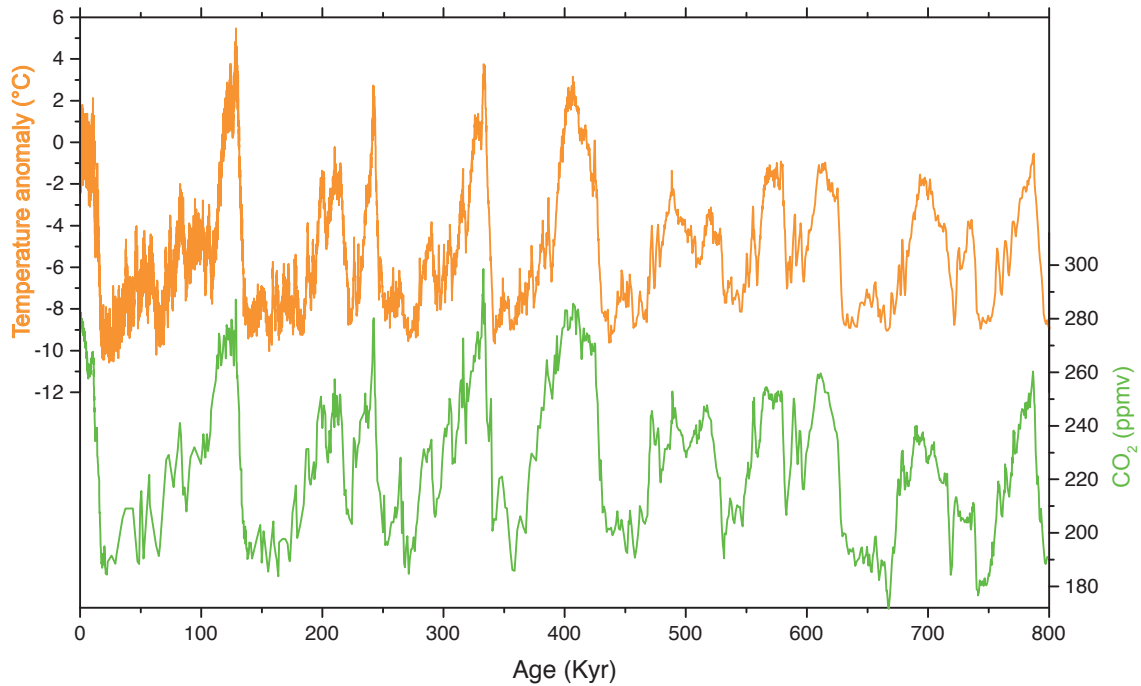


Figure 1.2: ~800.000 years of climate history extracted from Antarctic ice cores. Orange line: Antarctic temperature anomaly calculated from the average of the last 1000 years (Jouzel et al., 2007). Green line: Antarctic CO₂ (Lüthi et al., 2008). Both records were extracted from the EPICA Dome C ice (EDC) core in East Antarctica.

The modern Atlantic ocean consists of a meridional overturning circulation (MOC) system with an upper and lower cell, which are fed by North Atlantic deep water (NADW) and Antarctic Bottom water (AABW), respectively (Talley, 2013) (Fig. 1.3). Both cells are connected through mixing and upwelling in the SO around the Antarctic continent (Fig. 1.3) (Marshall and Speer, 2012; Talley, 2013). In particular, the upwelling branch of the MOC in the SO is thought to significantly affect the global climate system over G/IG time scales because it controls the communication between the deep and the surface ocean and therefore also controls the storage and release of carbon to the atmosphere (Fig. 1.4 a and b) (Huybers and Wunsch, 2010; Talley, 2013; Ronge et al., 2016). The relationship of atmospheric CO₂ and upwelling was, for example, shown by Anderson et al. (2009). They found that increased upwelling rates in the SO correspond with deglacial warming in Antarctica and with increased atmospheric CO₂ concentrations.

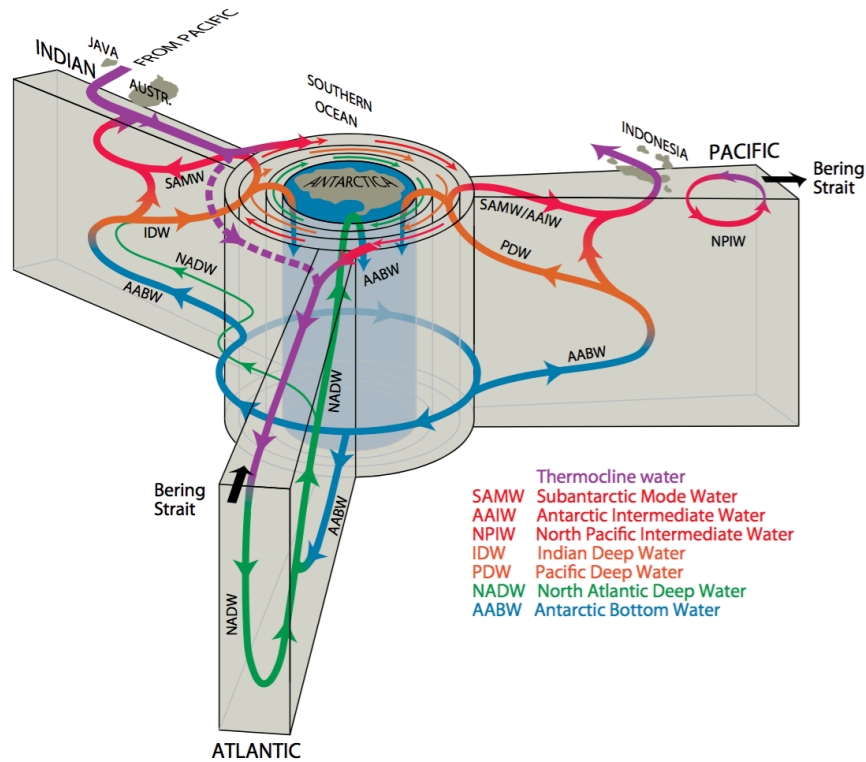


Figure 1.3: Schematic view of the global overturning circulation from a Southern Ocean perspective (from Talley, 2013).

The glacial drawdown of atmospheric CO_2 was enabled through the northernmost extend of sea ice coupled with equatorward shifted SWW and a pronounced SO water mass stratification, which favored the storage of carbon in deep water masses (Fig. 1.4 a) (e.g. Sigman et al., 2010; Ronge et al., 2016). Additionally, atmospheric dust in the glacial SO is considered to play a major role in the carbon storage through iron fertilization (see 1.2.2).

In contrast, the deglacial rise in atmospheric CO_2 was enabled by a combination of reduced sea ice cover around Antarctica coupled with a southward expansion/shift of the SWW (e.g. Toggweiler et al., 2006; Skinner et al., 2010; Ronge et al., 2016). These factors may have led to enhanced upwelling of deep and carbon-rich water masses in the SO resulting in increased outgassing of CO_2 to the atmosphere (Fig. 1.4 b) (e.g. Anderson et al., 2009; Skinner et al., 2010).

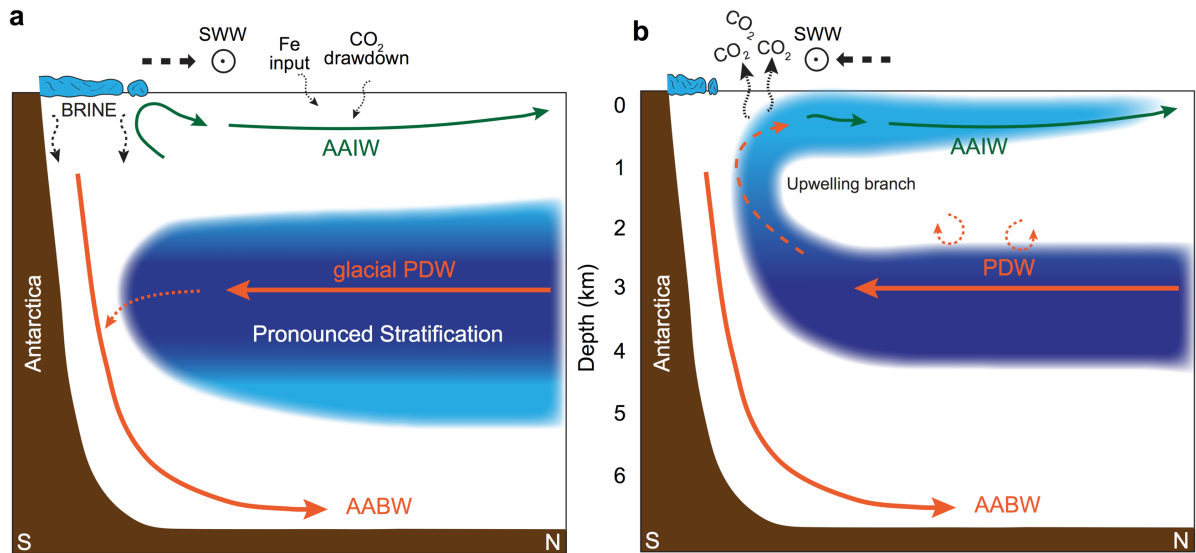


Figure 1.4: Schematic view of water masses in the Southern Ocean illustrating the process of carbon storage and release to the atmosphere (modified from Ronge et al., 2016). a: Glacial conditions. The northernmost extend of sea ice coupled with equatorward shifted SWW and a pronounced SO water mass stratification favored the storage of carbon in deep water masses resulting in a drawdown of atmospheric CO₂. b: Deglacial conditions. Reduced sea ice cover around Antarctica coupled with a southward expansion/shift of the SWW resulted in enhanced upwelling of deep and carbon-rich water masses in the Southern Ocean. This process leads to increased outgassing of CO₂ to the atmosphere. SWW: Southern Westerly Winds. Abbreviations for water masses refer to the key of figure 1.3.

1.2 Atmospheric dust – a powerful tool for paleoclimate reconstructions

Atmospheric dust responds rapidly to paleoclimate changes in potential source areas (PSAs) (e.g. aridity, precipitation) and variations within the dust transporting winds (e.g. SWW). Subsequently, the interpretation of the dust variability in marine dust records downwind of the major Southern Hemisphere PSAs has the capability to contribute to a better understanding of paleoclimate changes over G/IG timescales. A good knowledge of the dust provenance, the dust grain size patterns and the dust distribution in the Pacific and Atlantic sectors of the SO is a prerequisite to accurately infer past climate changes from marine dust records.

1.2.1 Dust erosion, emission, transport and deposition in the Southern Hemisphere

The global dust cycle is built on different processes including dust erosion, emission, transport and deposition. On a global 20-year average $\sim 2323 \text{ Tg a}^{-1}$ of dust is emitted into the atmosphere. Dust source areas in the Northern Hemisphere contribute $\sim 90\%$ to the total global dust budget, with the largest amounts originating in northern Africa (Li et al., 2008). In contrast, the remaining $\sim 10\%$ is supplied by Australian/New Zealand, South American and South African PSAs (Fig. 1.5) (Li et al., 2008). Australia and New Zealand are considered to be the predominant PSAs in the Southern Hemisphere supplying almost the entire Pacific sector of the SO with dust (Fig. 1.5). In total, Australian PSAs emit $\sim 120 \pm 8.4 \text{ Tg a}^{-1}$ (20-year average) (Li et al., 2008). The second largest Southern Hemisphere PSA is South America covering the Atlantic sector of the SO and also large parts of East Antarctica (Fig. 1.5). The total amount of dust supplied from South American PSAs is $50 \pm 3 \text{ Tg a}^{-1}$ (20-year average) (Li et al., 2008). South African dust is predominantly distributed over the equatorial Atlantic and over parts of the Indian Ocean with a total emission of $34 \pm 2.1 \text{ Tg a}^{-1}$ (20-year average) (Fig. 1.5) (Li et al., 2008).

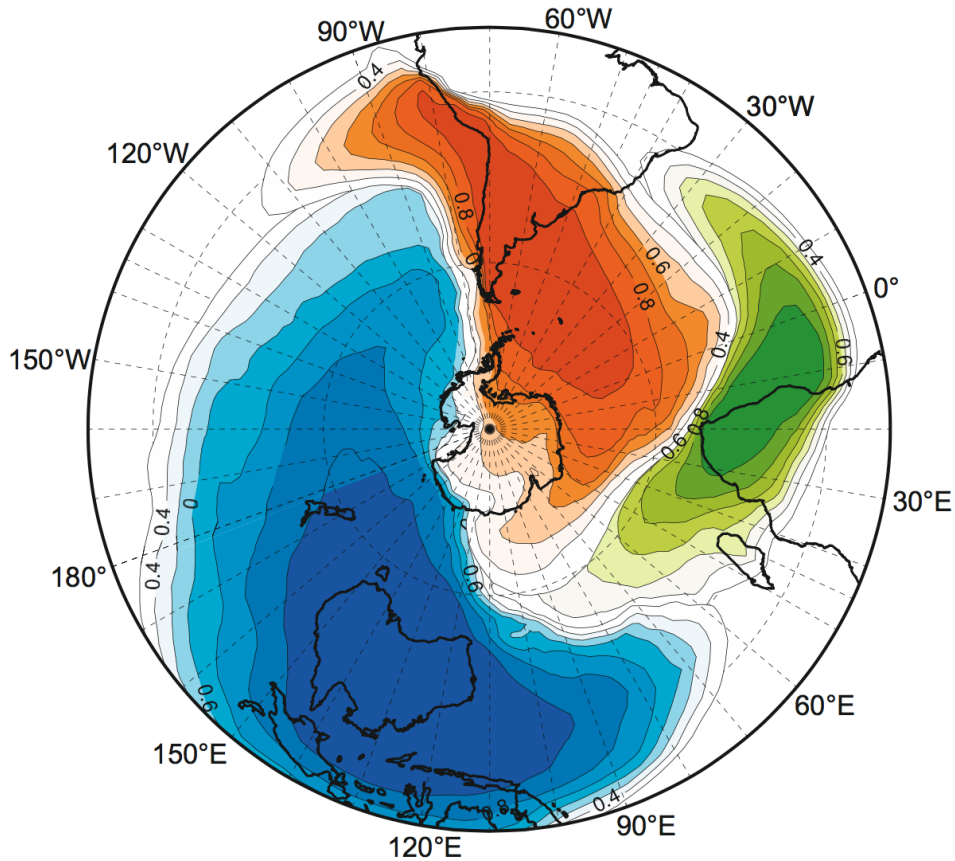


Figure 1.5: Major Southern Hemisphere PSAs and their contributions to the Southern Ocean (from Li et al., 2008).

Southern Hemisphere long-range dust transport is strongly associated with the SWW and variations within this wind belt are thought to affect the dust transport. Wind is an extremely size-selective transport medium resulting in a decrease of the dust grain size with increasing distance from the PSAs. However, prior to long-range dust transport several factors influence the availability of dust in the source areas.

Generally, dust erosion predominantly depends on the interaction of climatic conditions (e.g. aridity, precipitation), soil and terrain properties (e.g. vegetation cover) and wind stress in the PSAs. The erosion of dust is tightly coupled with forces holding the dust particles at the surface (erosion threshold): (1) the particle weight and (2) cohesion forces holding the dust particles together (Marticorena, 2014). Subsequently, dust emission only occurs when the erosion threshold, which depends on the surface roughness (e.g. vegetation, snow cover, pebbles, stones, salt crusts) in the PSAs, is reached (Maher et al., 2010; Marticorena, 2014). An increased surface roughness inhibits dust entrainment because it blocks the momentum induced by wind (Marticorena, 2014). Another crucial parameter that controls dust erosion is the soil

moisture. Depending on the salt content and the soil structure it can affect the erosion threshold (Maher et al., 2010). Subsequently, the main dust erosion areas are located in arid or semi-arid regions with low precipitation rates and almost no vegetation cover (Prospero et al., 2002). Dust erosion in the PSAs is controlled by different entrainment mechanisms, which are related to grain shape, grain size and grain density (Marticorena, 2014). The largest particles ($> 1000 \mu\text{m}$) are transported through a creeping motion at the soil surface (Marticorena, 2014). In detail, three dust entrainment mechanisms can be described: (1) direct entrainment of dust particles by wind. However, this process requires very strong wind friction velocities (Loosmore and Hunt, 2000) (Fig. 1.6 a); (2) dust emission through the impact of salting grains that hit the surface (sandblasting). The impact of the salting particles brakes the cohesion forces and releases dust (Fig. 1.6 b) (Gomes et al., 1990); (3) disaggregation of salting particles (auto-abrasion) (Fig. 1.6 c) (Warren et al., 2007). In field studies, it was shown that saltation is the most important process for dust entrainment (e.g. Sow et al., 2009) and particles $\sim < 20 \mu\text{m}$ resulting from saltation processes can easily be uplifted by wind (Marticorena, 2014).

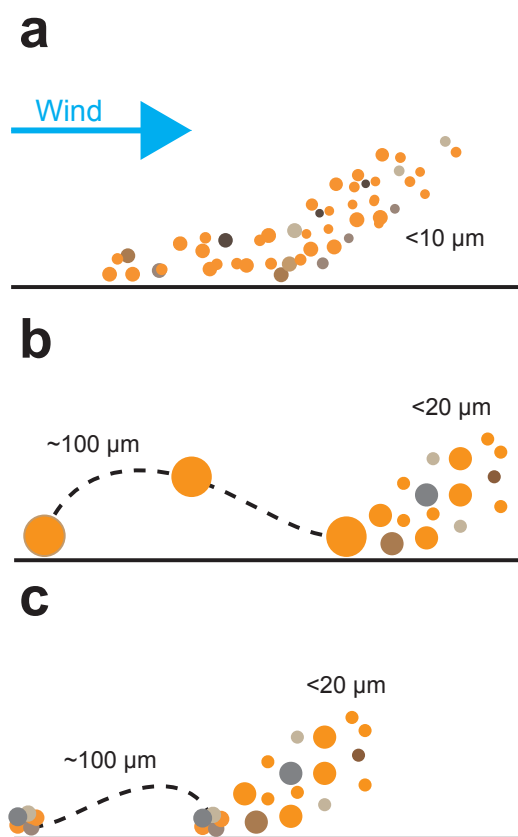


Figure 1.6: Schematic illustration of dust erosion processes in the PSAs. a: Direct entrainment of dust particles through wind. b: Dust erosion through salting grains. Salting grains hit the surface and their impact releases dust. c: Disaggregation of salting particles. Single grains form aggregates and disaggregate when they hit the ground (modified from Marticorena, 2014).

The atmospheric residence time of dust and its deposition is controlled by two processes: (1) dry deposition and (2) wet deposition. Dry deposition, largely controlled by gravitational settling (which depends on the grain shape, the grain size and the grain density), is the main removal process near to the PSAs (Zhao et al., 2003). In contrast, with increasing distance from the PSAs, wet deposition, driven by the presence of water (e.g. rain, snow), becomes increasingly important and can exceed the dry deposition by up to a factor of 10 (Zhao et al., 2003). For the SO, simulations show that wet deposition processes make up ~90 % of the total deposition for dust that originates in Australian PSAs (Li et al., 2008).

1.2.2 Atmospheric dust and its impact on the Southern Hemisphere climate

The role of dust in the climate system is associated with processes occurring in the atmosphere and in the ocean. Once the dust is in the atmosphere, it can be transported for thousands of kilometers (Tsoar and Pye, 1987) and has the capability to affect the global radiative balance in two ways: (1) directly, by influencing the radiative properties of the atmosphere through scattering and absorbing incoming sunlight. Both, the absorbing and scattering properties of atmospheric dust particles leads to a warming of the atmosphere and cooling of the surface through blocking incoming sunlight (Maher et al., 2010); (2) indirectly, by modifying cloud properties (Fig. 1.7) through acting as cloud condensation nuclei and/or ice nuclei (Arimoto, 2001; Sassen et al., 2003), which for example can affect precipitation patterns.

Furthermore, dust has the capability to influence the climate by supplying iron (Fe) to the ocean, which increases the surface ocean productivity (iron fertilization) (Fig. 1.7). In detail, the SO surface waters contain large amounts of macronutrients, such as nitrate and phosphate, but are simultaneously characterized by a limited biological productivity represented by low chlorophyll concentrations (Martínez-García et al., 2009; Fischer et al., 2010; Martínez-García et al., 2011; Martínez-García et al., 2014). Based on these properties, the SO is considered to be the world's largest high-nutrient low-chlorophyll (HNLC) region, where the reduced biological productivity is thought to be a result of the scarcity of Fe (Martin, 1990). John H. Martin (1990) suggested that elevated glacial dust fluxes to the SO would have increased the marine biological productivity and simultaneously the photosynthetic activity. As a result, carbon was removed from the atmosphere and stored in SO deep water masses resulting in a glacial drawdown of atmospheric CO₂ (Fig. 1.7). The effect of large-scale iron fertilization on the marine productivity has been demonstrated using down core sediment records from the Subantarctic zone of the Atlantic sector of the SO. The results show that an increased nitrate

consumption (indicative for increased biological productivity) through marine phytoplankton corresponds with intervals of high dust fluxes (Martínez-García et al., 2014).

The iron fertilization is an effective way of drawing down atmospheric CO₂ because carbon is sequestered in the deep ocean and in the sediments. Carbon, which is transported to the deep ocean layers and sediments of the SO, can be sequestered for decades to centuries or even longer (Smetacek et al., 2012). In contrast, carbon stored within the winter-mixed layer (upper 200 m) of the SO can be remineralized back to CO₂ through microbes and zooplankton and would be released to the atmosphere within months (Smetacek et al., 2012). To ensure transport of organic matter to the deep ocean and sediments, the grain size and shape of atmospheric dust particles play a crucial role. Dust particles and the carbon containing organic matter form aggregates, so that the transport of organic matter towards the sediment is accelerated and the remineralization back to CO₂ in the upper part of the ocean is prevented (ballasting effect) (Fig. 1.7) (Stuut and Prins, 2014). In general, the whole mechanism of atmospheric CO₂ removal from the atmosphere induced by iron fertilization and sequestration of carbon is referred to as “biological pump” (Fig. 1.7).

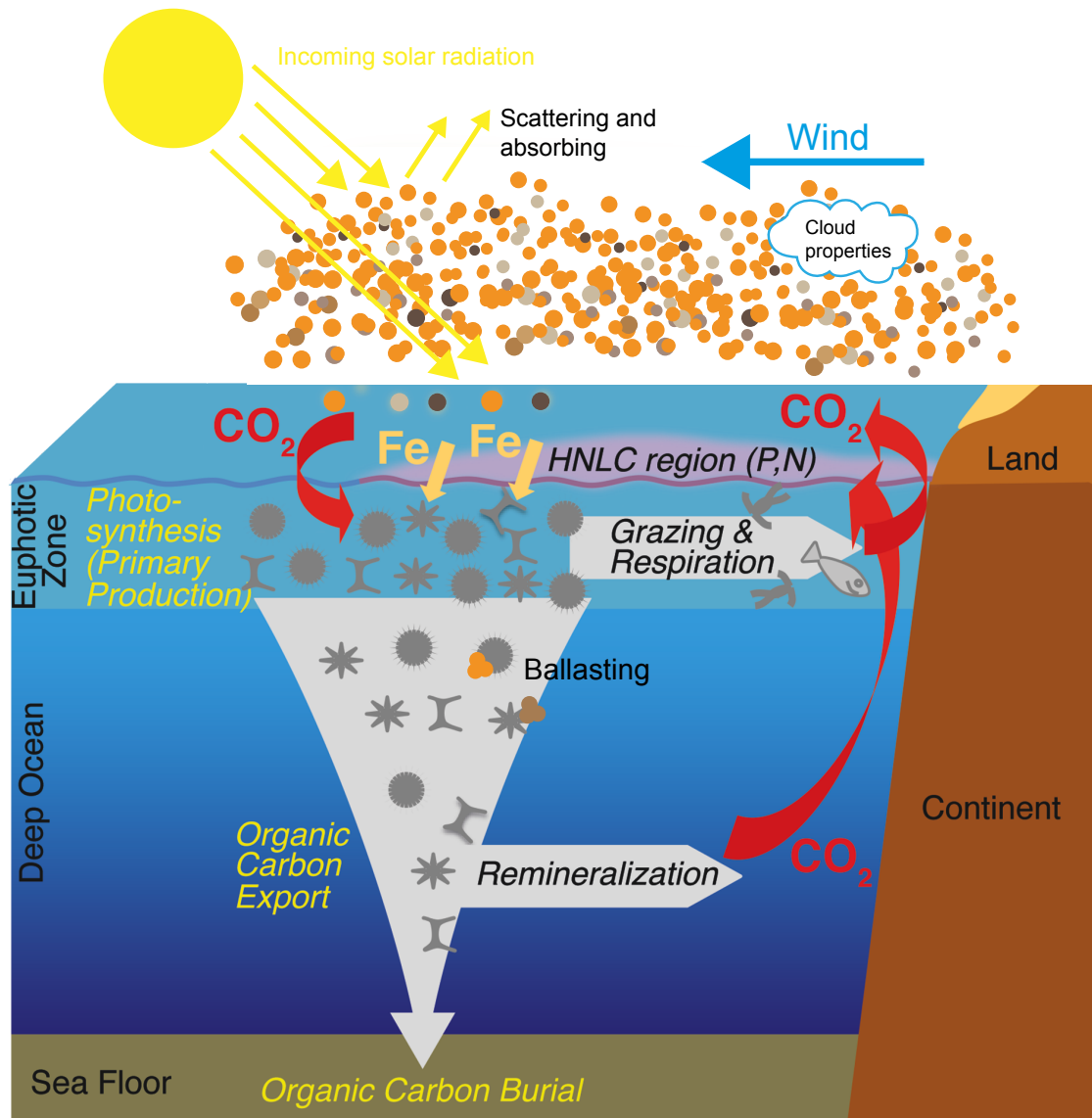


Figure 1.7: Schematic illustration of iron fertilization processes in the glacial ocean and dust related processes in the atmosphere (modified from Martínez-García and Winckler, 2014). The dust plume scatters and/or absorbs the incoming sunlight or affects the cloud properties. Increased glacial dust fluxes supply Fe to the ocean, which leads to an increased marine biological productivity and photosynthetic activity. As a result, carbon was removed from the atmosphere and stored in Southern Ocean deep water masses. This results in a glacial drawdown of atmospheric CO₂. Dust particles and the carbon containing organic matter form aggregates, so that the transport of organic matter towards the sediment is accelerated and the remineralization back to CO₂ in the upper part of the ocean is prevented (ballasting effect).

Based on distinct similarities of Antarctic CO₂, temperature and dust records (Jouzel et al., 2007; Lambert et al., 2008; Lüthi et al., 2008; Lambert et al., 2012) with Fe records from the Pacific and Atlantic sectors of the SO (Fig. 1.8) (Martínez-García et al., 2009; Lamy et al., 2014), it was suggested that the process of iron fertilization in the SO was, along with other processes (see. 1.1.2), an important driver of the G/IG offset in atmospheric CO₂ (80-100 ppmv in total) and likely responsible for an atmospheric CO₂ reduction of ~40 ppmv during glacial periods (Fig. 1.8 b) (Kohfeld et al., 2005; Martínez-García et al., 2009; Martínez-García et al., 2011). This corresponds with a ~25-fold increase in glacial Antarctic dust fluxes (Fig. 1.8 c) (Lambert et al., 2012) and a ~3-fold increase in glacial dust fluxes in the Pacific sector of the SO (Fig. 1.8 e) (Lamy et al., 2014). A biogeochemical model, which tested the impact of increased dust deposition rates on the marine biological productivity, suggests that the maximum dust input was only responsible for a < 30 ppmv reduction of atmospheric CO₂ (Bopp et al., 2003). Despite the discrepancy in the total amount of atmospheric CO₂ removed from the atmosphere, these studies clearly illustrate that dust is a crucial component of the global climate system.

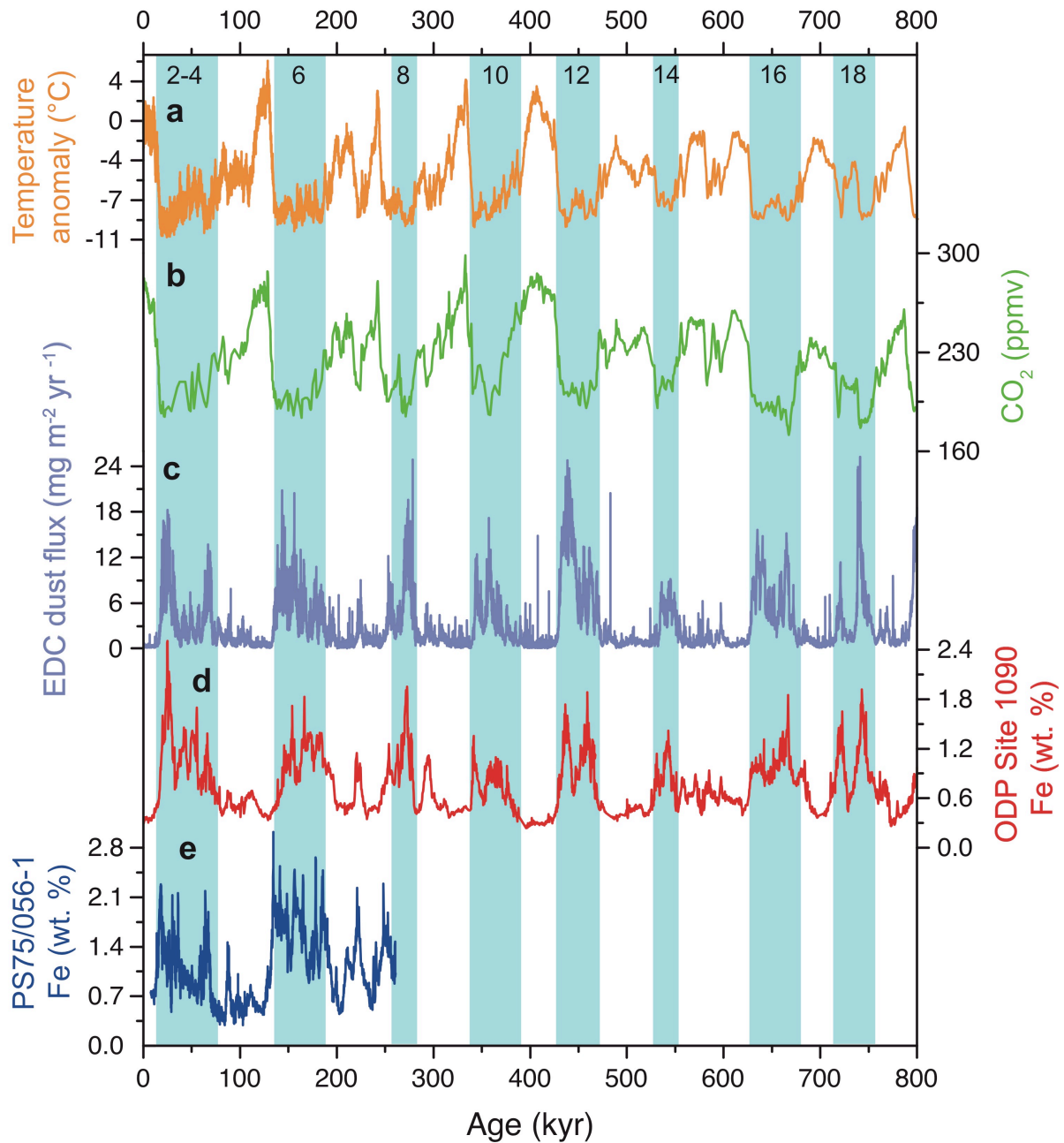


Figure 1.8: a: Antarctic temperature anomaly calculated from the average of the last 1000 years (Jouzel et al., 2007). b: Antarctic CO₂ (Lüthi et al., 2008). c: Antarctic dust flux (Lambert et al., 2012). d: Fe record from the Atlantic sector of the Southern Ocean (Martínez-García et al., 2009). e: Fe record from the Pacific sector of the Southern Ocean (Lamy et al., 2014). Light blue shadings refer to glacial periods. Numbers indicate the marine isotope stages. See chapter 4 for the location of the sediment cores PS75/056-1 and ODP Site 1090.

1.3 Motivation and objectives of the thesis

Current knowledge about the modern distribution of dust in the SO is largely based on modeling studies (Mahowald et al., 2006; Li et al., 2008; Maher et al., 2010; Albani et al., 2014; Neff and Bertler, 2015) and on satellite observations (e.g. Prospero et al., 2002; Gaiero et al., 2013). However, most dust deposition models for the SO underestimate dust deposition rates and therefore, large discrepancies exist between model and sediment data (Fig. 1.9). Sediment based data that provide insights on the spatial and temporal distribution of dust in the SO are limited to a small number of studies (Chase et al., 2003; Bradtmiller et al., 2009; Martínez-García et al., 2009; Martínez-García et al., 2011; Anderson et al., 2014; Lamy et al., 2014). For example, down core sediment records from the Pacific Sector of the SO document increased glacial dust supply accompanied by eastward decreasing lithogenic fluxes (Lamy et al., 2014). This observation is consistent with other studies, which similarly show increased lithogenic fluxes during the last glacial maximum (LGM) compared to the Holocene (Chase et al., 2003; Bradtmiller et al., 2009). In the Atlantic sector of the SO, dust variability reconstructions are restricted to a very few studies (Martínez-García et al., 2009; Martínez-García et al., 2011; Anderson et al., 2014; Martínez-García et al., 2014). For example, Martínez-García et al. (2009, 2011, 2014) used Fe, thorium (Th) and dust fluxes coupled with nitrate consumption data from a sediment core located in the eastern part of the Atlantic sector of the SO to estimate the coupling of dust and marine productivity. The results reveal the same G/IG dust accumulation pattern as the Pacific sector of the SO. Anderson et al. (2014) showed that lithogenic fluxes and paleo-productivity data from three sediment cores from the central Atlantic sector of the SO correspond with dust fluxes from the EPICA Dome C (EDC) ice core in East Antarctica.

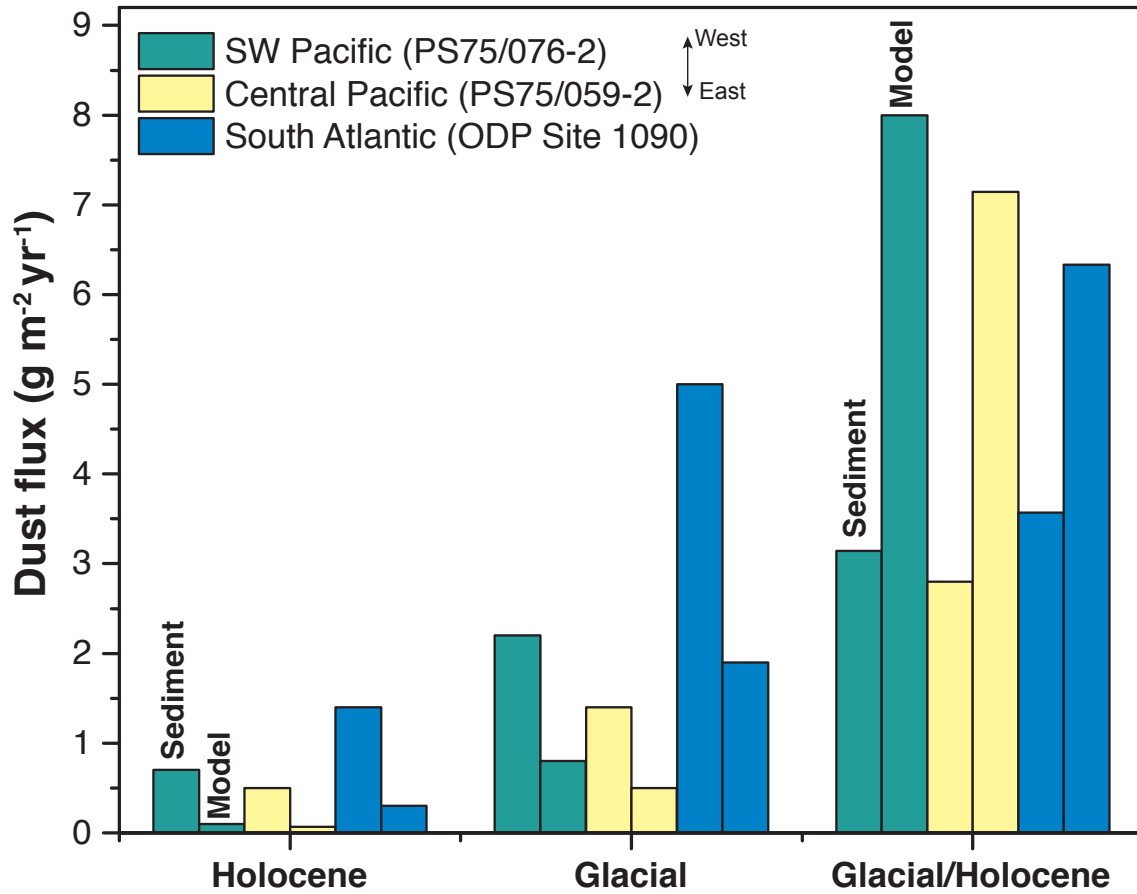


Figure 1.9: Comparison between sediment (Lamy et al., 2014) and model derived (Albani et al., 2012b) lithogenic fluxes ($\text{g m}^{-2} \text{yr}^{-1}$) in the Pacific and Atlantic sectors of the Southern Ocean. Note the eastward decrease in lithogenic fluxes in the Pacific sector of the Southern Ocean during glacial periods. In the Atlantic sector of the Southern Ocean lithogenic fluxes are generally higher compared to the Pacific sector.

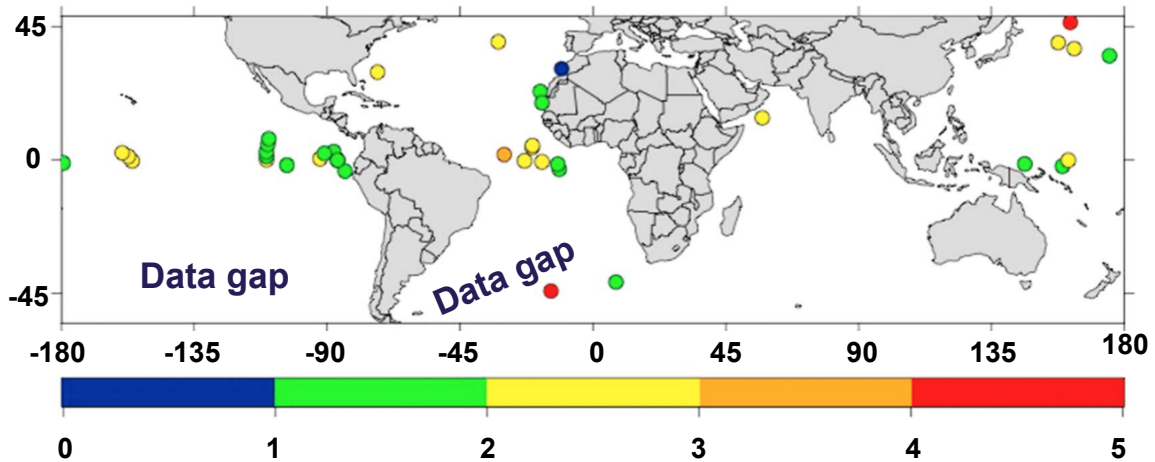


Figure 1.10: LGM/Holocene ratios of lithogenic fluxes ($\text{g m}^{-2} \text{ yr}^{-1}$) (from Kienast et al., 2016). It is noteworthy that large data gaps exist in the Pacific and Atlantic sectors of the SO.

As shown in figure 1.10, the availability of dust data sets is extremely scarce and large data gaps exist in the Pacific and Atlantic sectors of the SO. The main motivation for this thesis is to provide dust grain size, dust provenance and dust flux data in the Pacific and Atlantic sectors of the SO with the overarching objective to contribute to a better understanding of paleoclimate changes inferred from the dust variability of marine dust records from the SO. Based on this overarching objective the following general scientific questions arise.

- *Did the dust variability and provenance in the Pacific sector of SO change throughout the Holocene?*
- *Did the dust input and grain size vary over G/IG cycles in the Pacific and Atlantic sectors of SO?*

To achieve the thesis objectives, four manuscripts are presented, which each reveals different approaches and methods (chapters 3, 4, 5 and 6).

Manuscript one (chapter 3) provides new geochemical data from the Pacific sector of the SO. This study provides a unique data set that covers the entire polar and subpolar zones of the Pacific sector of the SO and combines lithogenic fluxes and a broad range of provenance sensitive proxies (REE, Sr, Nd and Pb isotopes). The major objective of this manuscript is to

reconstruct modern dust fluxes and to identify the modern dust provenance areas to the Pacific sector of the SO.

Manuscript two (chapter 4) provides the first coupled down core records from the subpolar zones of the Pacific and Atlantic sectors of the SO combining down core grain size analysis, lithogenic fluxes and Fe records. The main objective of this study is to understand the large-scale dust variability over G/IG cycles as consequence of changes in source area characteristics and the dust transporting SWW.

In the third manuscript (chapter 5) different biomarker analyses were conducted with the major objective to reconstruct modern dust variability, marine productivity and sea surface temperatures in the Pacific sector of the SO.

The major objective of manuscript four (chapter 6) is to reconstruct the Drake passage throughflow, which is linked to variations of the SWW. Considering that Southern Hemisphere long-range dust transport is tightly coupled to changes within the SWW the results of this study provide valuable information for dust transport to the Pacific and Atlantic sectors of the SO.

1.4 Authors contribution

A geochemical approach to reconstruct modern South Pacific dust fluxes and potential dust source areas (chapter 3)

Authors: *Marc Wengler*, Frank Lamy, Torben Struve, Alejandra Borunda, Philipp Böning, Walter Geibert, Gerhard Kuhn, Katharina Pahnke, Jenny Roberts, Ralf Tiedemann, Gisela Winckler

Publication status: Under review at *Geochimica et Cosmochimica Acta*

The sediment surface samples were recovered during expeditions with R/V *Polarstern* (PS75, PS58, PS35) and R/V *Sonne* (SO213) without my contribution. For the uranium-thorium (U-Th) series analysis of the SO213 samples, I performed the chemical treatment to dissolve the samples, all chemical steps to separate uranium (U) and Th from the matrix elements and the mass spectrometric analysis of the samples. The U-Th concentrations of the *Polarstern* samples were measured by Dr. Water Geibert and Dr. Sven Kretschmer. I calculated the Th-derived lithogenic fluxes for all samples (SO213, PS75, PS58, PS35).

For the provenance analysis, I performed all steps described in the manuscript including the chemical treatment to dissolve the samples and all chemical steps to separate rare earth elements (REE), neodymium (Nd), strontium (Sr) and lead (Pb) from the matrix elements. Additionally, I conducted the mass spectrometric analysis of the REE, Nd, Sr and Pb isotopes. I wrote the entire manuscript and all co-authors reviewed the draft version and contributed to the manuscript.

Opposing dust grain size changes in the Pacific and Atlantic sectors of the Southern Ocean during the last 260 kyr (chapter 4)

Authors: *Marc Wengler*, Frank Lamy, Alfredo Martínez-García, Gerhard Kuhn, Jan-Berend Stuut, Ralf Tiedemann, Gisela Winckler

Publication status: In preparation for *Earth and Planetary Science Letters*

The sediment cores were recovered during expeditions with R/V *Polarstern* (PS75) and *JOIDES Resolution* (ODP Site 1090, Leg 177) without my contribution. I conducted all chemical leaching steps of sediment core PS75/056-1 to receive the terrigenous fraction for the grain size analysis. I developed a new method to obtain the terrigenous fraction from extremely opal-rich sediments (see chapter 4). Moreover, I performed the grain size analysis, the subsequent data analysis and calculation of the grain size statistics. The Fe and Th-derived lithogenic flux data were provided by Gisela Winckler from the *Lamont-Doherty Earth Observatory*.

The grain size data of ODP Site 1090 were provided by Alfredo Martínez-García from the *Max Planck Institute for chemistry*.

A biomarker perspective on dust, productivity, and sea surface temperature in the Pacific sector of the Southern Ocean (chapter 5)

Authors: Andrea Jaeschke, **Marc Wengler**, Jens Hefter, Thomas A. Ronge, Walter Geibert, Gesine Mollenhauer, Rainer Gersonde, Frank Lamy

Publication status: Published in *Geochimica et Cosmochimica Acta*

I conducted the U-Th series analysis of the SO213 samples including the chemical treatment to dissolve the samples, all chemical steps to separate U and Th from the matrix elements and the mass spectrometric analysis of the samples. The U-Th concentrations of the *Polarstern* samples were measured by Dr. Walter Geibert and Dr. Sven Kretschmer. I calculated the Th-derived lithogenic fluxes for all samples (SO213, PS75, PS58, PS35). Additionally, I wrote the section “Th and U isotope analysis and flux calculations” and contributed to the interpretation of the results and discussion during the writing and review processes.

Glacial reduction and millennial-scale variations in Drake Passage throughflow (chapter 6)

Authors: Frank Lamy, Helge W. Arz, Rolf Kilian, Carina B. Lange, Lester Lembke-Jene, **Marc Wengler**, Jérôme Kaiser, Oscar Baeza-Urrea, Naomi Harada, Ralf Tiedemann

Publication status: Published in *Proceedings of the National Academy of Sciences of the United States of America*

I performed all chemical leaching steps of sediment core MR0806-PC9 to extract the terrigenous fraction for the grain size analysis. Additionally, I conducted the grain size analysis and calculated the grain size statistics. I contributed to the interpretation of the results and discussion during the writing and review processes.

2 Sediment material and methodology

2.1 Sediment material

Figure 2.1 shows all sediment samples that I used to produce the data provided in chapters 3, 4, 5 and 6. The sample material that is not shown in figure 2.1 but is part of the studies presented in chapters 5 and 6 is described in the manuscripts, respectively.

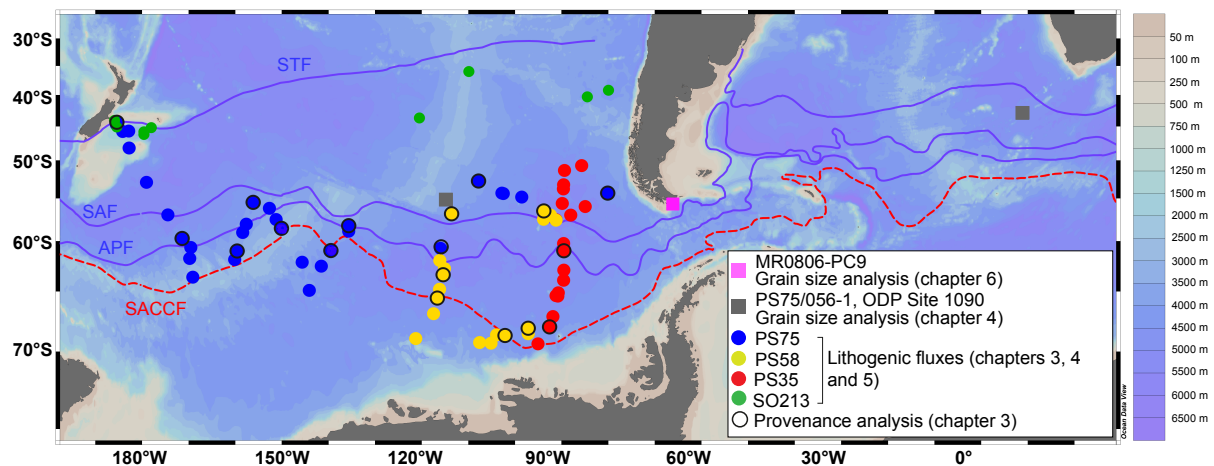


Figure 2.1: Overview map of the Pacific and Atlantic sectors of the Southern Ocean. The colored dots refer to sediment surface samples used in chapters 3, 4 and 5 for provenance analysis (black frame) and lithogenic flux calculations. The color codes refer to different expeditions with R/V *Polarstern* (PS75, 58 and 35) (Gersonde, 1995; Gersonde, 2001; Gersonde, 2011) and R/V *Sonne* (SO213) (Tiedemann, 2012). The dark grey squares refer to sediment core PS75/056-1 and ODP Site 1090 used in chapter 4 for grain size analysis. The pink square shows sediment core MR0806-PC9 used in chapter 6 for grain size analysis. Colored lines refer to the mean positions of the major front systems (Orsi et al., 1995). STF: Subtropical Front, SAF: Subantarctic Front, APF: Antarctic Polar Front. SACCF: Southern Antarctic Circumpolar Current Front. The map was generated using the Ocean Data View software (Schlitzer, 2015).

2.2 Methodology

In the following, I describe the basis of the methods that I conducted to produce my data contribution to chapters 3, 4, 5 and 6. The methods that are not explained in the following but are part of the studies presented in chapters 5 and 6 were conducted by the co-authors and are described in the manuscripts methods section, respectively.

2.2.1 ^{230}Th -normalized fluxes as tracer for dust input

The ^{230}Th isotope is important in paleoclimate studies because it can be used as a constant flux proxy allowing the reconstruction of sediment (dust) fluxes to the seafloor. A detailed description and application of this proxy is given in chapter 3.

The ^{230}Th isotope is a product of the ^{238}U decay series (Francois et al., 2004) with a half-life time of 75.548 ± 110 years (Cheng et al., 2013). It is produced by its parent isotope ^{234}U through an α -decay ($^{238}\text{U} \rightarrow ^{234}\text{Th} \rightarrow ^{234}\text{Pa} \rightarrow ^{234}\text{U} \rightarrow ^{230}\text{Th}$) (Francois et al., 2004). Continental weathering of crustal rocks is of essential importance for the use of the U-series in paleoceanographic studies because U exits as a minor element in most crustal rocks (Francois et al., 2004). In old crustal rocks, which are not affected by weathering, the U-decay series is in secular equilibrium, which means that the activity of the ^{230}Th isotope is equal to the activity of the remaining isotopes within the U-decay series (Francois et al., 2004). However, during weathering processes, U isotopes are more mobile than Th isotopes, so that Th isotopes remain in the rocks (solid phase), whereas U isotopes are released into solution (Francois et al., 2004). Of the two U isotopes, ^{234}U is more readily released into solution during weathering than ^{238}U (Chabaux et al., 2003). As a result, seawater is enriched in ^{234}U relative to ^{238}U (activity ratio 1.14) and depleted in ^{230}Th . A fraction of ^{230}Th called “detrital” Th is delivered to the ocean predominantly by dust input and particles reaching the ocean by rivers (Francois et al., 2004). The transport of U isotopes to the ocean is also associated with “detrital” U attached to mineral particles (Henderson and Anderson, 2003). However, the additions of both “detrital” ^{230}Th and “detrital” U are of minor interest for using ^{230}Th as a constant flux proxy (Chase, 2008).

In dissolved form, the U concentration in seawater reveals a conservative behavior and its concentration is proportional to seawater salinity (Francois et al., 2004). It is estimated that U has a residence time of ~ 320 - ~ 560 kyr in the water column before it is removed into marine sediments (Dunk et al., 2002; Henderson, 2002; Henderson and Anderson, 2003). Hence, U is well mixed in the seawater and produces ^{230}Th at a uniform and well-known rate ($\beta = 0.0267$

dpm m⁻³year⁻¹) (Francois et al., 2004). The production of ²³⁰Th from ²³⁴U in the water column can be calculated by multiplying the ²³⁰Th decay constant ($\lambda = 9.2174 * 10^{-6} \text{ yr}^{-1}$) with the ²³⁴U activity (~2910 dpm m⁻³). In seawater, ²³⁰Th is extremely insoluble and highly particle reactive. Attached to sinking particles, ²³⁰Th is rapidly transported to the seafloor (scavenging) (Thomson et al., 1993; Francois et al., 2004). This results in a very low average residence time of ²³⁰Th in the water column of approximately 20 years (Henderson and Anderson, 2003). Sediment particles in the water column are assumed to contain a detrital fraction of ²³⁰Th approximately in a secular equilibrium with ²³⁴U. However, the total amount of ²³⁰Th in deep-sea sediments near the sediment surface exceeds the amount supported by ²³⁴U. This fraction of ²³⁰Th is called ²³⁰Th_{xs} (230-Thorium excess) and forms the basis for the ²³⁰Th-normalization method (Francois et al., 2004).

Through normalizing ²³²Th (common Th) concentrations to the flux of ²³⁰Th_{xs}, dust fluxes to the seafloor can be calculated, which are unaffected by lateral sediment redistribution at the seafloor. Any correction for lateral sediment redistribution relies on the assumption that the lateral distributed and the vertically deposited sediment have identical Th concentrations, so that the flux calculation is not biased through lateral input (Geibert et al., 2005). In the remote open ocean, the ²³²Th isotope can be used as a dust proxy because particles derived from continents are the only known source of ²³²Th to the ocean (Brewer et al., 1980). The principle of this concept is that the upper continental crust is distinctly enriched in ²³²Th (10.7 ppm) (Taylor and McLennan, 1995) and that particles derived from crustal material, such as mineral dust, are close to 10.7 ppm.

2.2.2 Radiogenic isotopes and rare earth elements as tracers for dust provenance

For a detailed description of radiogenic isotopes and rare earth elements (REE) as dust provenance tracers see chapter 3. The reconstruction of the dust provenance to the SO allows to infer paleoclimate changes within the atmospheric circulation and conditions in the PSAs over G/IG timescales.

Radiogenic isotopes, such as strontium (Sr), neodymium (Nd) and lead (Pb) combined with REE, can be powerful tools to infer the dust provenance in the marine realm. The concept of extracting the concentrations of radiogenic isotopes (Sr, Nd, Pb) and REE from marine sediment samples relies on the assumption that the concentrations of these elements are representative of PSAs. Dust particles can be derived from mantle- (e.g. basaltic rocks, tephra and particles originating from these lithologies, weathered and eroded mafic particles) or

crustal-like compositions (e.g. soils, sediments). Depending on these two sources, radiogenic isotopes allow discrimination between different source lithologies (Grousset and Biscaye, 2005).

The radiogenic ^{87}Sr isotope is a decay product of the parent isotope ^{87}Rb (rubidium) (β -decay; half-life time 48.8 Gyr) (Dickin, 1995b). By contrast, ^{86}Sr is not part of the radioactive decay process and therefore used for normalization. The main principle of the Rb-Sr isotope system in provenance analysis relies on the fractionation of both elements during partial melting of the earth's mantle. Rb is more incompatible than Sr and therefore enriched in the melt and subsequently in the earth's crust, whereas Sr remains in the mantle. As a result, the earth's crust is characterized by higher Rb/Sr and consequently higher $^{87}\text{Sr}/^{86}\text{Sr}$ ratios, whereas the mantle has lower ratios (Okrusch and Matthes, 2005).

The same principle forms the basis for the use of the Sm-Nd isotope system as a tracer for atmospheric dust provenance. The radiogenic ^{143}Nd isotope is produced from ^{147}Sm (samarium) by an α -decay with a half-life time of 106 Gyr (Dickin, 1995c). Sm is enriched in the earth's mantle and depleted in the crust. In contrast, Nd is enriched in the earth's crust and depleted in the mantle. Because of the fractionation process between the two elements the mantle is characterized by higher Sm/Nd and consequently higher $^{143}\text{Nd}/^{144}\text{Nd}$ ratios compared to the crust. As Nd isotopes ($^{143}\text{Nd}/^{144}\text{Nd}$) are expressed in epsilon notation, $\epsilon\text{Nd} = [(^{143}\text{Nd}/^{144}\text{Nd})_{\text{sample}} / (^{143}\text{Nd}/^{144}\text{Nd})_{\text{CHUR}} - 1] * 10^4$, where CHUR is the Chondritic Uniform Reservoir ($^{143}\text{Nd}/^{144}\text{Nd} = 0.512638$) (Jacobsen and Wasserburg, 1980), this results in more radiogenic ϵNd values (more positive) for the mantle and least radiogenic ϵNd values (more negative) for the crust (Okrusch and Matthes, 2005).

The Pb isotope system is based on a radioactive decay chain, where U and Th produce three radiogenic Pb isotopes ($^{238}\text{U} \rightarrow ^{206}\text{Pb}$, half-life time 4.47 Gyr; $^{235}\text{U} \rightarrow ^{207}\text{Pb}$, half-life time 0.704 Gyr; $^{232}\text{Th} \rightarrow ^{208}\text{Pb}$, half-life time 14.01 Gyr) (Dickin, 1995a). ^{204}Pb is not a product of the radioactive decay and therefore often used for normalization. In similarity to the Rb-Sr and Sm-Nd isotope systems, the Pb isotope ratios are diagnostic of different reservoirs (Okrusch and Matthes, 2005).

The use of REE as dust provenance tracer can be a valuable addition to the application of radiogenic isotopes to discriminate between PSAs, as they are characterized by similar chemical properties and low solubility during weathering processes (Piper, 1974; Klaver and van Weering, 1993; Taylor and McLennan, 1995; Munksgaard et al., 2003). The group of REE consists of the lanthanide elements from lanthanum (La) to lutetium (Lu) with increasing

atomic numbers from La to Lu (57-71) (Taylor and McLennan, 1995; Okrusch and Matthes, 2005). Based on the atomic number the REE can be separated into light rare earth elements (LREE), middle rare earth elements (MREE) and heavy rare earth elements (HREE), so that variations within these groups can be diagnostic for different PSAs.

Under ideal conditions the geochemical signal from PSAs is inherited in the geochemical composition of dust particles and remains the same after deposition in the ocean (Grousset and Biscaye, 2005). However, grain size fractionation can affect the concentrations of radiogenic isotopes and REE. While it has been shown that Nd and Pb isotopes show only very little grain size dependency (Goldstein et al., 1984; Gili et al., 2016; Gili et al., 2017) the grain size effect on Sr isotopes needs to be considered. Sr isotopes tend towards substantially higher isotopic ratios in the fine fraction (Dasch, 1969), which is the result of weathering conditions in the source areas. During chemical weathering, ^{87}Sr is released into solution from the source rocks because of the preferential breakdown of Rb-bearing phases (e.g. mica and K-feldspar) resulting in lower $^{87}\text{Sr}/^{86}\text{Sr}$ ratios in the source rocks and increased $^{87}\text{Sr}/^{86}\text{Sr}$ ratios in the fine fraction (Dasch, 1969; Blum et al., 1993; Blum and Erel, 1997). The grain size dependency on REE has exclusively been studied using concentrations (Honda et al., 2004; Feng et al., 2011; Gili et al., 2017) without taking ratios into account. Previous studies have shown that the grain size effects on REE concentrations may be dependent on the source region. While Asian surface sands showed large variations in REE concentrations with grain size, REE concentrations of Chinese dust and loess samples are almost grain size independent (Honda et al., 2004; Kanayama et al., 2005; Feng et al., 2011). Gili et al. (2017) found that southern South American surface samples have significantly lower REE concentrations within the fine fraction ($< 5 \mu\text{m}$) compared to the coarse fraction ($< 63 \mu\text{m}$).

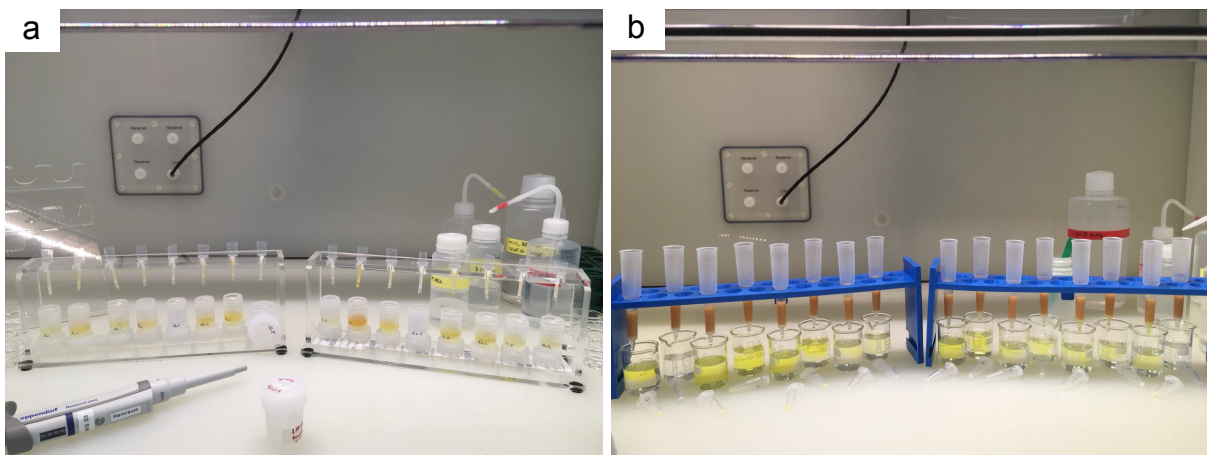


Figure 2.2: The procedures of the ion exchange chromatography described in chapter 3. a: Pb extraction. b: Separation of the alkaline earth metals (Sr from the REE). The chemical separation was conducted in a clean laboratory certified after ISO class 4-5 at the ICBM, University of Oldenburg.

2.2.3 Grain size analysis as tracer for the past dust variability

A detailed description of grain size analysis as dust tracer is given in chapter 4. Grain size analysis, in particular the mean dust grain size, can provide valuable information on paleoclimate changes. However, the application of grain size analysis as a paleoclimate proxy is scarce (at least in the SO). As a result, the dust grain size is not defined as a standardized unit. Several climatic processes control the dust erosion in PSAs, the subsequent transport in the atmosphere and the deposition of dust in the ocean (see 1.2.1). Subsequently, dust grain size analysis of marine sediments provides a coupled signal of changes in source area characteristics, wind forcing in the PSAs and variations within the dust transporting winds.

Additionally, grain size analysis of marine sediment samples can be used to reconstruct near bottom-current speed in deep-sea sediments through measuring the “sortable silt” fraction (e.g. McCave et al., 1995). This proxy is based on grain size analysis of the 10-63 μm fraction (sortable silt) because smaller particles tend to form aggregates (e.g. McCave et al., 1995). Changes in the sortable silt mean grain size (\overline{SS}) are considered to reveal variations in bottom current speeds, in as much as coarser \overline{SS} indicates faster bottom currents and vice versa. Based on sortable silt analysis in the SO, it is possible to reconstruct a picture of past variations in ACC flow speed. This can be related back to changes in the position and intensity of the SWW, which in turn provides information on atmospheric dust transport. A detailed description of the sortable silt proxy is given in chapter 6.

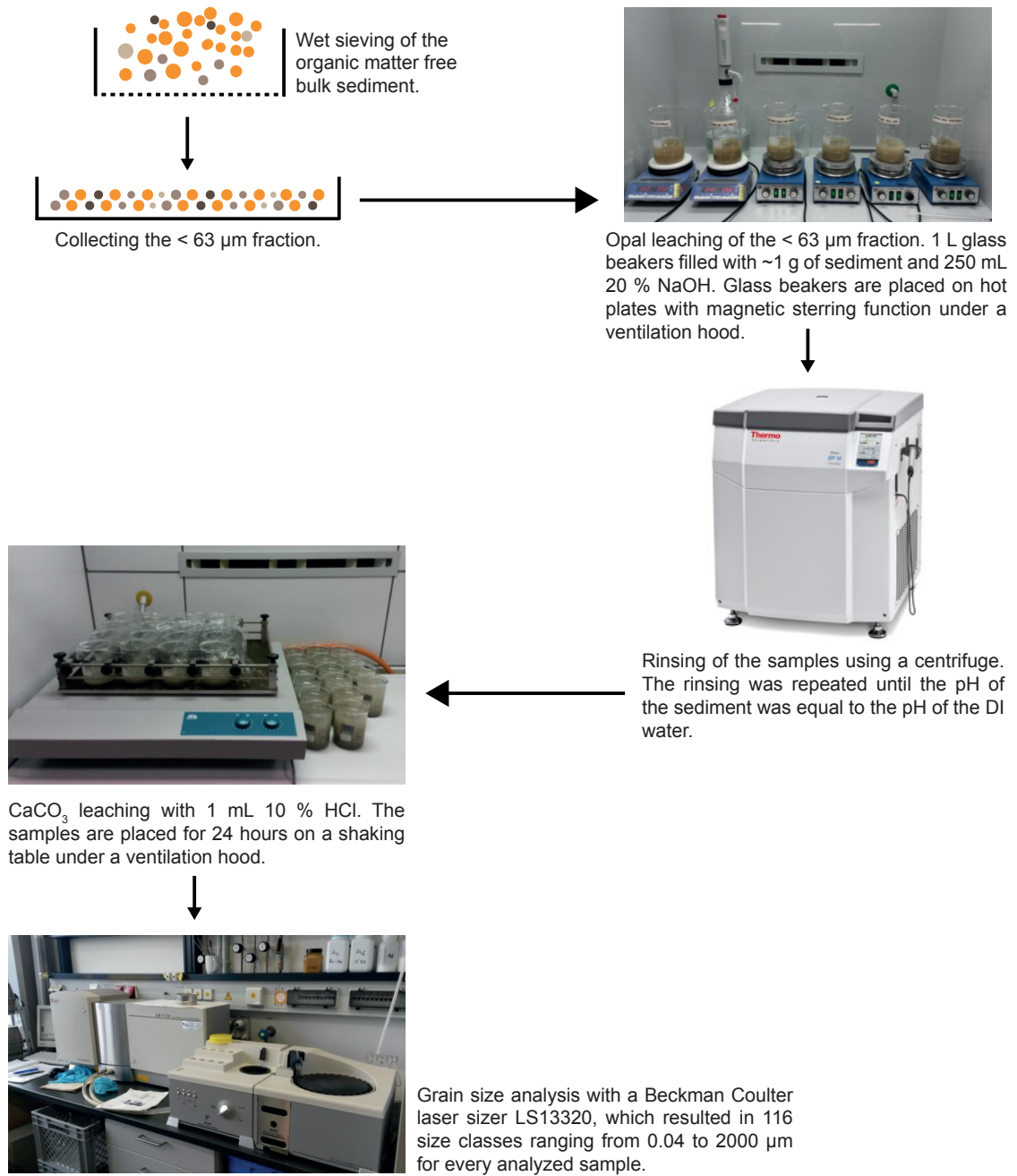


Figure 2.3: The procedure to remove biogenic opal and CaCO_3 from the samples described in chapter 4.

3 A geochemical approach to reconstruct modern South Pacific dust fluxes and potential dust source areas

Marc Wengler^{a,b,*}, Frank Lamy^{a,b}, Torben Struve^c, Alejandra Borunda^d, Philipp Böning^c, Walter Geibert^a, Gerhard Kuhn^a, Katharina Pahnke^c, Jenny Roberts^a, Ralf Tiedemann^a, Gisela Winckler^d

^aAlfred Wegener Institute, Helmholtz Center for Polar and Marine Research, Department for Marine Geology, D-27515 Bremerhaven, Germany

^bMARUM Center for Marine Environmental Sciences, University of Bremen, D-28334 Bremen, Germany

^cMax Planck Research Group for Marine Isotope Geochemistry, Institute for Chemistry and Biology of the Marine Environment (ICBM), Carl von Ossietzky University, D-26111 Oldenburg, Germany

^dLamont-Doherty Earth Observatory, Columbia University, Palisades, 10964 New York, USA

*Correspondence to: marc.wengler@awi.de

Keywords: South Pacific, Modern dust provenance, Lithogenic fluxes, Rare earth elements, Radiogenic isotopes

Under review at *Geochimica et Cosmochimica Acta*

Abstract

We present the first comprehensive dust provenance and lithogenic flux data set extracted from surface sediments distributed across the entire polar and subpolar South Pacific. The dataset comprises ^{230}Th -normalized lithogenic fluxes combined with rare earth elements (REE), strontium (Sr), neodymium (Nd) and lead (Pb) isotope data to determine lithogenic fluxes, sources and the spatial distribution of dust ($< 10 \mu\text{m}$) in the study area during the Holocene. We observe the highest lithogenic fluxes in surface sediments near New Zealand, which most likely indicate a combination of accumulated dust and riverine input from Australia/New Zealand. Similarly, high fluxes off West Antarctica are ascribed to sediment input from the nearby continental shelf and margin. In contrast, the lithogenic fluxes at sampling sites in the remote open ocean are derived from eolian input. Isotopic and REE data suggest that the Lake Eyre Basin is the most prominent potential source area (PSA) for dust distributed over the South Pacific during the Holocene. However, the Murray-Darling Basin in southeast Australia probably also contributed to the Holocene dust deposition in the South Pacific. Furthermore, based on our provenance analysis we cannot entirely exclude contributions of dust from southern South American PSAs.

3.1 Introduction

Recent studies have shown that dust plays a crucial role in modulating the global climate system (e.g. Tegen and Fung, 1994; Kohfeld and Harrison, 2001; Jickells et al., 2005). Dust either impacts the climate directly, by influencing the radiative properties of the atmosphere through scattering and absorbing light, or indirectly, by modifying cloud properties (Arimoto, 2001; Sassen et al., 2003). Furthermore, dust is capable of influencing the climate through its effect on surface ocean productivity. According to the iron hypothesis (Martin, 1990), elevated dust fluxes to the ocean can enhance marine productivity in high-nutrient low-chlorophyll regions, such as the Southern Ocean (SO), resulting in a drawdown of atmospheric CO_2 . High-resolution dust records from the SO seem to support the iron hypothesis, indicating higher dust deposition rates in glacials compared to interglacials, coupled with higher export productivity (Chase et al., 2003; Bradtmiller et al., 2009; Martínez-García et al., 2009; Martínez-García et al., 2011; Martínez-García et al., 2014; Lamy et al., 2014).

Current knowledge about the distribution of dust in the Southern Hemisphere is largely based on modeling studies, in particular in the Pacific sector of the Southern Ocean (Mahowald et al., 2006; Maher et al., 2010; Albani et al., 2014; Neff and Bertler, 2015). The entrainment

of dust in potential source areas (PSAs) strongly depends on climatic conditions influencing soil and terrain properties (Goudie, 2008; Maher et al., 2010) and on the strength of the prevailing southern westerly winds (SWW). The seasonally varying position and intensity of the SWW (Lamy et al., 2010) might have affected dust entrainment in PSAs and accumulation in the SO.

The ^{230}Th isotope is insoluble in seawater and highly particle reactive and is transported to the seafloor attached to sinking particles (Thomson et al., 1993; Francois et al., 2004). Based on this concept, we reconstruct the spatial accumulation of lithogenic material in the Pacific sector of the Southern Ocean using the ^{230}Th normalization method (Thomson et al., 1993; Francois et al., 2004). Furthermore, we complete our study with provenance sensitive proxies, including rare earth elements (REE), strontium (Sr), neodymium (Nd) and lead (Pb) isotopes. The isotopic composition of radiogenic isotopes strongly depends on the geological setting in the PSAs because terrigenous particles can be derived from source rocks with a mantle- or crustal-like composition (Grousset and Biscaye, 2005). On this basis, the use of radiogenic isotopes as dust tracers allows discrimination between different source lithologies (Grousset and Biscaye, 2005). We take advantage of this concept and conduct a provenance analysis to identify PSAs to the Pacific sector of the Southern Ocean.

Our dust provenance analysis can provide a powerful approach to reconstruct variations in the position and strength of the SWW, with implications for better understanding paleoclimate changes over glacial-interglacial timescales.

3.2 Settings of potential Southern Hemisphere source areas

3.2.1 Australia

The Australian continent is characterized by extensive arid and semi-arid areas, which act as PSAs (e.g. McTainsh, 1989; Ekström et al., 2004). Modern dust entrainment in central and southeast Australia occurs predominantly in two major dust source regions; the Lake Eyre Basin and the Murray-Darling Basin (Fig. 3.5 d). The Lake Eyre Basin in central Australia is the most active dust storm area on the continent (McTainsh, 1989) (Fig. 3.5 d). The rivers in the Lake Eyre Basin can be characterized as ephemeral because they are mostly affected by monsoonal summer rains (McTainsh, 1989). Dust activity in the Lake Eyre Basin may occur anytime throughout the year, with highest dust entrainment activities during late spring and early summer (September - December), when precipitation rates are lowest (Ekström et al.,

2004). Dust entrainment in the Lake Eyre Basin needs favorable atmospheric conditions (Tsoar and Pye, 1987; McGowan and Clark, 2008), such as the presence of sub-tropical cold fronts (McGowan and Clark, 2008). When such conditions affect the basin almost on a weekly cycle during late spring and early summer, they are shallow, mostly not exceeding 1000-1500 m in height with an increasing intensity at night (Reeder et al., 2000).

In addition to the Lake Eyre Basin, the Murray-Darling Basin in southeast Australia represents the largest river system on the continent, making it an important source of modern dust (McTainsh, 1989; De Deckker et al., 2010; Marx and Kamber, 2010) (Fig. 3.5 d). The Murray-Darling Basin is known as perennial system because the rivers originate in the relatively high rain fall regions (McTainsh, 1989). Because of the geographical extend of the Murry-Darling Basin, it experiences different rainfall seasonality, which ensures flowing rivers throughout the year (McTainsh, 1989). The Murray-Darling Basin is affected by seasonal flooding events leading to the accumulation of fine sediments in the floodplains of the Basin, which are vulnerable to dust entrainment (McTainsh, 1989).

After dust entrainment, long-range dust transport from both areas follows the southeast dust transport corridor, which describes the major dust transport direction over southeast Australia (Fig. 3.5 d) (Bowler, 1976; McGowan and Clark, 2008). The core of this corridor extends in southeasterly direction between 25°S and 50°S (Bowler, 1976; McGowan and Clark, 2008), after which the SWW continue to transport the dust across the SO (Fig 3.5 d).

3.2.2 New Zealand

New Zealand is located in the mid-latitudes between 34°S and 45°S and its climate is significantly affected by the northeast to southwest orientated Southern Alps (Marx et al., 2005) (Fig. 3.1). In New Zealand, loess areas cover large parts of both the North and South Island. On the South Island, the majority of the loess areas, which are concentrated at the east coast, were derived from the Southern Alps during Quaternary cold-climate processes (e.g. freeze/thaw and glacial grinding) (Eden and Hammond, 2003). Because New Zealand is predominately under the influence of the prevailing SWW, the loess areas on the South Island might have acted as a modern PSA. Although the deposition of Australian-sourced dust at the east coast cannot entirely be excluded, locally sourced material dominates over Australian derived material (Marx et al., 2005; Marx and McGowan, 2005). Because of the geographical position of New Zealand's South Island, which is almost perpendicular to the SWW, wind from Australia is forced to ascend the Southern Alps after crossing the Tasman Sea (Marx et al.,

2005). As a result, the majority of atmospheric dust is removed from the airstream as it passes the Southern Alps (Marx et al., 2005), which leads to enhanced wet deposition of Australian sourced dust (Knight et al., 1995; Marx et al., 2005).

3.2.3 Southern South America

Southern South America can be subdivided into three main PSAs; the Puna-Altiplano Plateau, Central-Western-Argentina and Patagonia (Fig. 3.4 d) (Gili et al., 2016; Gili et al., 2017). The Puna-Altiplano Plateau is located in the central Andes and has a latitudinal extension of 1000 km, a longitudinal extension of 200 km and an elevation of ~4000 m above sea level. The region is dominated by dried-out playas and alluvial fans with large amounts of silty sediments (Gaiero et al., 2003). The area is affected by the subtropical jet stream (Koch et al., 2006), which increases during austral winter resulting in numerous dust storms (Gaiero et al., 2003). Therefore, the Puna-Altiplano Plateau is considered as a region of significant dust entrainment and deflation (Prospero et al., 2002).

Central-Western-Argentina is located between ~27°S and ~39°S and extends from the eastern flank of the Andes to the western slope of the Sierra Pampeanas (Gili et al., 2017). While northeasterly surface winds prevail in the austral summer, the austral winter is dominated by northwesterly winds. Katabatic winds (locally called zonda) occur in austral autumn-winter blowing from the west to east (Norte et al., 2008). These hot and dry winds dominate between 28°-37°S but also occur further south, where strong westerly winds cross the Andes producing a strong downslope airflow (Garreaud et al., 2013).

Patagonia, including Tierra del Fuego, covers the area between 38°S to 55°S. Due to its position in the mid-latitudes, the Patagonian climate is dominated by strong SWW throughout the year. As the SWW discharge most of their moisture at the western flank of the Andes, the winds leaving the eastern flank of the Andes are dry (Gaiero et al., 2003; Garreaud et al., 2013). This circulation pattern results in a strong east to west precipitation gradient across the Andean climate divide (Garreaud et al., 2013), which results in a moist western and dry eastern side.

3.3 Methods

3.3.1 Sample Selection

We analyzed sediment surface samples from across the Pacific sector of the SO recovered during several expeditions with R/V *Polarstern* (PS75, PS58, PS35) (Gersonde, 1995; Gersonde, 2001; Gersonde, 2011) and R/V *Sonne* (SO213) (Tiedemann, 2012) (Fig. 3.1). All samples were collected with a multicorer between 39°S to 70°S along a transect that extends from 175°E to 80°W. Within this longitudinal range, the study area is subdivided into western (175°E to 150°W), central (145°W to 107°W) and eastern parts (105°W to 80°W) (Fig. 3.1). Our sample transects extend across the Antarctic Circumpolar Current from the Antarctic Zone south of the winter sea-ice margin, across the Polar Frontal Zone into the sub-Antarctic Zone (Fig. 3.1). The surface samples are assumed to be representative of the Holocene because they are closely located to sediment cores that imply core top ages of < 11 kyr BP (Fig. 3.1) (Benz et al., 2016). Lithogenic fluxes were determined on the bulk sediment of 79 surface samples using the ^{230}Th normalization method (Francois et al., 2004) (Fig. 3.2). Provenance analysis, including measurements of REE, Sr, Nd and Pb isotopes were performed on the < 10 μm fraction of 18 sediment surface samples (Fig. 3.1). The < 10 μm fraction typically becomes cohesive in nature and forms aggregates (McCave et al., 1995; Hall and McCave, 2000). Subsequently, this fraction is mostly unaffected by bottom current redistribution and we consider this fraction as representative for dust deposited in the South Pacific.

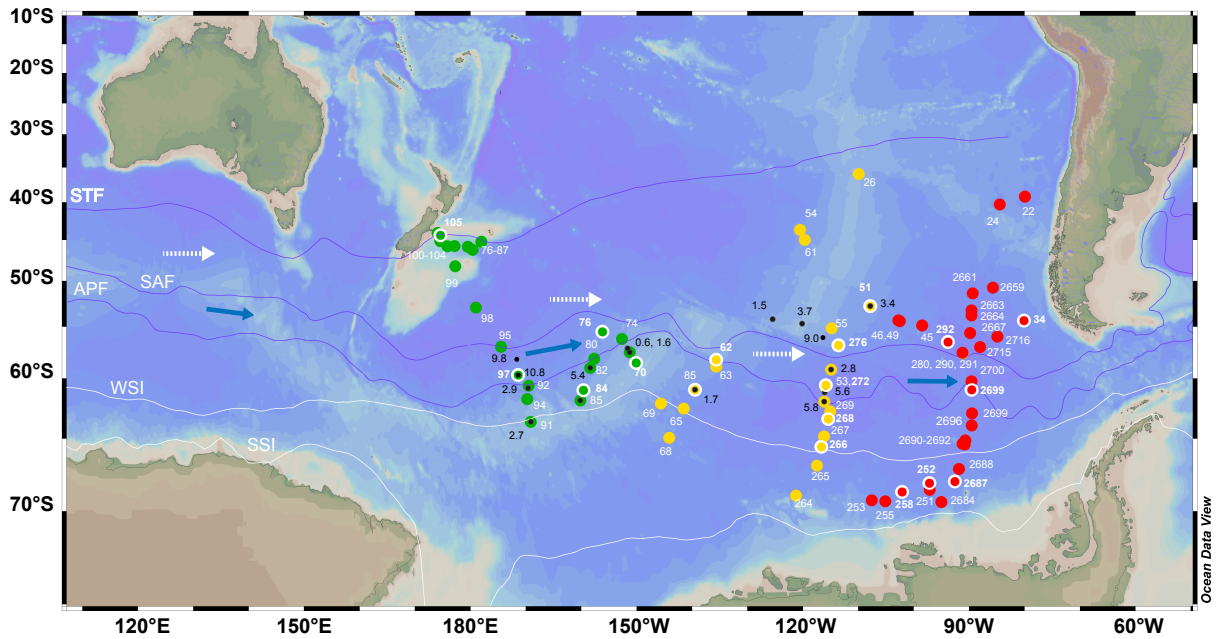


Figure 3.1: Map of the South Pacific with locations of surface samples recovered during R/V *Polarstern* and R/V *Sonne* expeditions. Green dots: Western South Pacific, Yellow dots: Central South Pacific, Red dots: Eastern South Pacific. The white frame highlights the samples that were used for provenance analysis. White numbers attached to the sampling locations refer to the station number, respectively. Small black dots highlight sediment cores with age models (Benz et al., 2016). Black numbers illustrate the core top age in kyr. See Benz et al., (2016) for detailed information about the age models. Colored lines refer to mean positions of major front systems (Orsi et al., 1995). STF: Subtropical Front, SAF: Subantarctic Front, APF: Polar Front. Mean extension of winter and summer sea ice (WSI and SSI) is indicated by white lines. Blue arrows indicate the flow direction of the Antarctic Circumpolar Current (ACC). White dashed arrows show the direction of the Southern Westerly Winds (SWW). The map was generated using the Ocean Data View software (Schlitzer, 2015).

3.3.2 Uranium-Thorium methodology

The ^{230}Th isotope is a product of the ^{238}U decay series (Francois et al., 2004) with a half-life time of 75.548 ± 110 years (Cheng et al., 2013). The parent isotope ^{234}U produces (through α -decay) the highly insoluble (in seawater) and particle reactive ^{230}Th isotope at a uniform and well-known rate ($\beta = 0.0267 \text{ dpm m}^{-3} \text{ year}^{-1}$). Attached to sinking particles ^{230}Th is transported to the seafloor (Thomson et al., 1993; Francois et al., 2004). Sediment particles are assumed to contain a fraction of ^{230}Th in a secular equilibrium with lithogenic ^{234}U . However, the total amount of ^{230}Th in deep-sea sediments near the sediment surface exceeds the amount supported

by ^{234}U . This fraction of ^{230}Th is called $^{230}\text{Th}_{\text{xs}}$ (230-Thorium excess) (Francois et al., 2004). This relationship forms the basis for the ^{230}Th normalization method (Thomson et al., 1993). To determine the concentrations of Th and U isotopes, approximately 50 mg of freeze-dried bulk sediment was spiked with known amounts of ^{229}Th and ^{236}U . The sediment was digested in a CEM Mars X-press microwave system in 2 mL concentrated HCl, 3 mL concentrated HNO_3 and 0.5 mL HF 40% (suprapur®). The resulting solution was evaporated to near dryness using the microwave Evapoclean accessory and redissolved in 1 M HNO_3 in the microwave system. Three consecutive steps of iron precipitation were then applied to separate Th and U isotopes from the sample matrix. The precipitate that contained Th and U was dissolved in 3 M HNO_3 and passed through equilibrated 2 mL columns filled with Eichrom UTEVA resin for separation of Th and U isotopes from iron. Th and U isotopes were measured separately by sector-field ICP-MS (Thermo Element 2 equipped with an ESI Apex desolvator) in low-resolution mode. External reproducibility was monitored using a certified reference material (UREM 11) and procedural blanks were run alongside the samples. Corrections for tailing from ^{232}Th (^{238}U), mass bias and procedural blanks were applied as appropriate and considered in the error propagation. Propagated analytical uncertainties of $^{230}\text{Th}_{\text{xs}}$ are less than 5% (1σ). ^{238}U was calculated from ^{235}U using the natural isotope abundance. Supported ^{230}Th was calculated according to Francois et al., (2004), using a $^{238}\text{U}/^{232}\text{Th}$ activity ratio of 0.4 ± 0.1 (Henderson and Anderson, 2003) for the majority of the samples. However, a $^{238}\text{U}/^{232}\text{Th}$ activity ratio of 0.8 was used for 9 samples. This ratio was inferred from samples that showed no evidence for authigenic uranium in their $^{234}\text{U}/^{238}\text{U}$ ratio and in their U concentration. $^{230}\text{Th}_{\text{xs}}$ was used to calculate the preserved vertical lithogenic fluxes by multiplying the uniform ^{230}Th production rate ($\beta = 0.267 \text{ dpm m}^{-3} \text{ yr}^{-1}$) and the water depth divided by the $^{230}\text{Th}_{\text{xs}}$ concentrations (dpm g^{-1}) (Francois et al., 2004; Geibert et al., 2005; Martínez-García et al., 2009; Lamy et al., 2014). ^{232}Th concentrations were used to determine the lithogenic fraction in the surface samples assuming an average ^{232}Th concentration of 10 ppm for the upper continental crust. The lithogenic end-member of 10 ppm for the upper continental crust was inferred from the relationship of the measured ^{232}Th concentrations vs. the sum of non-lithogenic fractions. In the following text, we refer to the sediment redistribution-corrected vertical lithogenic fluxes in short as lithogenic fluxes. The decay of ^{230}Th was considered to be insignificant because our data set exclusively uses surface samples.

3.3.3 Grain size separation and leaching

To extract the dust fraction from the bulk sediment samples, all samples were initially wet sieved to separate the $< 63 \mu\text{m}$ fraction followed by Stokes-based separation of the $< 10 \mu\text{m}$ fraction. To avoid aggregation, ammonia was added to the Atterberg settling tubes. The grain size separation was conducted at the Alfred Wegener Institute in Bremerhaven (AWI) followed by sequential leaching at the Institute for Chemistry and Biology of the Marine Environment in Oldenburg (ICBM, University of Oldenburg). All samples and certified USGS rock reference materials AGV-1 and BCR-2 were exposed to 5% H_2O_2 to remove organic material and acetic acid ($\text{pH} = 5$) to eliminate carbonate before Stokes-based separation. To ensure that all authigenic coatings and contaminant phases were completely removed, the samples were exposed to 1 M HCl overnight, rinsed with MQ and bathed again overnight in 0.03 M EDTA. A different leaching procedure was applied to the samples used for REE analysis after Stokes-based separation of the $< 10 \mu\text{m}$ fraction. Two consecutive steps with 13 mL of 0.02 M hydroxylamine hydrochloride (HH) were used to remove authigenic and contaminant phases. All leaching steps were repeated until no more chemical reactions between the reagents and the sediment were detected.

3.3.4 Chemical separation of strontium, neodymium and lead isotopes

All chemical and analytical processing, including digestion, ion exchange chromatography and mass spectrometric analysis was carried out at the ICBM in Oldenburg using ultra-pure reagents. Sample digestion and ion exchange chromatography were carried out in two individual batches. The 2σ external reproducibility (2SD) of our procedure was assessed with repeated analyses of USGS rock reference materials AGV-1 and BCR-2 included in each batch of samples. The sample digestion of ~ 50 mg of the freeze-dried sediment was first treated with aqua regia to remove any remaining organics and followed by HNO_3 -HF- HClO_4 based pressure digestion at 180°C for 12 hours (e.g. Yokoyama et al., 1999). The resulting clear solutions were fumed off three times with half-diluted HCl and converted to bromide form with HBr. An aliquot of the solutions was then passed through a two-stage HBr- HNO_3 based Pb extraction using 100 μL AG1-X8 resin (modified from Paul et al., 2015). The alkaline earth metals including Sr were separated from the REE using a HCl-based procedure with Biorad[®] AG50W X-8 resin (Struve et al., 2016). Strontium was isolated from the remaining sample matrix using Eichrom Sr spec[®] resin (Horwitz et al., 1992) and Nd was separated from the REE applying a

Eichrom LnSpec[®] chemistry (Pin and Zalduegui, 1997). For REE analysis, another aliquot in 9M HCl was dried and taken up in 0.3M HNO₃.

3.3.5 Analysis of rare earth elements, strontium, neodymium and lead isotopes

The analysis of REE, Sr, Nd and Pb isotopes was carried out at the ICBM in Oldenburg. The contents of REE were determined using high resolution ICP-MS (Thermo Fisher Element 2) in low resolution mode ($m = 300$) and indium as an internal standard. Analytical precision and accuracy (determined by simultaneous runs of AGV-1 and BCR-2; $n = 5$) was better than 4% and 7% relative SD (1s), respectively. Procedural blanks were insignificant, $\leq 1\%$ of the signal intensity of the samples.

Nd, Sr and Pb isotope compositions were determined using a multi-collector ICP-MS (Neptune Plus, Thermo Scientific). For Nd isotope analysis internal mass bias was corrected for Nd isotopes using $^{146}\text{Nd}/^{144}\text{Nd} = 0.7219$ and an exponential law. To correct for instrumental offset, the mass bias corrected $^{143}\text{Nd}/^{144}\text{Nd}$ ratios of the samples were normalized to the JNdi-1 reference ratio of 0.512115 ± 0.000007 (Tanaka et al., 2000). The external reproducibility (2SD) of normalized BCR-2 and AGV-1 reference material was 0.512643 ± 0.000011 ($n = 8$) and 0.512797 ± 0.000013 ($n = 8$), respectively. The sample results are expressed in epsilon notation, $\epsilon_{\text{Nd}} = [(^{143}\text{Nd}/^{144}\text{Nd})_{\text{sample}} / (^{143}\text{Nd}/^{144}\text{Nd})_{\text{CHUR}} - 1] * 10^4$, where CHUR is the Chondritic Uniform Reservoir (Jacobsen and Wasserburg, 1980).

For Sr isotope analysis internal mass bias was corrected using $^{86}\text{Sr}/^{88}\text{Sr} = 0.1194$ and an exponential law. Measurements were accompanied by analysis of NBS987 (generally every 4 samples), and $^{87}\text{Sr}/^{86}\text{Sr}$ values of all samples were normalized to the reported NBS987 value of 0.710248 (Thirlwall, 1991). The analysis of BCR-2 and AGV-1 ($n = 8$) yielded $^{87}\text{Sr}/^{86}\text{Sr} = 0.705000$ and 0.703948 , while the external reproducibility (2SD) was ± 0.000007 and ± 0.000032 , respectively. Krypton ‘gas blanks’ measured on ^{83}Kr used to correct for ^{86}Kr on ^{86}Sr were below 0.1 mV (while ^{86}Sr was measured at 2–3 V).

The analysis of the Pb isotopic compositions were performed as standard-sample bracketing using NIST SRM 981 as bracketing standard (Albarède et al., 2004) and correcting for isobaric interference of Hg. The mass bias of samples and certified reference materials were corrected for by normalization of the raw SRM 981 values to the literature values as reported in Taylor et al. (2015). The external reproducibility (2SD) of BCR-2 ($n = 10$) was $^{208}\text{Pb}/^{204}\text{Pb} = 38.8345 \pm 0.0030$, $^{207}\text{Pb}/^{204}\text{Pb} = 15.6281 \pm 0.001$, $^{206}\text{Pb}/^{204}\text{Pb} = 18.8028 \pm 0.0013$, $^{207}\text{Pb}/^{206}\text{Pb} = 2.06528 \pm 0.00009$, $^{208}\text{Pb}/^{206}\text{Pb} = 0.83112 \pm 0.00003$. Repeat analyses of AGV-1 ($n = 10$) yielded

$^{208}\text{Pb}/^{204}\text{Pb} = 38.5757 \pm 0.0034$, $^{207}\text{Pb}/^{204}\text{Pb} = 15.6180 \pm 0.0005$, $^{206}\text{Pb}/^{204}\text{Pb} = 18.9039 \pm 0.0011$, $^{207}\text{Pb}/^{206}\text{Pb} = 2.04055 \pm 0.00007$, $^{208}\text{Pb}/^{206}\text{Pb} = 0.82615 \pm 0.00004$. Our Nd, Sr and Pb isotopic results on AGV-1 and BCR-2 agreed within analytical uncertainty with previously published values obtained from leached residues (Weis et al., 2006; Jweda et al., 2016). The procedural blanks for Nd, Pb and Sr were below 40 pg, 110 pg and 2.5 ng, respectively and therefore less than 1%.

3.4 Results

3.4.1 Lithogenic fluxes

The lithogenic fluxes range from 0.24 to 20.47 g m⁻² yr⁻¹ (Fig. 3.2). The locations located offshore New Zealand's South Island show the highest lithogenic fluxes in the study area (0.72 to 20.47 g m⁻² yr⁻¹) and decrease with increasing distance from New Zealand (Fig. 3.2). The lithogenic fluxes in this area indicate a clear drop at the Subtropical Front (STF) with highest values north of the STF (SO213_87-1; 20.47 g m⁻² yr⁻¹) and approximately 9 g m⁻² yr⁻¹ south of STF (Fig. 3.2). Locations close to the western Antarctic continental margin at approximately 70°S and 120°W to 90°W represent the area with the second highest lithogenic fluxes ranging from 1.97 to 6.85 g m⁻² yr⁻¹. East of 145°W, lithogenic fluxes increase along two south-north transects (~120°W and ~90°W transect) spanning the winter sea ice limit (WSI), Antarctic Polar Front (APF) and Sub-Antarctic Front (SAF). Both transects reveal highest values south of the WSI and a northward decrease in lithogenic fluxes (Fig. 3.2). However, the ~90°W transect has slightly higher absolute lithogenic fluxes than the ~120°W transect and shows a prominent decrease at the APF (Fig. 3.2). In contrast, lithogenic fluxes along the ~120° W transect decrease continuously from the South to the North (Fig. 3.2). In the southeast Pacific north of the SAF, the lithogenic fluxes increase towards Patagonia (0.96 to 2.50 g m⁻² yr⁻¹). The samples located in the open ocean between 55°S to 65°S and 180°E to 135°W show the lowest lithogenic fluxes among all samples (0.38 to 1.06 g m⁻² yr⁻¹) (Fig. 3.2).

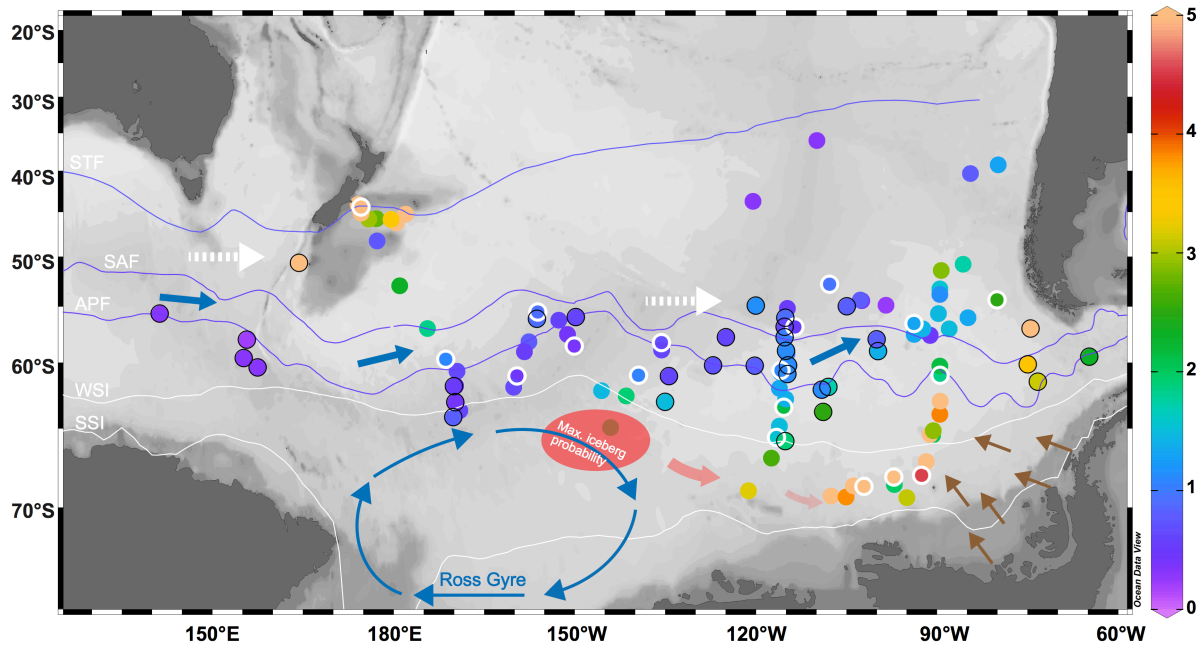


Figure 3.2: Spatial distribution of ^{230}Th -normalized lithogenic fluxes in the study area given in $\text{g m}^{-2} \text{yr}^{-1}$. Colored lines refer to mean positions of major front systems (Orsi et al., 1995). STF: Subtropical Front, SAF: Subantarctic Front, APF: Polar Front. Mean extension of winter and summer sea ice (WSI and SSI) is indicated by white lines. Thin blue arrows refer to the Ross Gyre (Assmann et al., 2005). Thick blue arrows indicate the flow direction of the Antarctic Circumpolar Current (ACC). Brown arrows indicate terrigenous sediment input in the flat Bellingshausen abyssal plain (Rebesco et al., 1996; Hillenbrand, 2000). Red area refers to the maximum iceberg probability with eastward decreasing abundances (red arrows with fading colors) (Tournadre et al., 2012). White frame highlights the samples that were used for provenance analysis. Black frame shows Holocene data from Bradtmiller et al., (2009) and Chase et al., (2003). The map was generated using the Ocean Data View software (Schlitzer, 2015).

3.4.2 Provenance sensitive proxies

3.4.2.1 Rare earth elements

The REE results are normalized to the Upper Continental Crust (UCC) (Taylor and McLennan, 1995) and presented as HREE/LREE_N (Tm + Yb + Lu) / (La + Pr + Nd) versus MREE/MREE*_N (Gd + Tb + Dy) / [(Tm + Yb + Lu + La + Pr + Nd) / 2] (Fig. 3.3 a). The ratios include the majority of the REE but exclude Ce and Eu to minimize the variable effects of both elements (Martin et al., 2010). HREE/LREE_N ratios range from 1.06 to 1.60 and MREE/MREE*_N ratios range from 1 to 1.19 (n = 16). The samples PS75/84-1 and 64-2 are excluded from the data set because their extremely low REE concentrations were close to or below the limit of detection.

3.4.2.2 Strontium and neodymium isotopes

The Sr isotope results range from $^{87}\text{Sr}/^{86}\text{Sr} = 0.7086$ to $^{87}\text{Sr}/^{86}\text{Sr} = 0.7117$ and ϵ_{Nd} values from -3.0 to -6.0 (n = 18) (Fig. 3.3 b). The majority of the samples (n = 12) can be characterized by high $^{87}\text{Sr}/^{86}\text{Sr}$ ratios ranging from 0.7096 to 0.7104 paired with relatively unradiogenic Nd isotopic compositions of $\epsilon_{\text{Nd}} = -4.2$ to $\epsilon_{\text{Nd}} = -5.0$. Furthermore, a few samples (n = 6) show lower $^{87}\text{Sr}/^{86}\text{Sr}$ ratios ranging from 0.7085 to 0.7091 and more radiogenic Nd isotopic compositions between $\epsilon_{\text{Nd}} = -3.0$ and $\epsilon_{\text{Nd}} = -4.4$.

3.4.2.3 Lead isotopes

Our Pb isotope results (n = 18) show a consistent positive correlation from unradiogenic ratios ($^{208}\text{Pb}/^{204}\text{Pb} = 38.34$ and $^{206}\text{Pb}/^{204}\text{Pb} = 18.40$) towards more radiogenic Pb isotopic compositions ($^{208}\text{Pb}/^{204}\text{Pb} = 39.50$ and $^{206}\text{Pb}/^{204}\text{Pb} = 19.44$) (Fig. 3.3 c). The majority of our samples show intermediate $^{206}\text{Pb}/^{204}\text{Pb}$ ratios (18.65 to 18.97) and $^{208}\text{Pb}/^{204}\text{Pb}$ (38.55 to 38.93) comprising samples from across the entire study area (Fig. 3.3 c). Four samples illustrate less radiogenic values ranging from $^{208}\text{Pb}/^{204}\text{Pb} = 38.34$ to $^{208}\text{Pb}/^{204}\text{Pb} = 38.55$ paired with $^{206}\text{Pb}/^{204}\text{Pb}$ ratios between 18.40 and 18.65. These samples are exclusively located in the central western part of the study area (Fig. 3.3 c and d). However, the Pb blanks of the samples PS75/70-1 and 84-1 exceed the critical value of 1% (70-1 = 4%, 84-1 = 2.7%) which could have caused a deviation from their real Pb ratios. Sample PS75/105-1 located off New Zealand shows unusual Pb isotopic compositions ($^{208}\text{Pb}/^{204}\text{Pb} = 39.50$ and $^{206}\text{Pb}/^{204}\text{Pb} = 19.45$),

inconsistent with the REE and Sr-Nd isotope data from the same sample and possible local background and cross contamination. However, we cannot reconcile this offset with the available data, and therefore exclude the Pb results of PS75/105-1 from the discussion.

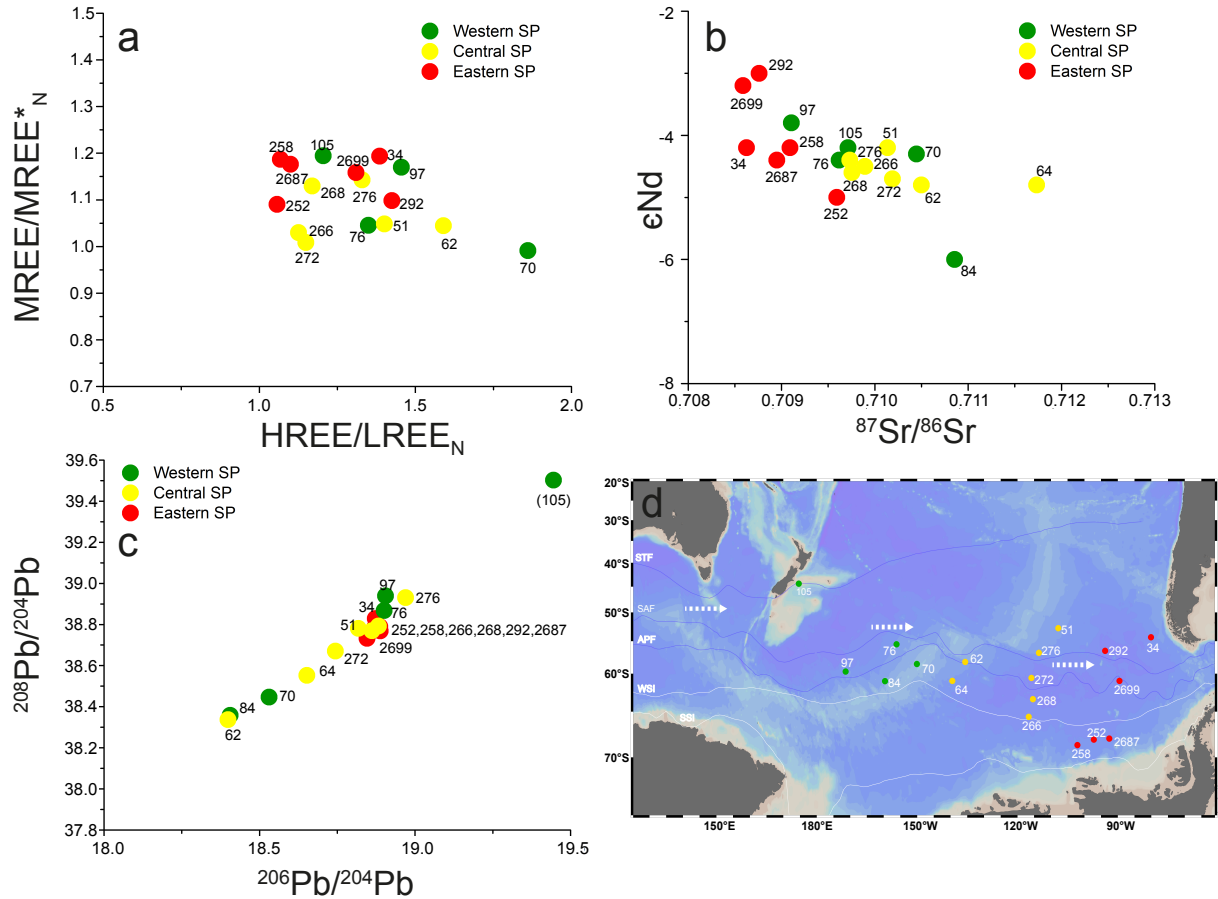


Figure 3.3: Geochemical composition of South Pacific dust samples. a: Rare earth element data are normalized to Upper Continental Crust (UCC) (Taylor and McLennan, 1995) and illustrated as $HREE/LREE_N = (Tm + Yb + Lu) / (La + Pr + Nd)$ versus $MREE/MREE*_N = (Gd + Tb + Dy) / [(Tm + Yb + Lu + La + Pr + Nd) / 2]$. b: Neodymium and strontium isotope results are expressed as ϵNd vs. $^{87}Sr/^{86}Sr$ ratios, respectively. c: Lead isotope results are presented as $^{208}Pb/^{204}Pb$ vs. $^{206}Pb/^{204}Pb$. Color code refers to Fig. 3.1. Error bars for ϵNd values, $^{87}Sr/^{86}Sr$, $^{208}Pb/^{204}Pb$ and $^{206}Pb/^{204}Pb$ ratios are smaller than the symbols. d: Map of the South Pacific with locations of surface samples used for provenance analysis. Colored lines refer to mean positions of major front systems (Orsi et al., 1995). STF: Subtropical Front, SAF: Subantarctic Front, APF: Polar Front. Mean extension of winter and summer sea ice (WSI and SSI) is indicated by white lines. White dashed arrows show the direction of the Southern Westerly Winds (SWW). Color code refers to Fig. 3.1. The map was generated using the Ocean Data View software (Schlitzer, 2015).

3.5 Discussion

3.5.1 Lithogenic fluxes

Only a few studies (e.g. Chase et al., 2003; Bradtmiller et al., 2009) have published lithogenic flux data for the Pacific sector of the SO. Consequently, most dust deposition estimates for this area are based on climate/dust models (e.g. Mahowald et al., 2006; Maher et al., 2010; Albani et al., 2012a; Albani et al., 2014). While our modern lithogenic fluxes are consistent with the data provided by Chase et al. (2003) and Bradtmiller et al. (2009) (Fig. 3.2) the modern modeled deposition in the SO (e.g. Albani et al., 2014) predicts considerably lower values. The strength of our data set is the broad spatial coverage from New Zealand's South Island to southern South America extending the spatial coverage of the previous studies (Fig. 3.2).

The highest lithogenic fluxes offshore New Zealand's South Island might reflect a combination of Australian/New Zealand sourced dust input likely admixed with riverine input from New Zealand sources (Fig. 3.2). Terrigenous tracers including plant wax n-alkanes and soil derived branched glycerol dialkyl glycerol tetraethers (Jaeschke et al., 2017) provide independent evidence for increased terrigenous input at our sample locations. The observed drop in lithogenic fluxes at the STF might be a combination of increasing water depth and/or increasing distance to New Zealand, thereby reducing the influence of riverine input. Further east, lithogenic fluxes decrease to an average of $\sim 2.5 \text{ g m}^{-2} \text{ yr}^{-1}$ ($n = 4$) most likely representing eolian input (Fig. 3.2). South of New Zealand (50°S and 164°E) at the southern rim of the southeast dust transport corridor, lithogenic fluxes increase to $8.30 \text{ g m}^{-2} \text{ yr}^{-1}$ (Fig. 3.2) (Bradtmiller et al., 2009). Because New Zealand sourced inputs can be excluded at this location the lithogenic fluxes are probably related to Australian dust input. The lowest lithogenic fluxes in the remote open ocean (55°S to 65°S and 180°E to 150°W) are consistent with detected leaf wax n-alkanes, which show deposition of relatively fresh plant material, indicating eolian transport to the remote open ocean (Jaeschke et al., 2017) (Fig. A 3.1). Lithogenic fluxes north of the SAF between 51°S to 57°S and 115°W to 80°W range from 0.96 to $2.50 \text{ g m}^{-2} \text{ yr}^{-1}$ with increasing lithogenic fluxes towards Patagonia, likely indicating a slightly increased eolian deposition signal (Fig. 3.2). We suggest that the high lithogenic fluxes in the $\sim 120^{\circ}\text{W}$ transect likely represent a mixed signal, where the influence of ice-rafted sediment results in increased lithogenic fluxes south of the APF. North of the APF the lithogenic input is derived from dust (Fig. 3.2). The high lithogenic fluxes south of the WSI in the $\sim 90^{\circ}\text{W}$ transect cannot be solely explained by ice-rafted sediment input, because of an eastward decrease in iceberg probability (Tournadre et al., 2012). Rather we argue that this increase might reflect the presence of

Antarctic Peninsula-derived turbidity currents (Rebesco et al., 1996; Hillenbrand, 2000) resulting in elevated lithogenic fluxes, whereas dust is considered to be the dominant source north of the APF (Fig. 3.2).

3.5.2 Geochemical fingerprinting of South Pacific dust

Our radiogenic isotope and REE data clearly show that there is no longitudinal gradient across the South Pacific in all applied provenance proxies (Fig. 3.3 a-d). Furthermore, our data are remarkably homogeneous compared to the PSA data, which is perhaps surprising given the spatial extent of our study area and the number of PSAs. Here we discuss the PSAs to the South Pacific given the geochemical constraints.

We compare our dust fraction ($< 10 \mu\text{m}$) to PSA data from southern South America, New Zealand and Australia. It should be noted that the southern South American PSA data have been measured on the $< 5 \mu\text{m}$ fraction (Delmonte et al., 2004a; Sugden et al., 2009; Gili et al., 2016; Gili et al., 2017). The REE data from Australia include the coarse fraction ($< 90 \mu\text{m}$), whereas REE data from New Zealand have been measured on material from dust traps, glacier and loess deposits (Marx et al., 2005; McGowan et al., 2005; Marx and Kamber, 2010; this work). The Australian and New Zealand Sr, Nd and Pb PSA data were obtained from the fine fraction ($< 2 \mu\text{m}$ and $< 5 \mu\text{m}$) (Delmonte et al., 2004a; Gingele and De Deckker, 2005; Revel-Rolland et al., 2006; De Deckker et al., 2010; Vallelonga et al., 2010). The PSA data from Victoria Land, the McMurdo Sound sector and the Dry Valleys of Antarctica ($< 5 \mu\text{m}$) broadly encircle our data in Sr-Nd space (Delmonte et al., 2004a; Blakowski et al., 2016) (Fig. 3.4 a). However, given the broad variability in Sr-Nd space of the Antarctic data, we exclude this region as a PSA to our South Pacific dust samples. Furthermore, we argue that an eolian transport from these PSAs is rather unlikely.

While it has been shown that Nd and Pb isotopes show only very little grain size dependency (Goldstein et al., 1984; Meyer et al., 2011; Gili et al., 2016; Gili et al., 2017), the grain size effect on Sr isotopes needs to be considered. Sr isotopes tend towards substantially higher isotopic ratios in the fine fraction (Dasch, 1969), which is the result of weathering conditions in the source area. To our knowledge, grain size dependency on REE has exclusively been studied using REE concentrations (Honda et al., 2004; Feng et al., 2011; Gili et al., 2017).

3.5.2.1 Southern South American potential dust source areas

The Nd and Sr isotopic compositions show that samples from Southern Puna ($\epsilon_{Nd} = -3.4$ to -4.7 ; $^{87}Sr/^{86}Sr = 0.7084 - 0.7113$) and two samples from southern Central-Western-Argentina have ϵ_{Nd} values and $^{87}Sr/^{86}Sr$ ratios ($\epsilon_{Nd} = -3.7$; $^{87}Sr/^{86}Sr = 0.7091 - 0.7114$) similar to our South Pacific dust samples ($\epsilon_{Nd} = -3.0$ to -6.0 ; $^{87}Sr/^{86}Sr = 0.7086 - 0.7117$) (Fig. 3.4 a). While the samples from Northern and Middle Central-Western-Argentina have ϵ_{Nd} values comparable to our South Pacific dust samples ($\epsilon_{Nd} = -4.6$ to -6.4), their $^{87}Sr/^{86}Sr$ ratios are distinctly higher ($^{87}Sr/^{86}Sr = 0.7169 - 0.7273$) (Fig. 3.4 a). However, a potential grain size effect on Sr isotopes might explain the offset between these southern South American PSAs and our South Pacific dust samples (see 3.5.2). The majority of the southernmost areas of Patagonia show ϵ_{Nd} values and $^{87}Sr/^{86}Sr$ ratios distinctly different to our South Pacific dust samples ($\epsilon_{Nd} = 4.79$ to -1.23 ; $^{87}Sr/^{86}Sr = 0.7053 - 0.7086$) (Fig. 3.4 a). However, five samples from the flanks of the Strait of Magellan (Sugden et al., 2009) are consistent with our South Pacific dust samples, which might indicate the activity of this specific area as a PSA in the Holocene ($\epsilon_{Nd} = -4.0$ to -4.6 ; $^{87}Sr/^{86}Sr = 0.7098 - 0.7118$) (Fig. 3.4 a).

Our $^{208}Pb/^{204}Pb$ (38.34 - 38.94) and $^{206}Pb/^{204}Pb$ (18.40 - 18.97) ratios are consistent with Pb isotope data from Southern Puna and Middle Central-Western-Argentina ($^{208}Pb/^{204}Pb = 38.64 - 38.94$; $^{206}Pb/^{204}Pb = 18.68 - 19.94$), whereas Patagonian PSAs ($^{208}Pb/^{204}Pb = 38.35 - 38.65$; $^{206}Pb/^{204}Pb = 18.56 - 19.70$) exclusively correspond with South Pacific dust samples from the western part of our study area (Figs. 3.3 d and 3.4 b). Based on the Sr-Nd and Pb isotopic comparisons, it seems that our South Pacific dust samples could be explained by mixing of PSAs areas from southern Puna to Patagonia (Fig. 3.4 a and b).

However, all PSA data from southern South America have distinctly higher MREE/MREE*_N (1.09 - 1.40) values compared to our South Pacific dust samples (1.0 - 1.19) (Fig. 3.4 c). Therefore, we argue that our data cannot be adequately described by mixing from southern South American PSAs. It should be noted that a little grain size dependency has been observed for the coarse ($< 63 \mu m$) and the fine ($< 5 \mu m$) fraction of southern South American PSA data, tending towards slightly higher MREE/MREE*_N ratios in the fine fraction (Fig. A 3.2). However, we show that the fine and coarse fraction of southern South American PSA data have considerably higher MREE/MREE*_N ratios than our South Pacific dust samples (Fig. A 3.2). Therefore, our interpretation that the source of dust cannot be solely derived from southern South American PSAs is unaffected by a grain size effect (Fig. A 3.3 a-c).

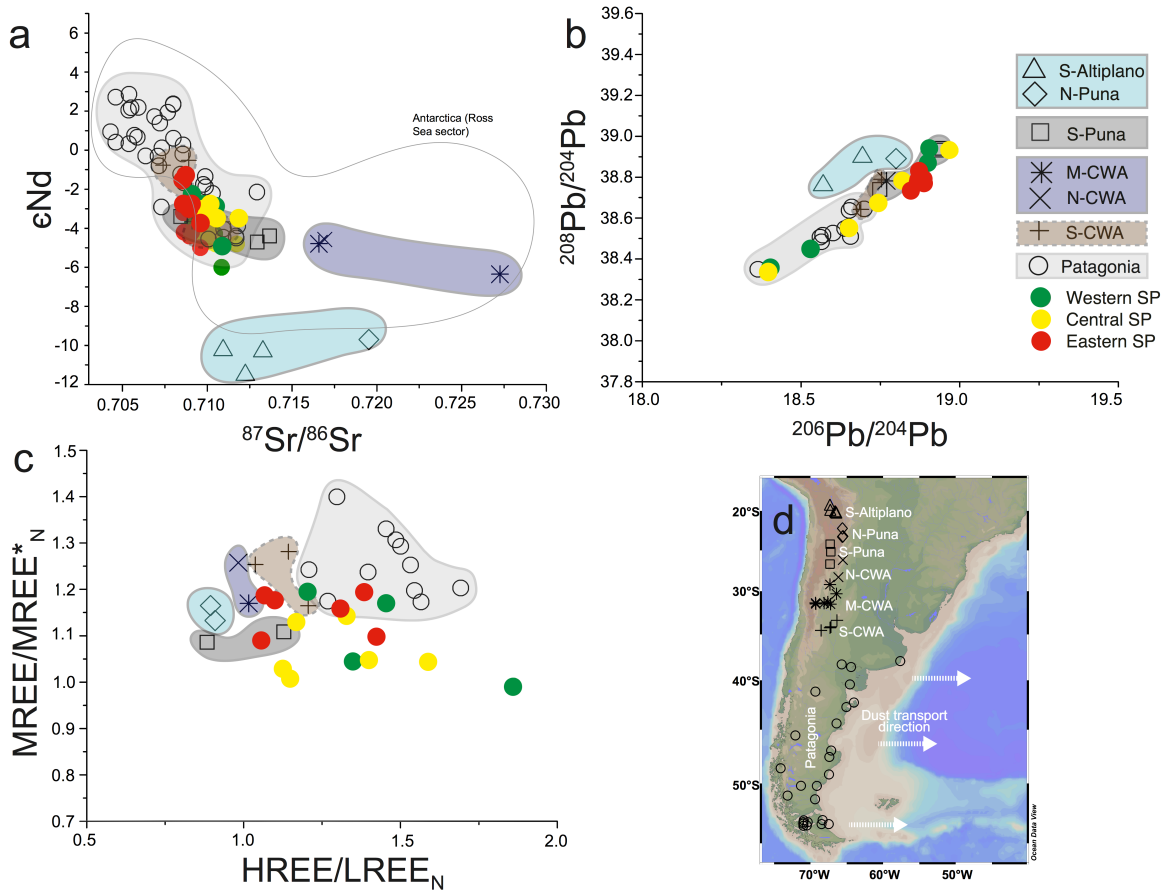


Figure 3.4: Geochemical composition from samples located in southern South American source areas versus South Pacific dust samples. a: Neodymium and strontium isotope results are expressed as ϵNd vs. $^{87}Sr/^{86}Sr$ ratios, respectively. Southern South America including Patagonia ($< 5 \mu m$) (Gili et al., 2017) and additional PSA data from Patagonia ($< 5 \mu m$) (Delmonte et al., 2004a; Sugden et al., 2009). Thin gray polygon reveals data from Victoria Land and the McMurdo Sound sector and Dry Valleys of Antarctica ($< 5 \mu m$) (Delmonte et al., 2004a; Blakowski et al., 2016) b: Lead isotope results are presented as $^{208}Pb/^{204}Pb$ vs. $^{206}Pb/^{204}Pb$. Southern South America including Patagonia ($< 5 \mu m$) (Gili et al., 2016). c: Rare earth element data are normalized to Upper Continental Crust (UCC) (Taylor and McLennan, 1995) and illustrated as $HREE/LREE^*_N = (Tm + Yb + Lu) / (La + Pr + Nd)$ versus $MREE/MREE^*_N = (Gd + Tb + Dy) / [(Tm + Yb + Lu + La + Pr + Nd) / 2]$. Southern South America including Patagonia ($< 5 \mu m$) (Gili et al., 2017). Color code refers to Fig. 3.1. Figure caption is continued on the next page.

d: Map of southern South America with PSA data. S-Altiplano refers to Southern Altiplano, N-Puna and S-Puna refers to Northern and Southern Puna. N-CWA, M-CWA and S-CWA refers to Northern, Middle and Southern Central-Western-Argentina. The South Pacific dust samples were measured on the $< 10 \mu\text{m}$ fraction. The map was generated using the Ocean Data View software (Schlitzer, 2015).

3.5.2.2 *Is there a southern South American component to the South Pacific dust?*

Many studies (e.g. Delmonte et al., 2004a; Vallelonga et al., 2010; Gili et al., 2016; Delmonte et al., 2017; Gili et al., 2017) strongly emphasize the role of dust derived from southern South America in locations as remote as Antarctica. Modern air mass modeling studies in the Southern Hemisphere show that wind trajectories originating in southern South America do not reach our study area (Li et al., 2008; Neff and Bertler, 2015). Additionally, modern southern South American sourced dust is predominately transported in the atmospheric boundary layer, which precludes long-range transport (Li et al., 2008) and also argues against dust deposition in the South Pacific. However, because of the geochemical similarities between Australian, New Zealand and southern South American PSAs we cannot entirely exclude contributions of dust from southern South American PSAs (Fig. A 3.3).

3.5.2.3 *New Zealand and Australian potential dust source areas*

Here we discuss the possibility whether dust to the South Pacific is derived solely from Australian and New Zealand PSAs.

The calculated South Pacific HREE/LREE_N (1.06 - 1.60) and MREE/MREE*_N (1.0 - 1.19) ratios enable us to effectively rule out New Zealand as a PSA to the South Pacific (Fig. 3.5 a). In general, REE data from New Zealand's west and east coast have considerably lower HREE/LREE_N (0.63 - 0.96) and higher MREE/MREE*_N (1.14 - 1.35) ratios compared to our South Pacific dust samples. Therefore, we suggest that the distinct non-match between our South Pacific dust samples and New Zealand PSAs in REE space clearly illustrates that New Zealand cannot be the source of dust to the South Pacific during the Holocene (Fig. 3.5 a).

Australian PSAs include data from the Lake Eyre Basin and the Murray-Darling Basin (Fig. 3.5 d). Our South Pacific HREE/LREE_N (1.06 - 1.60) and MREE/MREE*_N (1.0 - 1.19) ratios show a strong similarity to HREE/LREE_N (0.84 - 1.59) and MREE/MREE*_N (0.82 - 1.24) ratios representative of the Darling catchment (Fig. 3.5 a). There are only three samples from the Darling catchment ($\epsilon_{\text{Nd}} = 0.9$ to -5.2 ; $^{87}\text{Sr}/^{86}\text{Sr} = 0.7092 - 0.7141$) that clearly correspond

with our South Pacific dust samples in Sr-Nd space (Fig. 3.5 b), whereas the majority of the Darling catchment samples are more radiogenic in ϵ_{Nd} (Fig. 3.5 b). However, the $^{87}Sr/^{86}Sr$ ratios of Darling catchment samples are similar to that of our South Pacific dust samples. The samples from the Darling catchment have less radiogenic $^{208}Pb/^{204}Pb$ (37.85 - 38.74) and $^{206}Pb/^{204}Pb$ (17.93 - 18.74) ratios than the majority of our South Pacific dust samples ($^{208}Pb/^{204}Pb = 38.34 - 38.94$; $^{206}Pb/^{204}Pb = 18.40 - 18.97$) (Fig. 3.5 c). On this basis, the Darling catchment cannot be the only PSA of dust to the South Pacific.

The Murray catchment is potentially less important as a source of dust because HREE/LREE_N ratios (0.58 - 1.17) from this area are generally lower than our South Pacific HREE/LREE_N ratios (1.06 - 1.60) (Fig. 3.5 a). However, a few samples are consistent with our South Pacific dust samples (Fig. 3.5 a). The Nd and Sr data show distinctly different Sr-Nd isotopic compositions between the Murray catchment ($\epsilon_{Nd} = -5.7$ to -10.4 ; $^{87}Sr/^{86}Sr = 0.7160 - 0.7547$) and most South Pacific dust samples ($\epsilon_{Nd} = -3.0$ to -6.0 ; $^{87}Sr/^{86}Sr = 0.7086 - 0.7117$) (Fig. 3.5 b). However, the Murray data were obtained from the clay fraction (Gingele and De Deckker, 2005), so that the possible effects of grain size differences on Sr isotopes should be considered (see 3.5.2). Because the $< 2 \mu m$ fraction is characterized by elevated Sr isotopic compositions this effect could account for the offset between the Murray catchment and our South Pacific Sr isotope data. However, in Pb isotope space, the samples from the Murray catchment have less radiogenic $^{208}Pb/^{204}Pb$ (37.56 - 38.63) and $^{206}Pb/^{204}Pb$ (17.66 - 18.60) ratios than the majority of our South Pacific dust samples (Fig. 3.5 c). Therefore, we suggest that the Murray catchment cannot be the sole source of dust to the South Pacific.

Although the Lake Eyre Basin is only represented by five samples in REE space, its HREE/LREE_N (1.15 - 1.29) and MREE/MREE*_N (1.09 - 1.28) ratios clearly correspond with our samples from the South Pacific (Fig. 3.5 a). Additionally, ϵ_{Nd} values and $^{87}Sr/^{86}Sr$ ratios from the Lake Eyre Basin ($\epsilon_{Nd} = -2.9$ to -4.4 ; $^{87}Sr/^{86}Sr = 0.7090 - 0.7105$) show the best match to our South Pacific dust samples ($\epsilon_{Nd} = -3.0$ to -6.0 ; $^{87}Sr/^{86}Sr = 0.7086 - 0.7117$) among all Australian PSAs (Fig. 3.5 b). The calculated $^{208}Pb/^{204}Pb$ (38.58 - 38.81) and $^{206}Pb/^{204}Pb$ (18.74 - 18.99) ratios from the Lake Eyre Basin show a distinct similarity to our dust samples from the South Pacific ($^{208}Pb/^{204}Pb = 38.34 - 38.94$; $^{206}Pb/^{204}Pb = 18.40 - 18.97$) and clearly parallel them in Pb isotopic space (Fig. 3.5 c). Despite the good match between our South Pacific dust samples and the PSA data from the Lake Eyre Basin in all three applied proxies, the variability of our South Pacific dust samples is greater than the PSA data from the Lake Eyre Basin (Fig. 3.5 a-c). This suggests that additional PSAs contributed to the dust in the South Pacific.

Our geochemical data from the South Pacific are consistent with a combination of PSAs from Australia. Our REE data would be most consistent with a combination of Darling and Lake Eyre sourced dust. The Murray PSA data do not seem to contribute significantly to the REE signal, as the majority of the Murray data have lower HREE/LREE_N ratios than our South Pacific dust samples (Fig. 3.5 a). However, in Sr-Nd space there seems to be a contribution from the Murray catchment (Fig. 3.5 b). Taking the grain size dependency on Sr isotopes into account, the South Pacific dust Sr-Nd data could be completely explained by a combination of dust from Murray and Darling PSAs. However, it is clear from the Pb data that the Lake Eyre Basin is also an important source of dust to the South Pacific, as it provides the more radiogenic end-member, which is necessary to produce the Pb signal of our South Pacific dust samples (Fig. 3.5 d). In summary, based on the consistency between the Lake Eyre Basin PSA data and our South Pacific dust samples in all applied proxies, we suggest that the Lake Eyre Basin is the dominant source of dust to the South Pacific in the Holocene, however, the Murray-Darling Basin also provides an additional source of dust.

Li. et al. (2008) used a model-based investigation of the dust distribution in the Southern Hemisphere and showed that dust from the Australian continent has the potential to dominate dust accumulation across the whole Pacific sector of the SO. Simulations of the modern dust distribution also show that Australian sourced dust is transported in the free troposphere, which enables transport across longer distances (Li et al., 2008). McGowan and Clark (2008) modeled modern dust transport pathways originating in the Lake Eyre Basin and found that spring and early summer conditions enable dust to be transported via the southeast dust transport corridor and the prevailing SWW to large parts of the South Pacific, even as far as southern South America.

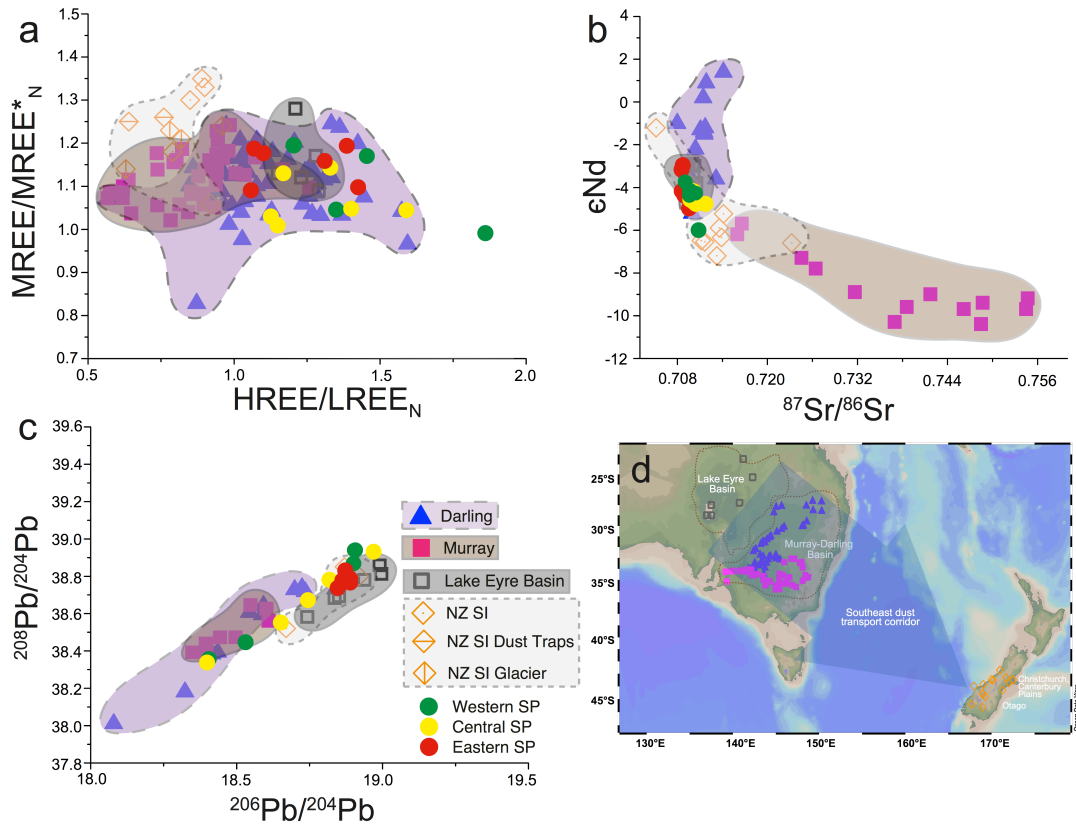


Figure 3.5: Geochemical composition from samples located in Australia and New Zealand source areas versus South Pacific dust samples. a: Rare earth element data are normalized to Upper Continental Crust (UCC) (Taylor and McLennan, 1995) and illustrated as $HREE/LREE_N = (Tm + Yb + Lu) / (La + Pr + Nd)$ versus $MREE/MREE*_N = (Gd + Tb + Dy) / [(Tm + Yb + Lu + La + Pr + Nd) / 2]$. Murray-Darling Basin ($< 90 \mu m$) (Marx and Kamber, 2010), Lake Eyre Basin ($< 5 \mu m$ and $< 80 \mu m$) (McGowan et al., 2005 and this work). New Zealand South Island (dust traps, glacier and loess deposits) (Marx et al., 2005). b: Neodymium and strontium isotope results are expressed as ϵNd vs. $^{87}Sr/^{86}Sr$ ratios, respectively. Murray-Darling Basin ($< 2 \mu m$) (Gingele and De Deckker, 2005), Lake Eyre ($< 5 \mu m$) (Revel-Rolland et al., 2006 and this work), New Zealand South Island ($< 5 \mu m$) (Delmonte et al., 2004a). c: Lead isotope results are presented as $^{208}Pb/^{204}Pb$ vs. $^{206}Pb/^{204}Pb$. Murray-Darling Basin ($< 2 \mu m$) (De Deckker et al., 2010), Lake Eyre Basin ($< 5 \mu m$) (this work). New Zealand ($< 5 \mu m$) (Vallelonga et al., 2010). Color code refers to Fig. 3.1. The South Pacific dust samples were measured on the $< 10 \mu m$ fraction. d: Map of central and southeast Australia and New Zealand with PSA data. Open squares show the Lake Eyre Basin. Triangles show to the Darling catchment. Filled squares show the Murray catchment. Open diamonds refer to New Zealand's South Island. Figure caption is continued on the next page.

The shaded blue arrow roughly indicates the extension and direction of the southeast Australian dust transport corridor (Bowler, 1976; McGowan and Clark, 2008). The map was generated using the Ocean Data View software (Schlitzer, 2015).

3.6 Conclusion

We present a comprehensive data set of surface sediment samples, representing terrigenous sedimentation through the Holocene in the Pacific sector of the Southern Ocean. To identify PSAs that deliver dust to the South Pacific, we combine lithogenic fluxes with provenance sensitive proxies (REE, Sr, Nd and Pb isotopes). Lithogenic fluxes provide a general overview of the distribution and different transport mechanisms of terrigenous material in our study area. We observe the highest lithogenic fluxes off New Zealand, which likely indicate a combination of accumulated dust from Australia/New Zealand admixed with riverine input from New Zealand, whereas the sites in the remote open ocean reflect a dust signal. Isotopic and REE data imply that southern South American PSAs cannot entirely be excluded. However, modern air mass modeling studies in the Southern Hemisphere show that wind trajectories originating in southern South America do not reach our study area. We conclude that the Lake Eyre Basin in central Australia is the most important PSA for atmospheric dust distributed over the South Pacific in the Holocene. However, we acknowledge the possibility of admixture from the Murray-Darling Basin. We emphasize the need for better characterization of PSAs, including the west coast of South America, New Zealand's South Island and Antarctica. Furthermore, provenance analysis in the Atlantic sector of the Southern Ocean is required to better evaluate the contributions from southern South America. These studies will provide the stepping-stones for understanding past variations in atmospheric dust, its link to climate variability.

Acknowledgements

We thank chief scientists, crews and participants of R/V *Polarstern* (PS35, PS58 and PS75) and R/V *Sonne* (SO213) for their support. We are grateful to R. Fröhlking-Teichert, S. Wiebe and M. Schulz for providing technical assistance. This study is part of the project "Polar Regions and Coasts in the changing Earth System (PACES II)" of the Alfred Wegener Institute (AWI) Helmholtz Centre for Polar and Marine Research. We acknowledge financial support for this work through the AWI and the MARUM-Center for Marine Environmental Sciences.

APPENDIX A. Supplementary data

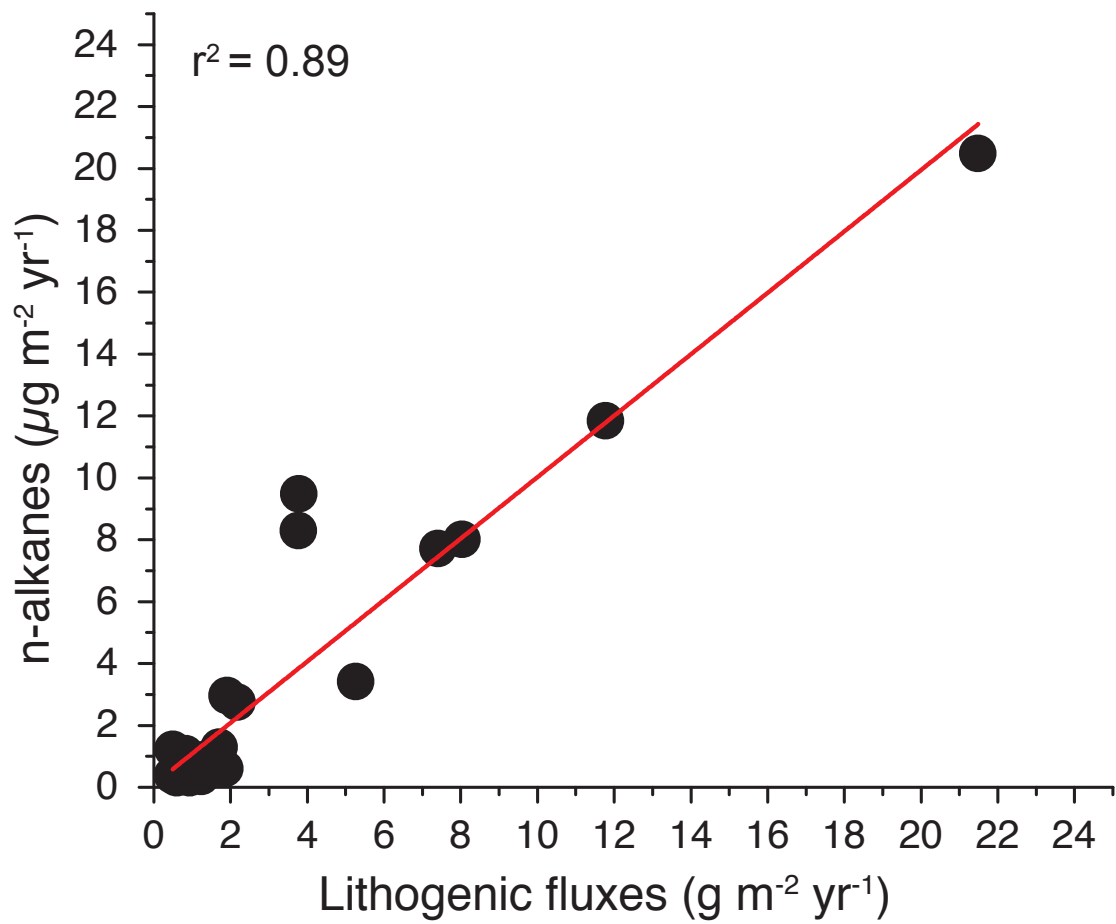


Figure A 3.1: Correlation of plant wax n-alkanes and lithogenic fluxes (Jaeschke et al., 2017, this work).

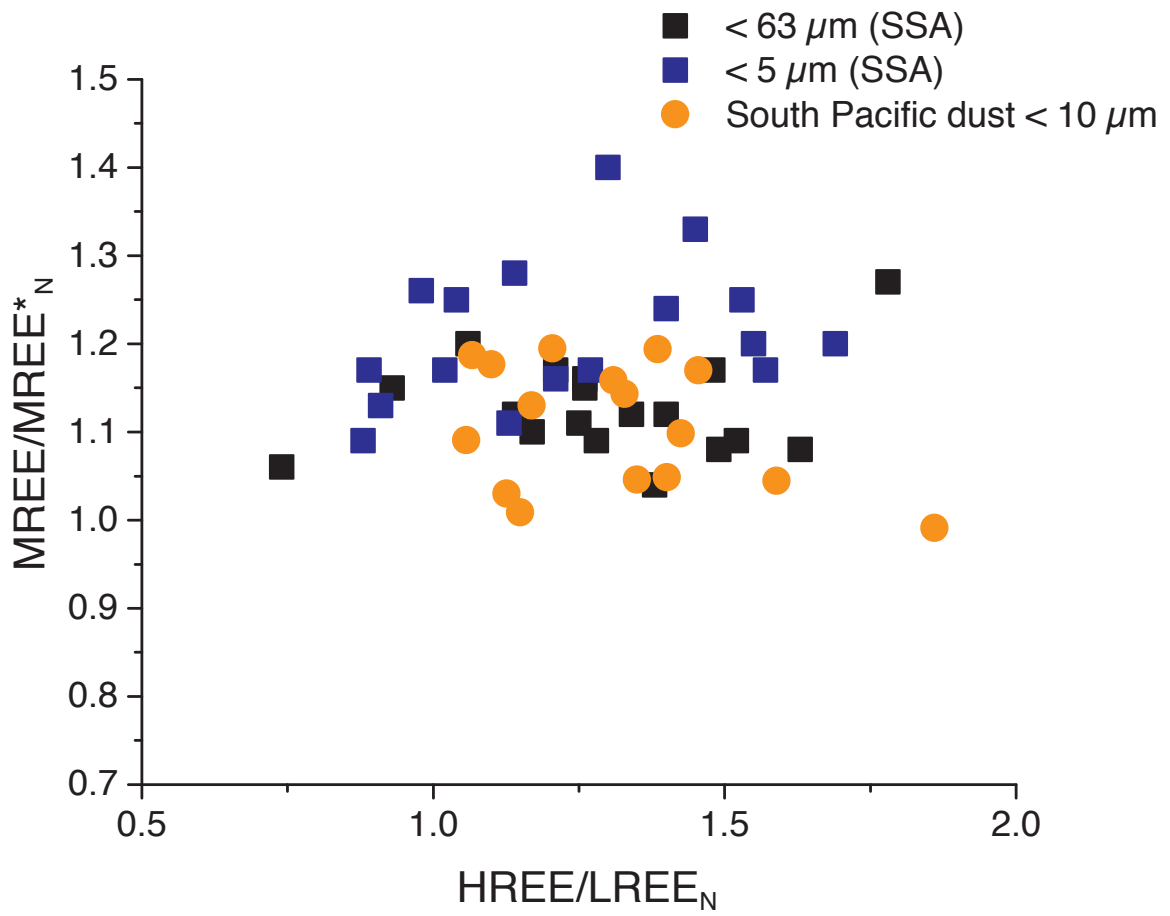


Figure A 3.2: Grain size comparison of southern South American samples (SSA) (Gili et al., 2016; Gili et al., 2017) and South Pacific dust samples.

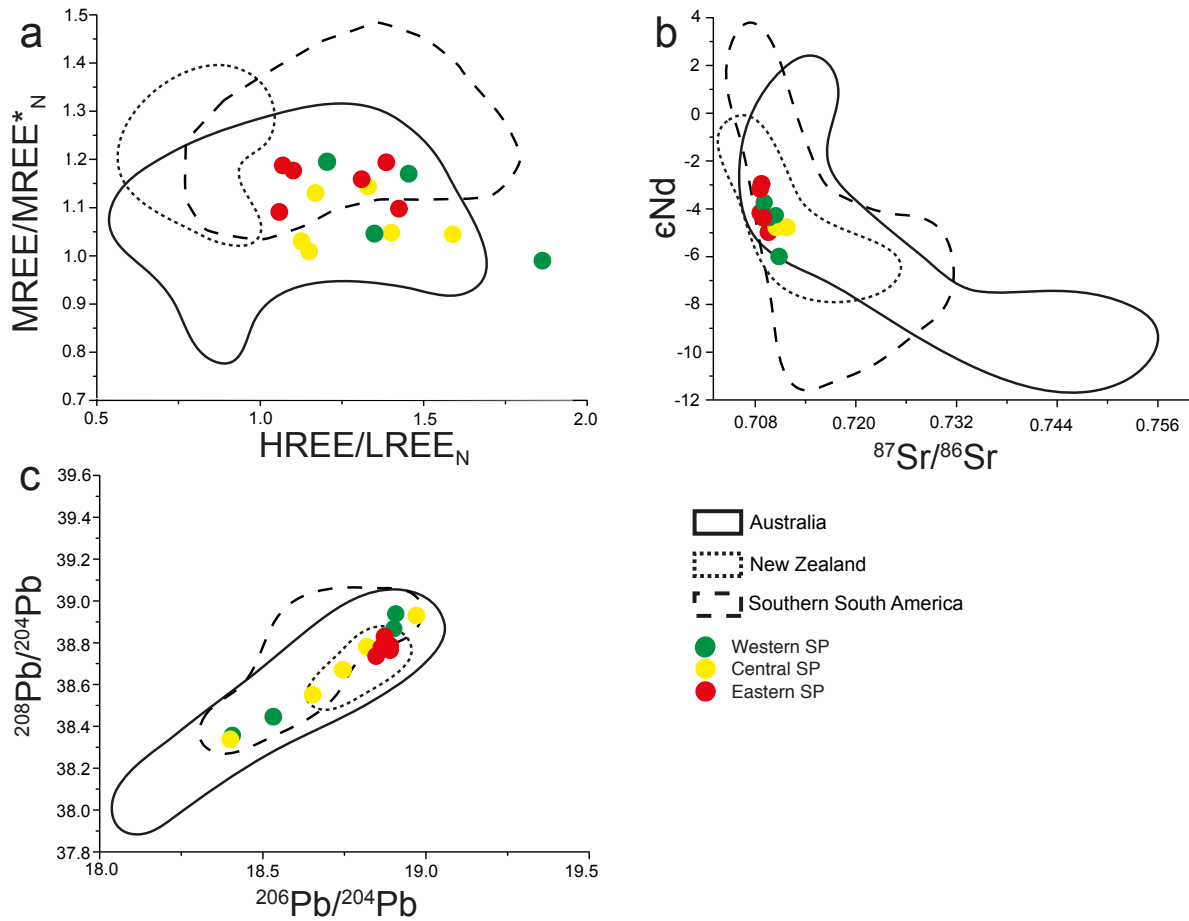


Figure A 3.3: Comparison between Australian (Gingele and De Deckker, 2005; McGowan et al., 2005; Revel-Rolland et al., 2006; De Deckker et al., 2010; Marx and Kamber, 2010), New Zealand (Delmonte et al., 2004a; Marx et al., 2005; Vallenga et al., 2010) and southern South American (Delmonte et al., 2004a; Sugden et al., 2009; Gili et al., 2016; Gili et al., 2017) potential source areas. a: Rare earth element data are normalized to Upper Continental Crust (UCC) (Taylor and McLennan, 1995) and illustrated as $HREE/LREE_N = (Tm + Yb + Lu) / (La + Pr + Nd)$ versus $MREE/MREE*_N = (Gd + Tb + Dy) / [(Tm + Yb + Lu + La + Pr + Nd) / 2]$. b: Neodymium and strontium isotope results are expressed as ϵNd vs. $^{87}Sr/^{86}Sr$ ratios, respectively. c: Lead isotope results are presented as $^{208}Pb/^{204}Pb$ vs. $^{206}Pb/^{204}Pb$.

4 Opposing dust grain size changes in the Pacific and Atlantic sectors of the Southern Ocean during the last 260 kyr

Marc Wengler^{a,b}, Frank Lamy^{a,b}, Alfredo Martínez-García^c, Gerhard Kuhn^a, Jan-Berend Stuut^d, Ralf Tiedemann^a, Gisela Winckler^e

^aAlfred Wegener Institute, Helmholtz Center for Polar and Marine Research, Department for Marine Geology, D-27515 Bremerhaven, Germany

^bMARUM Center for Marine Environmental Sciences, University of Bremen, D-28334 Bremen, Germany

^cMax Planck Institute for chemistry, Climate Geochemistry Group, D-55128 Mainz, Germany

^dNIOZ – Royal Netherlands Institute for Sea Research, P.O. Box 59, 1790 AB Den Burg, The Netherlands

^eLamont-Doherty Earth Observatory, Columbia University, Palisades, 10964 New York, USA

*Correspondence to: marc.wengler@awi.de

Keywords: Southern Ocean, Southern Westerly Winds, Eolian dust, Glacial-interglacial dust variability

In preparation for *Earth and Planetary Science Letters*

Abstract

We present the first comprehensive grain size data set extracted from two deep-sea sediment records from Pacific and Atlantic sectors of the Southern Ocean and detected large scale dust fluctuations during the last 260 kyr. We combine grain size analysis with ^{230}Th -normalized lithogenic fluxes (lithogenic flux) and Fe records because these proxies are well established indicators for atmospheric dust input in the Pacific and Atlantic sectors Southern Ocean. We calculated mean dust grain sizes for both sediments records and use it as a direct proxy to infer variations within the Southern Westerly Winds as well as for changes in potential source area characteristics (e.g. aridity, precipitation). Additionally, we reveal that the 2-10 μm fraction (fine silt) appears to be representative to reconstruct dust transport to the Southern Ocean. Our mean dust grain sizes show opposing glacial-interglacial dust variability with coarser grain sizes during glacial periods in the Pacific sector compared to the Atlantic. The mean dust grain size record combined with Fe and lithogenic flux data shows a synchronous pattern in the Pacific Southern Ocean indicating increased glacial dust availability in Australia and/or New Zealand coupled with increased and/or northward shifted Southern Westerly Winds. Simultaneously, increased Fe and lithogenic flux records during glacial periods in the Atlantic Southern Ocean likewise point to enhanced dust availability in southern South America. In contrast, reduced glacial mean dust grain sizes reveal that the glacial Southern Westerly Winds were decreased over Patagonia and were not able to erode large dust particles. Drier interglacial conditions over the northern parts of southern South America likely favored erosion of larger dust particles.

4.1 Introduction

Atmospheric dust plays a key role in the global climate system through impacting the climate either directly, by influencing the radiative properties of the atmosphere through scattering and absorbing light, or indirectly, by modifying cloud properties (Arimoto, 2001; Sassen et al., 2003). Furthermore, dust has the capability of influencing the climate through its effect on surface ocean productivity by supplying iron to the ocean and therefore affecting the global carbon cycle through iron fertilization of marine ecosystems (Martin, 1990; Martínez-García et al., 2014). According to the iron hypothesis elevated dust fluxes, especially during glacial periods, to the Southern Ocean (SO) may have enhanced marine productivity in high-nutrient low-chlorophyll regions, such as the SO, resulting in a drawdown of atmospheric CO_2 (Martin, 1990). However, the impact of other SO ocean processes such as sea-ice cover, overturning

circulation and water column stratification and their effect on the global CO₂ cycle are still under debate (Fischer et al., 2010; Sigman et al., 2010).

The erosion of dust in potential source areas (PSAs) strongly depends on climatic conditions influencing soil and terrain properties (e.g. vegetation cover, rainfall intensity, local winds) (e.g. Goudie, 2008) and its transport is based on the strength of the Southern Westerly Winds (SWW) as the main carrier of dust to the SO. However, seasonal variations of the SWW could have affected dust transport and accumulation in the SO (Lamy et al., 2010).

Antarctic ice cores have been analyzed to reconstruct the Earth's climate evolution by either providing temperature and CO₂ records (Jouzel et al., 2007; Lüthi et al., 2008) or by analyzing the provenance of dust in Antarctic ice cores (Delmonte et al., 2010; Gili et al., 2017). Paleoclimate reconstructions from the EPICA (European Project for Ice Coring in Antarctica) ice core at Dome C (EDC) in East Antarctica cover the last ~800 kyr and reveal a ~25-fold increase in glacial dust fluxes compared to interglacial periods corresponding with Antarctic temperature and CO₂ records (Lambert et al., 2008; Lüthi et al., 2008). Subsequently, Antarctic ice cores provide a valuable archive of dust deposition over several glacial-interglacial (G/IG) cycles.

Additional knowledge of the dust distribution in the Southern Hemisphere is based on modeling studies (Li et al., 2008; Albani et al., 2014; Neff and Bertler, 2015). Although dust modeling studies often underestimate the amount of dust transported to the ocean compared to marine sediment data, they reveal a valuable tool to infer PSAs and therefore dust transport directions.

High-resolution down core dust records from the SO indicate higher dust deposition rates in glacial compared to interglacial periods coupled with higher export productivity (Chase et al., 2003; Bradtmiller et al., 2009; Martínez-García et al., 2014; Lamy et al., 2014). Although these studies are predominantly based on Fe and Th contents (Martínez-García et al., 2014; Lamy et al., 2014), they allow a more direct estimation of dust supply to the SO (compared to model data) because these elements are strongly linked to dust transport to the ocean. Grain size analysis in the SO are presently restricted to two cores in the Tasman Sea revealing increased dust fluxes during glacial periods coupled with no substantial grain size changes from the Last Glacial Maximum (LGM) to the Holocene (Hesse and McTainsh, 1999).

The general lack of grain size data from the Pacific and Atlantic sectors of the SO strongly emphasizes the need for data from these areas for paleoclimate reconstructions, especially to infer changes in PSAs and the variations within the SWW. Therefore, we present the first grain size data set from the Subantarctic Zones of the Pacific and Atlantic sectors of the SO from

two deep-sea sediment records. Both sediment cores are located downwind of the major Southern Hemisphere dust source regions (Australia, New Zealand and Southern South America) and are therefore ideal to better understand temporal and spatial dust transport to the SO. We aim to link dust grain size variations to fluctuations within the SWW and changes in PSAs to reconstruct paleoclimate changes over G/IG timescales.

4.2 Material and Methods

4.2.1 Core material and core locations

We analyzed the marine sediment cores from site PS75/056 from the Pacific sector of the SO and ODP Site 1090 (leg 177) from the Atlantic sector of the SO (Fig. 4.1). Core PS75/056-1 (55°09.74'S; 114°47.31'W, 3581 m water depths, 10.21 m total length) covers the last 260 kyr Bp and was recovered during *R/V Polarstern* expedition PS75 from the Subantarctic Zone east of the East Pacific rise using a gravity corer (Gersonde, 2011) (Fig. 4.1). The sediment material predominantly consists of calcareous ooze during interglacial periods with maximum calcium carbonate (CaCO₃) values up to 82 wt. %. During glacial periods, the sediment material is mainly composed of diatom ooze resulting in maximum biogenic opal contents up to 60 wt. %. The age model of core PS75/056-1 was initially compiled by Ullermann et al. (2016) and updated by Basak et al. (2018). Briefly, the age model is based on the correlation of the benthic δ¹⁸O isotope record to the δ¹⁸O of core MD 97-2120 (Basak et al., 2018).

In total, five holes were drilled at ODP Site 1090 (42°54.8'S; 8°53.9'E, 3702 m water depths, 397 m total length (Hole 1090B)) during ODP Leg 177 in the central part of the Subantarctic Zone of the Atlantic sector of the SO at the southern flank of the Agulhas Ridge. ODP Site 1090 predominantly consists of calcareous ooze, mud bearing diatom and nannofossil ooze. Biogenic Opal and CaCO₃ contents were inferred from the nearby sediment core PS2489-2 (Diekmann and Kuhn, 2002). Biogenic opal is constantly less than 5 wt %, whereas CaCO₃ reaches values up to 90 wt. % in interglacial periods and up to 70 wt. % in glacial periods. The age model of ODP Site 1090 is described in Martinez-Garcia et al. (2014). Briefly, the age model was generated by graphic correlation of the high resolution ²³⁰Th normalized Fe flux from ODP Site 1090 to the ice core dust reconstruction from EDC (Lambert et al., 2012), using ice core chronology (AICC2012) (Bazin et al., 2013; Veres et al., 2013).

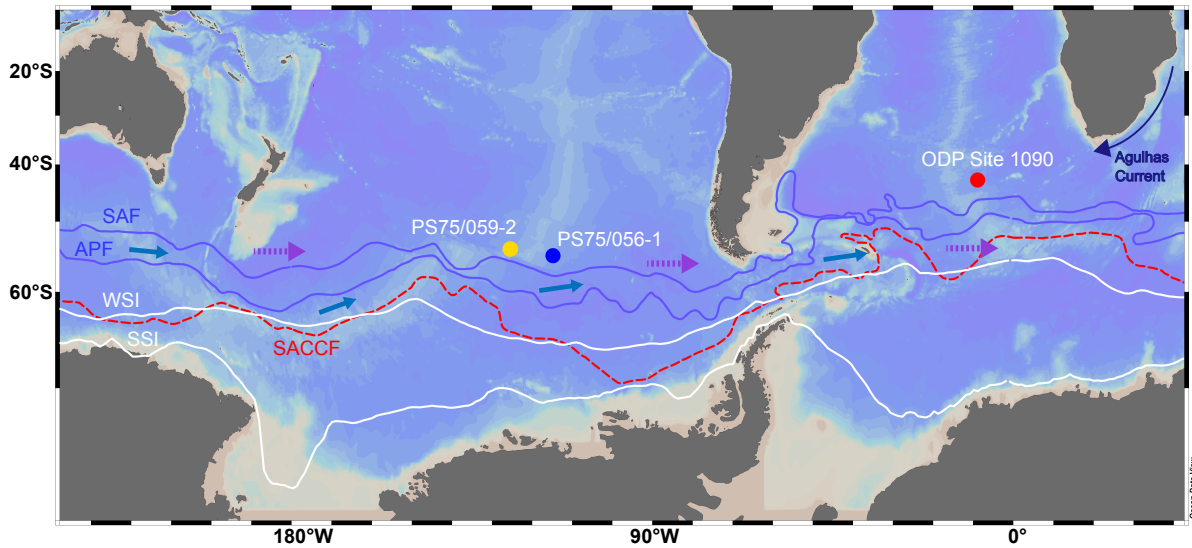


Figure 4.1: Map of the Pacific and Atlantic sectors of the SO with core locations recovered during R/V *Polarstern* (PS75) and *JOIDES Resolution* (leg 177) expeditions. Yellow dot: Sediment core PS75/059-2; used for biomarker analysis (Lamy et al., 2014). Blue dot: Sediment core PS75/056-1 (this study). Red dot: ODP Site 1090 (this study). Colored lines refer to mean positions of major front systems (Orsi et al., 1995). SAF: Subantarctic Front, APF: Polar Front. SACCF: Southern Antarctic Circumpolar Current Front. Mean extension of winter and summer sea ice (WSI and SSI) is indicated by white lines (Comiso, 2003). Blue arrows indicate the flow direction of the Antarctic Circumpolar Current (ACC). Purple dashed arrows show the direction of the Southern Westerly Winds (SWW). Thin dark blue arrow: Agulhas Current. The map was generated using the Ocean Data View software (Schlitzer, 2015).

4.2.2 Methods

4.2.2.1 Chemical leaching of organic matter, biogenic opal and CaCO_3

The chemical leaching of sediment core PS75/056-1 was conducted at the Alfred Wegener Institute in Bremerhaven (AWI), whereas ODP Site 1090 was chemically treated at the department of Earth Sciences at the Eidgenössische Technische Hochschule (ETH) in Zurich. Based on different biogenic opal and CaCO_3 contents individual leaching procedures were applied to the sediment cores.

Approximately 300 mg of the sediment was transferred into 15 mL centrifuge tubes and 5 mL HCl (10 %) was added to remove CaCO_3 from ODP Site 1090. The samples were centrifuged at 3000 rpm (for 5 minutes) and the overlying HCl was discarded. Subsequently, 10 mL of DI water was added and centrifuged to rinse the samples. Organic matter was removed by adding 5 mL of H_2O_2 (34 %) to the centrifuge tubes before they were transferred to a boiling water bath for 1 hour. The samples were centrifuged and the overlying H_2O_2 was discarded before the samples were rinsed again. Biogenic opal (< 5 wt. %) was removed with 5 mL NaOH (10 %). The samples were transferred to the boiling water bath for 30 minutes and rinsed to bring the pH to neutral.

To completely remove the organic matter from the sediment core PS75/056-1, 20 mL H_2O_2 (35 %) (hydrogen peroxide) was added to ~5 g of the dry bulk sediment. The mixture was placed on a shaking table for at least 24 hours or until the reaction between the sediment and the reagent ceased and excess H_2O_2 disintegrated into H_2O and O_2 . Subsequently, the sediment was wet sieved to the < 63 μm fraction. Given the increased biogenic opal content of sediment core PS75/056-1, we developed a new leaching procedure to ensure a complete removal of biogenic opal using NaOH (sodium hydroxide). Test samples with highest biogenic opal contents were used to select the most adequate concentration of NaOH. The test samples were leached with 10 % NaOH and 20 % NaOH solutions, respectively. Microscope analysis confirmed that the latter concentration most effectively removes biogenic opal from the sediment (Fig. A 4.1). Because of the relatively high concentrated NaOH solution, especially clay minerals could be affected by dissolution or grain shape alterations. Moreover, given that diatom fragments, sponge spicules, diatoms and radiolarian fragments would remain in the < 63 μm fraction due to incomplete leaching, the effect of such biological fragments on the grain size distribution would be more severe than dissolved or altered clay minerals.

Approximately ~1 g of the organic matter free < 63 μm fraction was transferred into 1 L glass beakers and 250 mL 20 % NaOH was added to remove biogenic opal. The beaker was placed on a hot plate with magnetic stirring function under a ventilation hood and the mixture was gently heated up to 85°C and held for exactly one hour. During the experimental phase, we found that biogenic opal dissolution is most efficient when the NaOH-sediment solution is permanently mixed, so that diatoms might additionally become instable due to the friction with the sediment. Afterwards, the NaOH-sediment solution was transferred into clean 1 L centrifuge beakers and demineralized water (DI water) was added to rinse the basic solution. The NaOH-sediment solution was centrifuged for 5 minutes at 20°C (including the acceleration and deceleration phase) with 5050 revolutions per minute (rpm) using a *Cryofuge 8500i* (Thermo Scientific) centrifuge. After every run, the overlying basic water was decanted and DI water was added to the sediment. It is noteworthy, that we used a squirt bottle filled with DI water to loosen up the sediment at the bottom of the centrifuge beaker to ensure a more effective rinsing of the sediment. The rinsing was repeated until the pH of the sediment was equal to the pH of the DI water (we needed at least four runs). We carefully checked the pH after every run because we found that a slightly basic solution resulted in a fluffy sediment structure, which was difficult to disaggregate. The biogenic opal free sediment was transferred into 125 mL transparent plastic beakers and filled up to 110 mL with DI water. Approximately ~1 mL of 10 % HCl (hydrochloric acid) was added to remove the remaining CaCO₃ and the acetic mixture was placed on a shaking table under a ventilation hood for 24 hours. To avoid moving the plastic beakers to do not disperse the settled sediment, we used a water jet pump to remove the overlying water. The rinsing process of the acetic sediment solution was repeated until the pH of the sediment was equal to the pH of the DI water (we needed at least two runs).

4.2.2.2 Grain size analysis

The grain size analysis of ODP Site 1090 was conducted at the ETH in Zurich. ODP Site 1090 was sampled in 1 cm intervals and grain size analysis was conducted on the bulk sediment fraction. Prior to the grain size analysis, 10 mL 2 % Na₄P₂O₇ 10H₂O (sodium pyrophosphate) was added to each sample for 48 hours to completely disaggregate the sediment. The particle size distributions of the terrigenous fraction were measured with a Malvern Mastersizer 2000, which resulted in 84 size classes ranging from 0.02 to 2000 μm for every analyzed sample.

The grain size analysis of sediment core PS75/056-1 was conducted at the Royal Netherlands Institute for Sea Research (NIOZ). The sediment core was sampled in 5 cm intervals and grain

size analysis was conducted on the $< 63 \mu\text{m}$ fraction. Prior to the grain size analysis, 20 mL 2 % $\text{Na}_4\text{P}_2\text{O}_7 \cdot 10\text{H}_2\text{O}$ was added to each sample and placed on shaking table for 24 hours to completely disaggregate the sediment. The particle size distributions of the terrigenous fraction were measured using a Beckman Coulter laser sizer LS13320, which resulted in 116 size classes ranging from 0.04 to 2000 μm for every analyzed sample. The calculation of the particle sizes relies on the Fraunhofer diffraction theory and the Polarization Intensity Differential Scattering (PIDS) for particles from 0.4 to 2000 μm and from 0.04 to 0.4 μm , respectively. To minimize the influence of gas bubbles degassed water was used during analysis.

Grain size mean values for both cores were calculated for the fine silt fraction (2-10 μm) using the software *Gradistat* (Blott and Pye, 2001). Mean grain size values are expressed in the Folk and Ward nomenclature because this method provides the most robust approach to compare compositionally variable sediments (Folk and Ward, 1957).

4.2.2.3 Uranium-Thorium isotope analysis

The ^{230}Th (thorium) isotope is a product of the ^{238}U (uranium) decay series (Francois et al., 2004) with a half-life time of 75.548 ± 110 years (Cheng et al., 2013). The parent isotope ^{234}U produces (through α -decay) the highly insoluble (in seawater) and particle reactive ^{230}Th isotope at a uniform and well-known rate ($\beta = 0.0267 \text{ dpm m}^{-3}\text{year}^{-1}$). Attached to sinking particles ^{230}Th is transported to the seafloor (Thomson et al., 1993; Francois et al., 2004). Sediment particles are assumed to contain a fraction of ^{230}Th in a secular equilibrium with lithogenic ^{234}U . However, the total amount of ^{230}Th in deep-sea sediments near the sediment surface exceeds the amount supported by ^{234}U . This fraction of ^{230}Th is called $^{230}\text{Th}_{\text{xs}}$ (230-Thorium excess) (Francois et al., 2004). This relationship forms the basis for the ^{230}Th normalization method (Thomson et al., 1993). The Th and U isotope analysis of PS75/056-1 and ODP Site 1090 are in detail explained in Shoenfelt et al. (submitted) and Martínez-García et al. (2009), respectively.

Supported ^{230}Th for both sediment cores was calculated according to Francois et al. (2004), using a $^{238}\text{U}/^{232}\text{Th}$ activity ratio of 0.4 ± 0.1 (Henderson and Anderson, 2003). $^{230}\text{Th}_{\text{xs}}$ was used to calculate the preserved vertical lithogenic fluxes by multiplying the uniform ^{230}Th production rate ($\beta = 0.0267 \text{ dpm m}^{-3} \text{ yr}^{-1}$) and the water depth divided by the $^{230}\text{Th}_{\text{xs}}$ concentrations (dpm g^{-1}) (Francois et al., 2004). ^{232}Th concentrations were used to determine the lithogenic fraction in the sediment cores assuming an average ^{232}Th concentration of 10.7

ppm for the upper continental crust (Taylor and McLennan, 1995). In the following text, we refer to the ^{230}Th -normalized fluxes of ^{232}Th in short as lithogenic fluxes.

4.3 Results and Discussion

4.3.1 Evaluation of the dust grain size in the Pacific sector of Southern Ocean (Sediment core PS75/056-1)

The sediment core PS75/056-1 covers the last 260 kyr and reaches back to Marine Isotope Stage 8 (MIS). All investigated samples from this sediment core show a bimodal grain size distribution with a main peak at $\sim 4\ \mu\text{m}$ and a less prominent peak at $\sim 30\ \mu\text{m}$ (Fig. 4.2). On average 90 Vol. % (volume percentage per size class; 116 size classes were measured) of the total sediment material is concentrated in the clay (0-2 μm) and fine silt (2-10 μm) fraction, whereas the medium and coarse silt (10-63 μm) fraction consists of only 10 Vol. % (on average) (Fig. 4.3). Further separations of the 0-10 μm fraction into the clay and the fine silt fractions reveal that 35 Vol. % (on average) are concentrated in the clay fraction (Fig. 4.3). Although the clay fraction most likely represents eolian dust to a large portion, it may be strongly affected by dissolution during the biogenic opal leaching process (see 4.2.2.1). The resulting grain shape alterations of the clay minerals produce an additional source of error, which is difficult to account for. The fine silt fraction constitutes 55 Vol. % (on average) of the grain size distribution (Figs. 4.2 and 4.3). Additionally, compared to medium and coarse grained silt, the fine silt fraction is not affected by current redistribution at the seafloor as this sediment fraction is cohesive and forms aggregates (McCave et al., 1995). Therefore, we focus on the fine silt fraction as being most likely entirely dust derived.

John H. Martin (1990) suggested that elevated glacial dust fluxes to the SO would have increased the marine biological productivity by adding iron (Fe) to the ocean (iron fertilization), which resulted in a drawdown of atmospheric CO_2 concentrations. It was shown that Fe records (bulk sediment) from the Pacific and Atlantic sectors of the SO (Martínez-García et al., 2009; Lamy et al., 2014) clearly correlate with Antarctic dust, CO_2 and temperature records over G/IG timescales (Jouzel et al., 2007; Lambert et al., 2008; Lüthi et al., 2008; Lambert et al., 2012). Additionally, Lamy et al. (2014) further showed that Fe down core contents from the Pacific sector of the SO largely co-vary with ^{232}Th -based dust flux estimates (lithogenic flux). We extend this finding to our sediment core PS75/056-1, which also shows a strong positive correlation between the Fe content and the lithogenic flux ($r^2 = 0.63$) (Figs. 4.4 a, 4.5 c and e). Subsequently, we compared the fine silt fraction to the Fe and

lithogenic flux records of our sediment core and find that the Fe and the lithogenic flux records show a strong linear correlation with the fine silt fraction (Fe, $r^2 = 0.55$; lithogenic flux, $r^2 = 0.62$) (Fig. 4.4 b and c). According to these relationships, we argue that the fine silt fraction is the most suitable grain size range to reconstruct dust transport to the Pacific sector of the SO.

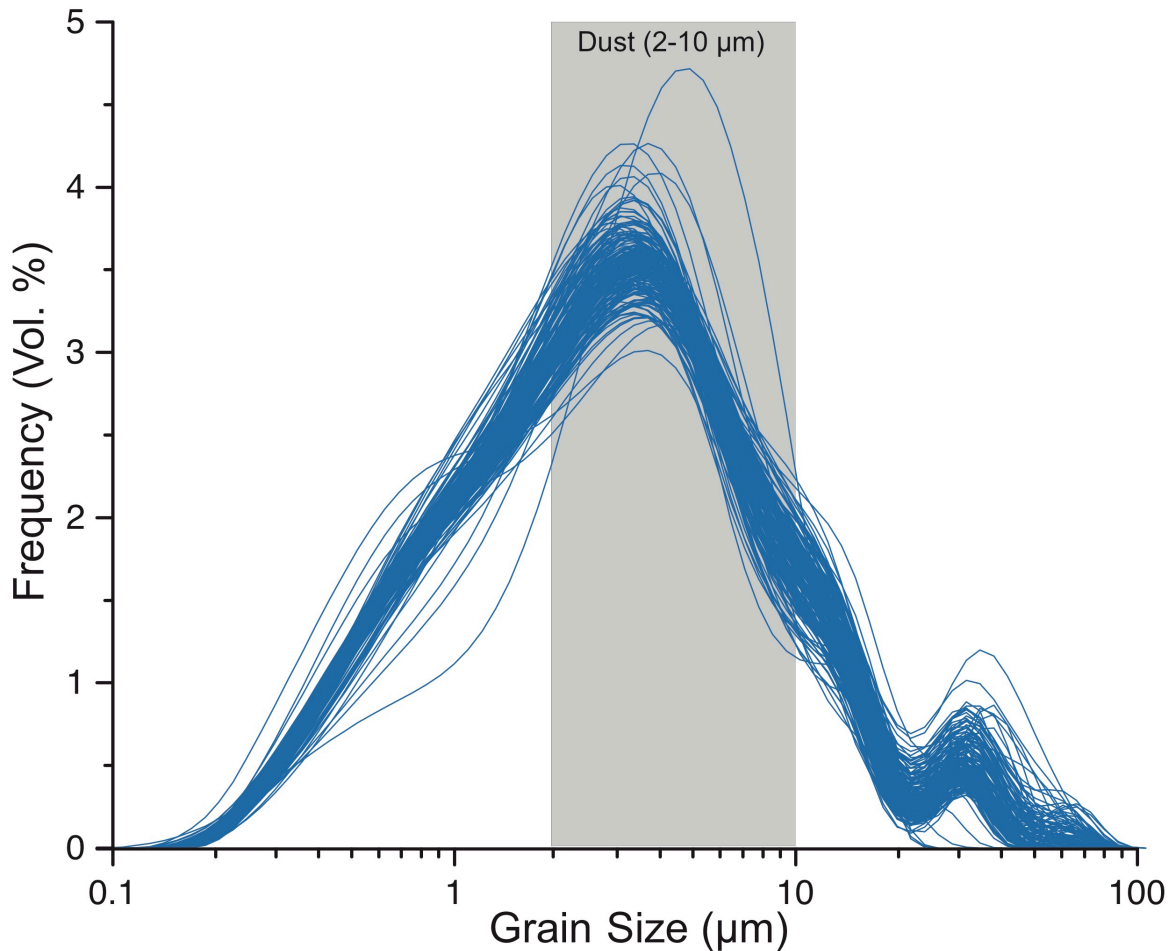


Figure 4.2: Grain size distribution of sediment core PS75/056-1. Grain sizes were measured on the $< 63 \mu\text{m}$ fraction. Grain sizes exceeding $63 \mu\text{m}$ most likely result from platy minerals (e.g. clay and mica minerals). Note the logarithmic scale on the x-axis. The y-axis shows the frequency given in volume percentage per size class. 116 size classes were measured. The grain size distribution shows a distinct maximum at $\sim 4 \mu\text{m}$ and a less pronounced peak at $\sim 30 \mu\text{m}$. 55 Vol. % are concentrated in the fine silt ($2-10 \mu\text{m}$) fraction (gray bar). The clay ($0-2 \mu\text{m}$) and medium to coarse silt fractions ($10-63 \mu\text{m}$) were excluded from our dust grain size analysis because they could be affected by dissolution during the opal leaching process ($0-2 \mu\text{m}$ fraction) or could be affected by bottom current redistribution at the seafloor ($10-63 \mu\text{m}$ fraction) (McCave et al., 1995).

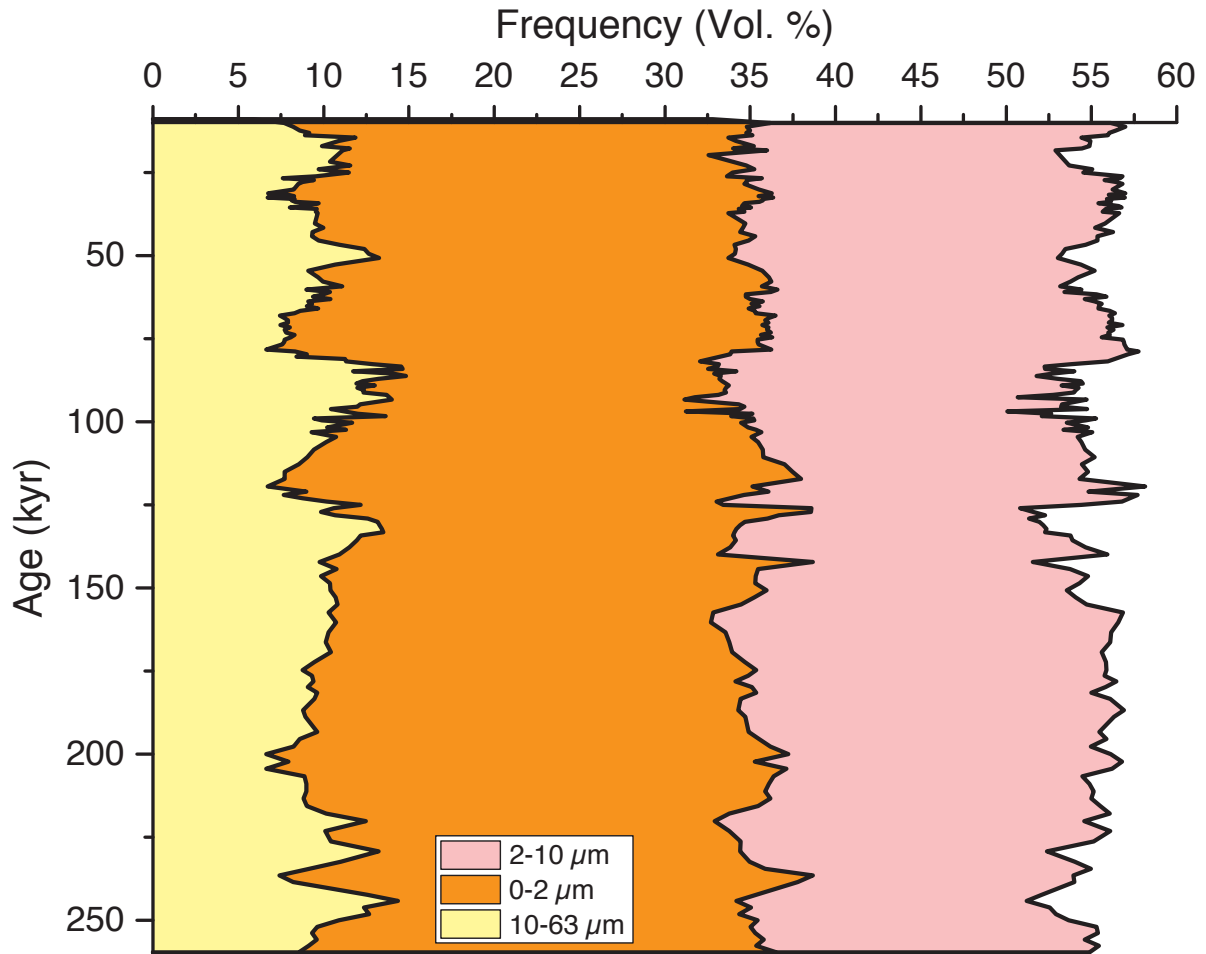


Figure 4.3: Grain size distribution of sediment core PS75/056-1 versus age. Note that the sum of the components equals 100 Vol. %. 90 Vol. % (volume percentage per size class; 116 size classes were measured) of the total sediment material is concentrated in the 0-10 μm fraction. The medium to coarse silt fraction (10-63 μm) consists of 10 Vol. %. Further separations of the 0-10 μm fraction into the clay (0-2 μm) and fine silt (2-10 μm) fractions reveal that 35 Vol. % are concentrated in the clay and 55 Vol. % are concentrated in the fine silt fractions. The given numbers are average values.

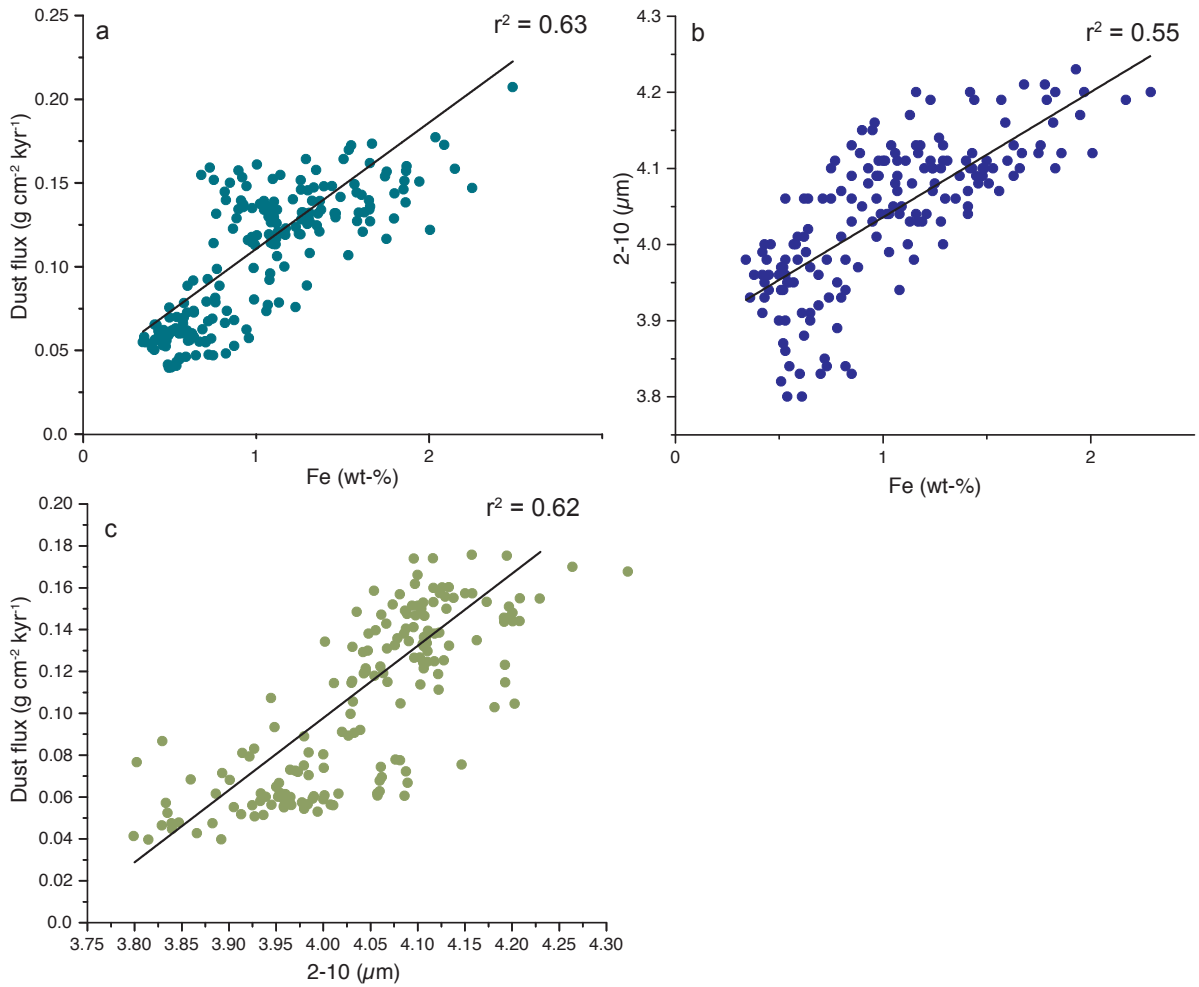


Figure 4.4: a: Linear regression of ²³⁰Th-normalized lithogenic fluxes (g cm⁻² kyr⁻¹) and Fe (wt. %). b: Linear regression between the fine silt fraction (2-10 μm) and Fe (wt. %). c: Linear regression between ²³⁰Th-normalized lithogenic fluxes (g cm⁻² kyr⁻¹) and fine silt fraction (2-10 μm). The distinct linear correlations between all proxies confirm that the fine silt fraction is the most suitable grain size range to reconstruct dust transport to the Pacific Sector of the SO.

4.3.2 Glacial-interglacial dust variability in the Pacific sector of Southern Ocean (Sediment core PS75/056-1)

The mean of the grain size range of the fine silt fraction, here defined as mean dust grain size, varies between 3.78 μm and 4.35 μm . Although the amplitude between the highest and lowest mean grain size is only 0.57 μm , we observe a distinct G/IG pattern with coarser mean dust grain sizes in glacial compared to interglacial periods (Fig. 4.5 d). Based on the geographical location of our sediment core, we cannot entirely exclude minor contributions of ice-rafted sediments. However, terrestrial biomarkers (long-chain n-alkanes) of a nearby sediment core (PS75/059-2) (Fig. 4.1) clearly reveal the presence of leaf-waxes typical for terrestrial plant material (Lamy et al., 2014), which is absent on the Antarctic continent (Aislabie et al., 2006). Therefore, contributions from ice-rafted sediments affecting the grain size distribution can be ruled out. Given the cohesive behavior of the fine silt fraction (McCave et al., 1995), we argue that sediment redistribution at the seafloor due to intensified bottom currents during glacial periods can also be ruled out. Reconstructions of Drake Passage Antarctic Circumpolar Current (ACC) through-flow show a substantial decrease during glacial periods (Lamy et al., 2015). Hence, lateral particle transport within the ACC was probably also reduced due to the lower transport volume.

Lamy et al. (2014) inferred that dust supply is the predominant transport mechanism of terrigenous material to our core site. The geographical position of our sediment core in the Subantarctic Zone east of the East Pacific rise and the direction of the SWW suggest that Australia and/or New Zealand are the major PSAs. Model-based investigations of the modern dust distribution in the Southern Hemisphere showed that approximately 86 % of dust in the Pacific sector of the SO originate from central and/or southeast Australian PSAs (Li et al., 2008). Simulations of the modern dust distribution also show that Australian sourced dust is transported in the free troposphere, which enables transport across long distances (Li et al., 2008). Additionally, a recent modern dust provenance study from the Pacific sector of the SO suggests, despite geochemical similarities between Australian, New Zealand and southern South American PSAs, that the Lake Eyre Basin in southeast Australia was the major dust supplier to the Pacific sector of the SO during the Holocene (Wengler et al., submitted).

The enhanced glacial Fe accumulation combined with increased mean dust grain sizes at our core site suggests both, more dust was available in PSAs and source area characteristics favored the erosion of larger dust particles. This might be a result of glacial climate conditions (e.g. reduced vegetation, reduced precipitation, arid conditions) leading to expanded arid areas that

avored enhanced dust erosion over central and southeast Australia (Hesse and McTainsh, 1999). Our lithogenic flux record shows the same G/IG pattern compared to the Fe accumulation and mean dust grain size (Fig. 4.5 c-e) corresponding with increased (decreased) LGM (Holocene) lithogenic fluxes in the Pacific sector of the SO (Fig. 4.6 a and b). The SWW are the main transport medium of dust to the SO and most paleo-data studies propose both, a northward shift and/or strengthening of the SWW during glacial periods (Kohfeld et al., 2013). However, most of these studies were conducted in southern South America and therefore might not be representative for SWW variations over Australia and New Zealand. Tasman Sea marine sediment deposits reveal distinctly higher dust fluxes during glacial periods coupled with no substantial change in grain size (Hesse, 1994; Hesse and McTainsh, 1999). This pattern documents a northward shift of the SWW accompanied by an expansion of the Australian dust transport corridor, rather than a general increase in the zonal SWW wind strength over Australia (Hesse, 1994). We observe a G/IG amplitude in the mean dust grain size of $0.57 \mu\text{m}$, which could point to slightly increased winds over central and southeast Australia leading to the erosion of larger dust particles combined with increased dust transporting SWW to the Pacific sector of the SO during glacial periods. However, this would contradict the results presented in Lamy et al. (2015), where a substantial decrease of Drake Passage ACC through-flow during glacial periods is linked to a northward shift of the SWW resulting in reduced SWW over their core zone. Alternatively, the increased glacial mean dust grain sizes could also result from an activation of Australian PSAs that were inactive during interglacial periods combined with a change in mineralogy.

Because New Zealand is predominately under the influence of the prevailing SWW, the South Island needs to be considered as an additional PSA (Neff and Bertler, 2015), especially during glacial periods. At the east coast of the South Island, large loess areas were formed through the deflation of dust from river floodplains (Cowie, 1964; Raeside, 1964). The dust was predominately derived from the Southern Alps during Quaternary cold-climate processes (e.g. freeze/thaw and glacial grinding) (Eden and Hammond, 2003). Increased erosion and/or weathering fluxes during glacial periods were detected in marine sediments at the eastern side of the South Island and are interpreted as a result of the glacial ice coverage (Cogez et al., 2015). Based on these glacial processes larger dust particles could have been available and increased SWW could have transported them to the SO.

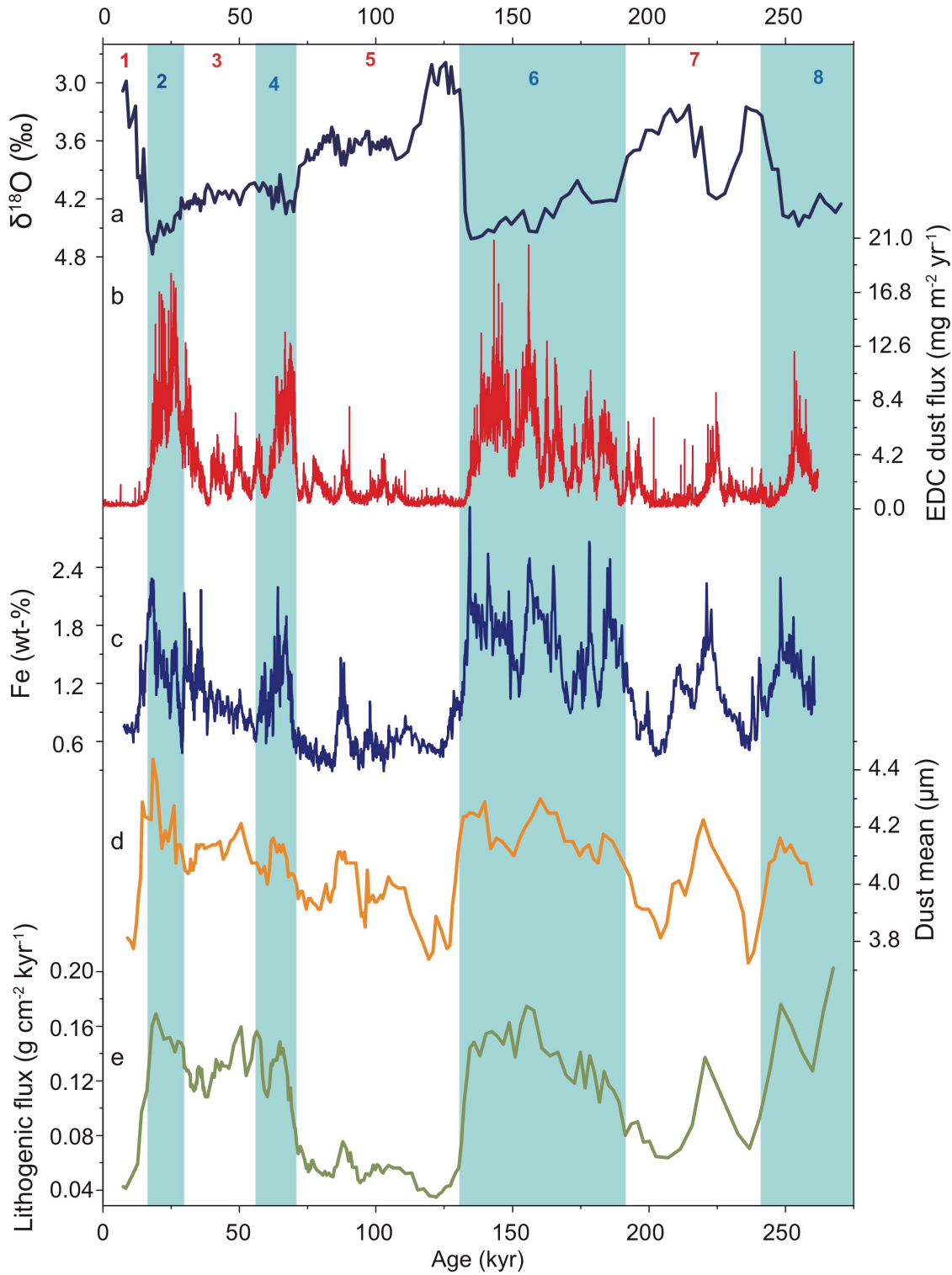


Figure 4.5: a: $\delta^{18}\text{O}$ (‰) of sediment core PS75/056-1. b: EDC dust flux ($\text{mg cm}^{-2} \text{yr}^{-1}$) (Lambert et al., 2012). c: Fe content (wt. %) of sediment core PS75/056-1 (Lamy et al., 2014). d: Mean dust grain size in μm (2-10 μm) of sediment core PS75/056-1. e: ^{230}Th -normalized lithogenic flux ($\text{g cm}^{-2} \text{kyr}^{-1}$) of sediment core PS75/056-1 (Shoenfelt et al., submitted). The light blue bars highlight glacial periods. The numbers refer to the marine isotope stages and the colors indicate glacial (blue) and interglacial (red) periods.

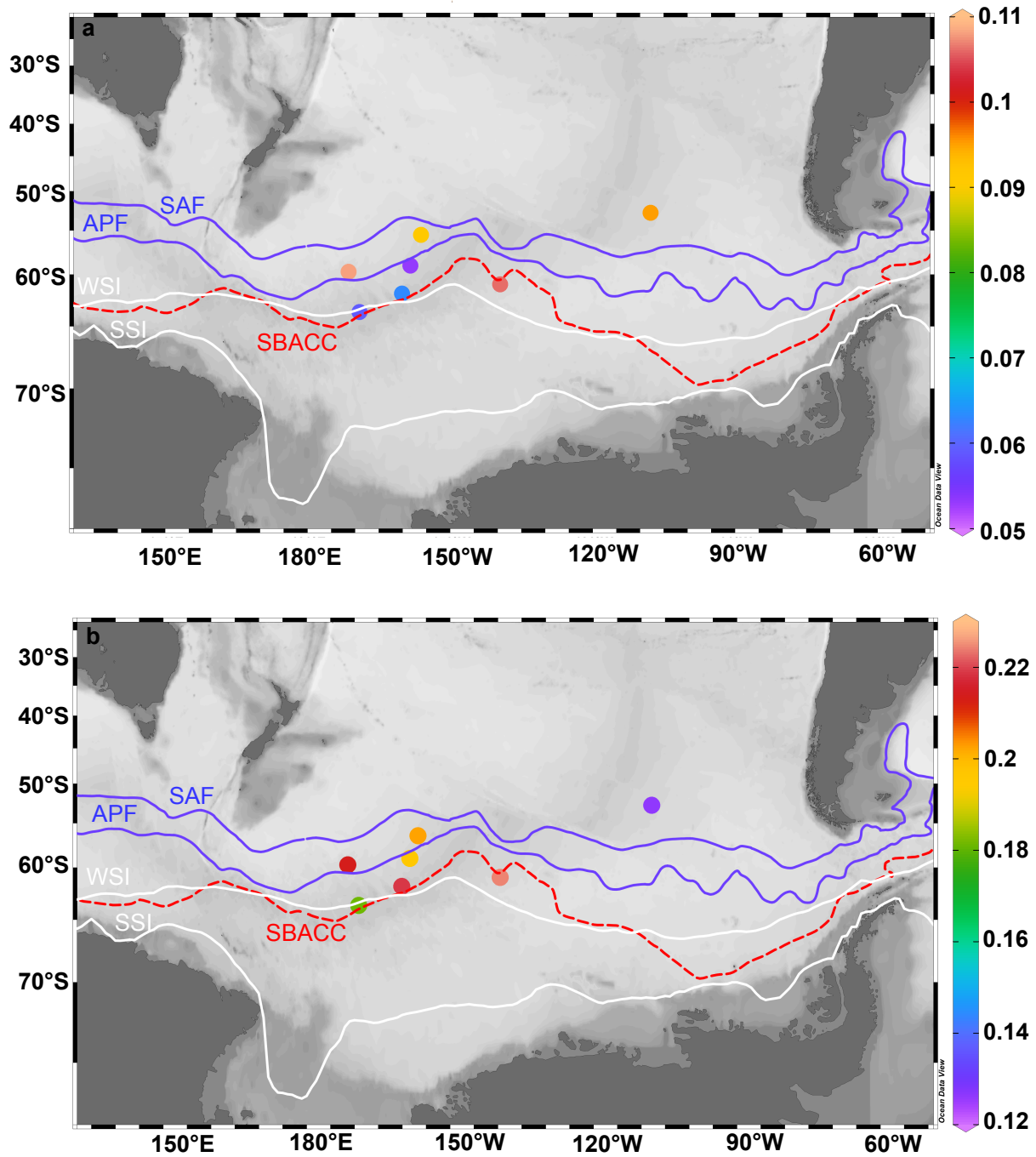


Figure 4.6: Holocene (upper panel) - LGM (lower panel) comparison of ^{230}Th -normalized lithogenic fluxes ($\text{g cm}^{-2} \text{ kyr}^{-1}$) in the Pacific sector of the SO. Note the increased LGM ^{230}Th -normalized lithogenic fluxes ($\text{g cm}^{-2} \text{ kyr}^{-1}$) compared to the Holocene. Five samples per time slice were measured and the average values are shown in the map. Colored lines refer to mean positions of major front systems (Orsi et al., 1995). SAF: Subantarctic Front, APF: Polar Front. SACCF: Southern Antarctic Circumpolar Current Front. Mean extension of winter and summer sea ice (WSI and SSI) is indicated by white lines (Comiso, 2003). The map was generated using the Ocean Data View software (Schlitzer, 2015).

4.3.3 Evaluation of the dust grain size in Atlantic sector of the Southern Ocean (ODP Site 1090)

We studied one complete glacial-interglacial cycle (the upper 160 kyr) at ODP Site 1090. The sediment record reveals a bimodal grain size distribution with a main peak at $\sim 3 \mu\text{m}$ (similar to sediment core PS75/056-1), whereas a second peak occurs at $\sim 11 \mu\text{m}$ (Fig. 4.7). The clay and fine silt fractions consist of 80 Vol. % (on average), whereas 19 Vol. % (on average) are concentrated in the medium and coarse silt fraction (Fig. 4.8). Although the clay fraction makes up 29 Vol. % (on average) (Fig. 4.8), it was excluded from our interpretation for the same reason as mentioned in section 4.3.1. The $> 63 \mu\text{m}$ fraction makes up less than 1 Vol. % (on average) of the entire grain size distribution and is therefore negligible.

Given the clear dominance of the fine silt fraction (51 Vol. % on average; Fig. 4.8) in our sediment record, we assume this fraction to be most representative for dust in the Atlantic sector of the SO. However, we find a poor correlation between the fine silt fraction and Fe accumulation ($r^2 = 0.05$) and the lithogenic flux ($r^2 = 0.01$) of ODP Site 1090 (Fig. 4.9 b and c). Does the lack of correlation indicate that the fine silt fraction cannot be used to reconstruct dust transport to Atlantic sector of the SO? Based on the distinct majority of the fine silt fraction (51 Vol. %), we argue that this fraction is most representative for dust and rather consider other factors (e.g. PSA characteristics, different G/IG PSAs and ice rafted sediments) to be responsible for G/IG grain size distribution.

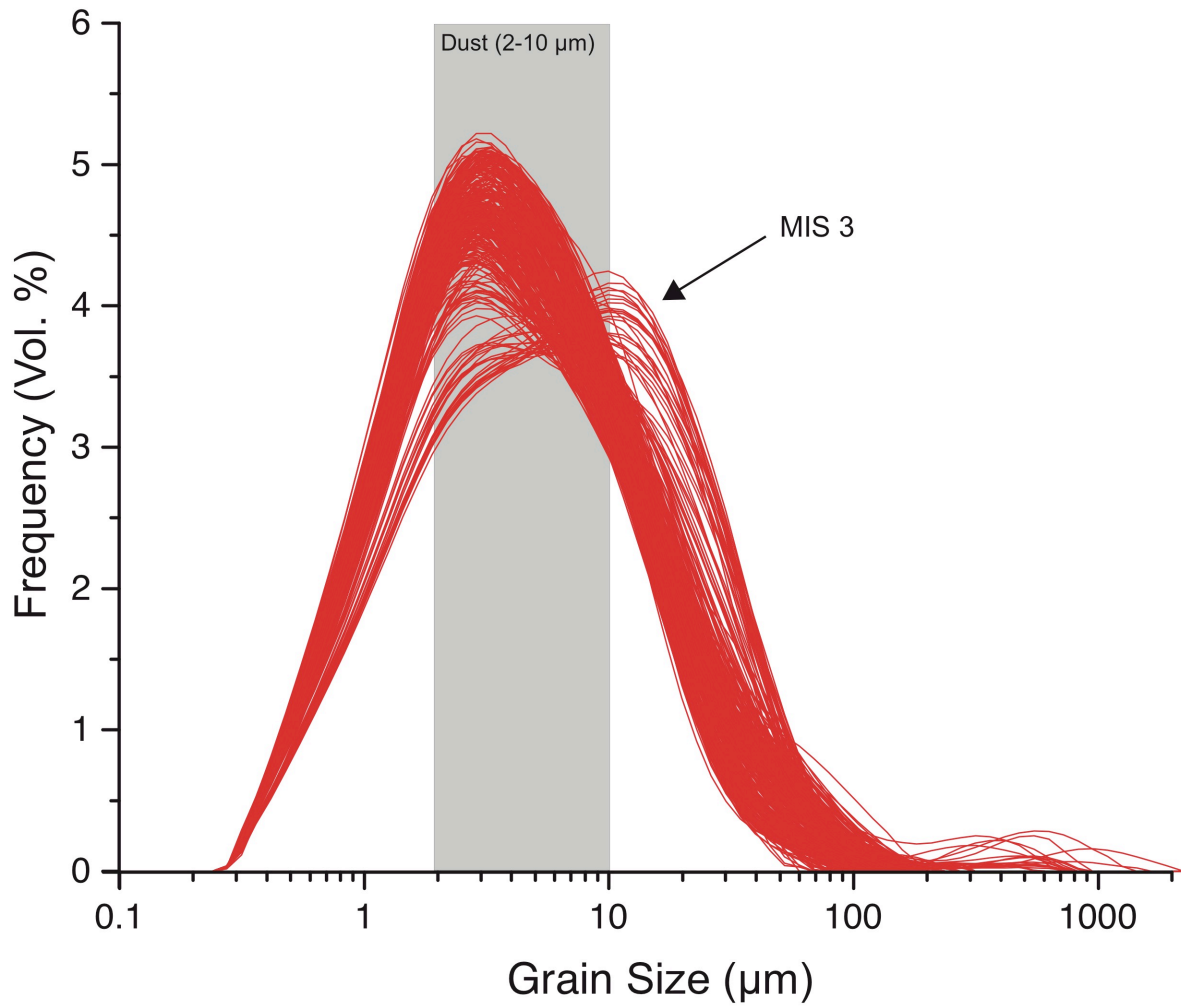


Figure 4.7: Average grain size distribution of ODP Site 1090. Grain sizes were measured on the bulk terrigenous fraction. Note the logarithmic scale on the x-axis. The y-axis shows the frequency given in volume percentage per size class. 84 size classes were measured. The grain size distribution shows a distinct maximum at $\sim 3 \mu\text{m}$ and a less pronounced peak at $\sim 11 \mu\text{m}$. The coarser grain size distributions refer to MIS 3 and likely indicate ice-rafted sediment input. 51 Vol. % are concentrated in the fine silt (2-10 μm) fraction (gray bar). The clay (0-2 μm) and medium to coarse silt fractions (10-63 μm) were excluded from our dust grain size analysis because they could be affected by dissolution during the opal leaching process (0-2 μm fraction) or could be affected by bottom current redistribution at the seafloor (10-63 μm fraction) (McCave et al., 1995).

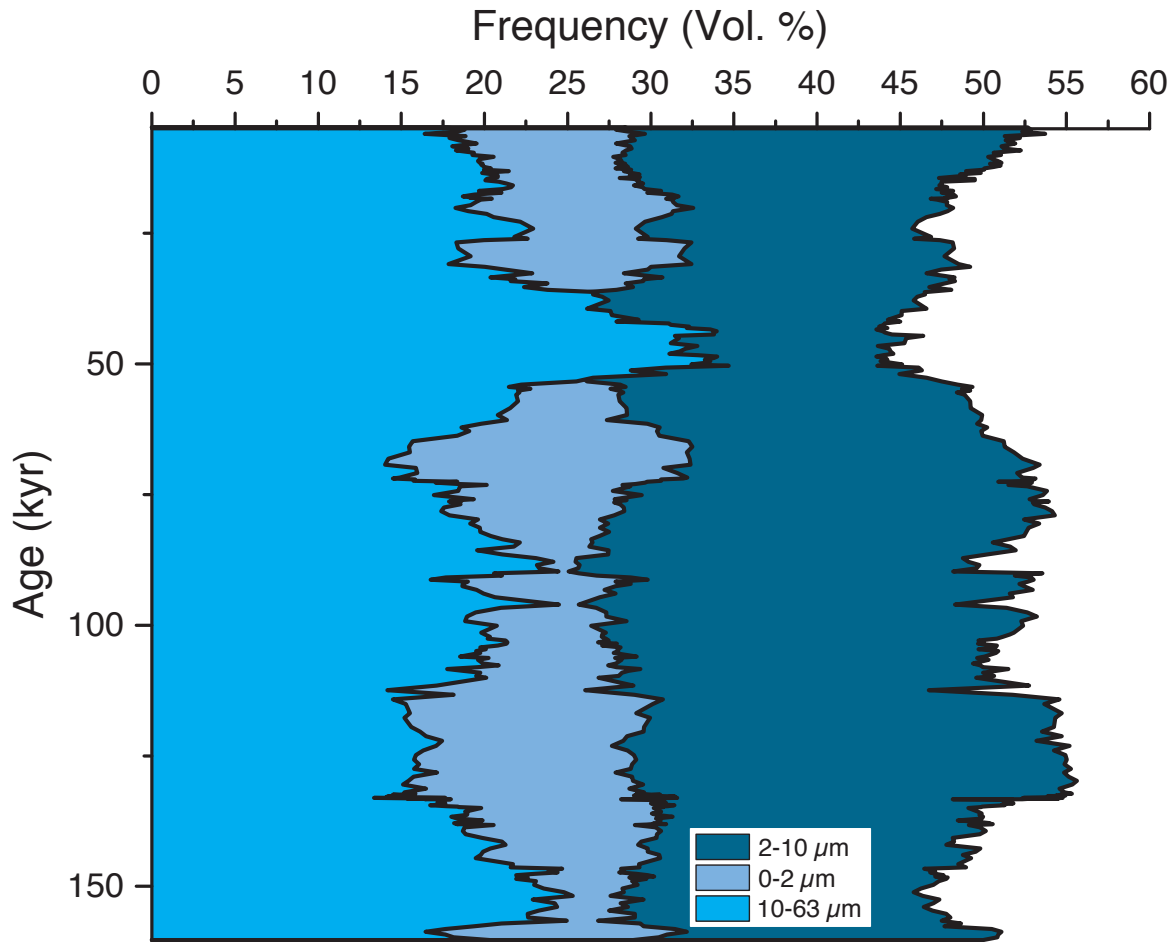


Figure 4.8: Grain size distribution of ODP Site 1090 versus age. Note that the sum of the components equals 100 Vol. %. 80 Vol. % (volume percentage per size class; 84 size classes were measured) of the total sediment material is concentrated in the 0-10 μm fraction. The medium to coarse silt fraction (10-63 μm) consists of 19 Vol. %. 29 Vol. % are concentrated in the clay (0-2 μm) and 51 Vol. % are concentrated in the fine silt (2-10 μm) fractions. The $> 63 \mu\text{m}$ fraction makes up less than 1 Vol. %. The given numbers are average values.

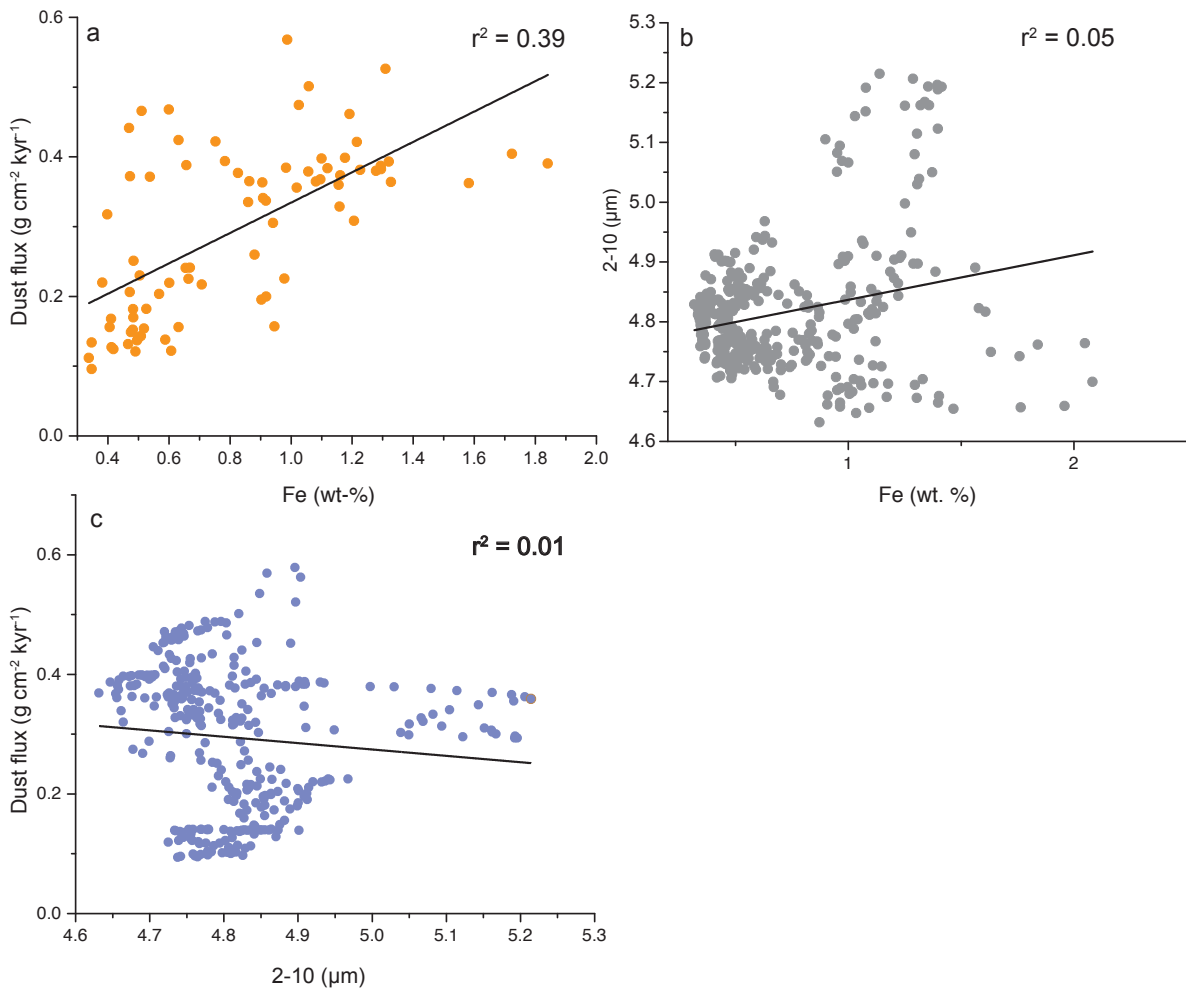


Figure 4.9: a: Linear regression between ^{230}Th -normalized lithogenic fluxes ($\text{g cm}^{-2} \text{ kyr}^{-1}$) and Fe (wt. %). b: Linear regression between the fine silt fraction (2-10 μm) and Fe (wt. %). c: Linear regression between ^{230}Th -normalized lithogenic fluxes ($\text{g cm}^{-2} \text{ kyr}^{-1}$) and the fine silt (2-10 μm). Given the distinct dominance of the fine silt fraction, it is probably the most suitable grain size range to reconstruct dust transport to the Atlantic Sector of the SO. The poor linear regressions shown in b and c do not eliminate the fine silt fraction as dust proxy but rather result from climate forcing over southern South American PSAs.

4.3.4 Glacial-interglacial dust variability in Atlantic sector of the Southern Ocean (ODP Site 1090)

The mean dust grain size distribution ranges from 4.68 μm to 5.21 μm . The amplitude between the highest and lowest mean grain size (0.53 μm) is similar to sediment core PS75/056-1 in the Pacific sector of the SO (0.51 μm) (Fig. 4.10 e). However, we observe a G/IG coarsening of approximately 0.9 μm in the Atlantic sector of the SO compared to the Pacific sector (mean dust grain size: 3.78 μm to 4.35 μm) (Figs. 4.5 d and 4.10 e). It is important to note that the G/IG mean dust grain size pattern at ODP Site 1090 is opposite to sediment core PS75/056-1 from the Pacific sector of the SO. In the South Atlantic, interglacial periods reveal coarser mean dust grain sizes compared to glacial periods (Fig. 4.10 e). Similar to our sediment record from the Pacific sector of the SO, increased Fe accumulation and lithogenic fluxes during glacial periods strongly indicate enhanced dust transport to ODP Site 1090. Based on these observations, we focus on the mechanism(s) being responsible for the opposed G/IG mean dust grain size patterns in the Pacific and Atlantic sectors of the SO. For the same reason as discussed in 4.3.1, we discard sediment redistribution at the seafloor. Additionally, given that the Subantarctic Front (SAF) defines the northern limit of the ACC (Orsi et al., 1995), we suggest that the location of ODP Site 1090 (north of the SAF) prevents sediment redistribution. Terrestrial biomarker analysis of long-chain n-alkanes lead to the conclusion that sediment input from ice-rafted sediments can be excluded (Martínez-García et al., 2009). Nevertheless, distinctly increased mean dust grain sizes during MIS 3 may indicate a secondary source of terrestrial material, which could be derived from ice-rafted sediment input (Figs. 4.7 and 4.10 e).

Martínez-García et al. (2009) suggest that dust supply is the most likely transport mechanism of terrigenous material to ODP Site 1090. The geographical position of ODP Site 1090 and the prevailing direction of the SWW indicate that southern South America is the most prominent PSA. This corresponds with model-based investigations of the modern and LGM dust distribution in the Southern Hemisphere revealing that ODP Site 1090 is covered by the southern South American dust plume (Li et al., 2008; Li et al., 2010; Albani et al., 2012b). In particular, 90 % of the total modern dust in the Atlantic sector of the SO originates in South America (Li et al., 2008).

Provenance studies strongly emphasize the role of dust from southern South American PSAs in east Antarctic ice cores (e.g. EDC) (Delmonte et al., 2010; Gili et al., 2017). Additionally, the strong similarity of the Fe accumulation at ODP Site 1090 and the EDC dust

flux supports the idea of southern South American dust supply to our core site (Fig. 4.10 b and d). Simultaneously, the lithogenic flux of ODP Site 1090 shows a similar G/IG pattern compared to the Fe accumulation, which is characteristic for increased dust accumulation during glacial periods (Fig. 4.10 d and f). Comparing the lithogenic fluxes in the Atlantic and Pacific sectors of the SO, we observe a ~3-fold increase during glacial periods and a ~2-fold increase during interglacial periods in the Atlantic sector (Figs. 4.5 e and 4.10 f). Based on this result, we infer a strong source area - atmosphere interaction with regard to dust erosion and availability in southern South American PSAs. Additionally, we infer that southern South American PSAs produced higher total amounts of dust during glacial periods compared to Australia/New Zealand.

Southern South American PSA extend along a ~4000 km latitudinal band from the Puna-Altiplano Plateau in the north to Patagonia in the south (Gili et al., 2017), which could explain the distinct G/IG mean dust grain size pattern observed at ODP Site 1090 (Fig. 4.10 e). Geochemical comparisons of southern South American PSAs to east Antarctic ice core dust records reveal that Patagonia predominantly supplied dust to east Antarctica during glacial periods (Gili et al., 2017). This agrees with dust modeling studies showing that Patagonia dominated dust deposition over Antarctica during the Last Glacial Maximum (LGM) (Albani et al., 2012b). It was shown that dust peaks in Antarctica correspond with increased meltwater discharge from Patagonian glaciers onto outwash plains, where dust can easily be mobilized (Sugden et al., 2009). This could explain the enhanced glacial Fe accumulation coupled with increased lithogenic fluxes at ODP Site 1090. Additionally, east Antarctic ice core dust (EDC) shows the same G/IG dust variability compared to our sediment core with increased dust fluxes but decreased grain sizes in glacial periods (Fig. 4.10 b, c, e) (Delmonte et al., 2004b; Lambert et al., 2008). It was suggested that a progressive coupling of the climates of Antarctica and lower latitudes resulted in enhanced southern South American dust erosion (Lambert et al., 2008). Simultaneously, a diminished hydrological cycle during glacial periods over the Atlantic sector of the SO reduced wet deposition processes and increased the particle lifetime during atmospheric transport leading to a ~25-fold increase in Antarctic glacial dust fluxes (EDC) (Fig. 4.10 b) (Lambert et al., 2012). Although more southern South American dust was available during glacial periods, erosion of larger dust particles was hampered. We suggest that fluctuations of the SWW over southern South America are the main mechanism being responsible for the G/IG mean dust grain size pattern. During glacial periods, the SWW probably shifted northward, which likely resulted in a diminished core over Patagonia (Lamy

et al., 2010). Accordingly, we infer that the local SWW were not strong enough to erode coarse dust particles in southern South America resulting in the distinct G/IG dust size pattern.

During interglacial periods the southern Altiplano area in the northern part of southern South America was the main source of dust to east Antarctic ice cores (Gili et al., 2017). In addition, paleo-data from the central Andes reveal drier conditions in the Altiplano area during the Holocene and older interglacials (Fornace et al., 2014; Baker and Fritz, 2015). This could be explained by contracted SWW resulting in increased precipitation over the southern PSA in southern South America. Although the interglacial SWW were likely reduced over the northern PSAs, we suggest that drier conditions could have enhanced the erosion of coarser dust particles during interglacial periods.

Because our core site is closely located to South Africa, sediment input from this region needs to be considered. Noble et al. (2012) inferred from a suite of sediment records from ODP Leg 177 (including ODP Site 1090) that Holocene lithogenic fluxes can be explained by a predominant sediment supply from South Africa via the Agulhas current. This may have been likewise important for older interglacials and could alternatively explain our increased mean dust grain sizes during interglacial periods. In contrast, increased LGM lithogenic fluxes at the same locations point to sediment transport driven by the ACC. This was inferred from LGM lithogenic fluxes that are an order of magnitude higher than glacial lithogenic fluxes in the equatorial Pacific, where lithogenic input is mainly based on dust (Winckler et al., 2008; Noble et al., 2012). However, our data show that glacial lithogenic fluxes are generally lower in the Pacific sector of the SO compared to the Atlantic sector (Figs. 4.5 e and 4.10 f). Subsequently, increased glacial lithogenic fluxes cannot simply be interpreted as current driven. Additionally, down core Th isotope data reveal relatively low sediment focusing rates for ODP Site 1090 (Martínez-García et al., 2009), also arguing against ACC and lateral transport in the water column.

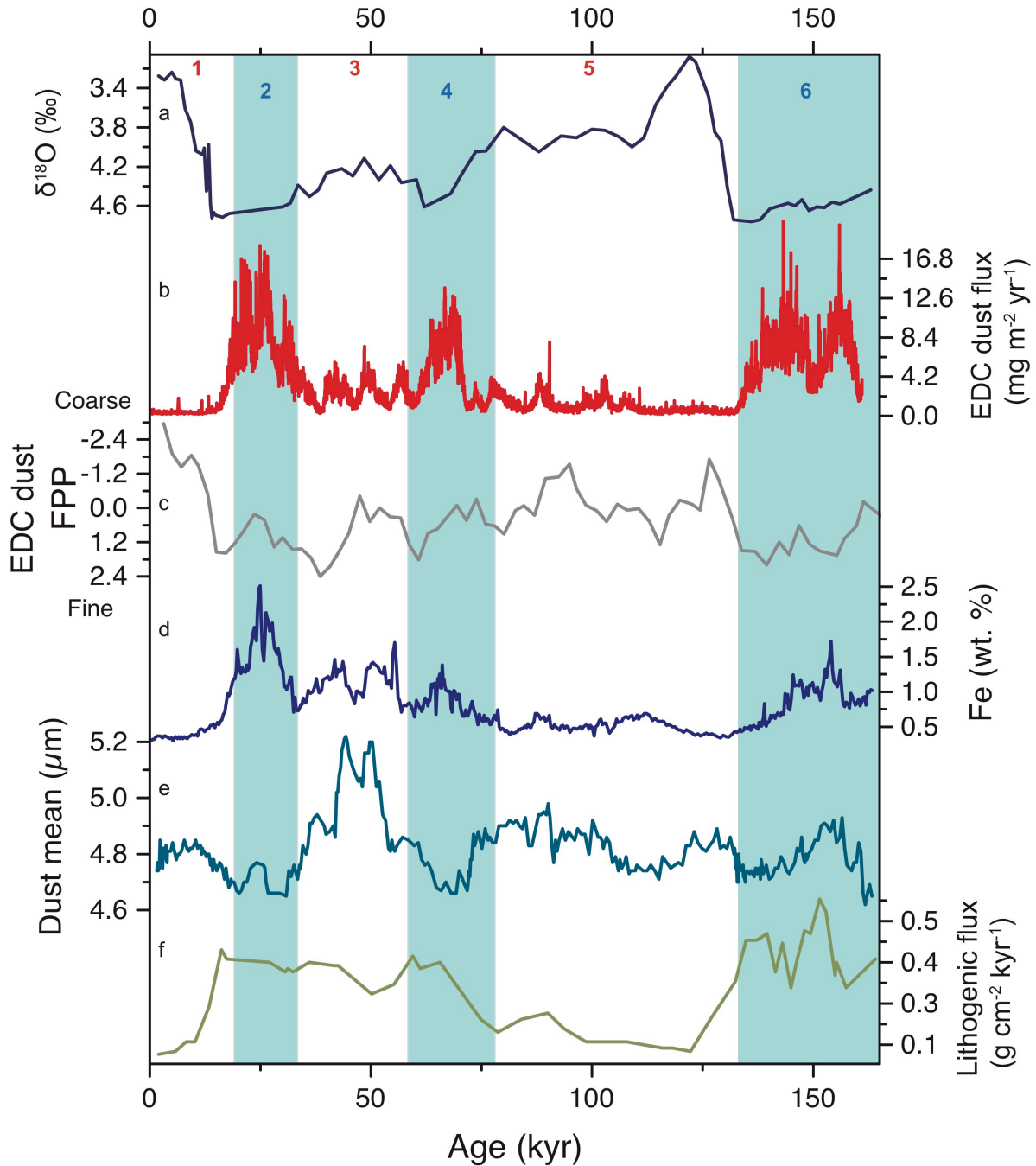


Figure 4.10: a: $\delta^{18}\text{O}$ (‰) of composite record PS2489-2/ODP Site 1090 (Becquey and Gersonde, 2003; Martínez-García et al., 2009). b: EDC dust flux ($\text{mg m}^{-2} \text{yr}^{-1}$) (Lambert et al., 2012). c: EDC dust fine particle percentage (Delmonte et al., 2004b; Lambert et al., 2008) d: Fe content (wt. %) of ODP Site 1090 (Martínez-García et al., 2009; Martínez-García et al., 2011). e: Mean dust grain size in μm (2-10 μm) of ODP Site 1090. f: ^{230}Th -normalized lithogenic flux ($\text{g cm}^{-2} \text{kyr}^{-1}$) of ODP Site 1090 (Martínez-García et al., 2009; Martínez-García et al., 2011). The light blue bars highlight glacial periods. The numbers refer to the marine isotope stages and the colors indicate glacial (blue) and interglacial (red) periods.

4.4 Conclusion

We show that the fine silt fraction dominates the grain size distribution in the Pacific and Atlantic sectors of the SO and therefore, we consider this fraction as most representative for atmospheric dust. Our data clearly reveal opposing down core grain size records in Pacific and Atlantic sectors of the SO. The grain size record in the Pacific sector is characterized by increased mean dust grain sizes during glacial and decreased mean dust grain sizes during interglacial periods corresponding with increased glacial Fe accumulation and lithogenic flux records in this sector. Subsequently, we argue that our G/IG grain size distribution is predominantly affected by changing PSA characteristics during glacial periods leading to expanded arid areas allowing for increased dust entrainment in Australia and/or New Zealand. Additionally, PSAs that were inactive during interglacial periods coupled with mineralogy changes could also be responsible for the distinct G/IG dust distribution.

The mean dust grain size data from the Atlantic sector of the SO show the opposite pattern with decreased grain sizes during glacial periods, whereas increased glacial Fe and lithogenic flux records indicate enhanced dust availability in southern South American sources. Glacial dust was predominantly derived from Patagonia but expanded glacial SWW coupled with a diminished core over Patagonia likely hampered the erosion of coarse dust particles. In contrast, interglacial dust mainly originated in the Puna Altiplano region, where the entrainment of coarser dust particles likely resulted from drier interglacial conditions. Australian and New Zealand PSAs are located further north compared to Patagonia, the predominant glacial PSA to Atlantic sector of the SO. As a result, a glacial northward shift of the SWW would likely more readily affect Australian/New Zealand sources rather than Patagonian PSAs.

Our grain size-based study reveals the complexity of paleoclimate reconstructions and shows that the SWW did probably not behave symmetrically in the Southern Hemisphere. It also addresses the need for more west to east and north to south down core transects in the Pacific and Atlantic sectors of the SO to accurately determine G/IG SWW variations. Moreover, we strongly emphasize the need for down core provenance studies to identify the origin of dust particles over G/IG timescales.

Acknowledgements

We thank chief scientists, crews and participants of R/V *Polarstern* (PS75) and *JOIDES Resolution* (ODP Leg 177) for their support. Additionally, we thank A. Martínez-García for providing grain size data of ODP Site 1090. We are grateful to R. Fröhlich-Teichert and S. Wiebe for providing technical assistance. This study is part of the project “Polar Regions and Coasts in the changing Earth System (PACES II)” of the Alfred Wegener Institute (AWI) Helmholtz Centre for Polar and Marine Research. We acknowledge financial support for this work through the AWI and the MARUM-Center for Marine Environmental Sciences.

APPENDIX A. Supplementary data

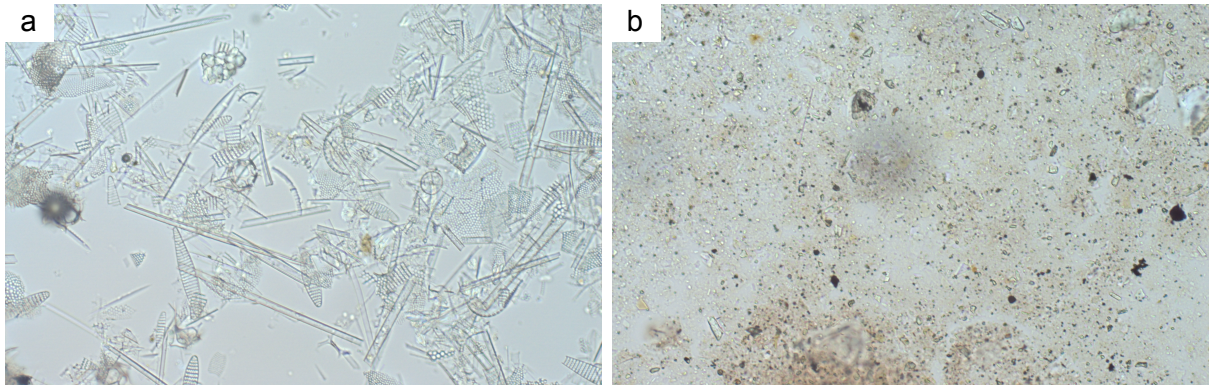


Figure A 4.1: A typical sample of sediment core PS75/056-1 before and after the leaching procedure described in chapter 4. a: Untreated sample with a biogenic opal content of ~60 %. b: The same sample after opal leaching. Biogenic opal is completely removed. The method was developed for sediment samples with extremely high biogenic opal contents. The images were taken with a Zeiss Axioplan 2 microscope using the x1000 magnification.

5 A biomarker perspective on dust, productivity, and sea surface temperature in the Pacific sector of the Southern Ocean

Andrea Jaeschke^{a,b*}, **Marc Wengler**^{a,b}, Jens Hefter^a, Thomas A. Ronge^a, Walter Geibert^a, Gesine Mollenhauer^{a,b}, Rainer Gersonde^{a,b}, Frank Lamy^{a,b}

^aAlfred Wegener Institute, Helmholtz Center for Polar and Marine Research, D-27515 Bremerhaven, Germany

^bMARUM Center for Marine Environmental Sciences, University of Bremen, D-28334 Bremen, Germany

*present address: Institute of Geology and Mineralogy, University of Cologne, Zùlpicher Str. 49a, 50674 Cologne, Germany

corresponding author: Andrea Jaeschke (andrea.jaeschke@uni-koeln.de)

Keywords: Biomarkers, Southern Ocean, dust, ²³⁰Th, GDGT, U₃₇^K, TEX₈₆

Published in *Geochimica et Cosmochimica Acta*

Abstract

In this study, we present a new multiproxy data set of terrigenous input, marine productivity and sea surface temperature (SST) from 52 surface sediment samples collected along E-W transects in the Pacific sector of the Southern Ocean. Allochthonous terrigenous input was characterized by the distribution of plant wax *n*-alkanes and soil-derived branched glycerol dialkyl glycerol tetraethers (brGDGTs). ^{230}Th -normalized burial of both compound groups were highest close to the potential sources in Australia and New Zealand and are strongly related to lithogenic contents (^{232}Th), indicating common sources and transport. Detection of both long-chain *n*-alkanes and brGDGTs at the most remote sites in the open ocean strongly suggests a primarily eolian transport mechanism to at least 110°W , i.e. by prevailing westerly winds. Two independent organic SST proxies were used, the U_{37}^K based on alkenones, and the TEX_{86} based on isoprenoid GDGTs. Both, U_{37}^K and TEX_{86} indices show robust relationships with temperature over a temperature range between 0.5 and 20°C , likely implying different seasonal and regional imprints on the temperature signal. Alkenone-based temperature estimates best reflect modern summer SST in the study area when using the polar calibration of Sikes et al. (1997). In contrast, TEX_{86} -derived temperatures may reflect a subsurface signal rather than surface. ^{230}Th -normalized burial of alkenones is highest close to the Subtropical Front and is positively related to the deposition of lithogenic material throughout the study area. In contrast, highest isoGDGT burial south of the Antarctic Polar Front may be largely controlled by diatom blooms, and thus high opal fluxes during austral summer.

5.1 Introduction

The Southern Ocean (SO) plays a crucial role in the climate system by influencing the meridional overturning circulation and the global carbon cycle (Fischer et al., 2010; Marshall and Speer, 2012). Wind-borne mineral aerosol (dust) is an important feedback in the climate system affecting radiation budgets, atmospheric chemistry, and providing nutrients to terrestrial and marine ecosystems (Jickells et al., 2005). According to the iron hypothesis (Martin, 1990), an increase in the supply of iron by dust may stimulate marine productivity in so-called high-nutrient low-chlorophyll (HNLC) regions, leading to the reduction of atmospheric CO_2 concentrations. In the Southern Hemisphere, the largest amount of dust is transported by the predominant mid-latitude westerly winds, which are an important driver of the large scale ocean circulation and play a major role in determining climate dynamics and precipitation regimes on adjacent land masses between 30°S and 60°S over seasonal to

millennial timescales (Lamy et al., 2010; Fletcher and Moreno, 2012; Lamy et al., 2014). A tight connection between eolian dust, climate state and ocean biogeochemistry was suggested, indicating that the world was much dustier during glacial climate stages, and consistent with overall cooler and drier conditions (Kohfeld and Harrison, 2001; Maher et al., 2010; Martínez-García et al., 2014; Lamy et al., 2014). The large variations in dust loading in the past may reflect changes in the source areas, wind speed, pattern, and gustiness as well as deposition along the dust transport pathway (Winckler et al., 2008; Martínez-García et al., 2009; Kohfeld et al., 2013). Several modeling attempts have been made to characterize the generation and transport of dust and its impacts on climate. However, estimates of modern dust sources, mobilization rates and deposition are still poorly constrained, resulting primarily from the scarcity of spatial data coverage for the Pacific sector of the SO. Therefore, major discrepancies exist about the contribution and relative importance of major dust sources in the Southern Hemisphere, i.e., South America and Australia/New Zealand (Prospero et al., 2002; Li et al., 2008; Maher et al., 2010; Albani et al., 2014; Neff and Bertler, 2015).

Lipid biomarkers are widely used to characterize the sources and distribution of organic matter (OM) in terrestrial and marine environments and are therefore a powerful tool for paleoclimate reconstructions (Eglinton and Eglinton, 2008). Land plant biomarkers in marine sedimentary archives provide useful information about past vegetation and its climate history on adjacent continents. This includes long-chain *n*-alkanes, which represent major lipid components of the protective waxes that coat the surface of higher land plants. They typically occur in the C₂₅-C₃₅ range with a strong odd over even carbon number predominance (Eglinton and Hamilton, 1967). Such plant-wax lipids are persistent in soil and can reach marine sediments by erosion, wind and river transport of particulates, and smoke aerosols (Eglinton and Eglinton, 2008). The transport of wind-borne terrestrial OM has been documented for dust in sediments from remote oceanic locations, and most studies focused on lipid components from higher plant leaf waxes, i.e. *n*-alkanes, *n*-alkanols, *n*-fatty acids (Simoneit, 1977; Kawamura, 1995; Bendle et al., 2007). There is, however, a wealth of biological aerosol particles in the atmosphere including pollen, spores, and microorganisms (Simoneit, 1977; Griffin et al., 2006; Després et al., 2012). A large proportion of the aerosol organic fraction thus likely remains overlooked. Branched glycerol dialkyl glycerol tetraethers (brGDGT) were recently detected in aerosol samples off NW-Africa (Fietz et al., 2013). These lipids are commonly used as a proxy for terrestrial (soil) OM input to the ocean, namely the branched and isoprenoid tetraether (BIT) index (Hopmans et al., 2004). BrGDGTs were first identified in peat bogs and are thought to derive from anaerobic soil bacteria (Weijers et al., 2006), likely

from members of the *Acidobacteria* (Sinninghe Damasté et al., 2011). They are frequently detected in lacustrine and coastal marine sediments, but also at remote ocean sites, where no direct impact from land erosion via rivers takes place (Fietz et al., 2011; Schouten et al., 2013a; Jaeschke et al., 2014). Long-chain *n*-alkanes have been applied as a dust proxy in individual sediment cores from the subpolar Atlantic and Pacific Oceans, where they co-varied with iron and CO₂ concentrations over multiple glacial-interglacial cycles (Martínez-García et al., 2009; Martínez-García et al., 2011; Lamy et al., 2014). Application of brGDGTs as important additional dust tracers for paleoclimate reconstructions remains as yet unexplored.

At present, subtropical to polar SST gradients vary seasonally and zonally in conjunction with changes in surface circulation, the position and intensity of the westerly wind belt and regional climate (e.g. Lamy et al., 2010; Kohfeld et al., 2013). Accurate determination of present and past sea surface temperature (SST) variations is therefore essential for assessing the Southern Ocean's influence on global climate. The most commonly used organic proxy for SST estimation is the U₃₇^{K'} index (Prah and Wakeham, 1987), which is based on the relative abundance of di- and tri-unsaturated alkenones produced by haptophyte algae (e.g. Brassell et al., 1986). The U₃₇^{K'} index has been proposed to quantify the degree of alkenone unsaturation, which is a function of growth temperature of the precursor organism. The initial *Emiliania huxleyi* culture-based calibration was later confirmed by those based on global core-top compilations (Müller et al., 1998; Conte et al., 2006). A more recently developed SST proxy is based on the relative abundance of isoprenoid GDGTs, produced by Marine Group I Thaumarchaeota (Sinninghe Damasté et al., 2011), namely the TEX₈₆ index (Schouten et al., 2002). The initial linear TEX₈₆ calibration has been extended including core-top sediments from (sub)polar oceans, and new indices and calibration models were defined for surface and subsurface temperatures (Kim et al., 2012a; Kim et al., 2012b; Tierney and Tingley, 2014; Ho and Laepple, 2016). The fact that Thaumarchaeota and thus GDGTs occur ubiquitously in the global ocean, including the polar regions where alkenones (and in general carbonate-rich sediments) are basically absent, suggests a major advantage of the TEX₈₆ paleothermometer in these regions. However, both alkenone- and GDGT-based temperature proxies suffer from uncertainties, e.g. the nonlinearity of U₃₇^{K'}/TEX₈₆ and SST at low temperatures, where changes in both index values are relatively minor. This effect may be related to low growth rates at such temperatures, which makes reliable SST reconstructions challenging for (sub)polar regions (Sikes et al., 1997; Kim et al., 2010; Ho et al., 2014). Recent studies also suggest that in addition to temperature, non-thermal secondary effects such as nutrient availability, archaeal ecotype

and growth phase may have a strong control on individual TEX₈₆ records (Elling et al., 2014; Qin et al., 2015; Hurley et al., 2016).

In this study, we present new comprehensive data sets of terrigenous input, marine productivity, and SST from surface sediments collected in the mid- and high-latitude Pacific SO based on lipid biomarker analyses. We use ²³⁰Th normalization to correct for post-depositional sediment redistribution (Francois et al., 2004), which can significantly alter vertical flux estimates in the SO (Geibert et al., 2005; Lamy et al., 2014). Our main objectives are a) to give quantitative estimates of terrigenous material deposited in the Pacific SO based on concentrations and ²³⁰Th-normalized burial of ²³²Th, long-chain *n*-alkanes and brGDGTs, thereby also evaluating the applicability of brGDGTs as a suitable dust marker, b) to assess the potential link between terrigenous input and marine export production based on alkenones and isoGDGTs, and c) revisit U₃₇^K and TEX₈₆ paleothermometries, defining advantages and caveats of their application. The results will improve our understanding of biomarker-based proxies in (sub)polar sediment archives of the Pacific SO that are still largely missing.

5.2 Oceanographic Setting

The SO is the most important connection between the Atlantic, Indian and Pacific Oceans. There are three major fronts that can be distinguished in the SO: the Subtropical Front (STF), Subantarctic Front (SAF), Antarctic Polar Front (APF), and the areas in between the fronts are referred to as Subantarctic Zone (SAZ), Polar Front Zone (PFZ), and Antarctic Zone (AZ) (Orsi et al., 1995) (Fig. 5.1). . The STF separates cool, fresh and nutrient-rich subantarctic water (SAW) in the south from warm, saline and nutrient-depleted subtropical water masses in the north (Orsi et al., 1995; Chiswell et al., 2015). The modern position of the STF around New Zealand is between 47°S and 50°S, forced around south of South Island (NZ) and topographically constrained along the Chatham Rise to the east but with eddy- and meander-like features (Chiswell et al., 2015). East of New Zealand, the temperature difference south to north of the STF is generally 10-14°C in winter and 14-18°C in summer (Chiswell, 1994; Belkin and Gordon, 1996). Further eastward at 80°W, the STF is less well defined and occurs further north between 25°S and 32°S (Tiedemann, 2012). The East Cape Current (ECC) east of North Island (NZ) transports subtropical water to the Chatham Rise where it is directed east by the Rise's northern flank. The ocean south of the STF is dominated by the eastward flowing Antarctic Circumpolar Current (ACC), driven by strong Southern Hemisphere westerly winds between 45°S and 55°S (Orsi et al., 1995). In the SE-Pacific, bifurcation of the northern branch

of the ACC directs cold subantarctic water masses equatorward along the coast of South America by the vigorous Peru-Chile Current (PCC), while a weaker branch continues poleward (Cape Horn Current, CHC). In the SW-Pacific, the position of the northern boundary of the ACC represented by the SAF is substantially affected by the topography of the Macquarie Ridge and Campbell Plateau south of New Zealand (Heath, 1981; Chiswell et al., 2015), as indicated by the green stippled line in Fig. 5.1. The Southland Current (SC) is a northward flow of water along the SE-coast of New Zealand transporting water of both subtropical and subantarctic origin where it turns east at the southern flank of Chatham Rise (Sutton, 2003; Smith et al., 2013). South of the APF, in the Antarctic Zone summer SST is generally below 4°C (Locarnini et al., 2010) and sea ice forms and melts seasonally.

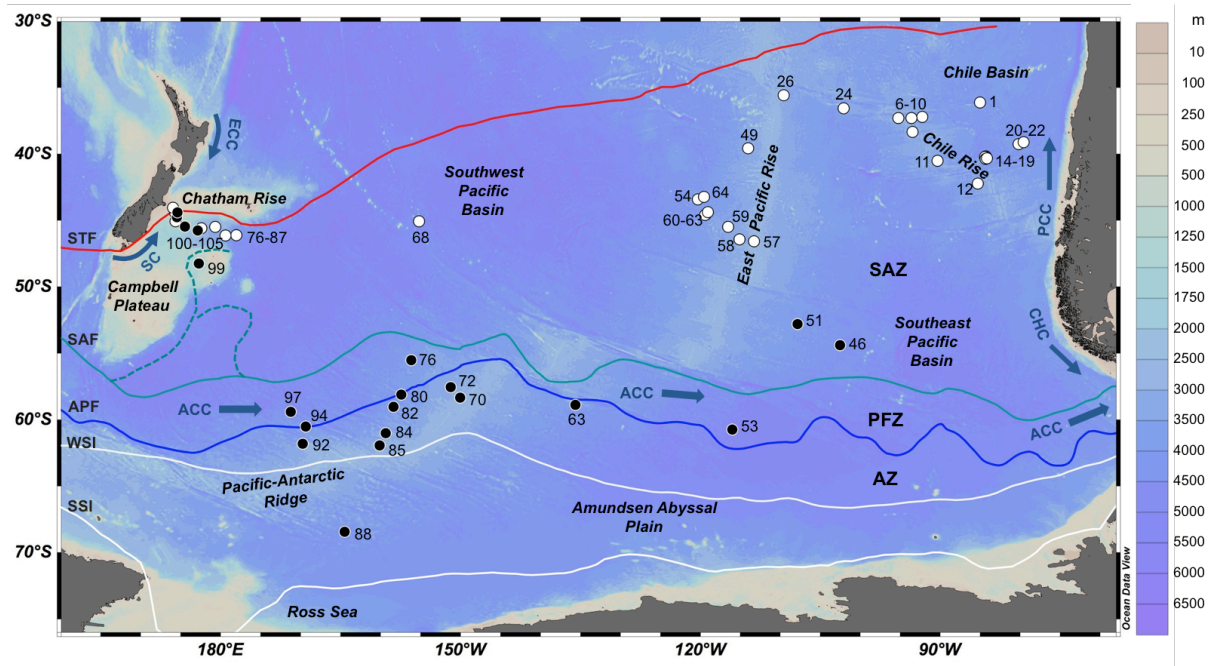


Figure 5.1: Map of the Pacific sector of the Southern Ocean with coarse bathymetry and locations of the sediment cores collected during R/V *Polarstern* cruise ANTXXVI-2 in 2009/10 (black dots Gersonde, 2011) and R/V *Sonne* cruise SO213 in 2010/11 (white dots Tiedemann, 2012). Colored lines indicate mean position of major front systems (Orsi et al., 1995): STF – Subtropical Front, SAF – Subantarctic Front, PF – Polar Front. The areas between the fronts are referred to as SAZ – Subantarctic Zone, PFZ – Polar Front Zone, and AZ – Antarctic Zone. The green stippled line indicates the position of the SAF branches, which are topographically steered by the Macquarie Ridge and Campbell Plateau (Chiswell et al., 2015). Mean extension of winter and summer sea ice (WSI/SSI) is indicated by white lines (Comiso, 2003). Major ocean currents are indicated by blue arrows: ACC – Antarctic Circumpolar Current, CHC – Cape Horn Current, ECC – East Cape Current, PCC – Peru-Chile Current, SC – Southland Current. The map was generated using the Ocean Data View software (Schlitzer, 2015).

5.3 Materials and Methods

5.3.1 Core locations and sampling

We analyzed 52 surface sediment samples collected during R/V *Polarstern* ANT-XXVI-2 and R/V *Sonne* SO213 cruises in austral summer 2009/10 and 2010/11, respectively (Gersonde, 2011; Tiedemann, 2012) along E-W transects in the Pacific sector of the SO using a multicorer (Fig. 5.1; Table 5.1). The longitudinal transects extending from central Chile to New Zealand encompass a large range of latitudes (36°S and 68°S) where modern annual mean temperatures of surface waters are between -1°C and 17°C (Locarnini, 2010). Surface sediments (0-1 cm) were sampled on board and kept frozen until further processing.

5.3.2 Elemental analysis

Total carbon (TC) and total nitrogen (TN) were analyzed using a vario EL III (CNS) elemental analyzer. Total organic carbon (TOC) was analyzed after decarbonation using an Eltra CS2000. Analytical precision was better than 0.02 for N and 0.1 for C. The C/N ratio was defined as the molar ratio between TOC and TN.

5.3.3 Lipid extraction and fractionation

Freeze-dried and homogenized surface sediment (4-7 g) was extracted by accelerated solvent extraction (ASE 350, Dionex) with a mixture of dichloromethane and methanol (DCM:MeOH, 9:1, v/v). The bulk of the solvent was subsequently removed by rotary evaporation under vacuum. The resulting total lipid extract (TLE) was further separated by column chromatography using silica gel as stationary phase. Hydrocarbons were eluted with hexane (5 ml), followed by an additional cleaning step using hexane:DCM (1:1; 5 ml) to remove wax esters. Alkenones were separated using DCM (5 ml), and GDGTs were eluted using DCM:MeOH (1:1; 5 ml). An aliquot of the alkenone fraction was further saponified to remove compounds co-eluting with the C_{37:4} alkenone. The dried polar fractions containing GDGTs were re-dissolved in hexane:isopropanol (99:1, v/v) and filtered through a 4 mm diameter PTFE syringe filter (0.45 µm). Internal standards (squalane, C₃₆ *n*-alkane, C₄₆-GDGT) added prior to extraction were used for quantification (Huguet et al., 2006b; Méheust et al., 2013).

5.3.4 Instrumental analysis

5.3.4.1 Gas chromatography (GC)

Alkenones and *n*-alkanes were analyzed by GC (HP-6891) fitted with a flame ionization detector (GC-FID) using Helium as carrier gas (1.5 ml min⁻¹ constant flow), and samples were injected in splitless mode. Chromatographic separation of compounds was achieved using a DB-5 capillary column (30 m length, 0.25 mm diameter, 0.25 μm film thickness). The oven temperature was programmed to be held at 60°C for 2 min, then increased at 15°C min⁻¹ to 150°C, at 3°C min⁻¹ until 320°C, and held for 20 min. *n*-alkanes were identified by comparison with an external *n*-alkane (*n*-C₈ to *n*-C₄₀) standard mixture. Identification of alkenones was achieved by comparing chromatographic retention times of the samples with those of a laboratory *E. huxleyi* culture extract that was routinely used as a working standard to control data quality. Analytical precision based on replicate analyses of the culture extract was better than 0.004 U₃₇^K units or 0.1°C. Reproducibility of alkenone concentration was 1-12 %, independent of total concentration.

5.3.4.2 High performance liquid chromatography (HPLC-MS)

GDGTs were analyzed by high performance liquid chromatography (HPLC) coupled via an atmospheric pressure chemical ionization (APCI) interface to a single quadrupole mass spectrometer (MS) according to Hopmans et al. (2000), with slight modifications. Analyses were performed on an Agilent 1200 series HPLC system and an Agilent 6120 MSD. Normal phase separation of individual GDGTs was achieved on a Prevail Cyano column (150 mm x 2.1 mm, 3 μm) maintained at 30°C. After sample injection (20 μL) and 5 min isocratic elution with mobile phase A (hexane/2-propanol/chloroform; 98:1:1) at a flow rate of 0.2 ml min⁻¹, the proportion of mobile phase B (hexane/2-propanol/chloroform; 89:10:1) was linearly increased to 10 % within 20 min, and thereafter to 100 % for the next 10 min. After another 7 min and prior to the analysis of the next sample, the column was cleaned in backflush mode for 5 min at a flow of 0.6 ml min⁻¹ and re-equilibrated with solvent A (10 min, flow 0.2 ml min⁻¹). APCI conditions were as follows: nebulizer pressure 50 psi, vaporizer temperature 350°C, N₂ drying gas temperature 350°C and flow 5 l min⁻¹, capillary voltage 3400 V, and corona discharge current 5 μA. GDGTs were detected by selective ion monitoring (SIM) of the (M+H)⁺ ions (dwell time 77ms) in the *m/z* range 1022-1302, i.e. 1022 (brGDGT-I), 1036 (brGDGT-II), 1050 (brGDGT-III), 1292.3 (Crenarchaeol and its regio-isomer), 1296.3 (GDGT-3), 1298.3 (GDGT-

2), 1300.3 (GDGT-1), 1302.3 (GDGT-0), and 744 (C₄₆-GDGT). Concentrations of GDGTs were calculated using the response factor from the C₄₆-GDGT standard (Huguet et al., 2006b). Reproducibility of estimated temperatures based on duplicate analysis was generally better than 0.7°C. Reproducibility of the GDGT quantification was in general better than 10 %.

5.3.5 Environmental reference data

The environmental data used in this study, i.e. sea surface water as well as depth-integrated (0-200 m water depth) annual mean temperature, were extracted from the World Ocean Atlas 2009 (WOA09) data set (Locarnini et al., 2010). The WOA09 SST data set has been suggested to be appropriate for proxy calibrations at low temperatures (Kim et al., 2012a; Kim et al., 2012b; Ho et al., 2014). For comparison of our TEX₈₆ and U₃₇^{K'} index data with seasonal mean SST, we used Southern hemisphere seasons as defined by the WOA09, i.e. summer: January-March, autumn: April-June, winter: July-September, spring: October-December.

Table 5.1: Site information, concentrations and indices based on different biomarker lipids determined in surface sediments from the Pacific sector of the Southern Ocean

| Station | Latitude | Longitude | Depth (m) | TOC (%) | TN (%) | C/N ratio | ²³² Th (ppm) | <i>n</i> -alkanes ^a (ng/g) | CPI ^b | ACL ^c | alkenones (ng/g) | isoGDGT (ug/g) | brGDGT ^d (ng/g) | BIT ^e | U ₃₇ ^{Kf} | TEX ₈₆ ^g |
|------------------------------|----------|-----------|--------------|------------|-----------|--------------|----------------------------|--|------------------|------------------|---------------------|-------------------|-------------------------------|------------------|-------------------------------|--------------------------------|
| <i>Chile Basin</i> | | | | | | | | | | | | | | | | |
| SO213-001-1 | 36.13°S | 85.02°W | 2806 | 0.15 | 0.02 | 8 | n.d. | 216 | 1.3 | 30.5 | 102 | 4.0 | 35 | 0.02 | 0.699 | 0.518 |
| SO213-012-1 | 42.23°S | 85.28°W | 3016 | 0.28 | 0.03 | 12 | n.d. | 106 | 2.0 | 29.9 | 15 | 1.4 | 23 | 0.03 | 0.544 | 0.455 |
| SO213-014-1 | 40.18°S | 84.28°W | 4050 | 0.27 | 0.05 | 7 | 3.08 | 394 | 3.9 | 29.7 | 24 | 5.5 | 194 | 0.06 | 0.596 | 0.462 |
| SO213-015-1 | 40.24°S | 84.39°W | 3246 | 0.26 | 0.02 | 16 | n.d. | 118 | 2.6 | 29.9 | 15 | 2.1 | 33 | 0.03 | 0.649 | 0.470 |
| SO213-017-1 | 40.37°S | 84.30°W | 2561 | 0.25 | 0.02 | 13 | n.d. | 67 | 3.3 | 29.1 | 37 | 3.6 | 57 | 0.03 | 0.691 | 0.476 |
| SO213-019-1 | 40.34°S | 84.13°W | 2951 | 0.20 | 0.02 | 10 | n.d. | 155 | 1.9 | 30.1 | 32 | 3.2 | 57 | 0.04 | 0.623 | 0.478 |
| SO213-020-1 | 39.27°S | 80.18°W | 2702 | 0.15 | 0.02 | 8 | n.d. | 127 | 4.1 | 29.9 | 19 | 6.6 | 46 | 0.02 | 0.619 | 0.483 |
| SO213-022-4 | 39.12°S | 79.55°W | 4125 | 0.42 | 0.08 | 6 | 4.69 | 626 | 5.1 | 29.9 | 66 | 11.4 | 463 | 0.09 | 0.658 | 0.473 |
| <i>Chile Rise</i> | | | | | | | | | | | | | | | | |
| SO213-006-1 | 37.21°S | 92.23°W | 2791 | 0.14 | 0.02 | 7 | n.d. | 135 | 1.3 | 29.9 | 74 | 2.7 | 44 | 0.03 | 0.673 | 0.482 |
| SO213-007-1 | 37.30°S | 93.57°W | 2571 | 0.51 | 0.03 | 23 | n.d. | 190 | 1.4 | 30.0 | 65 | 0.7 | 14 | 0.04 | 0.670 | 0.493 |
| SO213-008-1 | 37.29°S | 95.21°W | 2171 | 0.18 | 0.02 | 11 | n.d. | 52 | 2.8 | 29.3 | 23 | 2.2 | 24 | 0.02 | 0.641 | 0.513 |
| SO213-010-1 | 38.36°S | 93.43°W | 2977 | 0.09 | 0.02 | 6 | n.d. | 150 | 1.2 | 30.6 | 21 | 0.9 | 17 | 0.04 | 0.685 | 0.452 |
| SO213-011-1 | 40.52°S | 90.31°W | 1850 | 0.22 | 0.01 | 23 | n.d. | 53 | 1.7 | 29.7 | 36 | 4.7 | 36 | 0.02 | 0.559 | 0.470 |
| SO213-024-1 | 36.57°S | 102.07°W | 3092 | 0.28 | 0.02 | 15 | n.d. | 401 | 1.1 | 30.5 | 45 | 2.7 | 24 | 0.04 | 0.649 | 0.499 |
| <i>E-Pacific Rise</i> | | | | | | | | | | | | | | | | |
| SO213-026-1 | 35.60°S | 109.55°W | 2830 | 0.21 | 0.02 | 10 | 0.43 | 92 | 1.7 | 30.1 | 28 | 1.0 | 24 | 0.05 | 0.728 | 0.514 |
| SO213-049-3 | 39.57°S | 114.01°W | 3381 | 0.17 | 0.02 | 9 | n.d. | 137 | 2.8 | 29.8 | 20 | 1.6 | 42 | 0.05 | 0.656 | 0.481 |
| SO213-054-4 | 43.42°S | 120.30°W | 3840 | 0.27 | 0.02 | 14 | 0.71 | 233 | 4.4 | 30.2 | 18 | 2.2 | 50 | 0.05 | 0.487 | 0.443 |
| SO213-057-1 | 46.59°S | 113.27°W | 1194 | 0.06 | 0.02 | 4 | n.d. | 45 | 2.4 | 30.0 | 8 | 2.9 | 24 | 0.02 | 0.451 | 0.437 |
| SO213-058-1 | 46.45°S | 115.09°W | 1904 | 0.17 | 0.03 | 7 | n.d. | 41 | 2.8 | 29.5 | 13 | 8.3 | 39 | 0.01 | 0.420 | 0.440 |
| SO213-059-1 | 45.50°S | 116.53°W | 3159 | 0.11 | 0.03 | 5 | n.d. | 75 | 2.4 | 29.4 | 4 | 5.6 | 41 | 0.02 | 0.434 | 0.448 |
| SO213-060-2 | 44.58°S | 119.33°W | 3468 | 0.10 | 0.02 | 5 | n.d. | 200 | 1.5 | 30.5 | 12 | 2.0 | 32 | 0.03 | 0.490 | 0.448 |
| SO213-061-1 | 44.60°S | 119.38°W | 3616 | 0.13 | 0.02 | 8 | n.d. | 0 | n.d. | n.d. | 25 | 2.6 | 24 | 0.03 | 0.485 | 0.442 |
| SO213-063-1 | 44.40°S | 119.05°W | 3938 | 0.14 | 0.02 | 7 | n.d. | 0 | n.d. | n.d. | 3 | 1.0 | 34 | 0.05 | 0.550 | 0.442 |

| Station | Latitude | Longitude | Depth (m) | TOC (%) | TN (%) | C/N ratio | ²³² Th (ppm) | <i>n</i> -alkanes ^a (ng/g) | CPI ^b | ACL ^c | alkenones (ng/g) | isoGDGT (ug/g) | brGDGT ^d (ng/g) | BIT ^e | U ₃₇ ^{Kf} | TEX ₈₆ ^g |
|--------------------------------|----------|-----------|--------------|------------|-----------|--------------|----------------------------|--|------------------|------------------|---------------------|-------------------|-------------------------------|------------------|-------------------------------|--------------------------------|
| SO213-064-2 | 43.24°S | 119.53°W | 3922 | 0.12 | 0.02 | 6 | n.d. | 120 | 2.9 | 30.0 | 6 | 1.6 | 63 | 0.04 | 0.520 | 0.460 |
| <i>SE-Pacific Basin</i> | | | | | | | | | | | | | | | | |
| PS75/046-2 | 54.41°S | 102.50°W | 2984 | 0.11 | 0.02 | 6 | 0.24 | 87 | 1.8 | 29.5 | 10 | 12.9 | 62 | 0.01 | 0.241 | 0.413 |
| PS75/051-1 | 52.81°S | 107.81°W | 3949 | 0.16 | 0.03 | 6 | 1.27 | 111 | 2.6 | 29.5 | 18 | 20.3 | 166 | 0.02 | 0.256 | 0.432 |
| PS75/053-1 | 60.75°S | 115.98°W | 5130 | 0.59 | 0.10 | 7 | 3.34 | 139 | 3.0 | 30.0 | 10 | 19.6 | 83 | 0.01 | 0.098 | 0.404 |
| PS75/063-1 | 58.90°S | 135.62°W | 3795 | 0.60 | 0.10 | 7 | 0.52 | 161 | 2.1 | 29.8 | 10 | 70.8 | 0 | n.d. | 0.083 | 0.364 |
| <i>NZ margin</i> | | | | | | | | | | | | | | | | |
| SO213-076-1 | 46.13°S | 178.02°W | 4337 | 0.37 | 0.06 | 7 | 8.50 | 819 | 3.9 | 30.4 | 54 | 12.3 | 74 | 0.01 | 0.467 | 0.478 |
| SO213-078-1 | 46.15°S | 179.37°W | 3410 | 0.25 | 0.05 | 6 | 4.65 | 467 | 5.5 | 30.2 | 55 | 7.4 | 85 | 0.02 | 0.448 | 0.434 |
| SO213-079-1 | 45.51°S | 179.34°E | 3143 | 0.25 | 0.04 | 7 | 2.89 | 446 | 4.0 | 30.4 | 16 | 11.9 | 78 | 0.01 | 0.443 | 0.424 |
| SO213-081-1 | 45.59°S | 177.60°E | 2816 | 0.24 | 0.04 | 8 | n.d. | 350 | 5.8 | 30.1 | 46 | 15.9 | 52 | 0.01 | 0.403 | 0.421 |
| SO213-084-2 | 45.07°S | 174.35°E | 992 | 0.24 | 0.05 | 6 | 5.22 | 519 | 5.6 | 30.3 | 142 | 20.5 | 142 | 0.02 | 0.424 | 0.438 |
| SO213-085-1 | 44.46°S | 174.32°E | 832 | 0.33 | 0.05 | 8 | n.d. | 761 | 6.8 | 30.2 | 127 | 28.4 | 256 | 0.02 | 0.473 | 0.427 |
| SO213-087-1 | 44.06°S | 174.06°E | 542 | 0.35 | 0.06 | 7 | 7.12 | 748 | 6.6 | 30.2 | 424 | 31.8 | 656 | 0.04 | 0.480 | 0.406 |
| PS75/099-4 | 48.26°S | 177.27°E | 1272 | 0.28 | 0.05 | 7 | 0.77 | 184 | 4.1 | 30.2 | 32 | 26.1 | 189 | 0.02 | 0.319 | 0.427 |
| PS75/100-4 | 45.76°S | 177.15°E | 2498 | 0.24 | 0.04 | 7 | 2.48 | 197 | 10.0 | 30.2 | 340 | 6.9 | 16 | 0.01 | 0.296 | 0.435 |
| PS75/101-1 | 45.48°S | 175.53°E | 1770 | 0.31 | 0.06 | 6 | 2.97 | 193 | 7.5 | 30.2 | 308 | 28.4 | 107 | 0.01 | 0.272 | 0.425 |
| PS75/104-1 | 44.77°S | 174.53°E | 835 | 0.39 | 0.05 | 9 | 6.79 | 309 | 6.9 | 30.1 | 310 | 26.4 | 282 | 0.02 | 0.411 | 0.427 |
| PS75/105-2 | 44.41°S | 174.62°E | 668 | 0.47 | 0.08 | 7 | 7.68 | 307 | 7.5 | 30.2 | 526 | 38.5 | 662 | 0.04 | 0.451 | 0.423 |
| <i>SW-Pacific</i> | | | | | | | | | | | | | | | | |
| SO213-068-1 | 45.07°S | 155.17°W | 1988 | 0.15 | 0.01 | 13 | n.d. | 139 | 1.4 | 29.9 | 12 | 19.1 | 205 | 0.03 | 0.514 | 0.453 |
| PS75/070-1 | 58.35°S | 150.04°W | 2842 | 0.28 | 0.06 | 5 | 0.36 | 46 | 4.9 | 30.0 | 7 | 23.4 | 59 | 0.01 | 0.072 | 0.369 |
| PS75/072-3 | 57.56°S | 151.22°W | 3098 | 0.54 | 0.10 | 6 | 0.17 | 25 | 5.9 | 30.0 | 12 | 23.2 | 16 | 0.00 | 0.076 | 0.351 |
| PS75/076-1 | 55.53°S | 156.14°W | 3742 | 0.23 | 0.04 | 7 | 1.06 | 162 | 3.3 | 29.8 | 30 | 20.0 | 133 | 0.02 | 0.164 | 0.405 |
| PS75/080-2 | 58.11°S | 157.38°W | 3874 | 0.45 | 0.08 | 6 | 0.68 | 127 | 2.6 | 30.1 | 18 | 32.0 | 121 | 0.01 | 0.090 | 0.386 |
| PS75/082-2 | 59.04°S | 158.36°W | 4000 | 0.79 | 0.10 | 9 | 0.49 | 54 | 4.3 | 29.6 | 61 | 30.4 | 77 | 0.01 | 0.112 | 0.374 |
| PS75/084-1 | 61.03°S | 159.35°W | 3315 | 0.45 | 0.08 | 7 | 0.22 | 54 | 8.5 | 30.2 | 7 | 74.8 | 83 | 0.00 | 0.066 | 0.389 |
| PS75/085-2 | 61.94°S | 160.12°W | 3734 | 0.68 | 0.10 | 8 | 0.30 | 60 | 5.9 | 29.5 | 9 | 70.6 | 75 | 0.00 | 0.062 | 0.396 |
| PS75/088-3 | 68.44°S | 164.49°W | 3857 | 0.47 | 0.08 | 7 | n.d. | 0 | n.d. | n.d. | 0 | 21.5 | 259 | 0.11 | n.d. | 0.383 |
| PS75/092-1 | 60.52°S | 169.33°W | 3762 | 0.42 | 0.07 | 7 | 0.99 | 117 | 6.9 | 30.3 | 14 | 35.3 | 73 | 0.01 | 0.076 | 0.395 |

| Station | Latitude | Longitude | Depth (m) | TOC (%) | TN (%) | C/N ratio | ²³² Th (ppm) | <i>n</i> -alkanes ^a (ng/g) | CPI ^b | ACL ^c | alkenones (ng/g) | isoGDGT (ug/g) | brGDGT ^d (ng/g) | BIT ^e | U ₃₇ ^{Kf} | TEX ₈₆ ^g |
|------------|----------|-----------|--------------|------------|-----------|--------------|----------------------------|--|------------------|------------------|---------------------|-------------------|-------------------------------|------------------|-------------------------------|--------------------------------|
| PS75/094-3 | 61.82°S | 169.74°W | 3270 | 0.47 | 0.09 | 6 | 0.24 | 59 | 6.3 | 30.1 | 6 | 23.4 | 143 | 0.01 | 0.098 | 0.378 |
| PS75/097-5 | 59.42°S | 171.21°W | 4672 | 0.52 | 0.09 | 7 | 3.22 | 247 | 2.6 | 30.6 | 81 | 12.9 | 121 | 0.02 | 0.105 | 0.409 |

n.d. not determined

^a Sum of *n*-C₂₇, *n*-C₂₉, *n*-C₃₁, *n*-C₃₃ alkanes

^b $CPI_{27-33} = 0.5 \times \Sigma(C_{27}-C_{33}) / (C_{26}-C_{32}) + 0.5 \times \Sigma(C_{27}-C_{33}) / (C_{28}-C_{34})$

^c $ACL_{25-35} = \Sigma(i \times X_i) / \Sigma X_i$, where X is abundance and i ranges from *n*-C₂₅ to *n*-C₃₅

^d Sum of branched GDGT-Ia, -IIa and -IIIa

^e $BIT = (GDGT-Ia + GDGT-IIa + GDGT-IIIa) / (Crenarchaeol + GDGT-Ia + GDGT-IIa + GDGT-IIIa)$

^f $U_{37}^K = C_{37:2} / (C_{37:2} + C_{37:3})$

^g $TEX_{86} = (GDGT-2 + GDGT-3 + Cren') / (GDGT-1 + GDGT-2 + GDGT-3 + Cren')$

Table 5.2: ^{230}Th -normalized burial of lithogenic material (^{232}Th -based) and specific lipid biomarkers

| Station | lithogenics ($\text{g m}^{-2} \text{y}^{-1}$) | <i>n</i> -alkanes ($\mu\text{g m}^{-2} \text{y}^{-1}$) | brGDGTs ($\mu\text{g m}^{-2} \text{y}^{-1}$) | alkenones ($\mu\text{g m}^{-2} \text{y}^{-1}$) | isoGDGTs ($\mu\text{g m}^{-2} \text{y}^{-1}$) |
|------------|--|---|---|---|--|
| PS75/46-1 | 0.34 | 1.24 | 0.88 | 0.14 | 183.3 |
| PS75/51-2 | 0.95 | 0.83 | 1.24 | 0.13 | 151.4 |
| PS75/53-1 | 1.22 | 0.50 | 0.30 | 0.04 | 71.4 |
| PS75/63-1 | 0.59 | 1.86 | 0.00 | 0.11 | 815.0 |
| PS75/70-1 | 0.38 | 0.49 | 0.62 | 0.08 | 246.6 |
| PS75/72-3 | 0.40 | 0.57 | 0.37 | 0.28 | 537.9 |
| PS75/76-1 | 0.91 | 1.38 | 1.14 | 0.26 | 170.4 |
| PS75/80-2 | 0.78 | 1.47 | 1.41 | 0.21 | 369.6 |
| PS75/82-2 | 0.53 | 0.59 | 0.83 | 0.66 | 328.1 |
| PS75/84-1 | 0.43 | 1.02 | 1.58 | 0.14 | 1419.3 |
| PS75/85-2 | 0.63 | 1.24 | 1.56 | 0.19 | 1459.0 |
| PS75/88-3 | n.d. | 0.00 | 0.83 | 0.00 | 26.2 |
| PS75/92-1 | 0.62 | 0.72 | 0.45 | 0.09 | 133.3 |
| PS75/94-3 | 0.42 | 1.03 | 2.51 | 0.12 | 616.5 |
| PS75/97-5 | 1.08 | 0.83 | 0.41 | 0.27 | 43.4 |
| PS75/99-1 | 0.72 | 1.71 | 1.76 | 0.30 | 242.7 |
| PS75/100-1 | 2.74 | 2.18 | 0.18 | 3.76 | 76.5 |
| PS75/101-2 | 2.95 | 1.92 | 1.07 | 3.06 | 282.3 |
| PS75/104-2 | 8.28 | 3.77 | 3.45 | 3.78 | 322.4 |
| PS75/105-1 | 9.48 | 3.79 | 8.17 | 6.49 | 475.7 |
| SO213/14-1 | 0.76 | 0.97 | 0.48 | 0.06 | 13.5 |
| SO213-22-4 | 1.28 | 1.71 | 1.27 | 0.18 | 31.3 |
| SO213-26-1 | 0.29 | 0.61 | 0.16 | 0.18 | 6.5 |
| SO213-54-4 | 0.29 | 0.94 | 0.20 | 0.07 | 8.7 |
| SO213-76-2 | 7.70 | 7.41 | 0.67 | 0.49 | 111.3 |
| SO213-78-1 | 8.01 | 8.04 | 1.46 | 0.94 | 127.2 |
| SO213-79-1 | 3.41 | 5.27 | 0.92 | 0.18 | 139.9 |
| SO213-84-2 | 11.84 | 11.78 | 3.22 | 3.22 | 466.0 |
| SO213-87-1 | 20.47 | 21.49 | 18.86 | 12.18 | 913.4 |

n.d. not determined

5.3.6 Thorium and uranium isotope analysis and flux calculations

Methods for the determination of Th and U concentrations were similar to those described in Martínez-García et al. (2009) with some modifications. Briefly, approximately 50 mg of freeze-dried sediment was spiked with known amounts of ^{229}Th and ^{236}U and transferred into 55 ml Teflon® microwave vessels. In order to digest the sample material, 2 ml of subboiling-distilled concentrated HCl, 3 ml of subboiling-distilled concentrated HNO_3 and 0.5 ml of HF 40% (suprapur®) were added. The microwave vessels were placed in a pressure-assisted microwave digestion system (CEM Mars Xpress) and heated up to 230°C (held for 60 minutes). After the digestion process, the acid mixture was evaporated using a CEM Xvap accessory. In a subsequent step, the addition of 5 ml 1 M HNO_3 and gently heating up to 200°C (held for 10 minutes) in the Xpress rotor ensured that all particles were fully dissolved. In order to separate Th and U from other elements, three consecutive steps of iron precipitation were performed. The washed precipitate that contained Th and U was dissolved in 3 M HNO_3 and added onto equilibrated (2 column volumes (=CV) of 3M HNO_3) 2 ml columns filled with Eichrom UTEVA resin. Fe from the precipitate was eluted with 3 M HNO_3 (3 CV) prior to the separation of Th and U. Subsequently, different concentrations of HCl were used to collect Th and U. At first, 9 M HCl was applied to the columns (1 CV) followed by 5 M HCl (2 CV) to collect Th. Finally, U was collected by eluting with 3 CV of 0.02 M HCl. Th and U isotopes were measured separately by sector-field ICP-MS (Thermo Element2 equipped with an ESI Apex Q desolvator) in low resolution. External reproducibility was monitored using a certified reference material (UREM 11). Procedural blanks were run alongside the samples. Due to the large difference in isotopic abundance between ^{232}Th and ^{230}Th , the tailing of the ^{232}Th peak to lower masses affects count rates at mass ^{230}Th , making a correction necessary. Corrections for tailing, mass bias and procedural blanks were applied as appropriate and considered in the error propagation. ^{238}U was calculated from ^{235}U using the natural isotope abundance. ^{230}Th was calculated according to Francois et al. (2004), using a $^{238}\text{U}/^{232}\text{Th}$ activity ratio of 0.8. Thorium-230 in excess of its progenitor ^{234}U ($^{230}\text{Th}_{\text{ex}}$) can be readily converted into preserved vertical mass fluxes of a specific sedimentary component (Francois et al., 2004; Geibert et al., 2005; Martínez-García et al., 2009; Lamy et al., 2014). By normalizing the flux of a sedimentary component to the flux of thorium, we implicitly also correct for postdepositional sediment redistribution (focusing; Francois et al. 2004). Analytical uncertainties of $^{230}\text{Th}_{\text{ex}}$ after considering all corrections are typically below 5%. (1σ). ^{232}Th concentrations were used to quantify the fraction of lithogenic material in marine sediments assuming an average

concentration of 10 ppm for the upper continental crust (Taylor and McLennan, 1995; Winckler et al., 2008). The lithogenic end-member for the upper continental crust was inferred from the measured ^{232}Th concentrations. The resulting lithogenic contents are within the range of those calculated from bulk sediment parameters in the Pacific SO (Lamy et al., 2014).

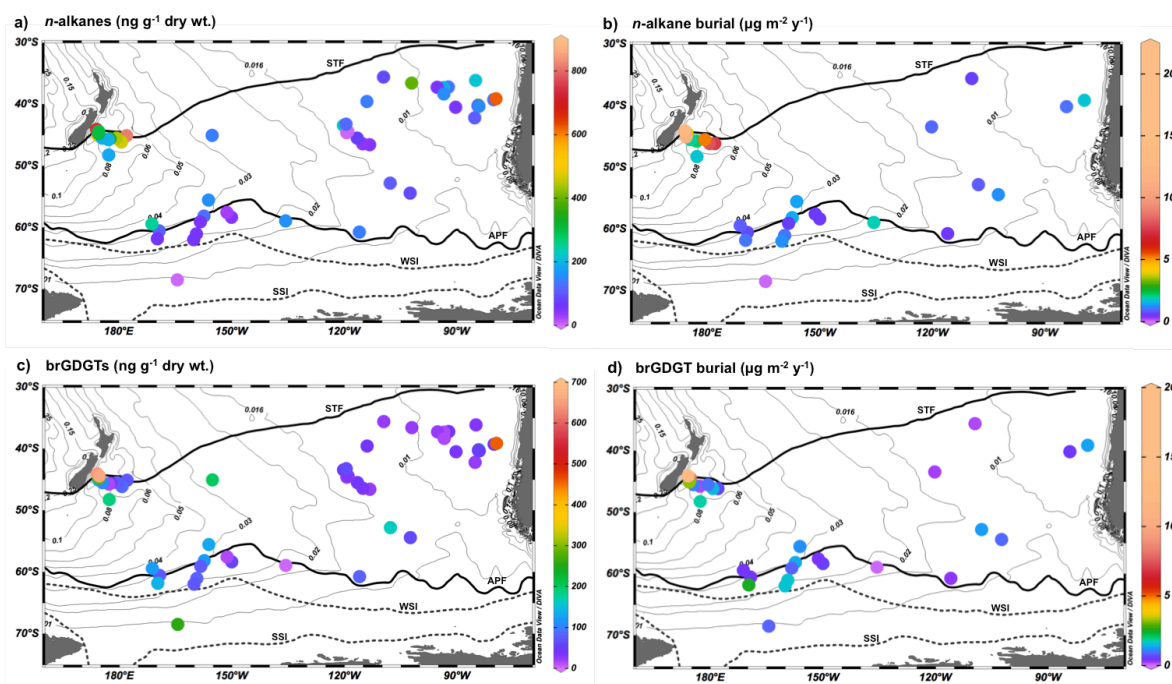


Figure 5.2: Spatial distribution of concentrations (ng g^{-1} dry wt.) and ^{230}Th -normalized sedimentary burial ($\mu\text{g m}^{-2} \text{yr}^{-1}$) of (a, c) long-chain ($n\text{-C}_{27}$ to $n\text{-C}_{33}$) alkanes and (b, d) brGDGTs I-III in surface sediments of the Pacific Southern Ocean. Grey lines denote the extent of modeled modern dust deposition fluxes ($\text{g m}^{-2} \text{yr}^{-1}$) after Albani et al. (2014).

5.4 Results

5.4.1 Total organic carbon, total nitrogen, and C/N ratio

TOC values are generally low in the surface sediments ranging between $<0.1\%$ and 0.8% with an average value of 0.3% (Table 5.1). Highest values are observed at the sites closest to New Zealand and the APF, while lowest values are found in the SE-Pacific. TN values are also overall low between 0.01% and 0.1% (Table 5.1). Organic matter C/N ratios exhibit large variations between 4 and 23 (Table 5.1) with an average of 8, suggesting different OM sources. Vascular land plants have C/N ratios of 20 or more, whereas in general lower average C/N ratios of 7 and 12 are indicative of phytoplankton and green macroalgae, respectively (Goni

and Hedges, 1995; Cloern et al., 2002), or microbially altered marine and terrigenous OM (C/N ratio of 4; Goni and Hedges, 1995; Meyers, 1997).

5.4.2 Lithogenic content

^{232}Th is used to quantitatively assess the inorganic fraction of continental material in the surface sediments. ^{232}Th concentrations range from <0.5 ppm in the southeast Pacific and south of the APF to 8.5 ppm off New Zealand (Table 5.1). Similarly, preserved lithogenic fluxes ("burial") based on the ^{230}Th -normalization method vary between $0.3 \text{ g m}^{-2} \text{ y}^{-1}$ at site PS75/046-2 and $20 \text{ g m}^{-2} \text{ y}^{-1}$ at site SO213-87-1 off New Zealand (Table 5.2).

5.4.3 *n*-alkanes

Long-chain *n*-alkanes derived from higher plants were detected in most surface sediment samples ($n = 49$) with total concentrations of odd-numbered *n*-C₂₇ to *n*-C₃₃ alkanes varying between 41 and 819 ng g⁻¹ sediment dry wt. (Table 5.1; Fig. 5.2 a). Th-normalized burial of *n*-alkanes show distinct variations between $0.5 \text{ } \mu\text{g m}^{-2} \text{ y}^{-1}$ close to the APF and $21.5 \text{ } \mu\text{g m}^{-2} \text{ y}^{-1}$ at Chatham Rise offshore New Zealand (Table 5.2; Fig. 5.2 b). Degradation of long-chain *n*-alkanes can be determined by the ratio of odd- to even-numbered *n*-alkane homologues, expressed by the carbon preference index (CPI; Bray and Evans, 1961). CPI values are between 1.1 and 10 (Table 5.1), a range between mature organic matter (CPI~1) and relatively fresh plant-derived material (CPI > 3; Eglinton and Hamilton, 1967). The changing abundance of individual *n*-alkanes is expressed by the average chain length (ACL₂₇₋₃₃). ACL values range from 29.1 to 30.6 in the surface sediments (Table 5.1), also indicating the dominance of a modern plant source.

5.4.4 Glycerol dialkyl glycerol tetraethers (GDGTs)

Branched (br) GDGTs (sum of GDGT-I to -III) were detected in nearly all surface sediments ($n = 51$) with variable total concentrations ranging between 14 ng g⁻¹ sediment dry wt. at site SO213-007-1 from the Chile Rise and 662 ng g⁻¹ sediment dry wt. at site PS75/105-2 offshore New Zealand (Table 5.1; Fig. 5.2 c). Burial of brGDGTs also shows pronounced variations between $0.16 \text{ } \mu\text{g m}^{-2} \text{ y}^{-1}$ at the East Pacific Rise and up to $18.9 \text{ } \mu\text{g m}^{-2} \text{ y}^{-1}$ at Chatham Rise (Table 5.2; Fig. 5.2 d). Isoprenoid (iso) GDGTs were detected in all surface sediments ($n = 52$) with highly variable total concentrations ranging between 0.7 and 11.4 $\mu\text{g g}^{-1}$ sediment dry wt.

in the SE-Pacific (i.e. Chile Basin/Rise, East Pacific Rise) and up to $75 \mu\text{g g}^{-1}$ south of the APF (Table 5.1). Burial of isoGDGTs reveals the most pronounced variations between $6.5 \mu\text{g m}^{-2} \text{y}^{-1}$ at the East Pacific Rise and $1459 \mu\text{g m}^{-2} \text{y}^{-1}$ south of the APF, which is in strong contrast to all other compounds (Table 5.2). The GDGT distribution in all surface sediments is strongly dominated by GDGT-0 and crenarchaeol, which is typical for open ocean settings. BIT index values are generally low in the study area and vary between 0.01 and 0.1 (Table 5.1).

5.4.5 Alkenones

$\text{C}_{37:2}$ and $\text{C}_{37:3}$ alkenones were detected in almost all sediment samples ($n = 51$) with lowest concentrations of 3 ng g^{-1} sediment dry wt. at the East Pacific Rise (SO213-063-1) and 526 ng g^{-1} sediment dry wt. at site PS75/105-2 offshore New Zealand (Table 5.1). Alkenone burial varies between 0.04 and $12.2 \mu\text{g m}^{-2} \text{y}^{-1}$ in the study area (Table 5.2). The tetra-unsaturated alkenone ($\text{C}_{37:4}$) was only present in a few sediment samples from the PFZ ($n = 5$) with relative abundances between 3 and 12 % of the total C_{37} alkenones. The $\text{C}_{37:4}$ alkenone did not show a relation with temperature and was therefore excluded from the temperature calculation.

5.4.6 Sea surface temperature proxy indices

The U_{37}^{K} index ranges from 0.062 to 0.728, revealing a wide range of 0.666 units in the investigated area. The TEX_{86} index shows less variation (0.167 units) and ranges from 0.351 to 0.518 (Table 5.1). Both indices, however, show a distinct latitudinal pattern (Table A 5.1). $\text{TEX}_{86}^{\text{L}}$ values range from -0.392 to -0.674, $\text{TEX}_{86}^{\text{H}}$ values vary between -0.286 and -0.455.

5.5 Discussion

5.5.1 Modern terrigenous OM deposition in the Pacific Southern Ocean

We compare two independent organic tracers, i.e. long-chain *n*-alkanes and brGDGTs with lithogenic contents derived from ^{232}Th measurements, to estimate modern terrigenous input to the Pacific sector of the SO. As deep-sea records of the SO can be affected by sediment focusing that may significantly alter vertical flux estimates (Francois et al., 2004; Geibert et al., 2005; Martínez-García et al., 2009; Lamy et al., 2014), we used the ^{230}Th -normalization method to better quantify biomarker burial for selected sites in our study area (Table 5.2). Concentrations and burial rates of ^{232}Th -based lithogenic material north and south of the APF

are comparable to those reported by Chase et al. (2003) and Bradtmiller et al. (2009). Long-chain *n*-alkanes were detected in most surface sediment samples with highest abundances determined in sediments from the New Zealand continental margin but also in a few sites located closest to the Chile continental margin (Table 5.1; Fig. 5.2 a and b). The distribution of C₂₇-C₃₃ *n*-alkanes in sediments offshore New Zealand exhibits a strong odd over even predominance (CPI 4-10) with carbon number maxima (C_{max}) at *n*-C₂₉ and *n*-C₃₁, which is typical for an origin from higher plant leaf waxes (Eglinton and Hamilton, 1967). The *n*-alkane abundances in the remote open ocean sites were generally low, however, CPI values of 3-6 observed in surface sediments located further eastwards between 160 and 110°W still suggest deposition of relatively fresh plant material (Table 5.1). Long-range transport of windborne terrigenous OM has been documented in dust and marine sediments using leaf wax *n*-alkanes (Simoneit, 1977; Bendle et al., 2007; Martínez-García et al., 2011; Lamy et al., 2014). In the Southern Ocean, prevailing westerlies may play a major role in transporting terrigenous OM with the mineral dust fraction from potential source areas in Australia and New Zealand to the open ocean (Hesse and McTainsh, 2003; Molina-Kescher et al., 2014; Lamy et al., 2014; Neff and Bertler, 2015). The strong positive correlation between concentrations ($r^2 = 0.71$, $p < 0.01$; Fig. 5.3 a) and burial ($r^2 = 0.89$, $p < 0.01$; Fig. 5.3 b) of *n*-alkanes and ²³²Th-based lithogenic material suggests similar origin and transport mechanisms for both terrigenous tracers. Therefore, we infer eolian transport of *n*-alkanes from potential sources in New Zealand and Australia by prevailing westerly winds to the open South Pacific to at least 110°W as the most plausible transport mechanism. This is also in agreement with a recent modeling study by Albani et al. (2014) indicating low modern dust deposition in the Pacific SO (Fig. 5.2). Interestingly, our *n*-alkane concentrations and burial rates in the open ocean sites are comparable to those reported for the Holocene and interglacial periods in the subantarctic Atlantic Ocean (Martinez-Garcia et al., 2009), despite the apparently different sources in Australia/New Zealand. The presence of high *n*-alkane concentrations with CPI values of 5 and C_{max} at *n*-C₂₉ and *n*-C₃₁ detected in surface sediments off Chile located at the northern rim of the main westerly wind belt (Table 1) may also indicate other sources and transport mechanisms. This material may be derived from a source in western South America, which is subsequently transported to the ocean by persistent coastal southerly winds and local wind systems (Garreaud et al., 2009) along the Andes. This has recently also been proposed by Molina-Kescher et al. (2014) based on combined Nd and Sr isotope analyses performed on the same set of surface sediments, indicating increased supply of weathered material from the Andes. Low CPI values of 1.1-1.7 found in sediments from the Chile Rise indicate substantial

contribution of reworked organic material, which is most likely a consequence of prolonged oxygen exposure and very low sedimentation rates that range from <1 to 20 mm kyr^{-1} (Tiedemann, 2012) and resulting surface sediment ages as old as 24 kyr before present (Molina-Kescher et al., 2014). On the other hand, sites PS75/084-1, 085-1, and 092-1 located at the southern rim of the modern westerly wind belt and close to the winter sea ice margin still exhibit *n*-alkane distributions indicative of higher plant material (Table 5.1), in general agreement with recent modeling studies (Fig. 5.2; Albani et al., 2014). The Antarctic continent as a potential source of long-chain *n*-alkanes can be neglected because of the virtual absence of plants (Aislabie et al., 2006). Thus subsequent transport of higher plant waxes to our core locations via ice rafted debris (IRD) can basically be ruled out.

The BIT index is commonly used as a tracer for soil OM input to the marine environment. It corresponds to the relative amount of terrestrial vs. marine OM and its variability is driven by changes in both brGDGTs and crenarchaeol (Hopmans et al., 2004). Here, overall low BIT values (0.01-0.1) are not related to the concentration of brGDGTs or other tracers for terrestrial matter input, i.e. long-chain *n*-alkanes and C/N ratios (Table A 5.1), but may be primarily determined by variations in crenarchaeol concentration as suggested by Fietz et al. (2011). In contrast, quantification of brGDGTs concentrations and burial rates give more reliable estimates on terrigenous OM input to the ocean, which is still largely missing (Fig. 5.2 c and d). BrGDGTs have been found in a range of terrestrial settings as well as in marginal marine sediments influenced by high terrigenous input (Hopmans et al., 2004; Schouten et al., 2013a). These compounds are thought to derive from anaerobic soil bacteria (Weijers et al., 2006; Sinninghe Damasté et al., 2011) but their detection in sediments from the open ocean, far away from any direct terrigenous impact suggests either long-range transport through the atmosphere or in situ production (Fietz et al., 2011; Schouten et al., 2013a; Jaeschke et al., 2014). Aerosol particles were shown to consist of a wealth of biological material like fungi, pollen, and viruses, but also Acidobacteria and Crenarchaeota, which may originate partly from resuspended soil (Després et al., 2012; Fröhlich-Nowoisky et al., 2014). The detection of GDGTs together with long-chain *n*-alkanes in dust samples collected off Northwest Africa was therefore not surprising (Fietz et al., 2013). Common marine sources for iso and brGDGTs have also been suspected (Peterse et al., 2009; Zhu et al., 2011), however, the specific source organisms remain largely unknown. The general lack of correlation between concentrations of iso and brGDGTs in our study suggests different sources of the compounds (Table A. 5.1). Identification of brGDGTs at the southernmost site PS75/088-3, which is influenced by winter sea ice may indicate input of soil OM from Antarctica that is eroded by glaciers and

subsequently transported and deposited by ice-rafted debris (IRD) during the spring/summer ice melt (Fig. 5.2 c and d). Antarctic soils typically devoid of vegetation are restricted to a few coastal areas, i.e. Ross Sea region, where Acidobacteria were reported to be among the dominant bacterial divisions, while archaea were present only in low abundance and diversity (Aislabie et al., 2006; Ayton et al., 2010). It is therefore likely that brGDGTs are also present in Antarctic soils. A significant linear relation is observed between burial of brGDGTs and lithogenic ^{232}Th ($r^2 = 0.70$, $p < 0.01$; Fig. 5.3 b) and *n*-alkanes ($r^2 = 0.66$, $p < 0.01$; not shown), which both are markers that have been used to quantify the amount of terrigenous material present in marine sediments (Martínez-García et al., 2009; Lamy et al., 2014). Differences in the terrigenous carbon pools (i.e. plant versus soil OM), source regions and transport pathways may thus explain the moderate correlation between concentrations of brGDGTs and *n*-alkanes in our study area (Table A 5.1), which is in good agreement with findings from ODP Site 1090 in the Atlantic sector of the SO (Fietz et al., 2011) and dust samples collected off northwest Africa (Fietz et al., 2013).

Estimates of modern dust sources, mobilization rates and deposition are still poorly constrained, resulting primarily from the limited spatial data coverage for the Pacific sector of the SO and adjacent land masses (Chase et al., 2003; Bradtmiller et al., 2009; Kohfeld et al., 2013). Hence, modeling studies reveal as yet major discrepancies about the contribution and relative importance of major dust sources in the Southern Hemisphere, i.e. South America and Australia/New Zealand (Li et al., 2008; Maher et al., 2010; Albani et al., 2014; Neff and Bertler, 2015). Reconstruction of dust deposition by means of inorganic tracers (Fe, Al, ^{232}Th) can be inconclusive as open ocean sites in the SO may be substantially affected by material of glacial (IRD) and/or bottom water-transported origin (e.g. Maher and Dennis, 2001). A combination of inorganic and organic tracers of dust, however, will give more reliable estimates of wind-transported continental material. A strong correlation of iron and ^{232}Th with long-chain *n*-alkanes has been shown for individual sites in the Atlantic SO (ODP Site 1090; Martínez-García et al., 2009) and the Pacific SO (PS75/059-2; Lamy et al., 2014), but our surface data extend these findings and indicate that this relationship also holds over a broader geographic region. A proposed follow-up study performing compound-specific carbon and hydrogen stable isotope analyses of the *n*-alkanes would offer the potential to better constrain vegetation type and hydrological conditions in the potential source areas. In contrast to plant-derived *n*-alkanes, brGDGTs still provide ambiguous evidence for terrigenous OM in sediments from the open ocean as these compounds may have multiple but as yet unknown

sources. Thus further research is definitely needed to identify the major terrigenous sources and possibly disguise additional marine sources for these compounds.

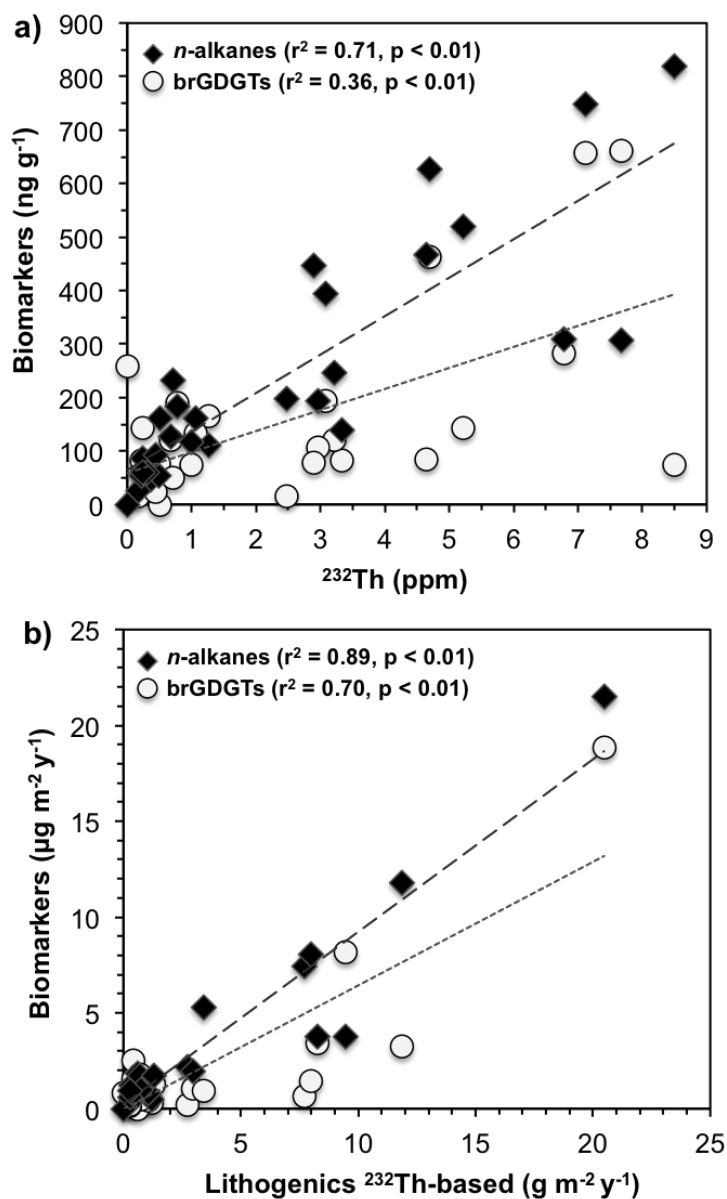


Figure 5.3: Correlation plots of a) concentrations and b) burial of ²³²Th-based lithogenic material with plant wax-derived n -alkanes (black diamonds) and soil-derived brGDGTs (white circles) in surface sediments of the Pacific sector of the Southern Ocean.

5.5.2 Effect of terrigenous material/dust on marine productivity

Mineral dust aerosols play a major role in present and past biogeochemical cycles by providing the surface ocean with micronutrients (iron) that are thought to be a limiting factor for phytoplankton growth in HNLC regions of the SO (e.g. Martin, 1990; Boyd and Ellwood, 2010). The good agreement between organic (*n*-alkanes and brGDGTs) and inorganic (^{232}Th) terrigenous markers suggests common sources and transport processes, i.e. primarily eolian by prevailing westerly winds (see section 5.5.1). Major regional differences are obvious from alkenone and isoGDGT concentrations (Table 5.1), and burial rates indicate different maxima in biomass production and export of haptophyte algae (*E. huxleyi*) and Thaumarchaeota (Table 5.2; Fig. 5.4 a and b). ^{230}Th -normalized burial of alkenones show a strong positive correlation with lithogenic material in the study area ($r^2 = 0.76$, $p < 0.01$, $n = 29$) while isoGDGT burial is related to ^{232}Th ($r^2 = 0.77$, $p < 0.01$, $n = 20$) when the sites south of the APF are excluded (Table 5.2; Fig. 5.5 a and b). This may indicate a fertilizing effect of terrigenous input (dust) on phytoplankton productivity or a ballast effect by dust (e.g. Jickells et al., 2005, and references therein), which is highest close to the potential sources in New Zealand and Australia. In contrast, low lithogenic and terrestrial OM burial in the open ocean may reflect the presently low dust input (Maher et al., 2010; Albani et al., 2014), especially in subantarctic waters and in the SE-Pacific (Chile/East Pacific Rise) which is consistent with the idea that primary production in surface waters is largely iron-limited in those regions (Honjo et al., 2000). In contrast to low burial rates of brGDGTs, *n*-alkanes and alkenones south of the APF, isoGDGT burial is among the highest observed in the study area (Fig. 5.5 b; Table 5.2). While N, P, and Fe limitations can restrict the total amount of carbon fixed in the photic zone of the ocean, Si availability determines the nature of the biological production, which is dominated by diatoms in the AZ (Honjo et al., 2000; Chase et al., 2015). Thaumarchaeota are nitrifiers and therefore they do not rely on iron as a nutrient (Könneke et al., 2005). However, an elevated release of ammonia by phytoplankton decay following major diatom blooms in austral summer may fuel thaumarchaeotal productivity. Thaumarchaeotal cells are too small ($< 1 \mu\text{m}$) to sink by themselves, thus processes such as repackaging in fecal pellets or entrainment in marine snow may be important (e.g. Huguet et al., 2006a; Mollenhauer et al., 2015). The ballasting effect of biogenic material (calcareous or siliceous) may be an important factor promoting export of isoGDGTs to the seafloor. Indeed, highest burial of isoGDGTs observed south of the APF but also offshore New Zealand (Table 5.2; Fig. 5.4 b) may be linked to high phytoplankton productivity in summer and thus high biogenic mass fluxes (Honjo et al., 2000; Geibert et al.,

2005; Yamamoto et al., 2012; Mollenhauer et al., 2015), which is also indicated by the strong correlation between isoGDGT and TOC fluxes ($r^2 = 0.73$, Fig. A 5.1). Maximum isoGDGT burial south of the APF may therefore relate to major diatom blooms during austral summer and thus high opal fluxes (Honjo et al., 2000; Geibert et al., 2005; Chase et al., 2015). The apparent mismatch between high burial of biogenic material and low lithogenic burial in the AZ (Fig. 5.5 b) was also shown in a recent study from Chase et al. (2015) and may be associated with iron sources other than dust, i.e., released from seasonal ice-melt, upwelling of deep, soluble iron, hydrothermal activity, volcanism or potential variations in the biological demand by the organisms (Boyd and Ellwood, 2010; Chase et al., 2015).

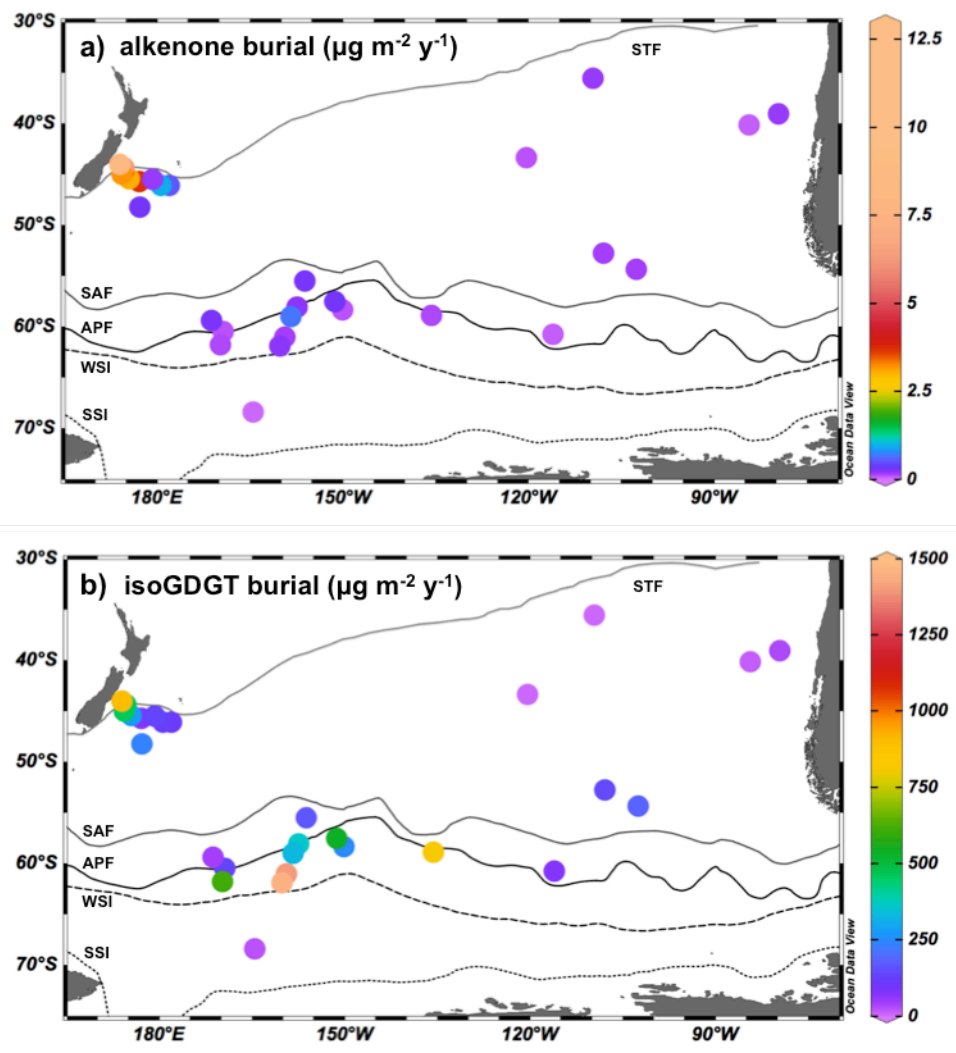


Figure 5.4: Spatial distribution of ^{230}Th -normalized sedimentary burial ($\mu\text{g m}^{-2} \text{yr}^{-1}$) of a) alkenones and b) isoGDGTs.

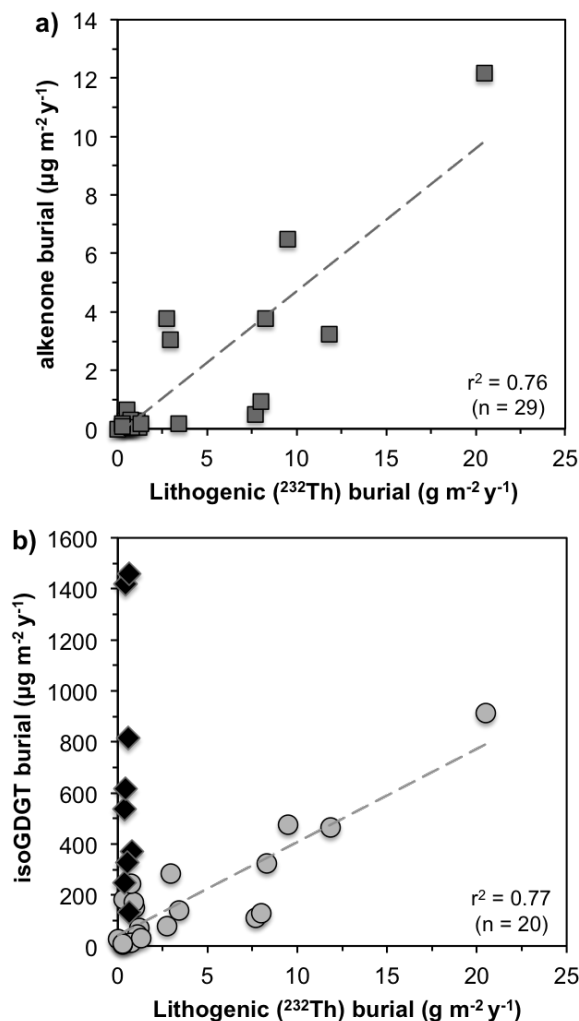


Figure 5.5: Correlation plots of ²³⁰Th-normalized burial of lithogenic material with a) alkenones and b) isoGDGTs from selected sites in the Pacific sector of the Southern Ocean. Note the lack of correlation between lithogenic content and isoGDGT burial for the sites south of the APF (black diamonds).

5.5.3 Sea (sub-)surface temperature proxies: U₃₇^{K'} and TEX₈₆

The choice of temperature calibration is critical in the study area, as temperatures from the Subantarctic to Antarctic Zone have to be faithfully reconstructed. Both U₃₇^{K'} and TEX₈₆ were shown to lose their sensitivity at cold (<5°C) temperatures, resulting in substantial scatter and a tendency to over-estimate temperatures in polar oceans (Sikes et al., 1997; Kim et al., 2010). While there is no doubt about the origin of the U₃₇^{K'}-based temperature signal, i.e. the photic zone, our understanding of TEX₈₆ remains ambiguous (e.g. Pearson and Ingalls, 2013; Schouten et al., 2013). Recent studies by Ho et al. (2012, 2014), however, suggested robust relationships between both U₃₇^{K'} and TEX₈₆ with annual mean WOA09 SST in the Pacific sector

of the SO. Here, we revisit some of the sites investigated by Ho et al. (2012, 2014) (Fig. A 5.2), and compare alkenone- and GDGT-derived temperature estimates in 52 surface sediments from the South Pacific with seasonal SST and subsurface (0-200 m water depth) temperatures extracted from the World Ocean Atlas (WOA09) data set (Locarnini, 2010). In Fig. 5.6, temperature estimates based on different indices and calibrations (Sikes et al., 1997; Müller et al., 1998; Kim et al., 2010; Kim et al., 2012a; Kim et al., 2012b) show an expected latitudinal trend but also exhibit major temperature differences south of 50°S. The strong correlation between TEX_{86} and $U_{37}^{K'}$ values ($r^2 = 0.84$) indicates that temperature is a substantial factor controlling both organic proxies in the study area. In the following sections, TEX_{86} and $U_{37}^{K'}$ indices will be discussed in more detail.

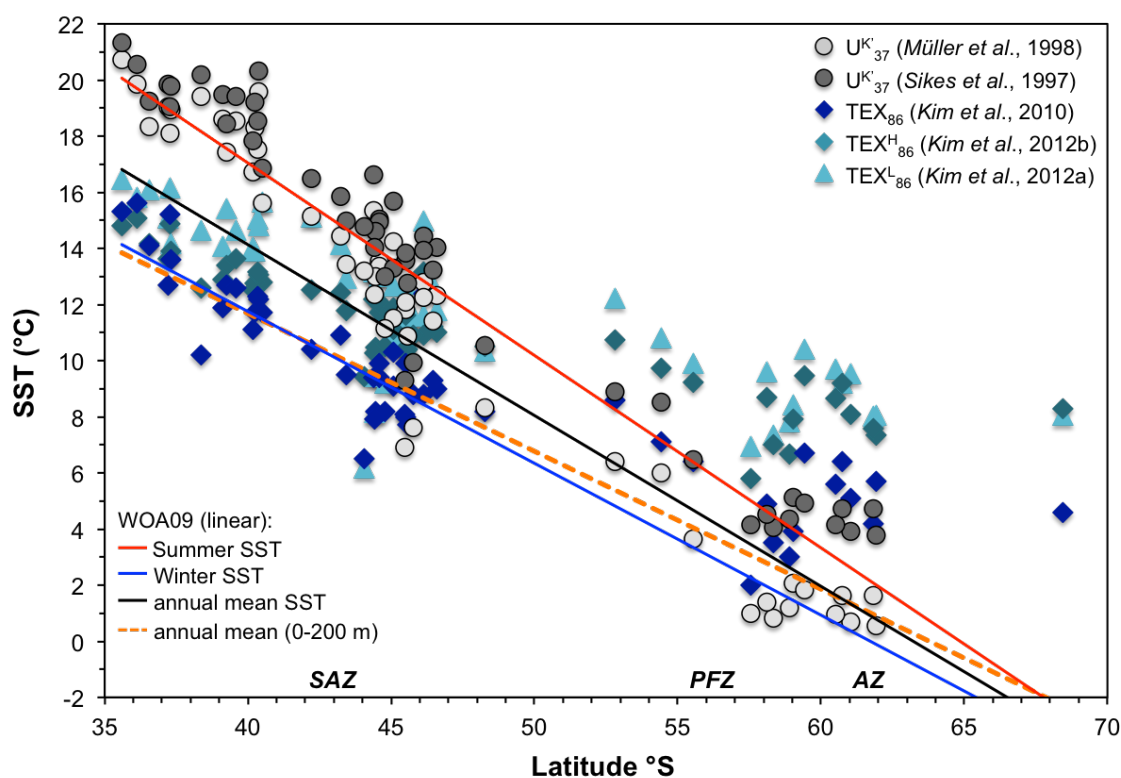


Figure 5.6: GDGT- and alkenone-derived temperature estimates from surface sediments compared with measured seasonal and annual mean sea (sub-)surface temperatures (Locarnini et al., 2010) in the Pacific sector of the Southern Ocean (35-68°S). AZ: Antarctic Zone, PFZ: Polar Front Zone, SAZ: Subantarctic Zone.

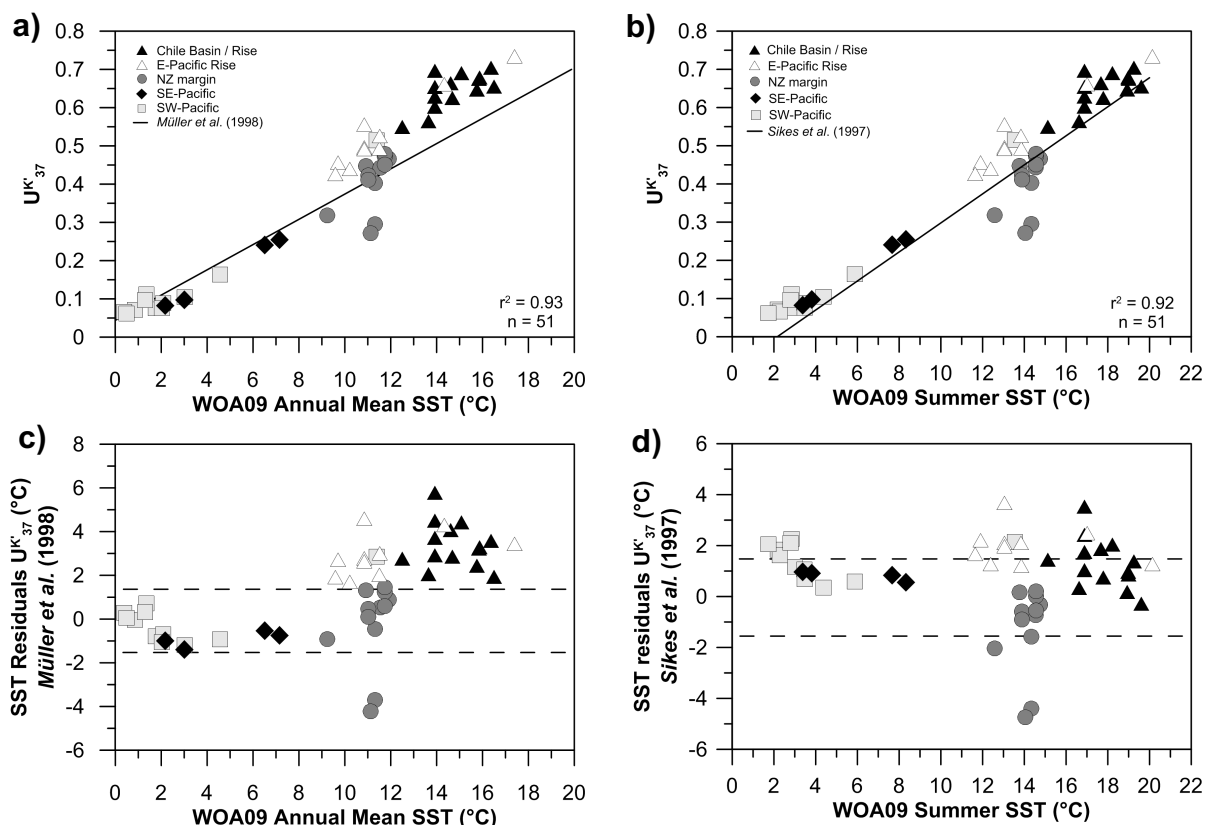


Figure 5.7: Correlation plots of U_{37}^K values with a) annual mean SST and b) summer SST derived from the World Ocean Atlas (WOA09; Locarnini et al., 2010). Black lines illustrate a) the global core-top calibration of Müller et al. (1998) and b) the polar calibration of Sikes et al. (1997). Residuals of temperature estimates derived from the c) global core-top calibration (Müller et al., 1998) and d) polar calibration (Sikes et al., 1997) for U_{37}^K . SST residuals are defined as the subtraction of WOA09 annual mean SST from the estimated SST. The dashed black lines represent the standard error of estimates for the calibration.

5.5.3.1 Alkenone-based SST

U_{37}^K -based SST reconstructions from surface sediments range from 0.5°C to 20.7°C applying the global core-top calibration of Müller et al. (1998) (Fig. 5.6). U_{37}^K values display a strong correlation with annual mean WOA09 SST ($r^2 = 0.93$; $n = 51$) for the same temperature range (Fig. 5.7 a), and most values fall well within seasonal SST between winter and summer. SST calculated with the polar calibration of Sikes et al. (1997) are generally warmer (3.8-21.3°C) bringing core-top temperature estimates closer to summer SST (Fig. 5.6). Moreover, U_{37}^K values are strongly correlated with summer WOA09 SST throughout the study area and the linear regression of these data can be expressed as $U_{37}^K = 0.037T - 0.034$ ($r^2 = 0.92$; $n = 51$; Fig.

5.7 b). To further evaluate the quality of the calibrations of Müller et al. (1998) and Sikes et al. (1997), respectively, residuals of the SST estimates were calculated, i.e., by subtracting WOA09 SST from the respective U_{37}^K -based SST. Diverging patterns in SST residuals exist between surface sediments from the Chile Basin and East Pacific Rise (ca. 35-46°S) and all other sites using the global calibration of Müller et al. (1998) (Fig. 5.7 c). South of 46°S, U_{37}^K -derived temperature estimates reflect annual mean SST well within the estimation error, in line with findings of Ho et al. (2012), while in the SE-Pacific alkenone-based temperatures largely correspond to summer SST (Figs. 5.6; 5.7 c and d). Productivity of alkenone-producing prymnesiophyte algae occurs seasonally rather than year round, therefore, the sedimentary alkenone record may reflect a strong seasonal temperature signal. In the SO, maximum biomass production and thus highest biomarker flux to the sediment may occur during spring/summer phytoplankton bloom (Sikes et al., 1997; Nodder and Northcote, 2001). Other studies from the Australian sector of the SO show a stronger relationship of the U_{37}^K proxy with annual mean SST (Pelejero et al., 2006; Calvo et al., 2007; Lopes dos Santos et al., 2013). This is also suggested by our alkenone-derived SST from the polar ocean, and in agreement with available SST data based on diatom assemblages (Esper and Gersonde, 2014; Fig. A 5.3). In the oligotrophic SE-Pacific, however, paleoceanographic studies are sparse and comprehensive SST data based on alkenones or GDGTs are largely missing. Given the wide range of latitudes and oceanographic settings encompassed by our study sites, it is likely that there are seasonal differences in major phytoplankton blooms for a specific region. Indeed, Prah et al. (2010) also observed a conspicuous ‘warm’ offset in U_{37}^K values recorded in surface sediments collected along the Peru-Chile continental margin, which was explained by a general shift in primary productivity towards the summer season in high latitude regions. Another potential explanation for the warm temperature bias in the SE-Pacific off Chile may be related to the preferential degradation of the $C_{37:3}$ alkenone, which would lead to temperature estimates above observed annual mean SST (Rontani et al., 2008; Huguet et al., 2009; Kim et al., 2009). Diagenetic effects on the U_{37}^K proxy is likely in sediments deposited under prolonged oxic conditions and thus with low sedimentation rates and low OC contents, which is the case for most of the South Pacific sediments. As discussed above for the *n*-alkanes (section 5.5.1), organic matter from the SE-Pacific has likely undergone extensive diagenetic alteration. Indeed, when comparing residual SST from selected radiocarbon dated surface sediments, SST estimates were up to 5.7°C warmer than observed annual mean SST in the oldest sediments at station SO213-017-1 (Fig. 5.7 c). In contrast, the U_{37}^K -derived temperature residual was only

0.5°C at station SO213-084-2 located on the New Zealand margin, where sedimentation rates are considerably higher (Molina-Kescher et al., 2014). Thus, in addition to seasonality in temperature effects and alkenone production, selective degradation of alkenones may also lead to decoupling of SST and sedimentary U_{37}^K values.

We also compared our sedimentary alkenone concentrations with available coccosphere and coccolith numbers from the upper 150 m of the water column at the same stations ($n = 10$) in the South Pacific (Saavedra-Pellitero et al., 2014). While comparison with coccosphere counts in the surface water (10 m) show only a moderate correlation ($r^2 = 0.51$), a strong relation is observed when using depth integrated (0-150 m) coccosphere counts ($r^2 = 0.8$) or maximum coccosphere numbers at a specific water depth (Fig. 5.8 a; $r^2 = 0.86$), which varies between 10 and 100 m at the investigated sites (Saavedra-Pellitero et al., 2014). While U_{37}^K -based temperature estimates display a generally good agreement with SST at the sites close to the STF at the New Zealand continental margin, PS75/100-4 and 101-1 show a cold bias by $>4^\circ\text{C}$ (Fig. 5.7 c and d). The cold temperature estimates at these specific sites may relate to alkenones produced by a different *E. huxleyi* strain or coccolithophore species thriving at deeper (60 m) water depths (Saavedra-Pellitero et al., 2014). Alternatively, contribution of alkenones produced by non-calcifying haptophytes such as *C. lamellosa* or *I. galbana* that occur in marginal marine environments may cause a temperature bias as these species reveal different U_{37}^K -temperature relationships than *E. huxleyi* (e.g. Versteegh et al., 2001; Rontani et al., 2004). The non-linear relation between alkenones and coccospheres may be due to rapid decomposition of alkenones during transport through the water column, which is largely related to the time of oxygen exposure. Alkenones also reveal a strong linear relation ($r^2 = 0.81$) with depth integrated (0-150 m) coccolith counts (Fig. 5.8 b). This suggests that alkenones carry a temperature signal from the upper 100-150 m of the water column that is efficiently transported to the sediment. Direct comparison of living coccolithophore species and alkenone-derived SST analyzed from the same water depths are, however, needed to better constrain the origin of the temperature signal.

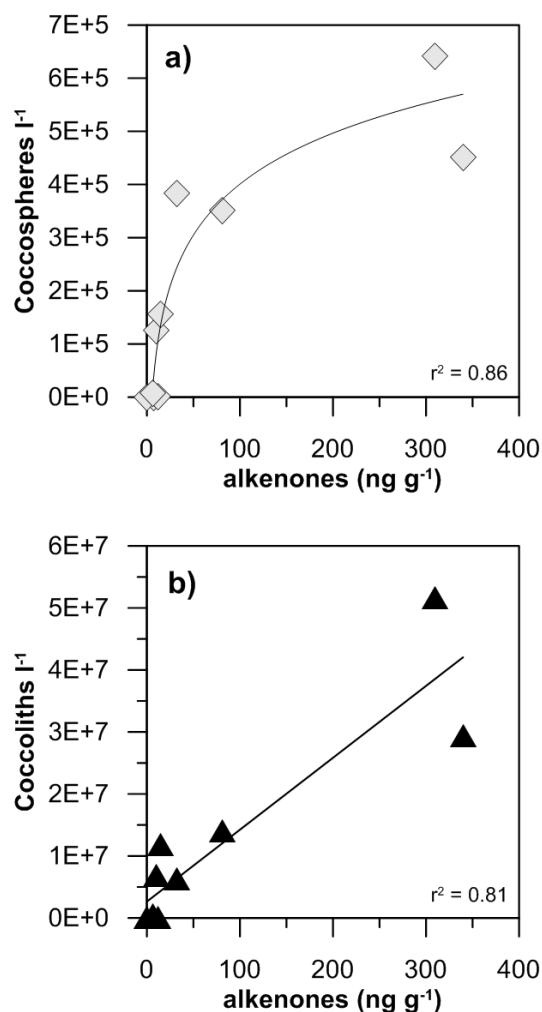


Figure 5.8: Correlation of alkenone concentrations in surface sediments with a) maximum coccosphere counts and b) the sum of coccolith counts in the upper 150 m water column at the same sites (Saavedra-Pellitero et al., 2014).

5.5.3.2 GDGT-based temperatures

At present, TEX₈₆ has mostly been used as a SST proxy, despite evidence that Thaumarchaeota occur throughout the water column and are often most abundant in subsurface waters (e.g. Karner et al., 2001; Pearson and Ingalls, 2013; Hurley et al., 2016). Here, we used the global TEX₈₆ calibration of Kim et al. (2010) that was previously suggested to yield reasonable temperature estimates for the Pacific SO (Ho et al., 2014). TEX₈₆-based temperatures range from 3.0 to 15.6°C in our study area (Fig. 5.6), and TEX₈₆ values display a strong linear correlation with WOA09 annual mean SST (0 m) over the same temperature range ($r^2 = 0.82$; Fig. 5.9 a). The correlation of TEX₈₆ with SST (0 m) is not fundamentally different from that with depth-integrated annual mean temperature for 0-200 m water depth ($r^2 = 0.81$; Fig. 5.9 b). In addition, we applied the modified TEX₈₆^L and TEX₈₆^H indices that were recalibrated for

subsurface (0-200 m) temperatures (Kim et al., 2012a; Kim et al., 2012b). The $\text{TEX}_{86}^{\text{L}}$ was recommended for application in polar oceans (i.e. SST $<10^{\circ}\text{C}$), where changes in TEX_{86} are relatively minor with temperature (Kim et al., 2010). Indeed, $\text{TEX}_{86}^{\text{L}}$ -derived subsurface temperature reconstruction for a sediment core from the Antarctic continental margin yielded warm temperatures that could be explained by intrusion of warm, nutrient-rich Modified Circumpolar Deep Water (MCDW) onto the shelf (Kim et al., 2012a). Applied to our surface sediments, the $\text{TEX}_{86}^{\text{L}}$ calibration systematically overestimated temperatures (Fig. 5.6) leading to large residuals especially at the lower temperature end ($<10^{\circ}\text{C}$; Fig. A 5.4 b), despite the strong correlation of $\text{TEX}_{86}^{\text{L}}$ with depth-integrated annual mean WOA09 temperature for 0-200 m water depth ($r^2 = 0.84$). The cold-biased temperatures observed at four shallow sites close to New Zealand (Fig. A 5.4 b) may relate to the influence of the Southland Current, which is transporting fresh subantarctic water (SAW) along the south-east coast of New Zealand (Sutton, 2003). Alternatively, coastal upwelling may transport archaea from deeper waters to the surface. This cold bias is observed in all TEX_{86} -derived temperature estimates, although less pronounced (Fig. A 5.4).

A systematic offset is observed between our TEX_{86} -SST relationship and that of the global calibration (black dashed line in Fig. 5.9 a), revealing a tendency to underestimate temperatures at the warmer sites ($>10^{\circ}\text{C}$) and overestimate temperatures at the cold sites ($<8^{\circ}\text{C}$). These apparently non-random residual patterns are shown in all existing global calibrations (Kim et al., 2010; Ho et al., 2014; Tierney and Tingley, 2014). A closer inspection of these latitudinal differences in TEX_{86} -derived temperatures suggests seasonal differences in the temperature signal shifting from winter in the SE-Pacific to summer in the PFZ and AZ, which is in general contrast to alkenone-derived SST (Fig. 5.6). The diverging TEX_{86} -SST relationship in different oceanographic regimes may result from a combination of factors. While intense diatom and haptophyte blooms are recorded for spring and summer in the SO, an ‘out-of-phase’ seasonal preference towards archaeal winter production is suggested to relate to the availability of ammonia that is generated by phytoplankton biomass decay (Murray et al., 1998; Manganelli et al., 2009; Lopes dos Santos et al., 2013). Alternatively, TEX_{86} -derived temperatures may preferably represent a subsurface temperature signal (Fig. 5.6). On the other hand, warm SST residuals observed in the PFZ/AZ may indicate a preference towards summer production. Here, TEX_{86} temperature estimates yield similar warm values as U_{37}^{K} -based SST using the polar calibration of Sikes et al. (1997), and also show a good consensus with SST estimates based on diatom assemblages (Esper and Gersonde, 2014; Fig. A 5.3). Surface sediment data

represent an integrated temperature signal of the entire water column and different seasons, which may vary as a function of the regional oceanographic regime. It is therefore difficult to unravel the effect of subsurface GDGT export and to target a specific depth origin of GDGTs that can be used for the calibration, especially in the polar ocean where seasonal SST variations are small (1-2°C). In addition, temperature differences between surface and subsurface are only minor in the PFZ/AZ (0-0.6°C). Our data suggest a generally flatter temperature gradient for the Pacific SO than that predicted by the global calibration. A compilation of presently available TEX₈₆ data from the Pacific SO confirms this (Fig. A 5.5).

A major bias for TEX₈₆ may be related to high terrestrial OM input or contribution of GDGT from alternative sources (e.g. Pearson and Ingalls, 2013; Schouten et al., 2013). As already stated, BIT-index values are generally low (≤ 0.1) suggesting that TEX₈₆ was not affected by soil OM input. Moreover, the GDGT distribution in all surface sediments is typical for open ocean settings suggesting that the TEX₈₆ signal is not affected by elevated GDGT input from sedimentary archaea involved in methane cycling (Zhang et al., 2011). GDGTs, as all other biomarkers, are subjected to diagenesis, which could potentially alter the distribution and thus TEX₈₆ values. Although a substantial amount of GDGTs is lost due to oxic degradation, no significant effect on the TEX₈₆ has been reported to date (Huguet et al., 2009; Kim et al., 2009; Yamamoto et al., 2012). However, recent studies indicate that non-thermal effects, including physiology and nutrient state, might have a strong control on individual TEX₈₆ records (Elling et al., 2014; Qin et al., 2015; Hurley et al., 2016). Polar regions may for instance support archaeal communities with fundamentally different GDGT compositions for a given temperature relative to other regions (Huguet et al., 2013). Indeed, archaeal groups were found to reveal a high diversity in Antarctic circumpolar deep waters (Alonso-Sáez et al., 2011), and Thaumarchaeota were even detected in Antarctic sea ice, where they represented more than 90% of the archaeal population (Cowie et al., 2011). Therefore, a better understanding of the potential impact of non-thermal effects, such as the ecophysiology of archaea in high latitude settings on the TEX₈₆ is needed.

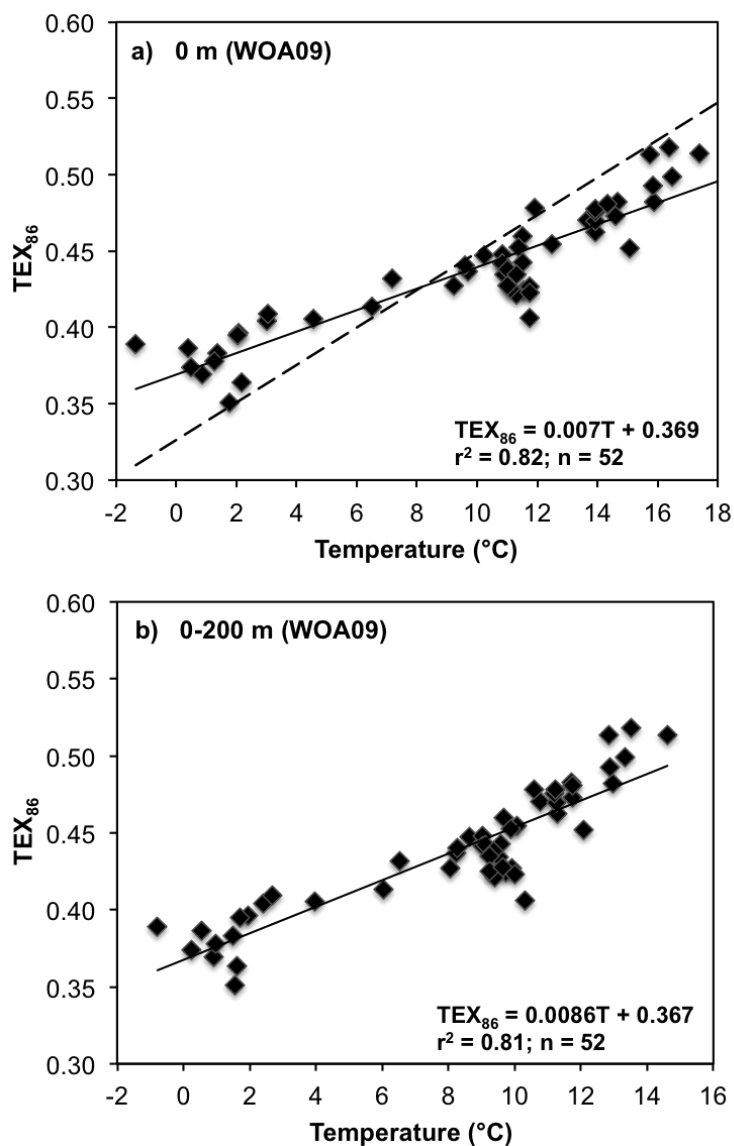


Figure 5.9: Correlation of TEX₈₆ values with a) SST and b) depth-integrated annual mean WOA09 temperature for 0-200 m water depth (Locarnini et al., 2010). Black dashed line denotes the global regression for TEX₈₆ (Kim et al., 2010).

5.5 Summary and Conclusions

In this study, we presented new findings based on different marine and terrigenous molecular proxies, which reveal a high potential for detailed paleo-environmental reconstructions in the Pacific sector of the SO. We estimated terrestrial OM deposition in surface sediments by quantifying the concentration and ²³⁰Th-normalized burial of long-chain *n*-alkanes and brGDGTs that were highest close to the potential source regions in New Zealand and Australia. The spatial distribution and the strong correlation observed between our organic and inorganic terrigenous proxies suggest similar origin and transport mechanisms, i.e. primarily eolian by

prevailing westerly winds. Besides a possible fertilizing effect on phytoplankton growth, dust may play a direct role in regulating export of biogenic material (i.e. alkenones and isoGDGTs) via the ballast effect. However, highest isoGDGT burial observed south of the APF may be largely controlled by the decay of diatoms and related opal flux. Comprehensive paleo-SST records from the (sub-)polar Southern Hemisphere are still sparse, which is mainly due to difficult access to these remote ocean areas and highly corrosive waters. Application of $U_{37}^{K'}$ and TEX_{86} temperature proxies in our surface sediments suggests robust relationships between both indices with temperature in the subpolar and polar Pacific SO. Especially, $U_{37}^{K'}$ -based SST estimates using the polar calibration of Sikes et al. (1997) faithfully reflect modern summer SST in the whole study area. In contrast, TEX_{86} -derived temperatures may reflect a subsurface signal rather than surface. Warm temperature residuals observed in the polar ocean may additionally relate to non-thermal effects, such as archaeal ecophysiology, impacting individual TEX_{86} records. Therefore, comprehensive water column studies combining molecular biological and geochemical methods are needed for the Pacific SO.

Acknowledgements

We would like to thank chief scientists, crews, and participants of R/V *Polarstern* (ANT-XXVI/2) and R/V *Sonne* (SO213) for their support. We are grateful to Ralf Tiedemann for providing surface sediments for this study. We thank Samuel Albani for sharing his latest dust model data. Kirsten Fahl and Walter Luttmer are thanked for precious lab support. We acknowledge financial support for this work through the AWI Helmholtz-Zentrum für Polar- und Meeresforschung and the MARUM-Center for Marine Environmental Sciences. TAR was funded by DFG SPP1158 project RO5057/1-1. We thank the associate editor Elizabeth Canuel and three anonymous reviewers for their constructive comments, which greatly improved the quality of this manuscript.

APPENDIX A. Supplementary Data

Supplementary data associated with this article can be found in the online version. The data discussed in this publication are archived at PANGAEA (<https://doi.pangaea.de/10.1594/PANGAEA.860666>).

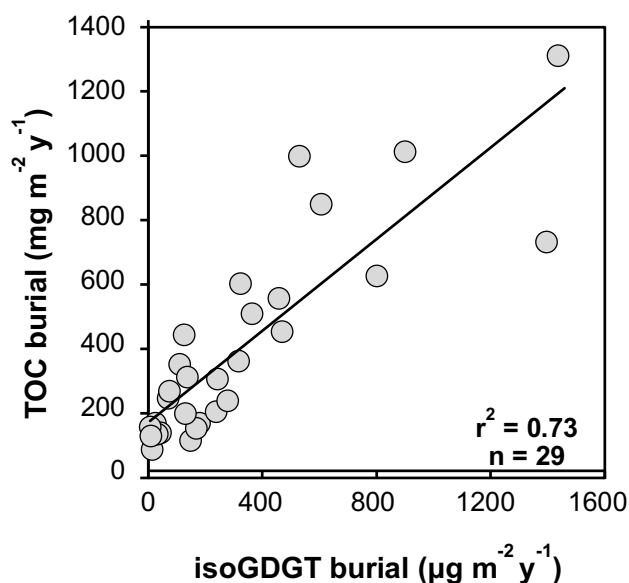


Figure A 5.1: Correlation of isoGDGT burial with TOC burial in surface sediments of the Pacific sector of the SO.

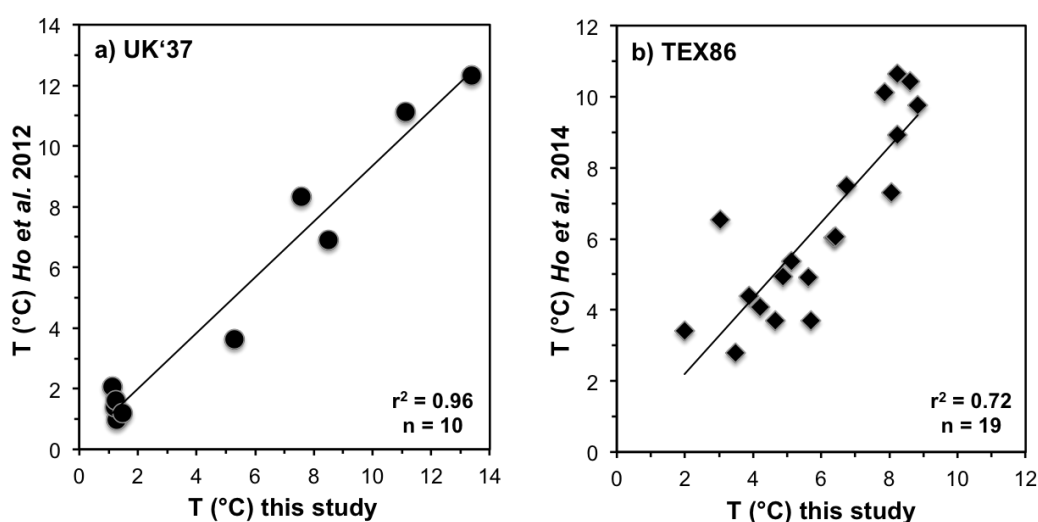


Figure A 5.2: Comparison of a) U_{37}^K - and b) TEX_{86} -derived temperature estimates with those from Ho et al. (2012; 2014) analyzed from the same set of samples (Gersonde, 2011). Differences between each dataset are well within the range reported from interlaboratory comparisons for U_{37}^K (Rosell-Melé et al., 2001) and TEX_{86} (Schouten et al., 2009; Schouten et al., 2013b).

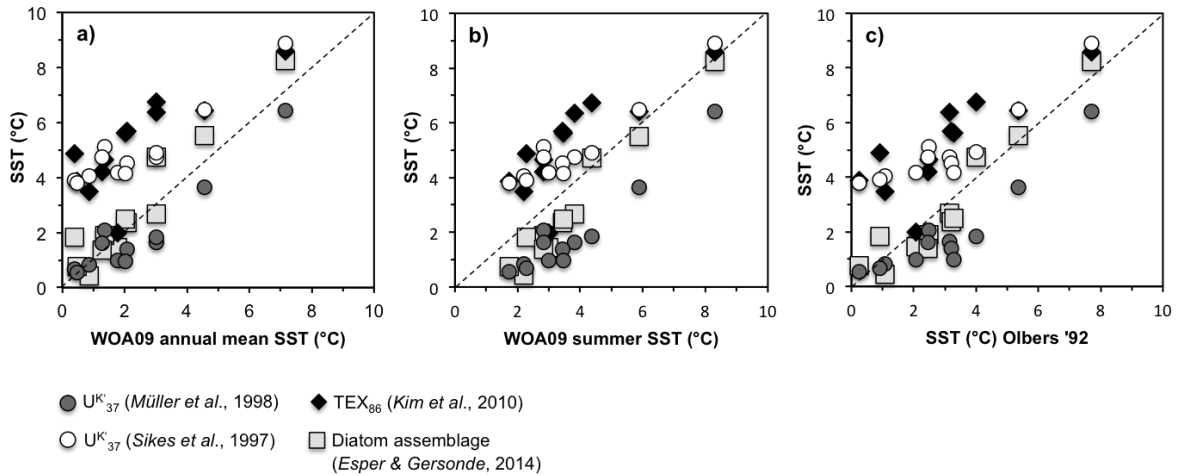
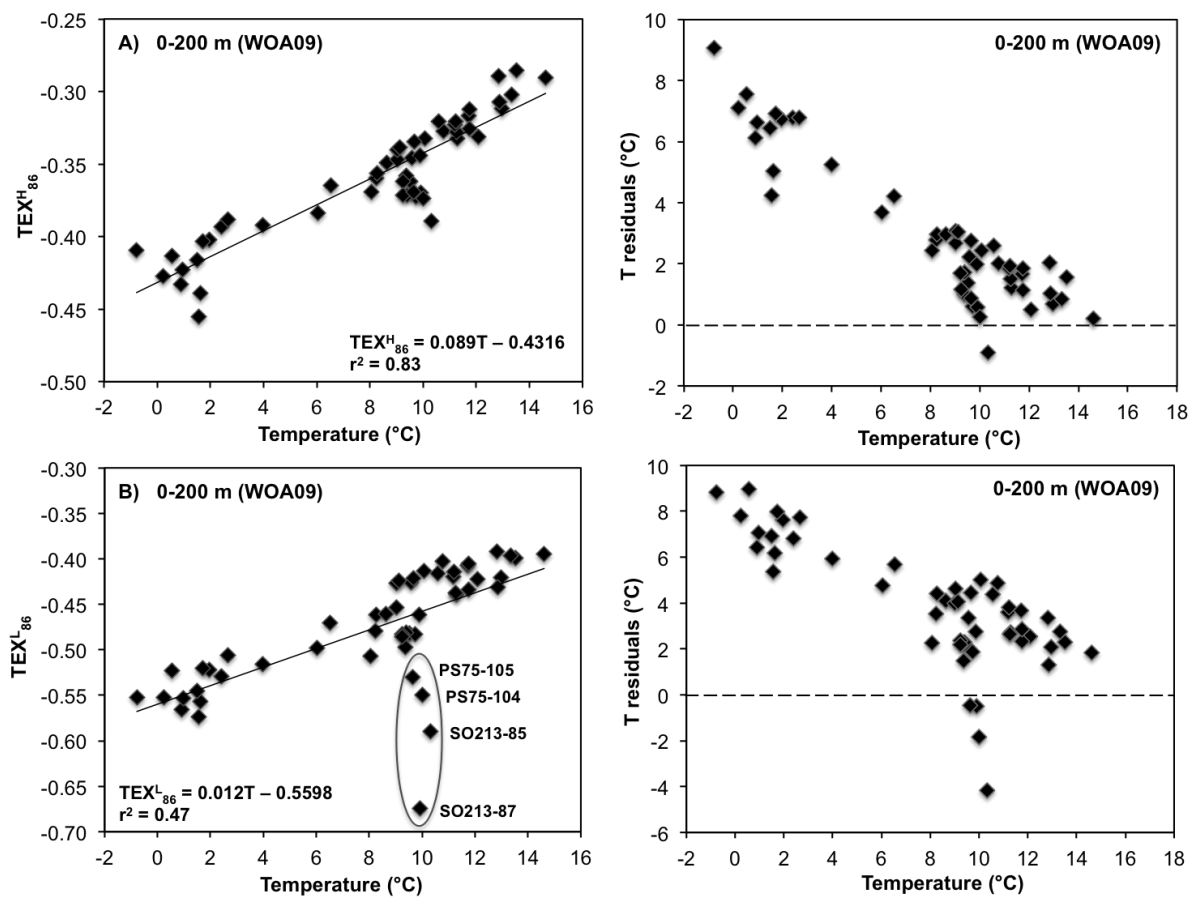


Figure A 5.3: Comparison of SST estimates based on U_{37}^K and TEX_{86} as well as diatom assemblages obtained from the same surface sediments of the Pacific SO (Esper and Gersonde, 2014) with WOA09 a) annual mean, b) summer SST (Locarnini et al., 2010), and c) SST based on Olbers et al. (1992). Dashed line indicates 1:1 line.



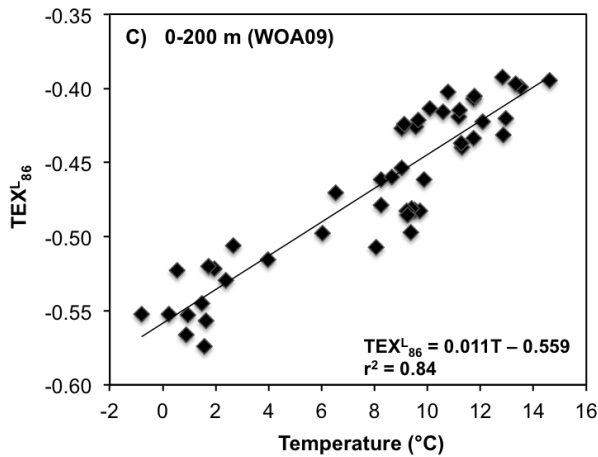


Figure A 5.4: Correlation of TEX_{86} values with depth-integrated annual mean WOA09 temperature for 0-200 m water depth (Locarnini et al., 2010). a) $\text{TEX}_{86}^{\text{H}}$ b) $\text{TEX}_{86}^{\text{L}}$ c) $\text{TEX}_{86}^{\text{L}}$ with exclusion of data from the sites located close to New Zealand (Fig. A 4 b). Residuals of temperature estimates are derived from the global core-top calibrations for TEX_{86} (Kim et al., 2012a; Kim et al., 2012b).

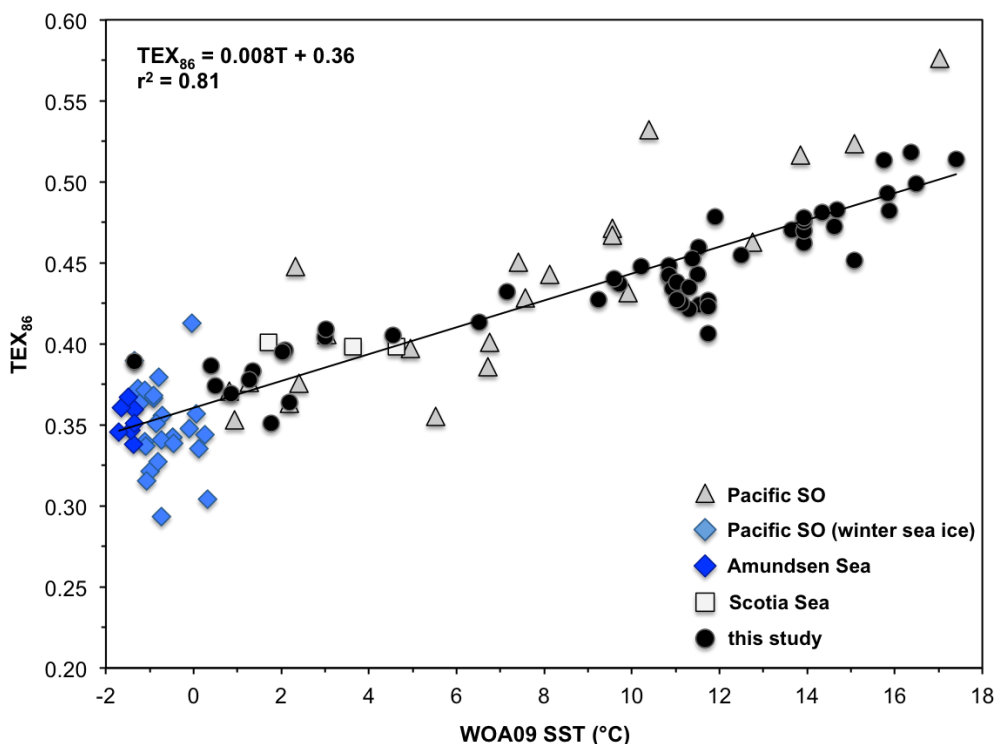


Figure A 5.5: Relationship of TEX_{86} with SST in the Pacific SO derived from the global core top calibration (Kim et al., 2010). Data are derived from Ho et al., (2011; 2014) and Kim et al., 2010). TEX_{86} data from the Antarctic Peninsula are excluded as they may imply a spatially local impact on the TEX_{86} -temperature relationship.

Table A 5.1: Pearson correlation coefficients and p -values (in italic) between variables (n=16) in surface sediments (n=49) of the Pacific SO. Significant correlations ($p \leq 0.005$) are highlighted in bold.

| | Lat | Long | Depth | TOC | TC | TN | C/N | n-alkanes | CPI | ACL | brGDGTs | BIT | isoGDGTs | alkenones | UK'37 | TEX86 |
|------------------|--------------|--------------|--------------|--------------|--------------|--------------|-------------|-------------|--------------|-------------|-------------|--------------|--------------|-------------|-------------|-------------|
| Lat | | <i>0.06</i> | <i>0.01</i> | 0.00 | 0.00 | 0.00 | 0.00 | <i>0.07</i> | <i>0.03</i> | <i>0.73</i> | <i>0.87</i> | 0.00 | 0.00 | <i>0.29</i> | 0.00 | 0.00 |
| Long | 0.27 | | 0.00 | <i>0.56</i> | <i>0.89</i> | <i>0.79</i> | <i>0.58</i> | 0.00 | 0.00 | <i>0.08</i> | 0.00 | <i>0.93</i> | <i>0.67</i> | 0.00 | <i>0.34</i> | <i>1.00</i> |
| Depth | -0.36 | -0.68 | | <i>0.06</i> | <i>0.13</i> | <i>0.05</i> | <i>0.47</i> | <i>0.24</i> | <i>0.07</i> | <i>0.80</i> | <i>0.00</i> | <i>0.97</i> | <i>0.90</i> | 0.00 | <i>0.05</i> | <i>0.44</i> |
| TOC | -0.61 | -0.09 | 0.27 | | 0.00 | 0.00 | <i>0.74</i> | <i>0.71</i> | <i>0.01</i> | <i>0.89</i> | <i>0.16</i> | <i>0.06</i> | 0.00 | <i>0.35</i> | 0.00 | 0.00 |
| TC | 0.66 | 0.02 | -0.22 | -0.82 | | 0.00 | <i>0.02</i> | <i>0.03</i> | 0.00 | <i>0.14</i> | <i>0.01</i> | <i>0.05</i> | 0.00 | <i>0.14</i> | 0.00 | 0.00 |
| TN | -0.75 | -0.04 | 0.28 | 0.88 | -0.92 | | <i>0.01</i> | <i>0.46</i> | 0.00 | <i>0.49</i> | <i>0.04</i> | <i>0.01</i> | 0.00 | <i>0.26</i> | 0.00 | 0.00 |
| C/N | 0.40 | -0.08 | -0.10 | 0.05 | 0.33 | -0.38 | | <i>0.44</i> | <i>0.03</i> | <i>0.29</i> | <i>0.21</i> | <i>0.11</i> | <i>0.05</i> | <i>0.57</i> | 0.00 | 0.00 |
| n-alkanes | 0.26 | 0.45 | -0.17 | 0.05 | -0.31 | 0.11 | -0.11 | | <i>0.07</i> | 0.00 | 0.00 | <i>0.04</i> | <i>0.93</i> | <i>0.01</i> | <i>0.11</i> | <i>0.39</i> |
| CPI | -0.32 | 0.48 | -0.26 | 0.35 | -0.51 | 0.49 | -0.32 | 0.27 | | <i>0.29</i> | <i>0.00</i> | <i>0.07</i> | 0.00 | 0.00 | 0.00 | 0.00 |
| ACL | 0.05 | 0.25 | -0.04 | 0.02 | -0.21 | 0.10 | -0.15 | 0.43 | 0.15 | | <i>0.46</i> | <i>0.75</i> | <i>0.83</i> | <i>0.09</i> | <i>1.00</i> | <i>0.91</i> |
| brGDGTs | 0.02 | 0.46 | -0.40 | 0.20 | -0.39 | 0.29 | -0.18 | 0.53 | 0.40 | 0.11 | | <i>0.01</i> | <i>0.05</i> | 0.00 | <i>0.92</i> | <i>0.31</i> |
| BIT | 0.65 | 0.01 | 0.01 | -0.27 | 0.28 | -0.36 | 0.23 | 0.29 | -0.26 | 0.05 | 0.36 | | 0.00 | <i>0.52</i> | 0.00 | 0.00 |
| isoGDGTs | -0.70 | 0.06 | -0.02 | 0.65 | -0.67 | 0.73 | -0.28 | -0.01 | 0.48 | -0.03 | 0.28 | -0.49 | | <i>0.28</i> | 0.00 | 0.00 |
| alkenones | 0.15 | 0.67 | -0.55 | 0.14 | -0.21 | 0.16 | -0.08 | 0.36 | 0.53 | 0.24 | 0.68 | 0.09 | 0.16 | | <i>0.78</i> | 0.00 |
| UK'37 | 0.97 | 0.14 | -0.28 | -0.59 | 0.64 | -0.76 | 0.42 | 0.23 | -0.40 | 0.00 | 0.01 | 0.70 | -0.70 | 0.04 | | 0.00 |
| TEX86 | 0.90 | 0.00 | -0.11 | -0.58 | 0.65 | -0.75 | 0.44 | 0.13 | -0.47 | -0.02 | -0.15 | 0.59 | -0.73 | -0.05 | 0.91 | |

6 Glacial reduction and millennial-scale variations in Drake Passage throughflow

F. Lamy¹, H.W. Arz², R. Kilian^{3,4}, C.B. Lange⁵, L. Lembke-Jene¹, **M. Wengler**¹, J. Kaiser², O. Baeza Urrea³, I.R. Hall⁶, N. Harada⁷ & R. Tiedemann¹

¹Alfred-Wegener-Institut Helmholtz-Zentrum für Polar- und Meeresforschung, Bremerhaven, Germany.

²Leibniz Institute for Baltic Sea Research, Rostock-Warnemünde, Germany

³Geologie, Fachbereich Raum- und Umweltwissenschaften, Universität Trier, Trier, Germany

⁴Instituto de la Patagonia, Universidad de Magallanes, Chile

⁵Department of Oceanography and Center for Oceanographic Research in the eastern South Pacific (COPAS), COPAS Sur-Austral Program, University of Concepción, Chile

⁶School of Earth and Ocean Sciences, Cardiff University, Cardiff, CF10 3AT, United Kingdom

⁷Research and Development Center for Global Change, Japan Agency for Marine-Earth Science and Technology, 2-15 Natsushimacho, Yokosuka 237-0061, Japan

Published in *Proceedings of the National Academy of Sciences of the United States of America*

Abstract

The Drake Passage (DP) is the major geographic constriction for the Antarctic Circumpolar Current (ACC) and exerts a strong control on the exchange of physical, chemical, and biological properties between the Atlantic, Pacific, and Indian ocean basins. Resolving changes in the flow of circumpolar water masses through this gateway is therefore crucial for advancing our understanding of the Southern Ocean's role in global ocean and climate variability. Here, we reconstruct changes in DP throughflow dynamics over the past 65,000 years based on grain size and geochemical properties of sediment records from the southernmost continental margin of South America. In combination with published sediment records from the Scotia Sea, we argue for a considerable total reduction of DP transport and reveal an up to ~40% decrease in flow speed along the northernmost ACC pathway entering the DP during glacial times. Superimposed on this long-term decrease are high-amplitude millennial-scale variations, which parallel Southern Ocean and Antarctic temperature patterns. The glacial intervals of strong weakening of the ACC entering the DP imply an enhanced export of northern ACC surface and intermediate waters into the South Pacific Gyre and reduced Pacific-Atlantic exchange *via* the DP ("cold-water route"). We conclude that changes in DP throughflow play a critical role for the global meridional overturning circulation and interbasin exchange in the Southern Ocean, most likely regulated by variations in the westerly wind field and changes in Antarctic sea-ice extent.

Significance Statement

The Drake Passage (DP) represents the most important oceanic gateway along the pathway of the world's largest current, the Antarctic Circumpolar Current (ACC). Resolving changes in the flow of circumpolar water masses through the DP is crucial for advancing our understanding of the Southern Ocean role in affecting ocean and climate change on a global scale. We reconstruct current intensity from marine sediment records around the southern tip of South America with unprecedented millennial-scale resolution covering the past ~65,000 years. For the last glacial period, we infer intervals of strong weakening of the ACC entering the DP implying an enhanced export of northern ACC surface and intermediate waters into the South Pacific Gyre and reduced Pacific-Atlantic exchange *via* the "cold-water route".

Main text

The Antarctic Circumpolar Current (ACC) is the world's largest current system. Through inducing pronounced upwelling and formation of new water masses, the ACC fundamentally affects the global meridional overturning circulation (Marshall and Speer, 2012) and the stability of Antarctica's ice sheets. The flow of the ACC is largely driven by strong westerly winds and is constricted to its narrowest extent in the Drake Passage (DP). This so-called "cold water route" transport through the DP is one important pathway for the return of fresh and cold waters to the Atlantic, which strongly affects the strength of the Atlantic meridional overturning circulation, in concert with the "warm water route" inflow of warm and salty Indian Ocean water masses through the Agulhas Current system (Gordon, 1986; Beal et al., 2011).

The DP is ~800 km wide and is located between Cape Horn and the western Antarctic Peninsula (Fig. 6.1). Numerous hydrographic surveys across the DP since the 1970s have contributed to the understanding of year-long and inter-annual variability in ACC transport through the DP and the mechanisms forcing physical and biological changes within the Southern Ocean (Cunningham et al., 2003; Meredith et al., 2011). However, even with hydrographic time-series reaching back 20 years (Koenig et al., 2014) in this well-constrained region of the ACC and more sophisticated model simulations (Meijers, 2014), important issues such as the role of zonal winds in forcing ACC transport remain controversial.

Compared to other parts of the Southern Ocean, the modern oceanography of the ACC within the DP is well monitored. The three major ACC oceanographic fronts (Orsi et al., 1995), the Subantarctic Front (SAF), the Polar Front (PF), and the Southern ACC Front (SACCF), can be identified from north to south within the DP. The exact location and occurrence of subsidiary fronts changes from year to year and strongly affects the current velocity pattern across the DP (Sokolov and Rintoul, 2009; Renault et al., 2011; Koenig et al., 2014) (Fig. 6.2 B). The modern winter sea-ice margin presently does not extend significantly north into the DP (Comiso, 2003). The total ACC volume transported through the DP is estimated between ~130 and 150 Sv (Cunningham et al., 2003; Meredith et al., 2011; Renault et al., 2011; Koenig et al., 2014). The many oceanographic studies robustly show that more than half of the total DP transport occurs at and north of the SAF (i.e., in the Subantarctic Zone), followed by the Polar Frontal Zone (between SAF and PF) (Fig. 6.2 A). The relative contribution of DP transport south of the PF is generally less than 20%.

Available proxy data and model simulations provide only little information on the potential role of the DP region in driving changes in the global ocean circulation at glacial-interglacial and millennial time-scales (Knorr and Lohmann, 2003; McCave et al., 2014). Downstream of the DP, a meridional section of low-resolution records from the Scotia Sea revealed little overall bottom current speed variations between the Last Glacial Maximum *sensu lato* (LGM, 18-28 thousand years ago) and the Holocene (McCave et al., 2014). In contrast, a 500,000-year record from the southern Indian Ocean (eastward from the Crozet-Kerguelen Plateau) suggests that the ACC was weak during warm stages and strong during glacial epochs (Mazaud et al., 2010). Likewise in the southwest Pacific, the deep western boundary current east of New Zealand intensified during glacial periods over the past 1.2 million years (Hall et al., 2001), which has been related to a northward extension of the ACC along the New Zealand continental margin (Weaver et al., 1998; Hall et al., 2001). Evidently, disagreement exists for ACC flow intensity and its potential impact on changes in DP throughflow, in response to glacial and interglacial cycles.

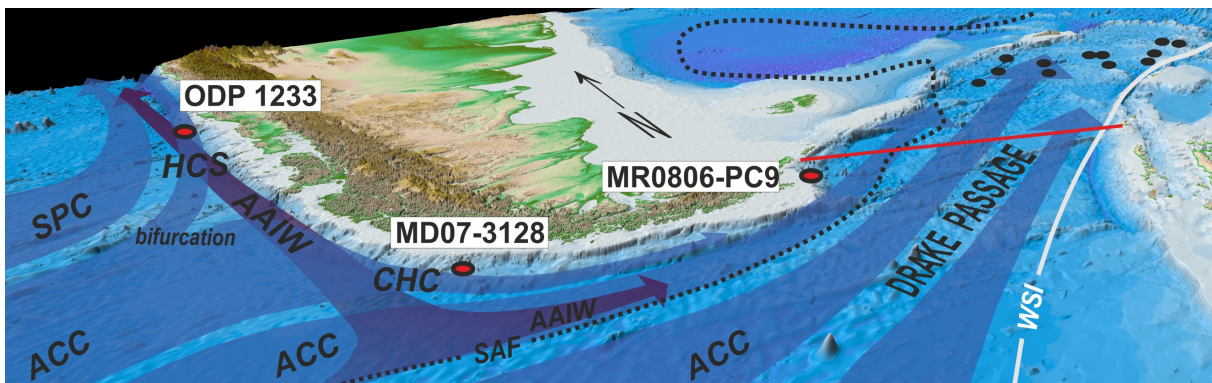


Figure 6.1: Schematic view of the Drake Passage region with major surface and intermediate water circulation, and location of sediment cores discussed (labeled red dots refer to own data, and unlabeled black dots indicate locations of cores in the Scotia Sea (McCave et al., 2014). Red line across the Drake Passage shows the oceanographic Jason track 104 (Koenig et al., 2014). ACC=Antarctic Circumpolar Current; SPC=South Pacific Current; HCS=Humboldt Current system; CHC=Cape Horn Current; AAIW=Antarctic Intermediate Water; SAF=Subantarctic Front; WSI=winter sea-ice; approximate locations after Orsi et al. (1995) and Comiso (2003).

Results and Discussion

Due to strong bottom currents and severe weather conditions, the recovery of sediment records directly within the DP is difficult. We therefore address changes in northern DP throughflow with high resolution sediment records recovered from the southernmost Chilean continental slope directly upstream of the DP (core MD07-3128; 52°39.57'S, 75°33.97'W; 1,032 m water depth), and from the Argentinian continental slope east of Cape Horn at the northern margin of the DP (core MR0806-PC09; 55°42.58' S, 66°08.06' W; 684 m water depth) (Fig. 6.1). Core MD07-3128 is located underneath the southward flowing Cape Horn Current (CHC), a northern branch of the ACC that continues towards the DP and provides a major fraction of the present day northern DP transport (Well and Roether, 2003). Satellite-tracked surface drifters reveal that, after crossing the East Pacific Rise, Subantarctic Surface water of the ACC is transported northeastward across the Southeast Pacific towards the Chilean coast at ~45°S/75°W (Chaigneau and Pizarro, 2005) (Figs. 6.1 and S 6.1). Here, presently only a minor part of ACC water is deflected northward into the Humboldt Current System whereas the major fraction is deviated southward towards the DP. The CHC thus transports a significant amount of northern ACC water towards the DP within a narrow belt of ~100-150 km width off the coast (Chaigneau and Pizarro, 2005) (Fig. S 6.1).

Site MD07-3128 provides a ~30 m long sediment core spanning the past ~65,000 years (Supporting Information). The age model (updated from Caniupán et al., 2011) is well constrained by radiocarbon dating, the occurrence of the Laschamp paleomagnetic excursion, and correlation to the well-dated sediment record from Ocean Drilling Program (ODP) Site 1233 (Kaiser and Lamy, 2010). High sedimentation rates during most of the glacial section (Fig. S 6.2) allow the investigation of CHC strength changes at millennial timescales, as an approximation of the northern ACC fraction of DP throughflow. Previous work on this core revealed substantial fluctuations of sea surface temperatures (SST) that largely follow the timing of temperature fluctuations observed in Antarctic ice cores (Caniupán et al., 2011). The lower-resolved, radiocarbon-dated core MR0806-PC09 (age model updated from Shiroya et al., 2013) is used to complement glacial-interglacial ACC strength estimates directly within the northern sector of the DP.

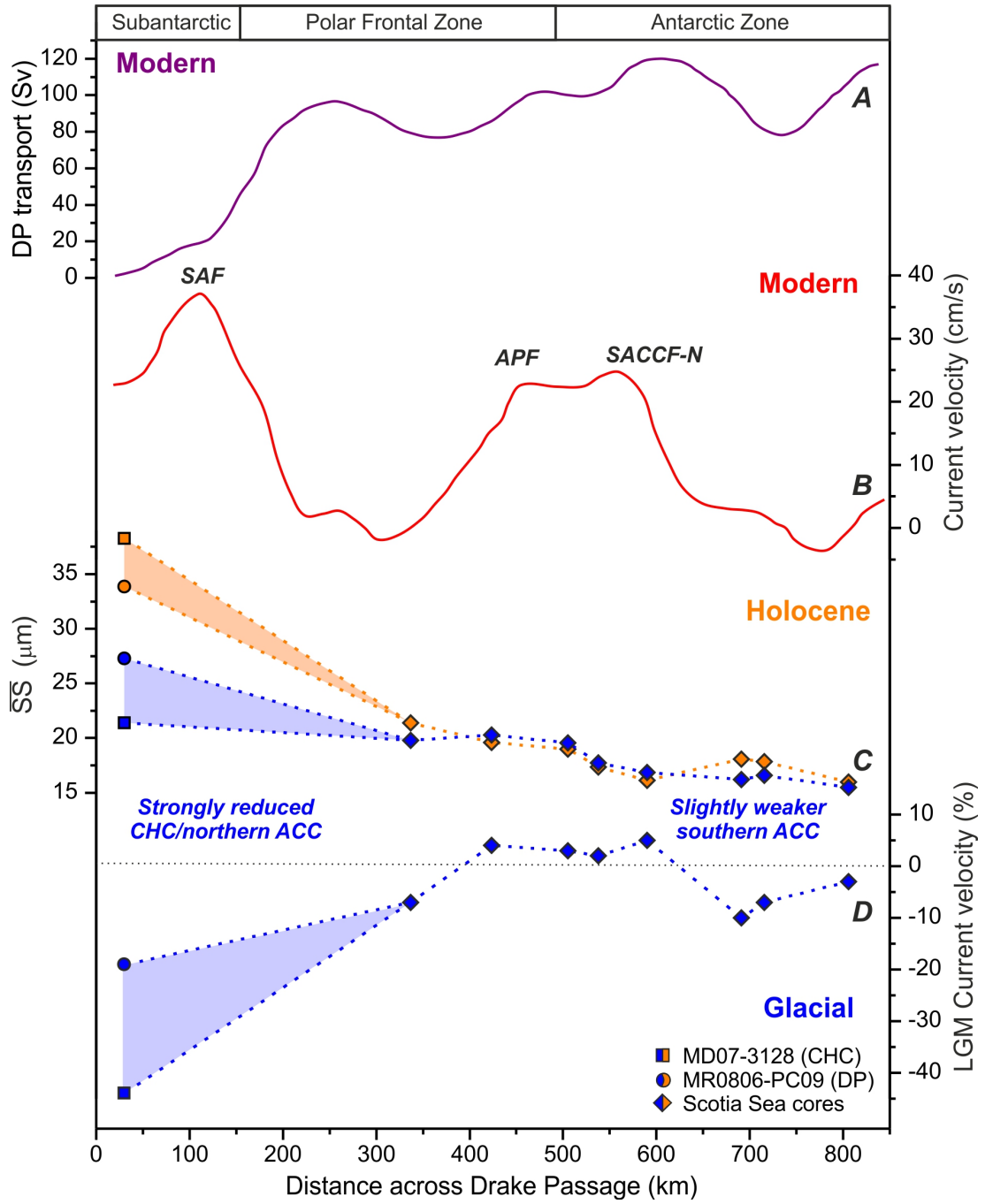


Figure caption is given on the next page.

Figure 6.2: Drake Passage throughflow during the Last Glacial Maximum compared to modern setting. (A) Modern DP cumulative volume transport above 3000 m water depth. Values are cumulated along DP Jason track 104 (Figs. 6.1 and S 6.1) from north to south. The volume transport is calculated from (B) across-track surface geostrophic velocities (Koenig et al., 2014). SAF=Subantarctic Front; APF=Antarctic Polar; SACCF-N=northern branch of southern ACC front (front positions based on the geostrophic velocities). (C) Holocene and Glacial (LGM *sensu lato*, 18,000–28,000 years ago) mean \overline{SS} data across the DP, including data south of the SAF in the Scotia Sea (McCave et al., 2014). Note that Holocene pattern reflect the northward increase in ACC flow across the DP. The location of each core was projected on the oceanographic Jason track 104 (Supporting Information). Error estimates ($2\sigma/\sqrt{n}$) are shown in Table S2. (D) Current speed changes (in %) during the LGM *sensu lato*. Compared to the Holocene, mean LGM values are lower by ~40% below the CHC and ~20% in the northern DP suggesting a substantial reduction of the subantarctic ACC contribution to DP throughflow.

Sedimentological and geochemical current strength proxies

In order to reconstruct variations in the CHC/northern ACC flow speed, we use changes in grain size and geochemical properties (Supporting Information). Our current strength proxies are the weight percent (wt.-%) of the 63 to 150 μm fine sand fraction and the mean sortable silt grain size (10 to 63 μm , \overline{SS}) of the terrigenous sediment fraction (Figs S 6.3 and S 6.4). The \overline{SS} proxy is commonly used for estimating relative changes in the near-bottom flow speed in deep-sea sediments (McCave et al., 1995). Modern surface current velocities within the CHC of >35 cm/s (Chaigneau and Pizarro, 2005) and high flow speeds of ~20 cm/s extending to mid-depths (Fig. S 6.1), as suggested by vertical current speed profiles in the CHC (Boisvert, 1969) and DP (Firing et al., 2011), reasonably explain the coarse grain size distributions observed during the Holocene (Figs S 6.3 and S 6.4). \overline{SS} data have been regionally calibrated with instrumental current meter data showing a linear relationship (McCave and Hall, 2006; Thornalley et al., 2013). The inference of flow intensity may be complicated by changes in sediment supply. Indeed, previous work at site MD07-3128 has shown that glacial sediments contain IRD (>150 μm) (Caniupán et al., 2011). Additional changes in sediment supply might be expected as the modern sediment depocenters in the proximal fjord systems become inactive with lower sea-level during glacials. However, the deposition of IRD at site MD07-3128 shows fluctuations that are independent of \overline{SS} and fine sand contents (Fig. S 6.3). Moreover, changes in \overline{SS} and the weight percent of the sortable silt component (SS %) are positively correlated, which is a strong

argument for primarily current controlled grain size changes within the silt fraction (McCave et al., 2014) (Fig. S 6.3).

Substantial changes in the geochemical composition of the sediments parallel grain size fluctuations at CHC site MD07-3128 (Fig. S 6.5). The different grain size and geochemical indicators show excellent correlations. Most notably, higher Zr/Rb and Si/Al ratios occur in the coarser grained intervals, as typical indicators for sediments affected by changes in current strength or eolian input (Chen et al., 2006). As biogenic opal contents are minor (1 to 4 wt-%), we interpret high Zr and Si contents to reflect coarser siliciclastic sediment components, whereas finer grained minerals including clay minerals are more Rb and Al-rich. Thus, ample changes in CHC strength and underlying water masses are revealed by the large grain size and sediment composition changes.

Evidence for a glacial reduction of DP transport

At site MD07-3128 below the CHC, the Holocene average SS grain size is $\sim 38 \mu\text{m}$. Using the latest calibration of \overline{SS} with North Atlantic current meter data (Thornalley et al., 2013), these \overline{SS} values translate to current speeds of $\sim 36 \text{ cm/s}$, consistent with modern velocity estimates within the CHC (Chaigneau and Pizarro, 2005). During the LGM, the average \overline{SS} is $\sim 21 \mu\text{m}$ indicating that the CHC strength was reduced by $\sim 40\%$ (Fig. 6.2 C, D). This strong decrease of flow speeds in the CHC implies a weakening of the northern (subantarctic) ACC limb entering the DP. This paleoceanographic inference is strongly supported by the geographic pattern of SST cooling in the South Pacific during the LGM (Fig. 6.3 and Table S 6.3). In the eastern subantarctic Pacific, the pronounced cooling of up to $\sim 7^\circ\text{C}$ is considerably larger than in the central subantarctic Pacific and implies a strong northward extension of the Antarctic cold-water influence in the Southeast Pacific during glacial conditions (Ho et al., 2012). The cold-water expansion decreases the back-flow of northern ACC water through the CHC to the DP but enhances its export into the South Pacific Gyre as indicated by the strong cooling observed in published SST records along the Humboldt Current system (Fig. 6.3 and Table S3). A similar northward extension of cold ACC waters occurred in the Southwest Pacific off New Zealand (Weaver et al., 1998; Nelson et al., 2000).

The reduction of northern (subantarctic) ACC flow as reconstructed from our CHC core MD07-3128, is also evident at our northern DP margin record (MR0806-PC09), which reveals $\sim 20\%$ finer \overline{SS} values (Fig. 6.2 C and D). The lower amplitude of the glacial-interglacial \overline{SS} change at this site might indicate an amplification of the signal within the CHC, for example

through variations in the vertical structure of the flow along the South American continental margin. However, the few available vertical current strength profiles from the CHC show that the high velocities reach down to >2000 m water depth (Boisvert, 1969) and we therefore do not expect large modifications of the vertical flow structure at our site since the last glacial. Alternatively, the northern DP record from core MR0806-PC09 might underestimate the glacial flow decrease because of the rather complex flow geometry with major eddy structures in this region (Renault et al., 2011; Ferrari et al., 2014; Koenig et al., 2014). Taken together, qualitatively, our two sediment core records uniformly document a substantial decrease in subantarctic CHC/ northern ACC flow speeds upstream and within the DP.

A more reliable quantification of the glacial flow speed decrease in the subantarctic section of the DP would require a more densely spaced core transect in the future. In order to obtain a more comprehensive view of last glacial changes in ACC flow in the vicinity of the DP, we combined our subantarctic ACC flow speed estimates upstream and within the DP with the published data from the central Scotia Sea downstream of the DP (McCave et al., 2014) (Figs. 6.1 and 6.2, and Table S 6.2). Together, these records extend across all major modern oceanographic zones within the ACC and DP. During the LGM, the combined \overline{SS} data indicate a strong reduction in flow speed in the northern sector (modern Subantarctic Zone) that extends to the present Polar Frontal Zone, whereas only minor changes occur south of the PF, except for a slight reduction in glacial ACC flow in the southern Antarctic Zone (Fig. 6.2). Modern oceanography suggests that current velocities and transport are overall closely linked in the DP region with the major transport and the highest current velocities occurring in the Subantarctic Zone (Fig. 6.2 B) (Meredith et al., 2011; Renault et al., 2011; Koenig et al., 2014). Therefore, we interpret our paleo-data in terms of a substantial LGM decrease of subantarctic DP throughflow combined with an additional slight reduction of ACC transport in the glacially extended sea-ice zone (McCave et al., 2014).

Today, Antarctic Intermediate Water (AAIW) formed in the Southeast Pacific is partly exported into the South Atlantic (Bostock et al., 2013). Strongly reduced CHC vigor and more sluggish DP transport during the LGM would plausibly decrease the export of Pacific surface and intermediate water masses into the South Atlantic and thus reduce the “cold-water route” contribution. Such glacial Southern Ocean circulation is in accordance with a stronger South Pacific gyre and the export of well-oxygenated AAIW along the Chilean margin (Muratli et al., 2009; Martínez-Méndez et al., 2013). Concurrently, proxy data indicate poorly ventilated intermediate waters in the glacial South Atlantic as contributions from the Pacific and Indian Oceans were reduced (Makou et al., 2010), consistent with reduced export from the major

modern intermediate water formation region in the Southeast Pacific through the DP (Fig. 6.1). Our suggested strongly enhanced glacial northward export of cold water masses to the tropical Pacific (Fig. 6.3) reinforces earlier modeling studies showing the importance of southerly-derived surface and intermediate water masses in the tropical Pacific for global cooling during the LGM (Liu et al., 2002).

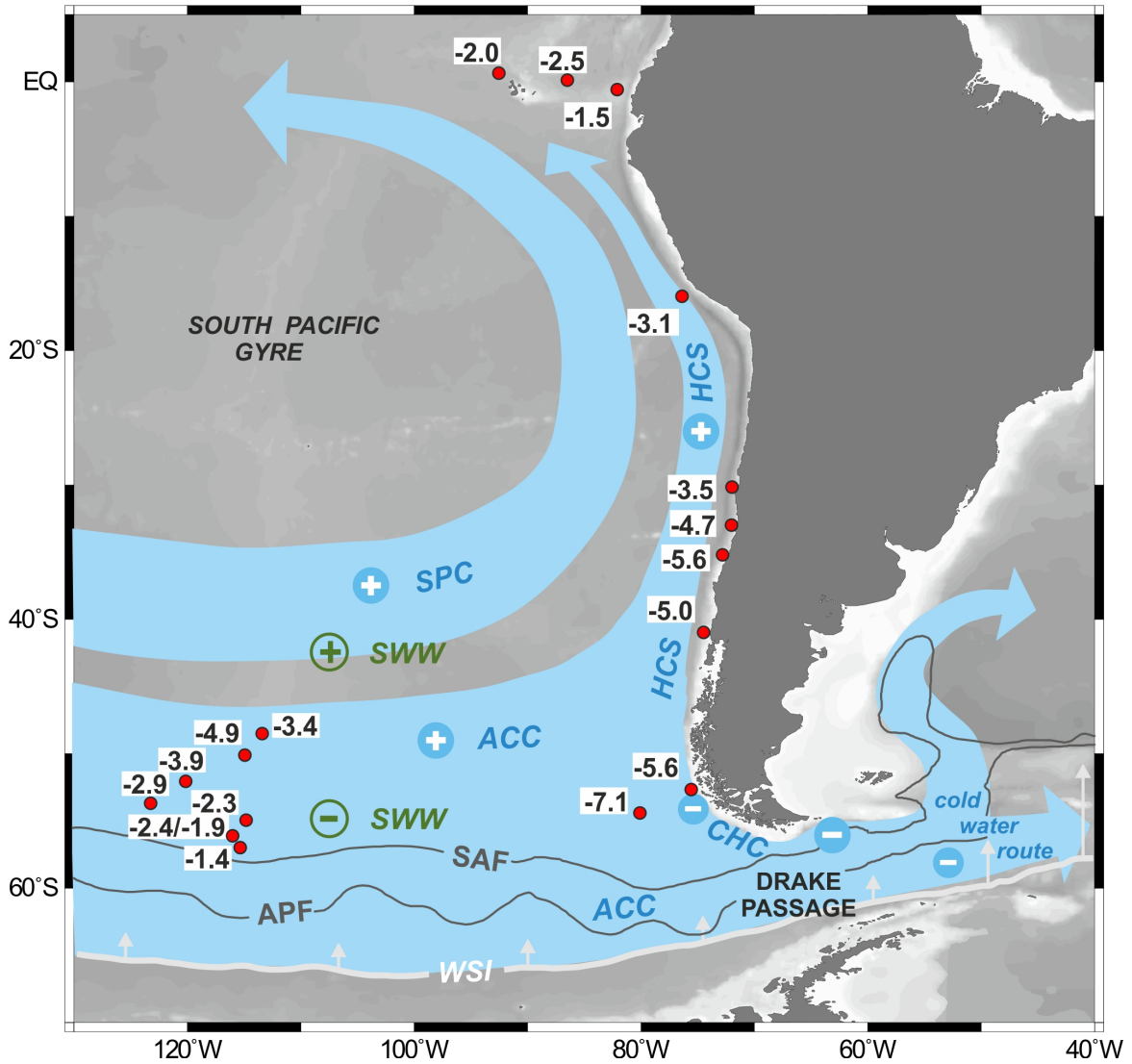


Figure 6.3: Map showing the Last Glacial Maximum paleoceanography of the Southeast Pacific and Drake Passage region. The pronounced glacial cooling in the eastern subantarctic Pacific is consistent with a northward extension of Antarctic cold-water influence (numbers indicate LGM cooling ($^{\circ}\text{C}$) compared to the Holocene mean, and red dots locations of SST sediment records; see Methods and Table S3). Reduced CHC and more sluggish glacial northern DP transport decreases the export of Pacific ACC water into the South Atlantic (“cold-water route”). Reduced SWW core and extended sea-ice diminish the wind forcing on the ACC and thus the DP transport. Stronger winds in the northern SWW enhance the South Pacific Gyre and the export of northern ACC water into the HCS. Background shows bathymetry. WSI=winter sea-ice; APF=Antarctic Polar Front; SAF=Subantarctic Front; modern locations after Orsi et al. (1995) and Comiso (2003). ACC=Antarctic Circumpolar Current; SPC=South Pacific Current; HCS=Humboldt Current system; CHC=Cape Horn Current; SWW=Southern Westerly Wind belt.

Millennial-scale variations during the last glacial

Superimposed on the long-term glacial reduction of DP throughflow, we observe prominent high-amplitude millennial-scale variability in the CHC/northern ACC flow speeds (Fig. 6.4), which is not resolved in the Scotia Sea records or any other previous ACC current strength record (Mazaud et al., 2010; McCave et al., 2014). Substantial changes in the geochemical sediment composition parallel these grain size fluctuations (Fig. S 6.5). Within age model uncertainties, most of the grain size maxima coincide with millennial-scale temperature maxima in Antarctica (EPICA Community Members, 2006) (Fig. 6.4), implying a strong sensitivity of the CHC and the northern ACC in the Southeast Pacific to suborbital climate variations. This pattern is particularly evident for the major Antarctic warmings that correspond to Heinrich stadials in Greenland (EPICA Community Members, 2006). Enhanced DP throughflow during these warm periods is consistent with the previously suggested impact of the bipolar seesaw mechanism on the Southern Ocean (Lamy et al., 2004; Barrows et al., 2007; Lamy et al., 2007; Anderson et al., 2009), leading to e.g. surface water warming, enhanced upwelling, and a stronger ACC due to southward shifted westerlies. The last millennial-scale increase in flow speeds at ~17.5 ka BP coincides with Heinrich Stadial 1, the beginning of Southern Ocean upwelling and the end of the last ice age on a global scale (Denton et al., 2010). The re-acceleration of subantarctic DP transport matches the major deglacial warming in the subantarctic Southeast Pacific and South Atlantic (Barker and Diz, 2014) (Fig. 6.4), suggesting a close coupling of DP throughflow to the initiation of Southern Hemisphere warming. Similar to the glacial-interglacial pattern, our inferred millennial-scale changes in DP throughflow are paralleled by SST changes in proxy records from the Southeast Pacific (ODP Site 1233) (Lamy et al., 2004; Kaiser and Lamy, 2010) extending north to the cold tongue in the eastern tropical Pacific (Lea et al., 2006) (Fig. 6.3). These data imply that substantial changes in the oceanographic dynamics of the South Pacific gyre are related to the northward deflection of ACC waters at millennial time scales.

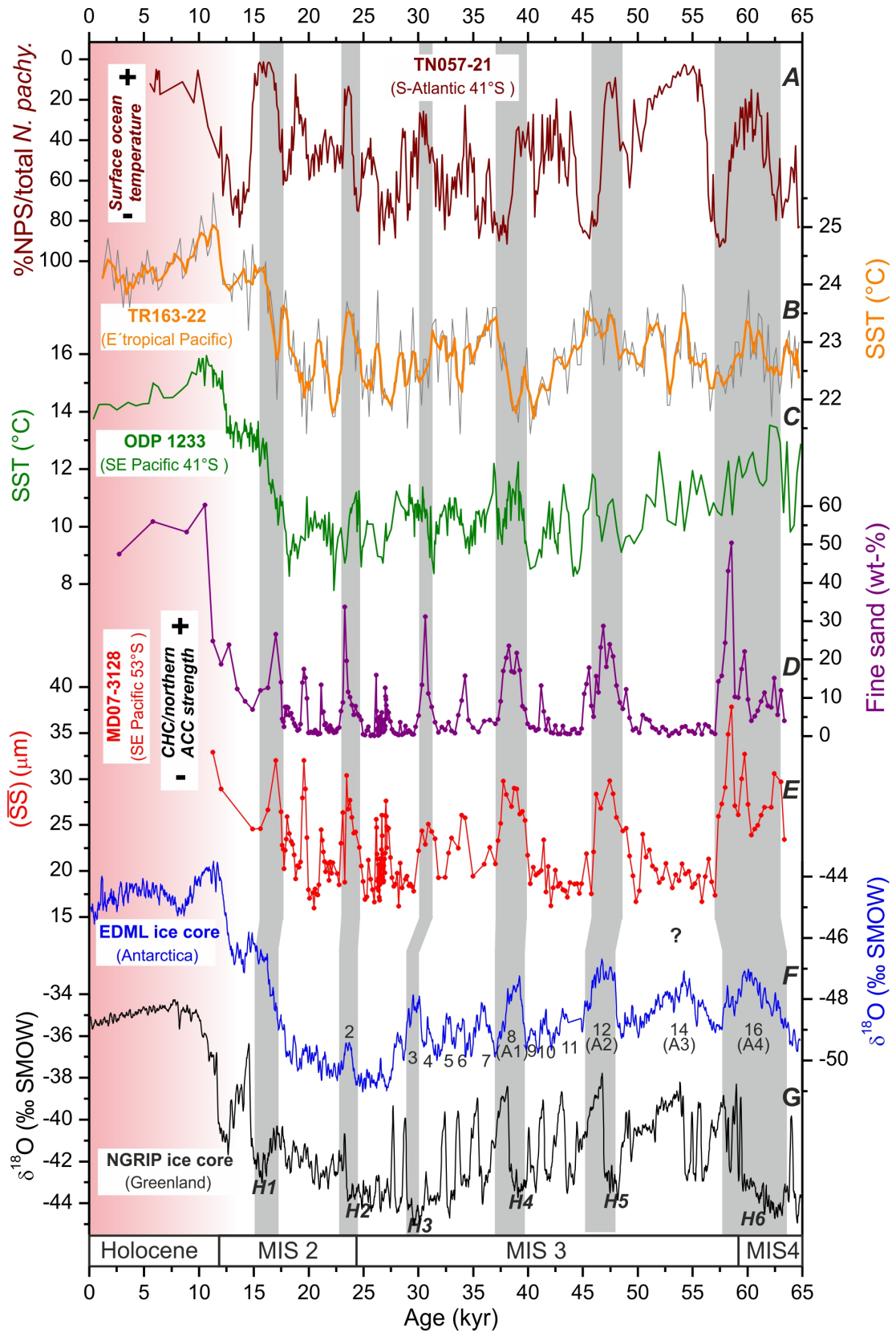


Figure caption is given on the next page.

Figure 6.4: Reconstructed changes in Cape Horn strength and Drake Passage throughflow compared to temperature records. *(A)* Ratio of planktic foraminifera *N. pachyderma* (sin.) to total *N. pachyderma* counts indicative of surface ocean temperature changes in the South Atlantic (Barker and Diz, 2014). *(B)* Mg/Ca SST record from the Galapagos region (Lea et al., 2006) representing eastern tropical Pacific SST changes. *(C)* Alkenone SST record from ODP Site 1233 located within the HCS at ~41°S (Kaiser and Lamy, 2010) (updated age-model, see Supporting Information). *(D, E)* Fine sand (63-150 μm) contents and $\overline{\text{SS}}$ as proxies for CHC/northern ACC strength. *(F)* Oxygen isotope record of the east Antarctic EDML ice core (EPICA Community Members, 2006) (AICC12 age scale). Numbers mark Antarctic Isotope Maxima, and largest Antarctic warmings A1 to A4. *(G)* Oxygen isotope record of the Greenland NGRIP ice-core (EPICA Community Members, 2006) (GICC05 age scale). H1-H6, Heinrich stadials. Vertical gray bars mark inferred millennial-scale DP throughflow peaks that correspond with millennial-scale temperature maxima in Antarctica and Heinrich stadials in Greenland. NPS=*N. pachyderma* (sin.)

Conclusions

Our study points to important changes of the “cold-water route” in the global meridional overturning circulation on both glacial-interglacial and millennial time scales through subantarctic DP transport, which generally weakens (increases) during cold (warm) climates. The glacial reduction of the “cold-water route” occurred in concert with the well-documented decrease of the “warm-water route” (Agulhas leakage (Beal et al., 2011)). We thus propose that both of these oceanographic corridors are critical for the South Atlantic contribution to glacial meridional overturning circulation strength changes.

Most oceanographic observations and models identify that variation in the position and strength of the southern westerly wind belt (SWW) impact changes in the strength of the ACC and DP throughflow (Völker and Köhler, 2013). This conceptual picture is consistent with our reconstructed glacial reduction of subantarctic DP throughflow being linked to a northward shift of the SWW, as supported by the majority of the proxy-based SWW reconstructions (Kohfeld et al., 2013). In particular, the reconstructions from southern South America indicate a substantial decrease of the westerly winds over their present core zone in the vicinity of the northern DP during colder intervals (Lamy et al., 2010). At the same time, stronger westerly winds extended northwards, as indicated by a variety of proxy records from the winter-rain zone of Chile (Latorre et al., 2007; Kohfeld et al., 2013) and are in line with our inferred

strengthening of the South Pacific gyre. In contrast to the proxy records pointing to a critical role of the SWW for DP throughflow and the global meridional overturning circulation during the past 65,000 years, current coupled ocean-atmosphere models do not show a coherent change in the position and strength of the SWW and the ACC during the LGM (Rojas et al., 2009; Sime et al., 2013). Hence, glacial ACC transport decreases might also be regulated by additional factors such as Southern Ocean sea ice extent that changes the effective wind stress acting on the ocean surface (McCave et al., 2014).

Though still hypothetical, important paleoceanographic changes in the subantarctic Southern Ocean are likely related to changes in the SWW. If applicable to modern time-scales, the strengthening and poleward shift of the SWW seen in the Coupled Model Intercomparison Project phase 5 (Meijers, 2014) might lead to a future increase in subantarctic DP transport, strengthening of the ACC and enhanced inter-basin exchange. However, recent instrumental volume transport time-series across the DP have not yet revealed any significant increase in response to strengthened westerly winds (Koenig et al., 2014). Thus, the response of the ACC to future climate changes remains a major challenge to be addressed.

Methods

We updated the published age models for cores MD07-3128 (Caniupán et al., 2011) and MR0806-PC09 (Shiroya et al., 2013) which are primarily based on radiocarbon dating. A detailed grain size analysis of the silt-fraction (2-63 μm) and the fine sand-fraction (63-150 μm) was performed by measurements with a Micromeritics SediGraph 5100 (Fig. S 6.3), a Coulter Counter, and a Beckman Coulter laser diffraction particle size analyzer. The glacial reduction of DP throughflow was calculated from the mean \overline{SS} values for the Holocene (0-11,500 years ago) and the LGM *sensu lato* (18,000-28,000 years ago). Geochemical data from core MD07-3128 were derived from discrete atomic absorption spectrophotometry (AAS) measurements on discrete samples and high resolution downcore scanning using an AVAATECH profiling X-ray Fluorescence (XRF) core scanner.

Acknowledgements

We thank the captain, crew, and scientific party of IMAGES R/V *Marion Dufresne* cruise MD159/PACHIDERME. We are grateful to V. Benz, C. Kissel, G. Knorr, G. Kuhn, N. McCave, and C. Purcell for discussions. We thank two anonymous reviewers for their constructive comments. R. Ahi, R. Fröhlking, and S. Wiebe provided technical support at AWI. We acknowledge financial support for this work through the Alfred-Wegener-Institut Helmholtz-Zentrum für Polar- und Meeresforschung, the MARUM–Center for Marine Environmental Sciences, the Deutsche Forschungsgemeinschaft (grants LA 1273/3-2, LA1273/5-1, and KI-456/9-1), and the Helmholtz Network Regional Climate Change (REKLIM). CL acknowledges 2014 fellowship from the Hanse-Wissenschaftskolleg (Germany). IRH acknowledges funding from the European Commission 7th Framework Marie Curie People programme through the Initial Training Network 'GATEWAYS' (grant 238512). Data are available at <http://doi.pangaea.de/10.1594/PANGAEA.848152>.

Author Contributions

F.L., H.W.A and R.K. conceived the idea for the study. F.L. wrote most of the manuscript with extensive input from H.W.A., C.B.L and L.L-J. M.W provided grain size data and N.H. contributed with sediment and data for core MR0806-PC09. J.K. analyzed and interpreted SST data from the SE Pacific. O.B.U contributed with bulk grain size and geochemistry data for core MD07-3128. I.R.H. provided silt grain size measurements for MD07-3128 and expertise in the interpretation of data. R.T. oversaw the study and contributed with expertise on the South Pacific paleoceanography. The figures were prepared by F.L. and H.W.A. All authors commented on the manuscript.

Supporting Information: Methods

Sediment Cores. Sediment core MD07-3128 was retrieved from the southern Chilean continental slope ~30 nm off the Pacific entrance to the Strait of Magellan (52°39.57'S, 75°33.97'W; 1,032 m water depth). The site is located below the Cape Horn Current (CHC), a branch of the Antarctic Circumpolar Current (ACC) that continues towards the Drake Passage (DP) where it joins the main subantarctic ACC (Figs. 6.1 and S 6.1). The sediment sequence consists of an upper unit of olive to yellow foraminifera ooze comprising the upper ~0.5 m of the core. This unit, representing the Holocene, is underlain by sand-bearing clayey silt to silty clay, the main lithology down to the base of the core representing the last glacial. This unit reveals meter-scale variations in color between gray and grayish olive with occasional, visually observed drop stones. These color changes largely parallel the variations in grain size and geochemistry shown in this paper. CaCO₃ contents are between ~30 and 55 wt-% in the Holocene and ~1 to 12 wt-% for the glacial part. Biogenic silica and organic matter contents range from 1 to 4 wt-% and 0.3 to 0.8 wt-%, respectively, throughout the core (Caniupán, 2011).

Sediment core MR0806-PC09 was recovered from the southernmost Argentinean continental slope to the east of Cape Horn (55°42.58' S, 66°08.06' W; 684 m water depth) within the northern sector of the Drake Passage (Fig. S 6.1). The upper surface unit (0.11 m) consists of fine to medium foraminifer sand. Below, the sediments are mostly dark gray clayey silt with lenses and layers of fine sand; they are bioturbated and ice rafted debris (IRD) is observed down to 7.8 m. A detailed lithological description is given by Shiroya et al. (2013). CaCO₃ contents range from 25 to 37 wt-% in the Holocene and from 1 to 15 wt-% for the glacial. Biogenic silica and organic carbon contents are 2 to 4wt-% and 0.1 to 0.4 wt-%, respectively, throughout the core.

Age Models. We updated the published age models for cores MD07-3128 (Caniupán et al., 2011) and MR0806-PC09 (Shiroya et al., 2013) by using the most recent calendar age conversion curve INTCAL13 and software Calib 7.0 (Reimer et al., 2013). Moreover, we considered the recent reservoir age estimates for the Holocene and the last deglaciation from core MD07-3088 located northward (46°S) at the Chilean continental margin (Siani et al., 2013). We used the oldest reservoir age given by Siani et al. (2013) as an estimate for glacial reservoir ages at our core location. For core MD07-3128, we kept the age control point represented by the Laschamp magnetic field excursion at ~41,250 years ago (Caniupán et al.,

2011). The pre-radiocarbon part of the age model of core MD07-3128 is based on graphical tuning of the alkenone SST record to that of the composite sequence at ODP Site 1233 (Kaiser and Lamy, 2010) (Fig. S 6.2). Age-control points are given in Table S1.

We also updated the age model of the ODP Site 1233 sediment record. As for cores MD07-3128 and MR0806-PC09, we used the most recent calendar age calibration curves and the reservoir age estimates by Siani et al. (2013), except for the Holocene. During this time interval, we assumed the global value of ~400 years consistent with the occurrence of an early Holocene ash layer at Site 1233 that has been dated on land (Lamy et al., 2004). We updated the pre-radiocarbon part of the Site 1233 age model, originally based on tuning of the SST record to the oxygen isotope record of the Byrd ice-core (Lamy et al., 2004; Kaiser and Lamy, 2010), by graphical tuning to the EDML ice-core record on the most recent Antarctic ice core chronology AICC12 (Bazin et al., 2013; Veres et al., 2013). Age-control points are given in Table S1.

Grain size determinations. Grain size data were obtained from cores MD07-3128 and MR0806-PC09 (Figs. S 6.3 and S 6.4). For core MD07-3128, samples for grain size measurements were taken at a spacing of 12 cm with an average temporal resolution of ~2,800 years for the upper part of the core corresponding to the Holocene and ~200–250 years for the glacial section. In order to separate the terrigenous sediment fraction, we used 35% H₂O₂ to remove organic matter and for disaggregation, and 10% acetic acid in order to dissolve carbonate. Since biogenic silica contents are low (1–4 wt-%), we did not dissolve opal. The separation of the 63–150 μm fine sand-fraction was achieved by wet-sieving, while the silt (2–63 μm) and clay fractions (<2 μm) were split by Stokes' law settling using Atterberg tubes (Müller, 1967). In order to separate the latter two size fractions almost completely, a 9–12 times repetition of the settling procedure was necessary. Coagulation of clay size particles was avoided by using a 0.1% sodium polyphosphate solution.

A detailed grain size analysis of the silt-fraction (2–63 μm) and the fine sand-fraction (63–150 μm) was performed by measurements with a Micromeritics SediGraph 5100 (Fig. S 6.3) at the Alfred Wegener Institute (AWI Bremerhaven). The SediGraph also detects remaining >150 μm sand and clay particles in the silt fraction, which have not been removed by Atterberg- and sieving-methods. The SediGraph analysis provides a high-resolution grain size distribution in steps of 0.1 phi and is based on the X-ray scanning of a settling suspension assuming Stokes' law settling. \overline{SS} is the mean grain size of the sortable silt-fraction (10–63 μm) as defined by McCave et al. (1995). The instrument precision of the SediGraph 5100 for pure standard

analysis is ± 0.3 to $\pm 1.9\%$ (Bianchi et al., 1999). Marine sediments with $>5\%$ SS yielded an analytical precision for \overline{SS} measurements and the weight percent of SS of $\pm 2\%$ and $\pm 9\%$ (Bianchi et al., 1999).

The Holocene section contains only very small amounts of terrigenous components as it is primarily composed of biogenic carbonate. Therefore, we could not reliably measure terrigenous silt and fine sand with the SediGraph for this interval as the amount was too small. We thus used a polynomial regression between strongly co-varying \overline{SS} and fine sand contents for the glacial section (Fig. S 6.3) in order to derive Holocene \overline{SS} estimates. Typical Holocene values were estimated in the range of $\sim 40 \mu\text{m}$, based on fine sand contents of $\sim 55 \text{ wt.}\%$.

The SediGraph is generally considered as the best suited device for measuring grain size as a proxy for current intensity as it employs the settling velocity principle measuring “dynamical” grain sizes closely related to transport and depositional processes (McCave and Hall, 2006). We compared our data to measurements with a Coulter Counter at Cardiff University on selected samples, showing very similar results (Fig. S 6.6). The Coulter Counter measures the volume-equivalent spherical diameter through electrical conductivity. The similar results obtained by these different devices support the robustness of our grain size measurement.

For core MR0806-PC09, samples for grain size measurements were taken at a spacing of 2-5 cm with an average temporal resolution of $\sim 1,000$ - $4,000$ years for the upper part of the core corresponding to the Holocene and ~ 100 - 300 years for the glacial section. Grain size measurements were performed with a Beckman Coulter laser diffraction particle size analyzer, type LS 13320 at the MARUM Center in Bremen. The laser itself is equipped with an Aquous Liquid Module and an Auto Prep Station and determines particle grain sizes from 0.04 to $2000 \mu\text{m}$ grouped into 116 size classes. Moreover, the laser uses degassed water to avoid bubbles during the measurements. Instrumental precision based on repeated sample diffraction is $\leq 3\%$. Before grain size analyses, we isolated the terrigenous fraction. Organic material was removed with ~ 10 ml of H_2O_2 (35 %) and calcium carbonate with HCl (10%). Finally, the samples were boiled with 300 mg of Sodium Pyrophosphate ($\text{Na}_4\text{P}_2\text{O}_7 \cdot 10\text{H}_2\text{O}$) to ensure disaggregation of all particles. Since biogenic silica contents are low (2-4 wt-%), we did not dissolve opal.

Glacial DP throughflow estimate. We calculated the glacial DP flow speed by combining the \overline{SS} record from CHC/northern ACC sites MD07-3128 and MR0806-PC09 with published \overline{SS} records from the southern Polar Frontal Zone and Antarctic Zone of the ACC in the Scotia Sea (McCave et al., 2014). In order to compare the individual reconstructed current speed records with modern DP current velocity and volume transport data, we projected each core onto the oceanographic Jason track 104 crossing the DP downstream of the Shackleton Fracture Zone (Fig. 6.1 C) beginning at the upper South American continental slope close to our core site MR0806-PC09. Core MD07-3128 likewise projects on the northern end of the section, as it is located below the CHC that contributes to subantarctic DP throughflow (Fig. S 6.1). The Scotia Sea cores were projected onto track 104 using the Scotia Sea projection line by McCave et al. (2014) and the relative distances between the major climatological oceanic fronts (Table S2). The glacial reduction of DP throughflow was calculated from the mean \overline{SS} values for the Holocene (0-11,500 years ago) and the LGM *sensu lato* (18,000-28,000 years ago).

Geochemistry. Geochemical data from core MD07-3128 include major and minor element concentrations (Fig. S 6.5), which were derived from discrete atomic absorption spectrophotometry (AAS) measurements on the bulk sediment. Measurements were performed with a VARIAN SeptrAA220 at the University of Trier. Samples of 100 mg of sediment were dried (105°C) and fused completely in Pt skillets with 400 mg of flux material (mixture of Lithiumtetraborate, Lithium carbonate and Lanthanum oxide). The produced glass beads were dissolved in 40 ml HCl (0.5N). Liquids of samples and international standards (MRG-1, SY-2 and JG-2) were measured by the AAS. Determined major elements plus loss of ignition (1050°C) and independently detected contents of CO₂ and SO₂ resulted in sums of 99 to 101 wt.-%. Zr and Rb concentrations were measured at 1cm downcore resolution using an AVAATECH profiling X-ray Fluorescence (XRF) core scanner at the Alfred Wegener Institute Bremerhaven.

Sea surface temperatures. SST changes between the Holocene and the LGM in the Southeast Pacific have been compiled from published records (Fig. 6.3 and Table S3). These include primarily alkenone-based SST reconstructions, except for two Mg/Ca-derived SST records from the eastern tropical Pacific and one from the East Pacific Rise. We also added published foraminifera transfer function-based SSTs from the east Pacific Rise.

Where possible, we calculated glacial cooling (Fig. 6.3 and Table S3) from the temperature difference between the mean Holocene (0–11,500 years ago) and for the LGM *sensu stricto* (19,000–23,000 years ago) SST estimates. This method provides glacial cooling estimates based on proxy SSTs uninfluenced from potential offsets of the absolute proxy calibration to modern world ocean atlas SSTs. Note that the LGM SSTs based on foraminifera assemblage are winter estimates whereas the alkenone SSTs, at least for the southern sector, most likely represent spring/summer temperatures (Prahl et al., 2010; Ho et al., 2012).

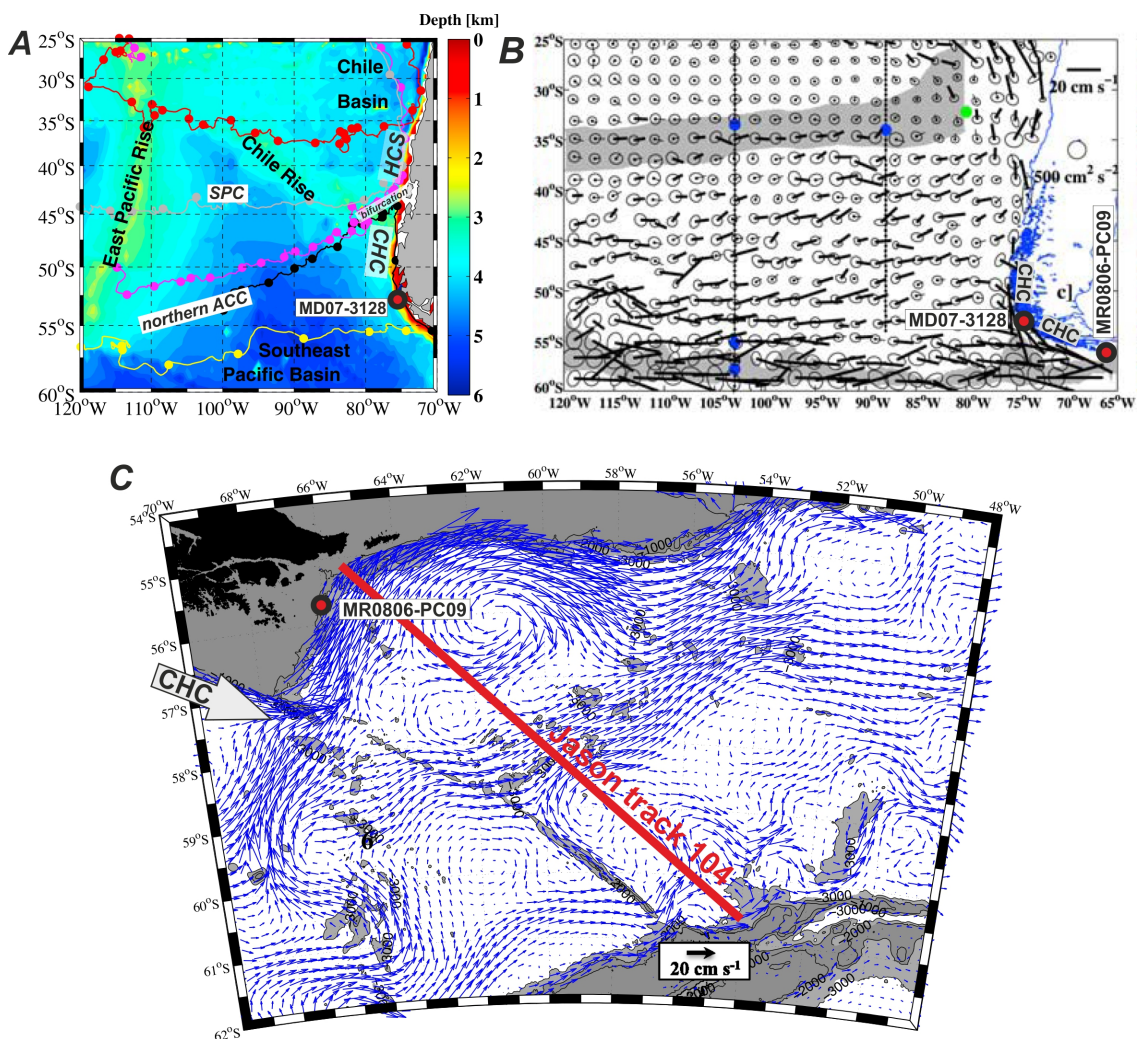


Figure caption is given on the next page.

Figure S 6.1: Surface and intermediate ocean circulation in the Southeast Pacific. **(A)** Examples of surface buoy trajectories (each 30-day positions are indicated by a circle) indicating northeast flow of northern ACC water after crossing the East Pacific Rise. Also shown is the bifurcation of surface waters close to the Chilean coast (at ca. 45° S) with northward flowing water in the Humboldt Current (HCS) and strongly accelerated southward flow in the Cape Horn Current (CHC) towards the Drake Passage (DP). West-east drifting buoys follow the South Pacific Current (SPC). **(B)** Surface velocities and velocity variance ellipses from drifter measurements (velocities > 6 cm/s are in bold). Note the high current velocities in the southern CHC in vicinity of our core MD07-3128 location. *A* und *B*, modified from Chaigneau and Pizarro (2005). The drifter measurements are averaged to 2*2° grid boxes, each of which containing more than 5 daily positions. **(C)** Mean velocity vectors at 500 m from model outputs (blue arrows) after Ferrari et al. (2014) showing strong flow along the northern border of the DP, where core MR0806-PC09 is located. Red line indicates location of Jason track 104. CHC=Cape Horn Current entering the DP.

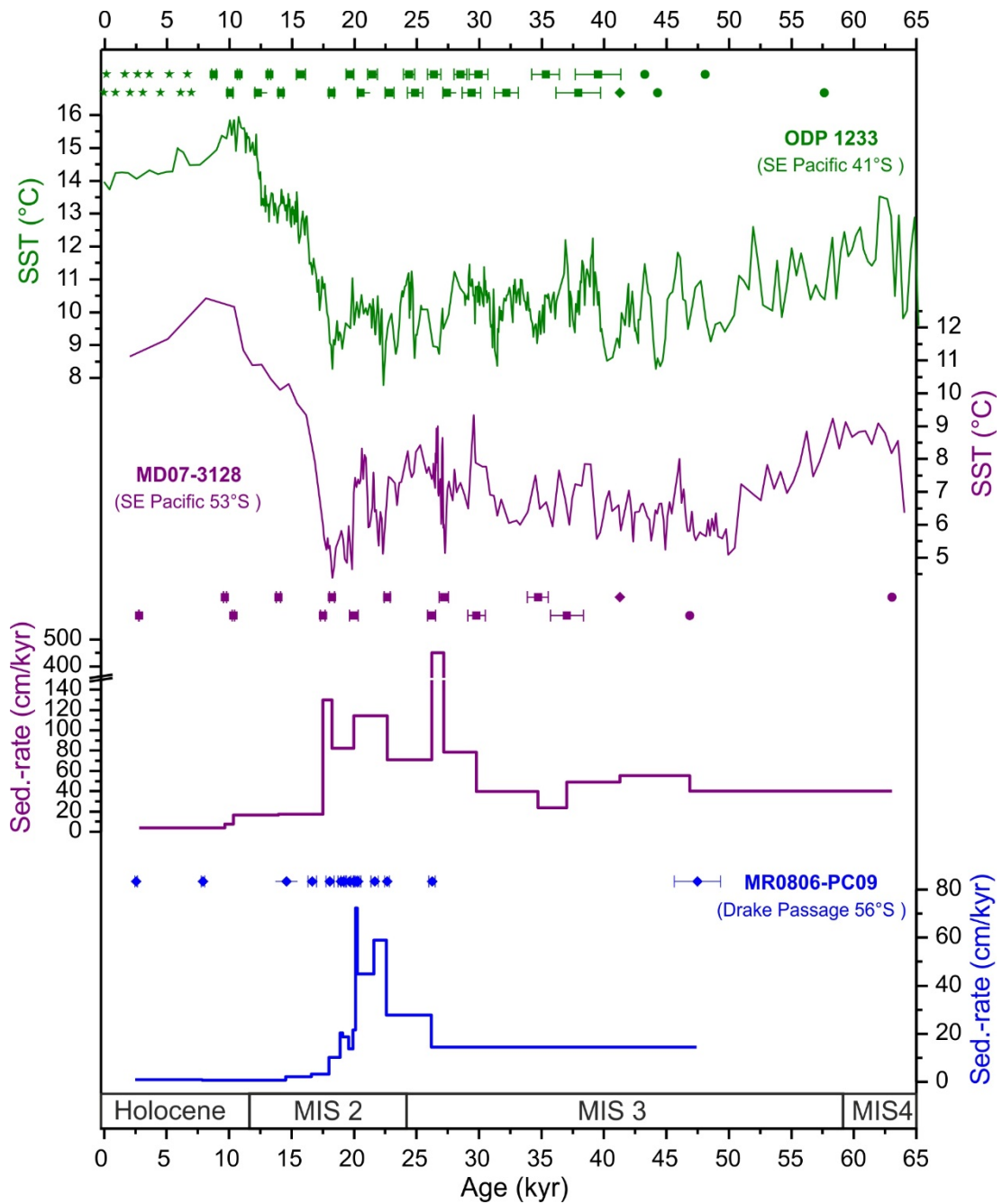


Figure S 6.2: Age models for cores MD07-3128 and MR0806-PC09. Age control is based on radiocarbon dates (squares with 2 sigma errors) (updated from Caniupán et al., 2011; Shiroya et al., 2013). Additionally, for core MD07-3128 we used the paleomagnetic Laschamp excursion (diamond), and graphical tuning of the SST record to that of ODP Site 1233. The age-model of the sediment sequence at Site 1233 has been updated from Kaiser and Lamy (2010). See “age-model” in the methods section of the Supporting Information for further details. Linear sedimentation-rates for cores MD07-3128 and MR0806-PC09 are shown at the bottom.

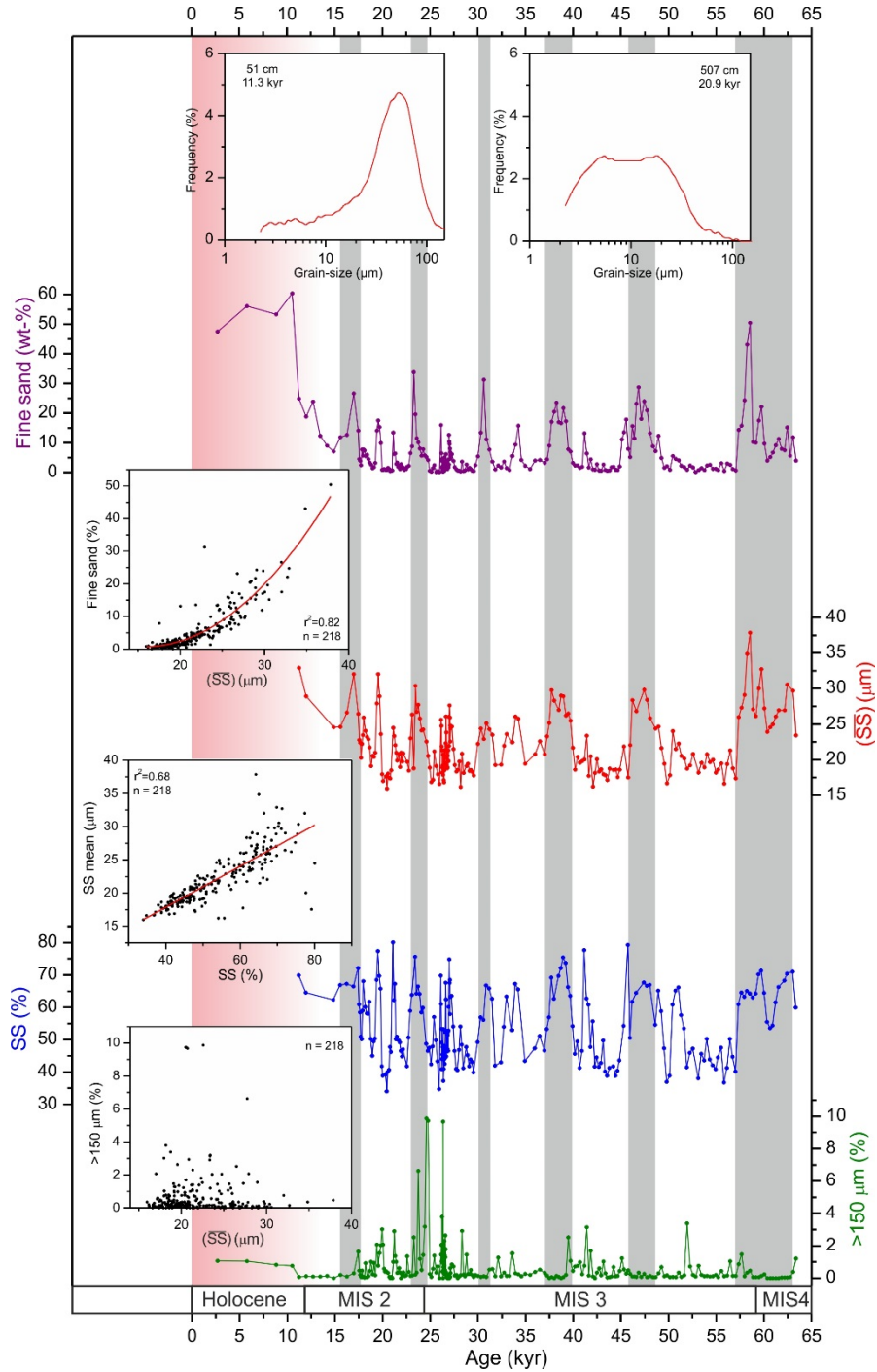


Figure S 6.3: Downcore grain size data from MD07-3128: Fine sand content (purple), \overline{SS} (red), sortable silt percentage (SS%, blue), and >150 μm fraction ("IRD", green from Caniupán et al., 2011). The two small inset figures in top panel show contrasting fine sand and silt grain size distributions from representative early Holocene (left) and LGM samples (right). Small figures to the left show polynomial regression between fine sand and \overline{SS} (top), linear relation between \overline{SS} and SS% (middle), and uncorrelated IRD with \overline{SS} (bottom). Vertical gray bars mark inferred millennial-scale Drake Passage throughflow maxima (as in Fig. 6.4).

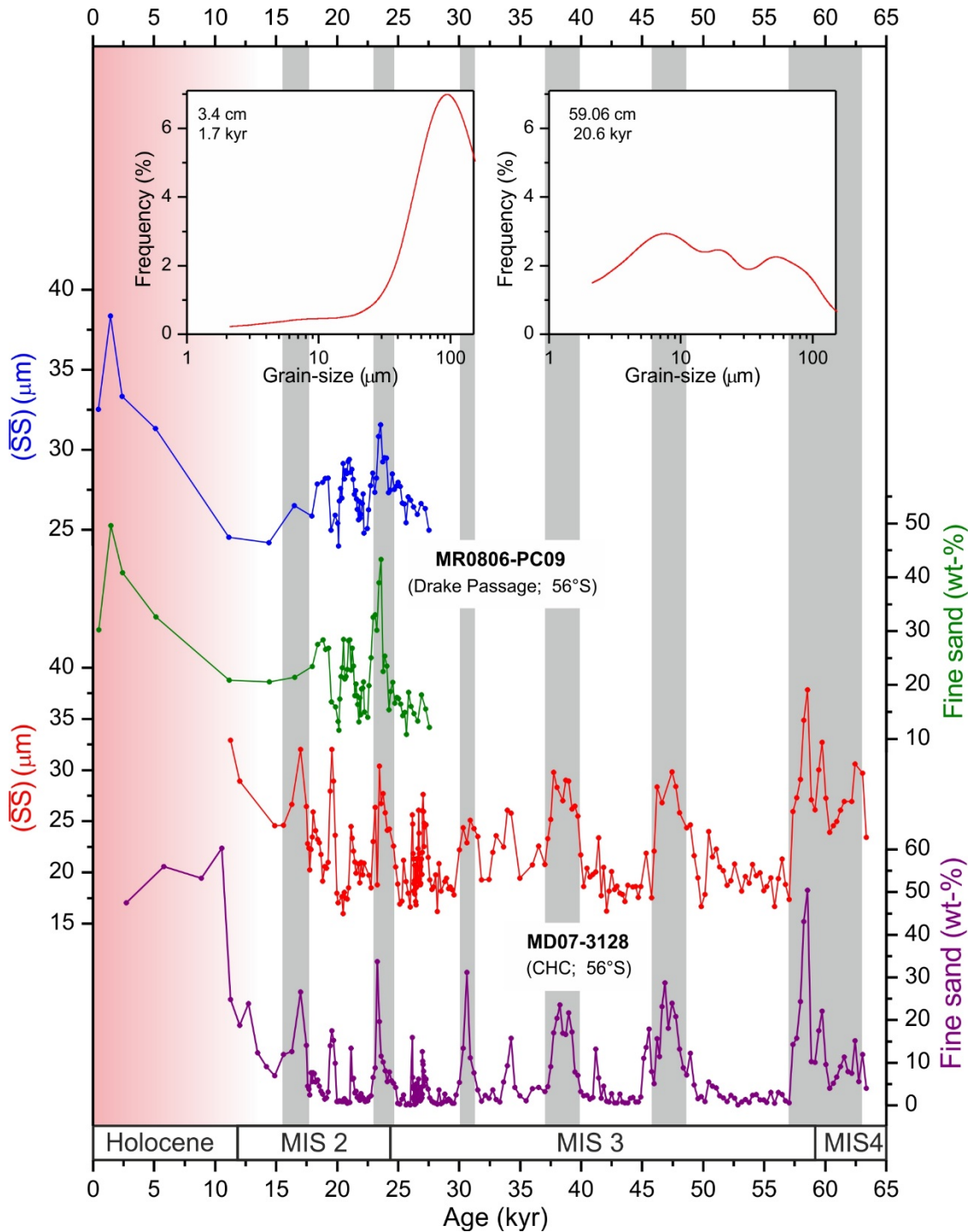


Figure S 6.4: Grain size data from cores MR0806-PC09 and MD07-3128: \overline{SS} (blue) and fine-sand (green) down-core records from core MR0806-PC09. The two small inset figures in top panel show contrasting fine sand and silt grain size distributions from representative Holocene (left) and LGM samples (right). Red and purple down-core records show \overline{SS} and fine-sand contents of core MD07-3128, respectively. Vertical gray bars mark inferred millennial-scale Drake Passage throughflow maxima (as in Fig. 6.4).

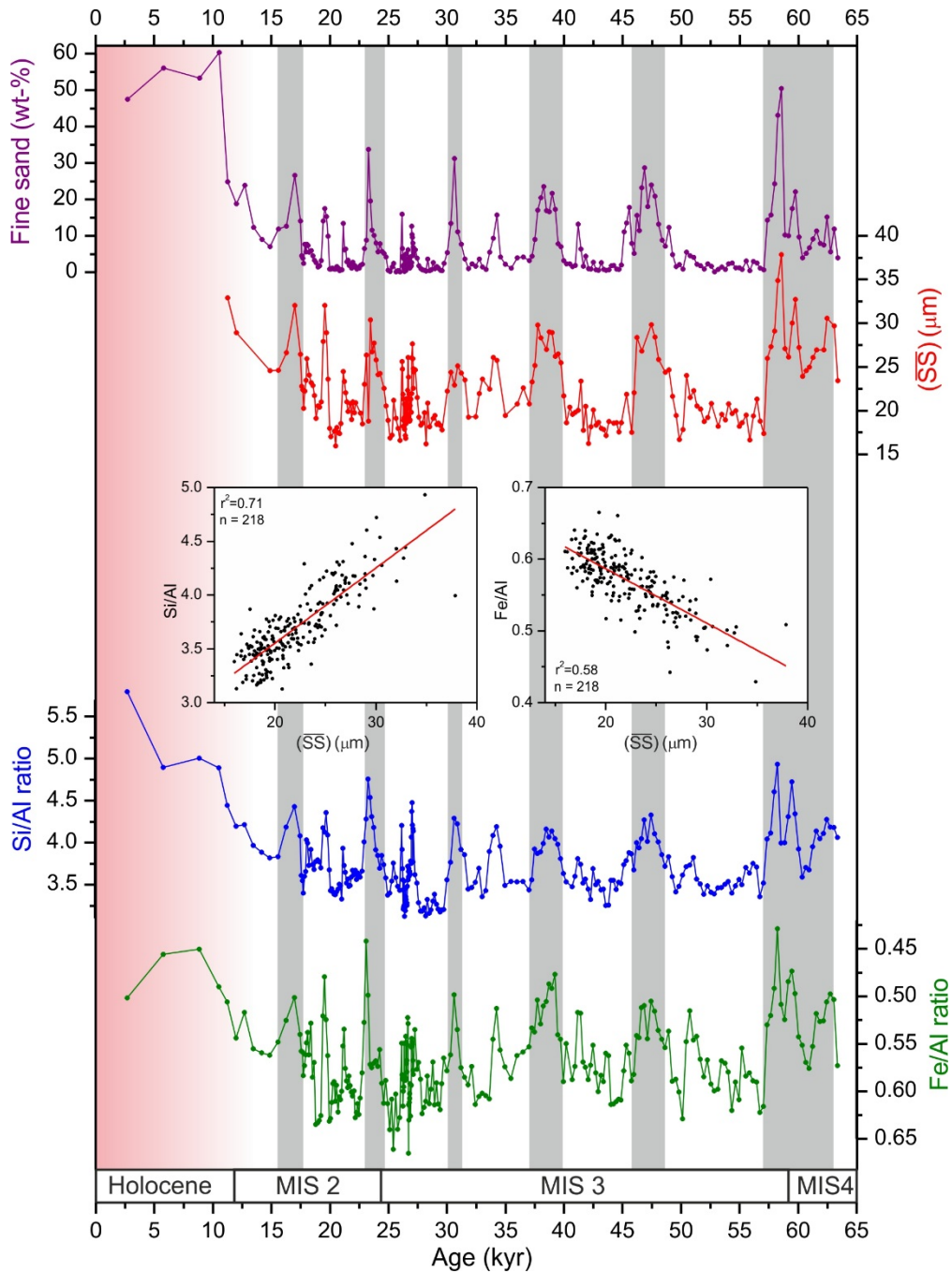


Figure S 6.5: Geochemistry data from core MD07-3128. Fine sand contents (purple) and \overline{SS} (red) compared to downcore records of Si/Al (blue) and Zr/Rb (green; 5-point moving average) ratios. As biogenic silica contents are very low (< 4 wt-%), Si contents reflect primarily changes in the siliciclastic fraction. This is consistent with co-varying changes in Si/Al and Zr/Rb ratios both primarily reflecting grain-size changes. Vertical gray bars mark inferred millennial-scale Drake Passage throughflow maxima (as in Fig. S 6.4).

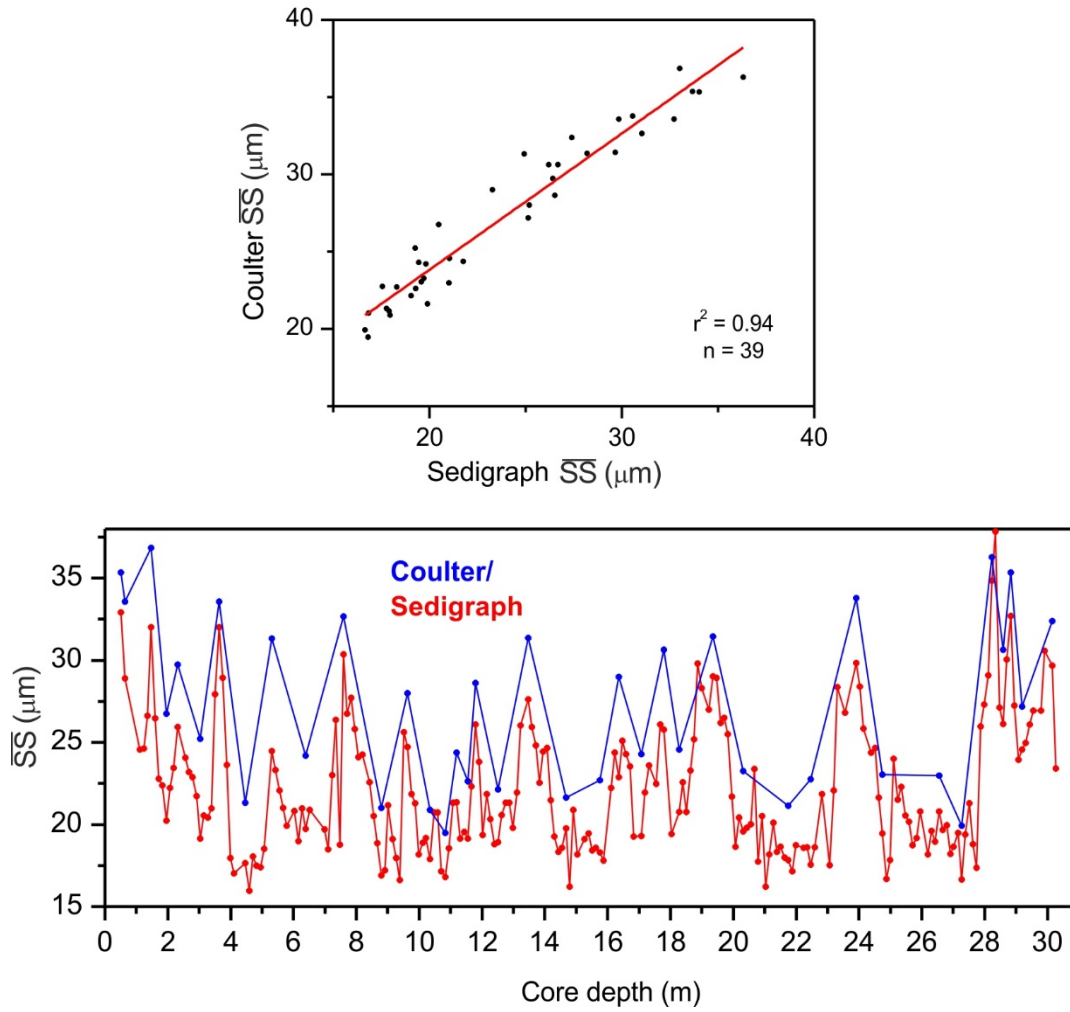


Figure S 6.6: Comparison between \overline{SS} obtained from Sedigraph and Coulter counter measurements in core MD07-3128. The similar results obtained by these different devices (top panel) supports the robustness of our grain size measurement. Absolute Coulter counter \overline{SS} values tend to be slightly higher but amplitudes are generally consistent (bottom panel).

Table S 6.1: Age control points for the construction of age models for cores MD07-3128, MR0806-PC09, and the ODP Site 1233 sediment record (update of published age models (Kaiser and Lamy, 2010; Caniupán et al., 2011; Shiroya et al., 2013)).

| Core depth (m/med) | ¹⁴ C raw age (ka BP) | ±Error (ka) | Reservoir age | Calibrated age (ka BP) | ±Error (ka) | Dating Method |
|-----------------------|------------------------------------|----------------|------------------|------------------------------|----------------|------------------|
| MD07-3128 | | | | | | |
| 0.03 | 3.41 | 0.025 | 0.80 | 2.75 | 0.02 | INTCAL13 |
| 0.3 | 9.49 | 0.045 | 0.81 | 9.63 | 0.12 | INTCAL13 |
| 0.35 | 9.95 | 0.045 | 0.81 | 10.29 | 0.10 | INTCAL13 |
| 0.94 | 13.04 | 0.06 | 0.98 | 13.91 | 0.16 | INTCAL13 |
| 1.55 | 15.46 | 0.07 | 1.13 | 17.46 | 0.24 | INTCAL13 |
| 2.5 | 16.10 | 0.07 | 1.13 | 18.19 | 0.21 | INTCAL13 |
| 3.93 | 17.33 | 0.13 | 0.81 | 19.93 | 0.34 | INTCAL13 |
| 7 | 19.56 | 0.1 | 0.81 | 22.62 | 0.24 | INTCAL13 |
| 9.52 | 22.76 | 0.15 | 0.81 | 26.17 | 0.33 | INTCAL13 |
| 13.96 | 23.61 | 0.15 | 0.81 | 27.16 | 0.38 | INTCAL13 |
| 16.01 | 26.40 | 0.24 | 0.81 | 29.76 | 0.68 | INTCAL13 |
| 17.96 | 31.54 | 0.465 | 0.81 | 34.69 | 0.85 | INTCAL13 |
| 18.51 | 33.66 | 0.54 | 0.81 | 37.02 | 1.33 | INTCAL13 |
| 20.58 | | | | 41.25 | | Laschamp |
| 23.67 | | | | 46.85 | | Tuning |
| 30.16 | | | | 63.06 | | Tuning |
| MR0806-PC09 | | | | | | |
| 0.06 | 3.21 | 0.05 | 0.80 | 2.45 | 0.10 | INTCAL13 |
| 0.10 | 7.76 | 0.08 | 0.81 | 7.80 | 0.14 | INTCAL13 |
| 0.15 | 13.6 | 0.08 | 1.23 | 14.49 | 0.40 | INTCAL13 |
| 0.19 | 15.0 | 0.11 | 1.32 | 16.55 | 0.36 | INTCAL13 |
| 0.24 | 15.65 | 0.13 | 0.89 | 17.97 | 0.32 | INTCAL13 |
| 0.33 | 16.4 | 0.11 | 0.81 | 18.85 | 0.24 | INTCAL13 |
| 0.37 | 16.6 | 0.09 | 0.81 | 19.07 | 0.23 | INTCAL13 |
| 0.46 | 17.0 | 0.12 | 0.81 | 19.55 | 0.34 | INTCAL13 |
| 0.51 | 17.3 | 0.09 | 0.81 | 19.88 | 0.26 | INTCAL13 |
| 0.55 | 17.45 | 0.08 | 0.81 | 20.09 | 0.24 | INTCAL13 |
| 0.64 | 17.55 | 0.08 | 0.81 | 20.21 | 0.24 | INTCAL13 |
| 1.24 | 18.6 | 0.09 | 0.81 | 21.55 | 0.29 | INTCAL13 |
| 1.82 | 19.45 | 0.09 | 0.81 | 22.54 | 0.20 | INTCAL13 |
| 2.82 | 22.7 | 0.12 | 0.81 | 26.14 | 0.27 | INTCAL13 |
| 5.89 | 44.8 | 0.87 | 0.81 | 47.40 | 1.84 | INTCAL13 |
| ODP 1233 | | | | | | |
| 10.55 | 8.3 | 0.06 | 0.40 | 8.74 | 0.19 | INTCAL13 |
| 12.94 | 9.34 | 0.08 | 0.40 | 10.04 | 0.23 | INTCAL13 |
| 14.21 | 9.87 | 0.05 | 0.40 | 10.72 | 0.11 | INTCAL13 |
| 17.01 | 10.8 | 0.07 | 0.40 | 12.27 | 0.25 | INTCAL13 |
| 20.22 | 12.28 | 0.07 | 0.95 | 13.18 | 0.12 | INTCAL13 |
| 21.39 | 13.18 | 0.06 | 0.98 | 14.10 | 0.19 | INTCAL13 |
| 25.1 | 14.42 | 0.11 | 1.32 | 15.70 | 0.36 | INTCAL13 |
| 27.97 | 15.75 | 0.07 | 0.81 | 18.16 | 0.21 | INTCAL13 |
| 29.81 | 17.07 | 0.11 | 0.81 | 19.64 | 0.32 | INTCAL13 |
| 31.47 | 17.81 | 0.09 | 0.81 | 20.51 | 0.27 | INTCAL13 |
| 33.51 | 18.52 | 0.13 | 0.81 | 21.44 | 0.39 | INTCAL13 |
| 36.56 | 19.74 | 0.14 | 0.81 | 22.80 | 0.36 | INTCAL13 |
| 39.5 | 21.08 | 0.15 | 0.81 | 24.36 | 0.45 | INTCAL13 |
| 41.17 | 21.44 | 0.24 | 0.81 | 24.85 | 0.62 | INTCAL13 |
| 43.72 | 22.93 | 0.23 | 0.81 | 26.37 | 0.54 | INTCAL13 |
| 45.53 | 23.88 | 0.17 | 0.81 | 27.38 | 0.30 | INTCAL13 |

| Core depth | ¹⁴ C raw age | ±Error | Reservoir age | Calibrated age | ±Error | Dating Method |
|------------|-------------------------|--------|---------------|----------------|--------|---------------|
| (m/mcd) | (ka BP) | (ka) | | (ka BP) | (ka) | |
| 49.11 | 26.1 | 0.29 | 0.81 | 29.37 | 0.74 | INTCAL13 |
| 50.72 | 26.52 | 0.30 | 0.81 | 29.92 | 0.75 | INTCAL13 |
| 55.02 | 29.03 | 0.39 | 0.81 | 32.16 | 0.95 | INTCAL13 |
| 59.03 | 32.19 | 0.58 | 0.81 | 35.31 | 1.11 | INTCAL13 |
| 62.5 | 34.48 | 0.75 | 0.81 | 37.92 | 1.78 | INTCAL13 |
| 64.81 | 35.77 | 0.79 | 0.81 | 39.50 | 1.83 | INTCAL13 |
| 67.8 | | | | 41.25 | | Laschamp |
| 73.54 | | | | 43.23 | | Tuning |
| 76.03 | | | | 44.28 | | Tuning |
| 82.60 | | | | 48.09 | | Tuning |
| 100.08 | | | | 57.63 | | Tuning |
| 129.10 | | | | 70.59 | | Tuning |
| 134.84 | | | | 73.47 | | Tuning |

ka BP = thousand years ago

Table S 6.2: Holocene and LGM (*sensu lato*, 18,000–28,000 years ago) mean \overline{SS} data across the Drake Passage, including data south of the SAF in the Scotia Sea (McCave et al., 2014) (see Fig. 6.1). $2\sigma/\sqrt{n}$ is the standard error of the mean (SEM). The analytical error of up to $\pm 3\%$ has not been propagated. SACCF=southern ACC front; APF=Antarctic Polar Front; SSAF=southern Subantarctic Front; SAF=Subantarctic Front; approximate locations after Orsi et al. (1995) and Sokolov and Rintoul (2009).

| Site | Holocene \overline{SS} mean (μm) | $2\sigma/\sqrt{n}$ | LGM \overline{SS} mean (μm) | $2\sigma/\sqrt{n}$ | LGM \overline{SS} reduction (%) | Projected on track 104 | Location on the line by McCave et al. (13) |
|-----------------|---|--------------------|--|--------------------|-----------------------------------|------------------------|--|
| MD07-3128 | 38.3 | 2.537 | 21.4 | 0.692 | -44 | 30 | n/a |
| MR0806-PC09 | 33.9 | 2.683 | 27.3 | 0.383 | -19 | 30 | n/a |
| SAF | n/a | n/a | n/a | n/a | n/a | 80 | n/a |
| SSAF | n/a | n/a | n/a | n/a | n/a | 280 | 15 |
| BAS TPC063 | 21.37 | 0.604 | 19.78 | 0.62 | -7 | 337 | 110 |
| BAS TPC077 | 19.6 | 0.811 | 20.29 | 0.597 | 4 | 423 | 250 |
| APF | n/a | n/a | n/a | n/a | n/a | 465 | 330 |
| PS2514-1 | 18.97 | 0.463 | 19.57 | 0.615 | 3 | 505 | 360 |
| PS67/197-1 | 17.35 | 0.625 | 17.72 | 0.499 | 2 | 538 | 425 |
| BAS TC290/PC078 | 16.11 | 0.334 | 16.86 | 0.283 | 5 | 590 | 480 |
| PS67/205-2 | 18.06 | 0.561 | 16.2 | 0.261 | -10 | 691 | 610 |
| PS67/219-1 | 17.84 | 0.238 | 16.58 | 0.54 | -7 | 715 | 680 |
| SACCF | n/a | n/a | n/a | n/a | n/a | 780 | 720 |
| PS67/224-1 | 15.97 | 0.261 | 15.47 | 0.315 | -3 | 806 | 735 |

Table S 6.3: Summary of sea surface temperature (SST) records shown in Fig. 6.3.

| Core | Latitude | Longitude | Holocene SST (°C) | LGM* SST (°C) | LGM-Holocene (°C) | SST Method | Reference |
|--|----------|-----------|-------------------------|---------------------|----------------------|---------------|------------------------------|
| East Pacific Rise (central Pacific) | | | | | | | |
| E20-18 | -44.55 | 248.67 | 9 ^a | 9.2 ^b | 0.2 | Foraminifera | Luz (60) |
| DWBG 70 | -48.48 | 246.72 | 6 ^a | 2.6 ^b | -3.4 | Foraminifera | Luz (60) |
| E25-10 | -50.10 | 245.22 | 6 ^a | 1.1 ^b | -4.9 | Foraminifera | Luz (60) |
| E21-15 | -52.02 | 239.98 | 5 ^a | 1.1 ^b | -3.9 | Foraminifera | Luz (60) |
| RC12-225 | -53.67 | 236.90 | 4 ^a | 1.1 ^b | -2.9 | Foraminifera | Luz (60) |
| E11-1 | -54.91 | 245.30 | 3 ^a | 0.7 ^b | -2.3 | Foraminifera | Luz (60) |
| E11-3 | -56.90 | 244.76 | 2 ^a | 0.6 ^b | -1.4 | Foraminifera | Luz (60) |
| E11-2 | -56.06 | 244.94 | 3 ^a | 0.6 ^b | -2.4 | Foraminifera | Luz (60) |
| E11-2 | -56.06 | 244.94 | 4.7 | 2.8 | -1.9 | Mg/Ca | Mashiotta <i>et al.</i> (61) |
| South East Pacific | | | | | | | |
| TG7 | -17.20 | 281.40 | 20.4 | 17.3 | -3.1 | Alkenones | Calvo <i>et al.</i> (62) |
| GeoB7139 | -30.20 | 288.02 | 18.5 | 15 | -3.5 | Alkenones | Kaiser <i>et al.</i> (63) |
| GeoB3302 | -33.22 | 287.91 | 17.4 ^c | 12.7 | -4.7 | Alkenones | Kim <i>et al.</i> (64) |
| GeoB3359 | -35.22 | 287.20 | 18 | 12.4 | -5.6 | Alkenones | Romero <i>et al.</i> (65) |
| ODP1233 | -41.00 | 285.55 | 14.9 | 9.9 | -5.0 | Alkenones | Kaiser & Lamy (20) |
| MD07-3128 | -52.66 | 284.44 | 12.1 | 6.5 | -5.6 | Alkenones | Caniupán <i>et al.</i> (51) |
| PS75/034-1 | -54.65 | 279.85 | 8.6 | 1.5 | -7.1 | Alkenones | Ho <i>et al.</i> (28) |
| East tropical Pacific | | | | | | | |
| TR163-22 | 0.52 | 267.60 | 24.4 | 22.4 | -2.0 | Mg/Ca | Lea <i>et al.</i> (43) |
| ODP1240 | 0.02 | 273.54 | 25.6 | 23.1 | -2.5 | Mg/Ca | Peña <i>et al.</i> (66) |
| ODP1239 | -0.67 | 277.92 | 24.9 | 23.4 | -1.5 | Alkenones | Rincón <i>et al.</i> (67) |

*LGM *sensu stricto* (19,000–23,000 years ago)^amodern winter SSTs (Mashiotta *et al.*, 1999)^bLGM winter SSTs (Mashiotta *et al.*, 1999)^cHolocene values from neighboring core GIK17748

7 Conclusions and perspectives

7.1 Main conclusions

The main objective of the thesis is to contribute to a better understanding of paleoclimate changes inferred from the dust variability of marine dust records from the SO.

Dust erosion predominantly depends on the interaction of climatic conditions in the source areas (e.g. aridity, precipitation, soil and terrain properties, vegetation cover and wind stress). Analyzing the dust variability of marine dust records deposited downwind of the major Southern Hemisphere source areas provides valuable information about paleoclimate conditions in the potential source areas (e.g. aridity, precipitation, wind forcing) and during dust transport (changes in the atmospheric circulation pattern, such as the SWW over the SO). In the following, the main conclusions of the thesis are summarized with respect to the scientific questions outlined in 1.3.

- *Did the dust variability and provenance in the Pacific sector of SO change throughout the Holocene?*

Manuscript one (chapter 3) presents the first multi-method approach to investigate the Holocene dust variability in the Pacific sector of the SO. An extensive set of sediment surface samples was used to determine lithogenic fluxes and the dust provenance (Sr, Nd, Pb isotopes and REE). The sediment surface samples were collected during R/V *Polarstern* and R/V *Sonne* expeditions in the Pacific sector of the SO and present for the first time a geographical coverage that allows to identify large-scale changes. Generally, the strength of this data set is the unique spatial coverage in the Pacific sector of the SO providing virtually the only lithogenic flux and provenance data for this area.

A solid understanding of the spatial distribution of lithogenic fluxes in the Pacific sector of the SO is a prerequisite to correctly understand the dust provenance. Lithogenic fluxes off New Zealand are highest among all samples and correspond with highest detected plant wax n-alkanes and soil derived branched glycerol dialkyl glycerol tetraethers (brGDGTs) (chapter 5). Both, n-alkanes and brGDGTs can be used as tracers for continental vegetation and soil bacteria transported by wind (attached to dust particles) and rivers to the ocean (Simoneit, 1977; Fietz et al., 2013). Here, they are interpreted as independent evidence for increased terrigenous input to the sample locations off New Zealand (chapters 3 and 5). With increasing

distance to New Zealand lithogenic fluxes, n-alkanes and brGDGTs decrease. Although lithogenic fluxes, n-alkanes and brGDGTs off New Zealand reveal increased terrigenous input, the provenance of these samples cannot entirely be deciphered and remains speculative. Probably, highest lithogenic fluxes off New Zealand reflect a combined Australian/New Zealand dust/riverine signal.

The lowest lithogenic fluxes in the remote open ocean are consistent with lowest detected leaf wax n-alkanes and brGDGTs and are interpreted as solely derived from dust (chapters 3 and 5). East of 150°W two north to south transects (~120°W and ~90°W) reveal an additional non-eolian terrigenous source. The southernmost samples are affected by ice-rafted sediments (~120°W transect) and Antarctic Peninsula-derived turbidity currents (~90°W transect). The northernmost samples of both transects are interpreted to be dust derived because the lithogenic fluxes decrease substantially to the north.

The samples revealing a distinct dust signal (low lithogenic fluxes, low n-alkane and brGDGTs concentrations) are well distributed over the Pacific sector of the SO and therefore ideal to analyze the dust provenance. The combined radiogenic isotope and REE data clearly show that there is no longitudinal gradient across the Pacific sector of the SO. Furthermore, the data are remarkably homogeneous compared to published data from the PSAs (Australia, New Zealand, southern South America), which is perhaps surprising given the spatial extent of our study area and the number of PSAs. Despite geochemical similarities between Australian, New Zealand and southern South American PSAs, the data show that the Lake Eyre Basin in central Australia is the most important source for atmospheric dust distributed over the Pacific sector of the SO in the Holocene.

In summary, the data clearly illustrate that the Holocene dust variability and dust provenance did not vary. Given that the entire Pacific sector of the SO reveals a Lake Eyre Basin signature, I make the following conclusions: 1) The Lake Eyre Basin was an arid area with low vegetation cover and a decreased surface roughness during the Holocene allowing increased dust erosion. 2) The SWW were strong enough to distribute Lake Eyre dust over the entire Pacific Sector of the SO. 3) The data show that central and southeast Australian sources were active during the Holocene, which can potentially be extended to older interglacial periods.

- *Did the dust input and dust grain size vary over G/IG cycles in the Pacific and Atlantic sectors of SO?*

The second manuscript (chapter 4) presents the first comprehensive down core grain size study of eolian sediments from the Pacific and Atlantic sectors of the SO to detect large-scale dust variability over G/IG timescales. The analyzed sediment cores are located in the Subantarctic Zones of the Pacific (PS75/056-1) and Atlantic sectors (ODP Site 1090) of the SO and cover the last eight G/IG cycles. Because of their location downwind of the major source areas in the Southern Hemisphere (Australia, New Zealand and southern South America) they are ideally located to study temporal and spatial dust transport. To link the large-scale dust variability to changes in the dust transporting SWW and to variations within PSAs, grain size analysis is combined with Fe and lithogenic flux records from both core sites.

In the Pacific sector, coarser dust particles during glacial periods correspond with increased glacial Fe and lithogenic flux records. The coarser glacial dust could be interpreted as a result of slightly enhanced SWW over Australia/New Zealand. However, this would contradict the results presented in manuscript 4 (chapter 6), where a substantial glacial decrease of Drake Passage ACC through-flow is linked to reduced SWW over their core zone. Subsequently, coarser glacial dust particles in the Pacific sector of the SO likely reflect a combination of expanded arid areas allowing increased dust erosion in Australia and/or New Zealand, northward shifted SWW and probably the activation of PSAs that were inactive during interglacial periods. In the Atlantic sector, dust accumulation is clearly increased compared to the Pacific sector of the SO, which indicates that South American source areas produced elevated total amounts of glacial dust compared to Australia/New Zealand. Coarser dust particles during interglacial periods are coupled with elevated glacial Fe and lithogenic fluxes. Enhanced glacial Fe and lithogenic fluxes reflect an increased dust availability in South America. It was shown that elevated dust accumulation in east Antarctic ice cores corresponds with increased meltwater discharge from Patagonian glaciers onto outwash plains, where dust can easily be mobilized. This likely explains the elevated glacial Fe and lithogenic fluxes in the Atlantic sector of the Southern Ocean. However, the finer glacial dust could result from a diminished SWW core over Patagonia likely hampering the erosion of coarse dust particles. Additionally, the Puna Altiplano region is a major source of dust to east Antarctic ice during interglacial periods. It was shown that this region was characterized by drier interglacial conditions likely favoring the erosion of coarser dust particles.

In summary, the data clearly reveal that dust input was constant in the Pacific and Atlantic sectors of the SO. In both oceanic sectors of the SO, increased glacial Fe accumulation and lithogenic fluxes suggest enhanced dust availability in the source areas (Australia/New Zealand and South America). In contrast, the mean dust grain sizes vary over G/IG timescales and reveal substantial changes in the Pacific and Atlantic sectors of the SO. In the Pacific sector, the coarser glacial mean dust grain size corresponds with the Fe accumulation and the lithogenic flux record. An opposing mean dust grain size pattern can be observed in the Atlantic sector of the SO, where the dust is coarser during interglacial periods.

The PSAs (Australia/New Zealand and South America) provided ideal conditions allowing elevated dust erosion during glacial periods. However, the inconsistent grain size data in the Pacific and Atlantic sector could reflect asymmetric changes within the SWW in the Southern Hemisphere. During austral winter, the core of the Pacific SWW divides into a northern subtropical jet and a southern subpolar jet approximately at the longitudes of western Australia (South Pacific split jet) (Chiang et al., 2014; Chiang et al., 2018). This well constraint meteorological feature is driven by sea surface temperature changes in the tropical Pacific (Inatsu and Hoskins, 2004). Patagonia, the main PSA to the Atlantic sector during glacial periods, is located further south compared to Australia/New Zealand and therefore more readily affected by changes within the SWW. However, assuming that the South Pacific split jet concept can be extended to G/IG timescales and that the subtropical jet was strengthened over Australia during glacial periods, this potentially supports the idea of an activation of northeastern Australian sources being responsible for coarser dust particles (as outlined in chapter 4).

7.2 Perspectives

As I have pointed out in the previous chapters, analyzing marine dust records deposited downwind of the major Southern Hemisphere PSAs can provide a powerful tool to infer paleoclimate changes. In the following I present some issues that should be addressed in future dust studies to enhance the knowledge of the dust variability and the impact on the past, current and future climate.

As I have demonstrated in chapter 3 the modern (Holocene) dust to the Pacific sector of the SO originates in central/southeast Australia. According to this result, down core dust provenance analysis should be conducted using representative sediment cores to completely understand the dust variability in the Pacific sector of the SO. The sediment cores should be

well distributed, ideally covering a broad range of latitudes and longitudes to detect changes within the SWW and the PSAs over G/IG timescales. For example, comparing Holocene dust provenance results to LGM dust provenance data would be an obvious next step in understanding the dust variability and would provide information on paleoclimate changes during warm and cold periods, respectively.

Additionally, further efforts should be made to understand the modern dust provenance in the Atlantic and Indic sectors of the SO to generate a circumpolar dust provenance map. In particular, the Atlantic sector of the SO should be part of extensive dust provenance analysis as it is located downwind of South America, the second largest dust source in the Southern Hemisphere. Similar to the Pacific sector of the SO, the dust provenance in the Atlantic sector should also be subject to time slice comparisons (e.g. Holocene versus LGM).

A problem that should be addressed for future provenance analysis is the grain size used to analyze isotopic and REE compositions. Australian and South American PSAs reveal similar isotopic and REE compositions but were measured on different grain sizes. To simplify dust provenance analysis, a uniform standard grain size would be of importance considering the grain size effect on Sr isotopes and REE.

In both the Pacific and Atlantic sectors of the SO, lithogenic flux analysis should be conducted using surface samples and sediment cores to determine the amount of dust deposited over G/IG timescales. These results could be important with regard to iron fertilization processes and recent and future atmospheric CO₂ levels. Moreover, I have shown that down core dust grain size analysis coupled with Fe records and lithogenic fluxes provide valuable tools to detect G/IG changes in PSAs and within the SWW (chapter 4). To take advantage of these tools, dust grain size analysis should be conducted on both, surface samples and sediment cores to understand the modern and past dust variability. As mentioned before, the sediment samples should cover the largest possible area to detect large-scale changes. From an analytical perspective, grain size analysis of biogenic opal rich sediments can be challenging because residues of biogenic opal in the sample material would affect the grain size distribution and would subsequently lead to misinterpretations. The introduced leaching protocol (chapter 4) was specifically developed for sediments with extremely high biogenic opal contents and therefore allows the application of grain size analysis to a broader range of sediment samples.

References

- Aislabie J. M., Chhour K.-L., Saul D. J., Miyauchi S., Ayton J., Paetzold R. F. and Balks M. R. (2006) Dominant bacteria in soils of Marble Point and Wright Valley, Victoria Land, Antarctica. *Soil Biol. Biochem.* **38**, 3041–3056.
- Albani S., Delmonte B., Maggi V., Baroni C., Petit J. R., Stenni B., Mazzola C. and Frezzotti M. (2012a) Interpreting last glacial to Holocene dust changes at Talos Dome (East Antarctica): Implications for atmospheric variations from regional to hemispheric scales. *Clim. Past* **8**, 741–750.
- Albani S., Mahowald N. M., Delomonte B., Maggi V. and Winckler G. (2012b) Comparing modeled and observed changes in mineral dust transport and deposition to Antarctica between the Last Glacial Maximum and current climates. *Clim. Dyn.* **38**, 1731–1755.
- Albani S., Mahowald N. M., Perry A. T., Scanza R. A., Zender C. S., Heavens N. G., Maggi V., Kok J. F. and Otto-Bliesner B. L. (2014) Improved dust representation in the Community Atmosphere Model. *J. Adv. Model. Earth Syst.* **6**, 541–570.
- Albarède F., Telouk P., Blichert-Toft J., Boyet M., Agranier A. and Nelson B. (2004) Precise and accurate isotopic measurements using multiple-collector ICPMS. *Geochim. Cosmochim. Acta* **68**, 2725–2744.
- Allison L. C., Johnson H. L., Marshall D. P. and Munday D. R. (2010) Where do winds drive the antarctic circumpolar current? *Geophys. Res. Lett.* **37**, 1–5.
- Alonso-Sáez L., Andersson A., Heinrich F. and Bertilsson S. (2011) High archaeal diversity in Antarctic circumpolar deep waters. *Environ. Microbiol. Rep.* **3**, 689–697.
- Anderson R. F., Ali S., Bradtmiller L. I., Nielsen S. H. H., Fleisher M. Q., Anderson B. E. and Burckle L. H. (2009) Wind-Driven Upwelling in the Southern Ocean and the Deglacial Rise in Atmospheric CO₂. *Science*. **323**, 1443–1448.
- Anderson R. F., Barker S., Fleisher M., Gersonde R., Goldstein S. L., Kuhn G., Mortyn P. G., Pahnke K. and Sachs J. P. (2014) Biological response to millennial variability of dust and nutrient supply in the Subantarctic South Atlantic Ocean. *Philos. Trans. R. Soc. A Math. Phys. Eng. Sci.* **372**.
- Arimoto R. (2001) Eolian dust and climate: relationships to sources, tropospheric chemistry, transport and deposition. *Earth-Science Rev.* **54**, 29–42.
- Assmann K. M., Hellmer H. H. and Jacobs S. S. (2005) Amundsen Sea ice production and transport. *J. Geophys. Res. Ocean.* **110**, 1–17.

- Ayton J., Aislabie J., Barker G. M., Saul D. and Turner S. (2010) Crenarchaeota affiliated with group 1.1b are prevalent in coastal mineral soils of the Ross Sea region of Antarctica. *Environ. Microbiol.* **12**, 689–703.
- Baker P. A. and Fritz S. C. (2015) Nature and causes of Quaternary climate variation of tropical South America. *Quat. Sci. Rev.* **124**, 31–47.
- Barker S. and Diz P. (2014) Timing of the descent into the last Ice Age determined by the bipolar seesaw. *Paleoceanography* **29**, 489–507.
- Barrows T. T., Juggins S., Deckker P. De, Calvo E. and Pelejero C. (2007) Long-term sea surface temperature and climate change in the Australian–New Zealand region. *Paleoceanography* **22**.
- Basak C., Fröllje H., Lamy F., Gersonde R., Benz V., Anderson R. F., Molina-Kescher M. and Pahnke K. (2018) Breakup of last glacial deep stratification in the South Pacific. *Science*. **359**, 900–904.
- Bazin L., Landais A., Lemieux-Dudon B., Toyé Mahamadou Kele H., Veres D., Parrenin F., Martinerie P., Ritz C., Capron E., Lipenkov V., Loutre M. F., Raynaud D., Vinther B., Svensson A., Rasmussen S. O., Severi M., Blunier T., Leuenberger M., Fischer H., Masson-Delmotte V., Chappellaz J. and Wolff E. (2013) An optimized multi-proxy, multi-site Antarctic ice and gas orbital chronology (AICC2012): 120–800 ka. *Clim. Past* **9**, 1715–1731.
- Beal L. M., De Ruijter W. P. M., Biastoch A., Zahn R., Cronin M., Hermes J., Lutjeharms J., Quartly G., Tozuka T., Baker-Yeboah S., Bornman T., Cipollini P., Dijkstra H., Hall I., Park W., Peeters F., Penven P., Ridderinkhof H. and Zinke J. (2011) On the role of the Agulhas system in ocean circulation and climate. *Nature* **472**, 429–436.
- Becquey S. and Gersonde R. (2003) A 0.55-Ma paleotemperature record from the subantarctic zone: Implications for Antarctic circumpolar current development. *Paleoceanography* **18**.
- Belkin I. M. and Gordon A. L. (1996) Southern Ocean fronts from the Greenwich meridian to Tasmania. *J. Geophys. Res. Ocean.* **101**, 3675–3696.
- Bendle J., Kawamura K., Yamazaki K. and Niwai T. (2007) Latitudinal distribution of terrestrial lipid biomarkers and n-alkane compound-specific stable carbon isotope ratios in the atmosphere over the western Pacific and Southern Ocean. *Geochim. Cosmochim. Acta* **71**, 5934–5955.
- Benz V., Esper O., Gersonde R., Lamy F. and Tiedemann R. (2016) Last Glacial Maximum sea surface temperature and sea-ice extent in the Pacific sector of the Southern Ocean. *Quat. Sci. Rev.* **146**, 216–237.

- Bianchi G. G., Hall I. R., McCave I. N. and Joseph L. (1999) Measurement of the sortable silt current speed proxy using the Sedigraph 5100 and Coulter Multisizer II: Precision and accuracy. *Sedimentology* **46**, 1001–1014.
- Blakowski M. A., Aciego S. M., Delmonte B., Baroni C., Salvatore M. C. and Sims K. W. W. (2016) A Sr-Nd-Hf isotope characterization of dust source areas in Victoria Land and the McMurdo Sound sector of Antarctica. *Quat. Sci. Rev.* **141**, 26–37.
- Blott S. J. and Pye K. (2001) Gradistat: A Grain Size Distribution and Statistics Package for the Analysis of Unconsolidated Sediments. *Earth Surf. Process. Landforms* **26**, 1237–1248.
- Blum J. D., Erel Y. and Brown K. (1993) $^{87}\text{Sr}/^{86}\text{Sr}$ ratios of sierra nevada stream waters: Implications for relative mineral weathering rates. *Geochim. Cosmochim. Acta* **57**, 5019–5025.
- Blum J. D. and Erel Y. (1997) Rb-Sr isotope systematics of a granitic soil chronosequence: The importance of biotite weathering. *Geochim. Cosmochim. Acta* **61**, 3193–3204.
- Boisvert W. E. (1969) Major currents off the west coasts of North and South America technical report. In Washington D.C.: Naval Oceanographic Office. p. 34.
- Bopp L., Kohfeld K. E., Le Quéré C. and Aumont O. (2003) Dust impact on marine biota and atmospheric CO₂ during glacial periods. *Paleoceanography* **18**.
- Bostock H. C., Sutton P. J., Williams M. J. M. and Opdyke B. N. (2013) Reviewing the circulation and mixing of Antarctic Intermediate Water in the South Pacific using evidence from geochemical tracers and Argo float trajectories. *Deep. Res. Part I Oceanogr. Res. Pap.* **73**, 84–98.
- Bowler J. M. (1976) Aridity in Australia: Age, origins and expression in aeolian landforms and sediments. *Earth Sci. Rev.* **12**, 279–310.
- Boyd P. W. and Ellwood M. J. (2010) The biogeochemical cycle of iron in the ocean. *Nat. Geosci.* **3**, 675.
- Bradt Miller L. I., Anderson R. F., Fleisher M. Q. and Burckle L. H. (2009) Comparing glacial and Holocene opal fluxes in the Pacific sector of the Southern Ocean. *Paleoceanography* **24**, 1–20.
- Brassell S. C., Eglinton G., Marlowe I. T., Pflaumann U. and Sarnthein M. (1986) Molecular stratigraphy: a new tool for climatic assessment. *Nature* **320**, 129.
- Bray E. E. and Evans E. D. (1961) Distribution of n-paraffins as a clue to recognition of source beds. *Geochim. Cosmochim. Acta* **22**, 2–15.
- Brewer P. ., Nozaki Y., Spencer D. . and Fleer A. . (1980) Sediment trap experiments in the

- deep North Atlantic: Isotopic and elemental fluxes. *J. Mar. Res.* **38**, 703–728.
- Broecker W. S. (1982) Glacial to interglacial changes in ocean chemistry. *Prog. Oceanogr.* **11**, 151–197.
- Calvo E., Pelejero C., Deckker P. De and Logan G. A. (2007) Antarctic deglacial pattern in a 30 kyr record of sea surface temperature offshore South Australia. *Geophys. Res. Lett.* **34**.
- Caniupán A. M. (2011) Paleoenvironmental history of the Chilean fjord region and the adjacent Southeast Pacific over the last 60 kyr BP: A multiproxy analysis on high resolution sediment cores. PhD thesis, University of Bremen.
- Caniupán M., Lamy F., Lange C. B., Kaiser J., Arz H., Kilian R., Urrea O. B., Aracena C., Hebbeln D., Kissel C., Laj C., Mollenhauer G. and Tiedemann R. (2011) Millennial-scale sea surface temperature and Patagonian Ice Sheet changes off southernmost Chile (53°S) over the past ~60 kyr. *Paleoceanography* **26**.
- Carter L., McCave I. N. and Williams M. J. M. (2008) Chapter 4 Circulation and Water Masses of the Southern Ocean: A Review. *Dev. Earth Environ. Sci.* **8**, 85–114.
- Chabaux F., Riotte J. and Dequincey O. (2003) U-Th-Ra fractionations during weathering and river transport. *Rev. Mineral. Geochemistry* **52**, 533–576.
- Chaigneau A. and Pizarro O. (2005) Surface circulation and fronts of the South Pacific Ocean, east of 120°W. *Geophys. Res. Lett.* **32**.
- Chase Z., Anderson R. F., Fleisher M. Q. and Kubik P. W. (2003) Accumulation of biogenic and lithogenic material in the Pacific sector of the Southern Ocean during the past 40,000 years. *Deep. Res. Part II Top. Stud. Oceanogr.* **50**, 799–832.
- Chase Z. (2008) Sediment Signatures of U- and Th-Series Nuclides and their Application as Paleoceanographic Tracers. In *U-Th Series Nuclides in Aquatic Systems* (eds. S. Krishnaswami and J. K. Cochran). Radioactivity in the Environment. Elsevier. pp. 383–416.
- Chase Z., Kohfeld K. E. and Matsumoto K. (2015) Controls on biogenic silica burial in the Southern Ocean. *Global Biogeochem. Cycles* **29**, 1599–1616.
- Chen J., Chen Y., Liu L., Ji J., Balsam W., Sun Y. and Lu H. (2006) Zr/Rb ratio in the Chinese loess sequences and its implication for changes in the East Asian winter monsoon strength. *Geochim. Cosmochim. Acta* **70**, 1471–1482.
- Cheng H., Lawrence Edwards R., Shen C.-C., Polyak V. J., Asmerom Y., Woodhead J., Hellstrom J., Wang Y., Kong X., Spötl C., Wang X. and Calvin Alexander E. (2013) Improvements in ²³⁰Th dating, ²³⁰Th and ²³⁴U half-life values, and U-Th isotopic measurements by multi-collector inductively coupled plasma mass spectrometry. *Earth*

- Planet. Sci. Lett.* **371–372**, 82–91.
- Chiang J. C. H., Lee S. Y., Putnam A. E. and Wang X. (2014) South Pacific Split Jet, ITCZ shifts, and atmospheric North-South linkages during abrupt climate changes of the last glacial period. *Earth Planet. Sci. Lett.* **406**, 233–246.
- Chiang J. C. H., Tokos K. S., Lee S. Y. and Matsumoto K. (2018) Contrasting Impacts of the South Pacific Split Jet and the Southern Annular Mode Modulation on Southern Ocean Circulation and Biogeochemistry. *Paleoceanogr. Paleoclimatology* **33**, 2–20.
- Chiswell S. M. (1994) Variability in sea surface temperature around New Zealand from AVHRR images. *New Zeal. J. Mar. Freshw. Res.* **28**, 179–192.
- Chiswell S. M., Bostock H. C., Sutton P. J. H. and Williams M. J. M. (2015) Physical oceanography of the deep seas around New Zealand: a review. *New Zeal. J. Mar. Freshw. Res.* **49**, 286–317.
- Cloern J. E., Canuel E. A. and Harris D. (2002) Stable carbon and nitrogen isotope composition of aquatic and terrestrial plants of the San Francisco Bay estuarine system. *Limnol. Oceanogr.* **47**, 713–729.
- Cogez A., Meynadier L., Allègre C., Limmois D., Herman F. and Gaillardet J. (2015) Constraints on the role of tectonic and climate on erosion revealed by two time series analysis of marine cores around New Zealand. *Earth Planet. Sci. Lett.* **410**, 174–185.
- Comiso J. C. (2003) Warming trends in the Arctic from clear sky satellite observations. *J. Clim.* **16**, 3498–3510.
- Conte M. H., Sicre M., Rühlemann C., Weber J. C., Schulte S., Schulz-Bull D. and Blanz T. (2006) Global temperature calibration of the alkenone unsaturation index (U_{37}^K) in surface waters and comparison with surface sediments. *Geochemistry, Geophys. Geosystems* **7**.
- Cowie J. D. (1964) Loess in the Manawatu district, New Zealand. *New Zeal. J. Geol. Geophys.* **7**, 389–396.
- Cowie R. O. M., Maas E. W. and Ryan K. G. (2011) Archaeal diversity revealed in Antarctic sea ice. *Antarct. Sci.* **23**, 531–536.
- Cunningham S. A., Alderson S. G., King B. A. and Brandon M. A. (2003) Transport and variability of the Antarctic Circumpolar Current in Drake Passage. *J. Geophys. Res. Ocean.* **108**.
- Dasch E. J. (1969) Strontium isotopes in weathering profiles, deep-sea sediments, and sedimentary rocks. *Geochim. Cosmochim. Acta* **33**, 1521–1552.
- De Deckker P., Norman M., Goodwin I. D., Wain A. and Gingele F. X. (2010) Lead isotopic

- evidence for an Australian source of aeolian dust to Antarctica at times over the last 170,000 years. *Palaeogeogr. Palaeoclimatol. Palaeoecol.* **285**, 205–223.
- Delmonte B., Basile-Doelsch I., Petit J.-R., Maggi V., Revel-Rolland M., Michard A., Jagoutz E. and Grousset F. (2004a) Comparing the Epica and Vostok dust records during the last 220,000 years: stratigraphical correlation and provenance in glacial periods. *Earth-Science Rev.* **66**, 63–87.
- Delmonte B., Petit J. R., Andersen K. K., Basile-Doelsch I., Maggi V. and Lipenkov V. Y. (2004b) Dust size evidence for opposite regional atmospheric circulation changes over east Antarctica during the last climatic transition. *Clim. Dyn.* **23**, 427–438.
- Delmonte B., Andersson P. S., Schöberg H., Hansson M., Petit J. R., Delmas R., Gaiero D. M., Maggi V. and Frezzotti M. (2010) Geographic provenance of aeolian dust in East Antarctica during Pleistocene glaciations: preliminary results from Talos Dome and comparison with East Antarctic and new Andean ice core data. *Quat. Sci. Rev.* **29**, 256–264.
- Delmonte B., Paleari C. I., Andò S., Garzanti E., Andersson P. S., Petit J. R., Crosta X., Narcisi B., Baroni C., Salvatore M. C., Baccolo G. and Maggi V. (2017) Causes of dust size variability in central East Antarctica (Dome B): Atmospheric transport from expanded South American sources during Marine Isotope Stage 2. *Quat. Sci. Rev.* **168**, 55–68.
- Denton G. H., Anderson R. F., Toggweiler J. R., Edwards R. L., Schaefer J. M. and Putnam A. E. (2010) The Last Glacial Termination. *Science*. **328**, 1652–1656.
- Després V. R., Huffman J. A., Burrows S. M., Hoose C., Safatov A. S., Buryak G., Fröhlich-Nowoisky J., Elbert W., Andreae M. O., Pöschl U. and Jaenicke R. (2012) Primary biological aerosol particles in the atmosphere: a review. *Tellus B Chem. Phys. Meteorol.* **64**.
- Dickin A. P. (1995a) Lead isotopes. In *Radiogenic Isotope Geology* Cambridge University Press, Cambridge. pp. 104–133.
- Dickin A. P. (1995b) The Rb-Sr method. In *Radiogenic Isotope Geology* Cambridge University Press, Cambridge. pp. 39–69.
- Dickin A. P. (1995c) The Sm-Nd method. In *Radiogenic Isotope Geology* Cambridge University Press, Cambridge. pp. 69–104.
- Diekmann B. and Kuhn G. (2002) Sedimentary record of the mid-Pleistocene climate transition in the southeastern South Atlantic (ODP Site 1090). *Palaeogeogr. Palaeoclimatol. Palaeoecol.* **182**, 241–258.
- Dunk R. M., Mills R. A. and Jenkins W. J. (2002) A reevaluation of the oceanic uranium budget

- for the Holocene. *Chem. Geol.* **190**, 45–67.
- Eden D. N. and Hammond A. P. (2003) Dust accumulation in the New Zealand region since the last glacial maximum. *Quat. Sci. Rev.* **22**, 2037–2052.
- Eglinton G. and Hamilton R. J. (1967) Leaf epicuticular waxes. *Science*. **156**, 1322–1335.
- Eglinton T. I. and Eglinton G. (2008) Molecular proxies for paleoclimatology. *Earth Planet. Sci. Lett.* **275**, 1–16.
- Ekström M., McTainsh G. H. and Chappell A. (2004) Australian dust storms: Temporal trends and relationships with synoptic pressure distributions (1960–99). *Int. J. Climatol.* **24**, 1581–1599.
- Elling F. J., Könneke M., Lipp J. S., Becker K. W., Gagen E. J. and Hinrichs K.-U. (2014) Effects of growth phase on the membrane lipid composition of the thaumarchaeon *Nitrosopumilus maritimus* and their implications for archaeal lipid distributions in the marine environment. *Geochim. Cosmochim. Acta* **141**, 579–597.
- EPICA Community Members (2006) One-to-one coupling of glacial climate variability in Greenland and Antarctica. *Nature* **444**, 195–198.
- Esper O. and Gersonde R. (2014) Quaternary surface water temperature estimations: New diatom transfer functions for the Southern Ocean. *Palaeogeogr. Palaeoclimatol. Palaeoecol.* **414**, 1–19.
- Feng J. L., Hu Z. G., Ju J. T. and Zhu L. P. (2011) Variations in trace element (including rare earth element) concentrations with grain sizes in loess and their implications for tracing the provenance of eolian deposits. *Quat. Int.* **236**, 116–126.
- Ferrari R., Provost C., Park Y., Sennéchaël N., Koenig Z., Sekma H., Garric G. and Bourdallé-Badie R. (2014) Heat fluxes across the Antarctic Circumpolar Current in Drake Passage: Mean flow and eddy contributions. *J. Geophys. Res. Ocean.* **119**, 6381–6402.
- Fietz S., Martínez-García A., Huguet C., Rueda G. and Rosell-Melé A. (2011) Constraints in the application of the Branched and Isoprenoid Tetraether index as a terrestrial input proxy. *J. Geophys. Res. Ocean.* **116**.
- Fietz S., Prahel F. G., Moraleda N. and Rosell-Melé A. (2013) Eolian transport of glycerol dialkyl glycerol tetraethers (GDGTs) off northwest Africa. *Org. Geochem.* **64**, 112–118.
- Firing Y. L., Chereskin T. K. and Matzloff M. R. (2011) Vertical structure and transport of the Antarctic Circumpolar Current in Drake Passage from direct velocity observations. *J. Geophys. Res. Ocean.* **116**.
- Fischer H., Schmitt J., Lüthi D., Stocker T. F., Tschumi T., Parekh P., Joos F., Köhler P., Völker C., Gersonde R., Barbante C., Le Floch M., Raynaud D. and Wolff E. (2010) The

- role of Southern Ocean processes in orbital and millennial CO₂ variations - A synthesis. *Quat. Sci. Rev.* **29**, 193–205.
- Fletcher M. S. and Moreno P. I. (2012) Have the Southern Westerlies changed in a zonally symmetric manner over the last 14,000 years? A hemisphere-wide take on a controversial problem. *Quat. Int.* **253**, 32–46.
- Folk R. L. and Ward W. C. (1957) Brazos River bar: a study in the significance of grain size parameters. *J. Sediment. Petrol.* **27**, 3–32.
- Fornace K. L., Hughen K. A., Shanahan T. M., Fritz S. C., Baker P. A. and Sylva S. P. (2014) A 60,000-year record of hydrologic variability in the Central Andes from the hydrogen isotopic composition of leaf waxes in Lake Titicaca sediments. *Earth Planet. Sci. Lett.* **408**, 263–271.
- Francois R., Frank M., Rutgers van der Loeff M. M. and Bacon M. P. (2004) ²³⁰Th normalization: An essential tool for interpreting sedimentary fluxes during the late Quaternary. *Paleoceanography* **19**.
- Fröhlich-Nowoisky J., Ruzene Nespoli C., Pickersgil D. A., Galand P. E., Müller-Germann I., Nunes T., Gomes Cardoso J., Almeida S. M., Pio C., Andreae M. O., Conrad R., Pöschl U. and Després V. R. (2014) Diversity and seasonal dynamics of airborne archaea. *Biogeosciences* **11**, 6067–6079.
- Gaiero D. M., Probst J. L., Depetris P. J., Bidart S. M. and Leleyter L. (2003) Iron and other transition metals in Patagonian riverborne and windborne materials: Geochemical control and transport to the southern South Atlantic Ocean. *Geochim. Cosmochim. Acta* **67**, 3603–3623.
- Gaiero D. M., Simonella L., Gassó S., Gili S., Stein A. F., Sosa P., Becchio R., Arce J. and Marelli H. (2013) Ground/satellite observations and atmospheric modeling of dust storms originating in the high Puna-Altiplano deserts (South America): Implications for the interpretation of paleo-climatic archives. *J. Geophys. Res. Atmos.* **118**, 3817–3831.
- Garreaud R. D., Vuille M., Compagnucci R. and Marengo J. (2009) Present-day South American climate. *Palaeogeogr. Palaeoclimatol. Palaeoecol.* **281**, 180–195.
- Garreaud R., Lopez P., Minvielle M. and Rojas M. (2013) Large-scale control on the Patagonian climate. *J. Clim.* **26**, 215–230.
- Geibert W., Rutgers van der Loeff M. M., Usbeck R., Gersonde R., Kuhn G. and Seeberg-Elverfeldt J. (2005) Quantifying the opal belt in the Atlantic and southeast Pacific sector of the Southern Ocean by means of ²³⁰Th normalization. *Global Biogeochem. Cycles* **19**.
- Gersonde R. (1995) The Expedition of the Research Vessel “Polarstern” to the Southeast

- Pacific in 1995 (ANT-XII/4). Alfred Wegener Institute, Bremerhaven.
- Gersonde R. (2001) The Expedition of the Research Vessel “Polarstern” to the South Pacific in 2001 (ANT-XVIII/5a). Alfred Wegener Institute, Bremerhaven.
- Gersonde R. (2011) The Expedition of the Research Vessel “Polarstern” to the polar South Pacific in 2009/2010 (ANT-XXXVI/2-BIPOMAC), *Berichte zur Polar- und Meeresforschung*. Alfred Wegener Institute, Bremerhaven.
- Gili S., Gaiero D. M., Goldstein S. L., Chemale F., Koester E., Jweda J., Vallelonga P. and Kaplan M. R. (2016) Provenance of dust to Antarctica: A lead isotopic perspective. *Geophys. Res. Lett.* **43**, 2291–2298.
- Gili S., Gaiero D. M., Goldstein S. L., Chemale F., Jweda J., Kaplan M. R., Becchio R. A. and Koester E. (2017) Glacial/interglacial changes of Southern Hemisphere wind circulation from the geochemistry of South American dust. *Earth Planet. Sci. Lett.* **469**, 98–109.
- Gingele F. X. and De Deckker P. (2005) Clay mineral, geochemical and Sr–Nd isotopic fingerprinting of sediments in the Murray–Darling fluvial system, southeast Australia. *Aust. J. Earth Sci.* **52**, 965–974.
- Goldstein S. L., O’Nions R. K. and Hamilton P. J. (1984) A Sm–Nd isotopic study of atmospheric dusts and particulates from major river systems. *Earth Planet. Sci. Lett.* **70**, 221–236.
- Gomes L., Bergametti G., Coudé-Gaussen G. and Rognon P. (1990) Submicron desert dusts: A sandblasting process. *J. Geophys. Res.* **95**, 13927.
- Goni M. A. and Hedges J. I. (1995) Sources and reactivities of marine-derived organic matter in coastal sediments as determined by alkaline CuO oxidation. *Geochim. Cosmochim. Acta* **59**, 2965–2981.
- Gordon A. L. (1986) Interocean exchange of thermocline water. *J. Geophys. Res.* **91**, 5037.
- Goudie A. S. (2008) The History and Nature of Wind Erosion in Deserts. *Annu. Rev. Earth Planet. Sci.* **36**, 97–119.
- Griffin D. W., Westphal D. L. and Gray M. A. (2006) Airborne microorganisms in the African desert dust corridor over the mid-Atlantic ridge, Ocean Drilling Program, Leg 209. *Aerobiologia (Bologna)*. **22**, 211–226.
- Grousset F. E. and Biscaye P. E. (2005) Tracing dust sources and transport patterns using Sr, Nd and Pb isotopes. *Chem. Geol.* **222**, 149–167.
- Hall I. R. and McCave I. N. (2000) Palaeocurrent reconstruction, sediment and thorium focussing on the Iberian margin over the last 140 ka. *Earth Planet. Sci. Lett.* **178**, 151–164.

- Hall I. R., McCave I. N., Shackleton N. J., Weedon G. P. and Harris S. E. (2001) Intensified deep Pacific inflow and ventilation in Pleistocene glacial times. *Nature* **412**, 809–812.
- Heath R. A. (1981) Oceanic fronts around southern New Zealand. *Deep Sea Res. Part A. Oceanogr. Res. Pap.* **28**, 547–560.
- Henderson G. M. (2002) Seawater ($^{234}\text{U}/^{238}\text{U}$) during the last 800 thousand years. *Earth Planet. Sci. Lett.* **199**, 97–110.
- Henderson G. M. and Anderson R. F. (2003) The U-series toolbox for paleoceanography. *Rev. Mineral. Geochemistry* **52**, 493–531.
- Hesse P. P. (1994) The record of continental dust in Tasman Sea sediments. *Quat. Sci. Rev.* **13**, 257–272.
- Hesse P. P. and McTainsh G. H. (1999) Last Glacial maximum to early Holocene wind strength in the mid latitudes of the Southern Hemisphere from aeolian dust in the Tasman Sea. *Quat. Res.* **52**, 343–349.
- Hesse P. P. and McTainsh G. H. (2003) Australian dust deposits: modern processes and the Quaternary record. *Quat. Sci. Rev.* **22**, 2007–2035.
- Hillenbrand C. D. (2000) Glaciomarine sedimentation on the continental margins of the Amundsen and Bellingshausen Seas, West Antarctica—indications for paleoenvironmental changes during the Quaternary climatic cycles. *Reports Polar Res.* **346**, 182.
- Ho S. L., Mollenhauer G., Lamy F., Martínez-García A., Mohtadi M., Gersonde R., Hebbeln D., Nunez-Ricardo S., Rosell-Melé A. and Tiedemann R. (2012) Sea surface temperature variability in the Pacific sector of the Southern Ocean over the past 700 kyr. *Paleoceanography* **27**.
- Ho S. L., Mollenhauer G., Fietz S., Martínez-García A., Lamy F., Rueda G., Schipper K., Méheust M., Rosell-Melé A., Stein R. and Tiedemann R. (2014) Appraisal of TEX₈₆ and TEX^L₈₆ thermometries in subpolar and polar regions. *Geochim. Cosmochim. Acta* **131**, 213–226.
- Ho S. L. and Laepple T. (2016) Flat meridional temperature gradient in the early Eocene in the subsurface rather than surface ocean. *Nat. Geosci.* **9**, 606.
- Hogg A. M. C. (2010) An Antarctic Circumpolar Current driven by surface buoyancy forcing. *Geophys. Res. Lett.* **37**, 1–5.
- Honda M., Yabuki S. and Shimizu H. (2004) Geochemical and isotopic studies of aeolian sediments in China. *Sedimentology* **51**, 211–230.
- Honjo S., Francois R., Manganini S., Dymond J. and Collier R. (2000) Particle fluxes to the interior of the Southern Ocean in the Western Pacific sector along 170°W. *Deep Sea Res.*

- Part II Top. Stud. Oceanogr.* **47**, 3521–3548.
- Hopmans E. C., Schouten S., Pancost R. D., van der Meer M. T. J. and Sinninghe Damasté J. S. (2000) Analysis of intact tetraether lipids in archaeal cell material and sediments by high performance liquid chromatography/atmospheric pressure chemical ionization mass spectrometry. *Rapid Commun. Mass Spectrom.* **14**, 585–589.
- Hopmans E. C., Weijers J. W. H., Schefuß E., Herfort L., Damsté J. S. S. and Schouten S. (2004) A novel proxy for terrestrial organic matter in sediments based on branched and isoprenoid tetraether lipids. *Earth Planet. Sci. Lett.* **224**, 107–116.
- Horwitz E. P., Dietz M. L. and Chiarizia R. (1992) A novel strontium-selective extraction chromatographic resin. *Solvent Extr. Ion Exch.* **10**, 313–336.
- Huguet C., Cartes J. E., Damsté J. S. S. and Schouten S. (2006a) Marine crenarchaeotal membrane lipids in decapods: Implications for the TEX₈₆ paleothermometer. *Geochemistry, Geophys. Geosystems* **7**.
- Huguet C., Hopmans E. C., Febo-Ayala W., Thompson D. H., Damsté J. S. S. and Schouten S. (2006b) An improved method to determine the absolute abundance of glycerol dibiphytanyl glycerol tetraether lipids. *Org. Geochem.* **37**, 1036–1041.
- Huguet C., Kim J.-H., de Lange G. J., Damsté J. S. S. and Schouten S. (2009) Effects of long term oxic degradation on the U₃₇^K, TEX₈₆ and BIT organic proxies. *Org. Geochem.* **40**, 1188–1194.
- Huguet C., Fietz S. and Rosell-Melé A. (2013) Global distribution patterns of hydroxy glycerol dialkyl glycerol tetraethers. *Org. Geochem.* **57**, 107–118.
- Hurley S. J., Elling F. J., Könneke M., Buchwald C., Wankel S. D., Santoro A. E., Lipp J. S., Hinrichs K.-U. and Pearson A. (2016) Influence of ammonia oxidation rate on thaumarchaeal lipid composition and the TEX₈₆ temperature proxy. *Proc. Natl. Acad. Sci.* **113**, 7762–7767.
- Huybers P. and Wunsch C. (2010) Paleophysical oceanography with an emphasis on transport rates. *Ann. Rev. Mar. Sci.* **2**, 1–34.
- Inatsu M. and Hoskins B. J. (2004) The Zonal Asymmetry of the Southern Hemisphere Winter Storm Track. *J. Clim.* **17**, 4882–4892.
- Jacobsen S. B. and Wasserburg G. J. (1980) Sm-Nd isotopic evolution of chondrites. *Earth Planet. Sci. Lett.* **50**, 139–155.
- Jaeschke A., Eickmann B., Lang S. Q., Bernasconi S. M., Strauss H. and Früh-Green G. L. (2014) Biosignatures in chimney structures and sediment from the Loki's Castle low-

- temperature hydrothermal vent field at the Arctic Mid-Ocean Ridge. *Extremophiles* **18**, 545–560.
- Jaeschke A., Wengler M., Hefter J., Ronge T. A., Geibert W., Mollenhauer G., Gersonde R. and Lamy F. (2017) A biomarker perspective on dust, productivity, and sea surface temperature in the Pacific sector of the Southern Ocean. *Geochim. Cosmochim. Acta* **204**, 120–139.
- Jickells T. D., An Z. S., Andersen K. K., Baker A. R., Bergametti G., Brooks N., Cao J. J., Boyd P. W., Duce R. A., Hunter K. A., Kawahata H., Kubilay N., LaRoche J., Liss P. S., Mahowald N., Prospero J. M., Ridgwell A. J., Tegen I. and Torres R. (2005) Global Iron Connections Between Desert Dust, Ocean Biogeochemistry, and Climate. *Science*. **308**, 67–71.
- Johnson G. C. and Bryden H. L. (1989) On the size of the Antarctic Circumpolar Current. *Deep Sea Res.* **36**, 39–53.
- Jouzel J., Masson-Delmotte V., Cattani O., Dreyfus G., Falourd S., Hoffmann G., Minster B., Nouet J., Barnola J. M., Chappellaz J., Fischer H., Gallet J. C., Johnsen S., Leuenberger M., Loulergue L., Luethi D., Oerter H., Parrenin F., Raisbeck G., Raynaud D., Schilt A., Schwander J., Selmo E., Souchez R., Spahni R., Stauffer B., Steffensen J. P., Stenni B., Stocker T. F., Tison J. L., Werner M. and Wolff E. W. (2007) Orbital and Millennial Antarctic Climate Variability over the Past 800,000 Years. *Science*. **317**, 793–796.
- Jung S. J. A., Davies G. R., Ganssen G. M. and Kroon D. (2004) Stepwise Holocene aridification in NE Africa deduced from dust-borne radiogenic isotope records. *Earth Planet. Sci. Lett.* **221**, 27–37.
- Jweda J., Bolge L., Class C. and Goldstein S. L. (2016) High Precision Sr-Nd-Hf-Pb Isotopic Compositions of USGS Reference Material BCR-2. *Geostand. Geoanalytical Res.* **40**, 101–115.
- Kaiser J. and Lamy F. (2010) Links between Patagonian Ice Sheet fluctuations and Antarctic dust variability during the last glacial period (MIS 4-2). *Quat. Sci. Rev.* **29**, 1464–1471.
- Kanayama S., Yabuki S., Zeng F., LIU M., SHEN Z., Liu L., Yanagisawa F. and Abe O. (2005) Size-Dependent Geochemical Characteristics of Asian Dust. *J. Meteorol. Soc. Japan. Ser. II* **83A**, 107–120.
- Karner M. B., DeLong E. F. and Karl D. M. (2001) Archaeal dominance in the mesopelagic zone of the Pacific Ocean. *Nature* **409**, 507.
- Kawamura K. (1995) Land-derived lipid class compounds in deep-sea sediments and marine aerosols from the North Pacific. In *Biochemical Processes and Ocean Flux in the Western*

- Pacific* (eds. H. Sakai and Y. Nozaki). Terra Scientific Publishing Company. pp. 31–51.
- Kienast S. S., Winckler G., Lippold J., Albani S. and Mahowald N. M. (2016) Tracing dust input to the global ocean using thorium isotopes in marine sediments: ThoroMap. *Global Biogeochem. Cycles*, 1526–1541.
- Kim J. H., Hugué C., Zonneveld K. A. F., Versteegh G. J. M., Roeder W., Damsté J. S. S. and Schouten S. (2009) An experimental field study to test the stability of lipids used for the TEX₈₆ and U₃₇^K palaeothermometers. *Geochim. Cosmochim. Acta* **73**, 2888–2898.
- Kim J. H., van der Meer J., Schouten S., Helmke P., Willmott V., Sangiorgi F., Koç N., Hopmans E. C. and Damsté J. S. S. (2010) New indices and calibrations derived from the distribution of crenarchaeal isoprenoid tetraether lipids: Implications for past sea surface temperature reconstructions. *Geochim. Cosmochim. Acta* **74**, 4639–4654.
- Kim J. H., Crosta X., Willmott V., Renssen H., Bonnin J., Helmke P., Schouten S. and Damsté J. S. S. (2012a) Holocene subsurface temperature variability in the eastern Antarctic continental margin. *Geophys. Res. Lett.* **39**.
- Kim J. H., Romero O. E., Lohmann G., Donner B., Laepple T., Haam E. and Damsté J. S. S. (2012b) Pronounced subsurface cooling of North Atlantic waters off Northwest Africa during Dansgaard-Oeschger interstadials. *Earth Planet. Sci. Lett.* **339–340**, 95–102.
- Klaver G. T. and van Weering T. C. E. (1993) Rare Earth Element fractionation by selective sediment dispersal in surface sediments: the Skagerrak. *Mar. Geol.* **111**, 345–359.
- Knight A. W., McTainsh G. H. and Simpson R. W. (1995) Sediment loads in an Australian dust storm: implications for present and past dust processes. *Catena* **24**, 195–213.
- Knorr G. and Lohmann G. (2003) Southern Ocean origin for the resumption of Atlantic thermohaline circulation during deglaciation. *Nature* **424**, 532.
- Koch D., Schmidt G. A. and Field C. V. (2006) Sulfur, sea salt, and radionuclide aerosols in GISS ModelE. *J. Geophys. Res.* **111**.
- Koenig Z., Provost C., Ferrari R., Sennéchaël N. and Rio M.-H. (2014) Volume transport of the Antarctic Circumpolar Current: Production and validation of a 20 year long time series obtained from in situ and satellite observations. *J. Geophys. Res. Ocean.* **119**, 5407–5433.
- Kohfeld K. E. and Harrison S. P. (2001) DIRTMAP: The geological record of dust. *Earth-Science Rev.* **54**, 81–114.
- Kohfeld K. E., Quéré C. Le, Harrison S. P. and Anderson R. F. (2005) Role of Marine Biology in Glacial-Interglacial CO₂ Cycles. *Science*. **308**, 74–78.
- Kohfeld K. E., Graham R. M., de Boer A. M., Sime L. C., Wolff E. W., Le Quéré C. and Bopp

- L. (2013) Southern Hemisphere westerly wind changes during the Last Glacial Maximum: Paleo-data synthesis. *Quat. Sci. Rev.* **68**, 76–95.
- Könneke M., Bernhard A. E., de la Torre J. R., Walker C. B., Waterbury J. B. and Stahl D. A. (2005) Isolation of an autotrophic ammonia-oxidizing marine archaeon. *Nature* **437**, 543.
- Lambert F., Delmonte B., Petit J. R., Bigler M., Kaufmann P. R., Hutterli M. A., Stocker T. F., Ruth U., Steffensen J. P. and Maggi V. (2008) Dust-climate couplings over the past 800,000 years from the EPICA Dome C ice core. *Nature* **452**, 616–619.
- Lambert F., Bigler M., Steffensen J. P., Hutterli M. and Fischer H. (2012) Centennial mineral dust variability in high-resolution ice core data from Dome C, Antarctica. *Clim. Past* **8**, 609–623.
- Lamy F., Kaiser J., Ninnemann U., Hebbeln D., Arz H. W. and Stoner J. (2004) Antarctic Timing of Surface Water Changes off Chile and Patagonian Ice Sheet Response. *Science*. **304**, 1959–1962.
- Lamy F., Kaiser J., Arz H. W., Hebbeln D., Ninnemann U., Timm O., Timmermann A. and Toggweiler J. R. (2007) Modulation of the bipolar seesaw in the Southeast Pacific during Termination 1. *Earth Planet. Sci. Lett.* **259**, 400–413.
- Lamy F., Kilian R., Arz H. W., Francois J.-P., Kaiser J., Prange M. and Steinke T. (2010) Holocene changes in the position and intensity of the southern westerly wind belt. *Nat. Geosci.* **3**, 695–699.
- Lamy F., Gersonde R., Winckler G., Esper O., Jaeschke A., Kuhn G., Ullermann J., Martinez-Garcia A., Lambert F. and Kilian R. (2014) Increased Dust Deposition in the Pacific Southern Ocean During Glacial Periods. *Science*. **343**, 403–407.
- Lamy F., Arz H. W., Kilian R., Lange C. B., Lembke-Jene L., Wengler M., Kaiser J., Baeza-Urrea O., Hall I. R., Harada N. and Tiedemann R. (2015) Glacial reduction and millennial-scale variations in Drake Passage throughflow. *Proc. Natl. Acad. Sci.* **112**, 13496–13501.
- Latorre C., Moreno P. I., Vargas G., Maldonado A., Villa-Martínez R., Armesto J. J., Villagrán C., Pino M., Núñez L. and Grosjean M. (2007) Late Quaternary environments and palaeoclimate. In *The Geology of Chile* (eds. T. Moreno and W. Gibbons). London Geological Society Press.
- Lea D. W., Pak D. K., Belanger C. L., Spero H. J., Hall M. A. and Shackleton N. J. (2006) Paleoclimate history of Galápagos surface waters over the last 135,000yr. *Quat. Sci. Rev.* **25**, 1152–1167.
- Li F., Ginoux P. and Ramaswamy V. (2008) Distribution, transport, and deposition of mineral dust in the Southern Ocean and Antarctica: Contribution of major sources. *J. Geophys.*

- Res. Atmos.* **113**, 1–15.
- Li F., Ginoux P. and Ramaswamy V. (2010) Transport of Patagonian dust to Antarctica. *J. Geophys. Res. Atmos.* **115**.
- Liu Z., Shin S., Otto-Bliesner B., Kutzbach J. E., Brady E. C. and Lee D. (2002) Tropical cooling at the last glacial maximum and extratropical ocean ventilation1. *Geophys. Res. Lett.* **29**, 44–48.
- Locarnini R. A. M., Antonov J. I., Boyer T. P., Garcia H. E., Baranova O. K., Zweng M. M. and Johnson D. R. (2010) *World Ocean Atlas 2009: Volume 1: Temperature.*, U.S Government Printing Office.
- Loosmore G. A. and Hunt J. R. (2000) Dust resuspension without saltation. *J. Geophys. Res. Atmos.* **105**, 20663–20671.
- Lopes dos Santos R. A., Spooner M. I., Barrows T. T., Deckker P. De, Damsté J. S. S. and Schouten S. (2013) Comparison of organic (U_{37}^K , TEX^H_{86} , LDI) and faunal proxies (foraminiferal assemblages) for reconstruction of late Quaternary sea surface temperature variability from offshore southeastern Australia. *Paleoceanography* **28**, 377–387.
- Lüthi D., Le Floch M., Bereiter B., Blunier T., Barnola J.-M., Siegenthaler U., Raynaud D., Jouzel J., Fischer H., Kawamura K. and Stocker T. F. (2008) High-resolution carbon dioxide concentration record 650,000–800,000 years before present. *Nature* **453**, 379.
- Maher B. A. and Dennis P. F. (2001) Evidence against dust-mediated control of glacial–interglacial changes in atmospheric CO₂. *Nature* **411**, 176.
- Maher B. A., Prospero J. M., Mackie D., Gaiero D., Hesse P. P. and Balkanski Y. (2010) Global connections between aeolian dust, climate and ocean biogeochemistry at the present day and at the last glacial maximum. *Earth-Science Rev.* **99**, 61–97.
- Mahowald N. M., Muhs D. R., Levis S., Rasch P. J., Yoshioka M., Zender C. S. and Luo C. (2006) Change in atmospheric mineral aerosols in response to climate: Last glacial period, preindustrial, modern, and doubled carbon dioxide climates. *J. Geophys. Res. Atmos.* **111**.
- Makou M. C., Oppo D. W. and Curry W. B. (2010) South Atlantic intermediate water mass geometry for the last glacial maximum from foraminiferal Cd/Ca. *Paleoceanography* **25**.
- Manganelli M., Malfatti F., Samo T. J., Mitchell B. G., Wang H. and Azam F. (2009) Major Role of Microbes in Carbon Fluxes during Austral Winter in the Southern Drake Passage. *PLoS One* **4**, 1–11.
- Marshall J. and Speer K. (2012) Closure of the meridional overturning circulation through Southern Ocean upwelling. *Nat. Geosci.* **5**, 171–180.

- Marticorena B. (2014) Dust Production Mechanisms. In *Mineral Dust A Key Player in the Earth System* (eds. P. Knippertz and J.-B. W. Stuut). Springer. pp. 93–120.
- Martin E. E., Blair S. W., Kamenov G. D., Scher H. D., Bourbon E., Basak C. and Newkirk D. N. (2010) Extraction of Nd isotopes from bulk deep sea sediments for paleoceanographic studies on Cenozoic time scales. *Chem. Geol.* **269**, 414–431.
- Martin J. H. (1990) Glacial-interglacial CO₂ change: The Iron Hypothesis. *Paleoceanography* **5**, 1–13.
- Martínez-García A., Rosell-Melé A., Geibert W., Gersonde R., Masqué P., Gaspari V. and Barbante C. (2009) Links between iron supply, marine productivity, sea surface temperature, and CO₂ over the last 1.1 Ma. *Paleoceanography* **24**, 1–14.
- Martínez-García A., Rosell-Melé A., Jaccard S. L., Geibert W., Sigman D. M. and Haug G. H. (2011) Southern Ocean dust–climate coupling over the past four million years. *Nature* **476**, 312–315.
- Martínez-García A., Sigman D. M., Ren H., Anderson R. F., Straub M., Hodell D. A., Jaccard S. L., Eglinton T. I. and Haug G. H. (2014) Iron fertilization of the subantarctic ocean during the last ice age. *Science*. **343**, 1347–1350.
- Martínez-García A. and Winckler G. (2014) Iron fertilization in the glacial ocean. *Past Glob. Chang.* 82–83.
- Martínez-Méndez G., Hebbeln D., Mohtadi M., Lamy F., Pol-Holz R. De, Reyes-Macaya D. and Freudenthal T. (2013) Changes in the advection of Antarctic Intermediate Water to the northern Chilean coast during the last 970 kyr. *Paleoceanography* **28**, 607–618.
- Marx S. K., Kamber B. S. and McGowan H. A. (2005) Provenance of long-travelled dust determined with ultra-trace-element composition: A pilot study with samples from New Zealand glaciers. *Earth Surf. Process. Landforms* **30**, 699–716.
- Marx S. K. and McGowan H. A. (2005) Dust transportation and deposition in a superhumid environment, West Coast, South Island, New Zealand. *Catena* **59**, 147–171.
- Marx S. K. and Kamber B. S. (2010) Trace-element systematics of sediments in the Murray-Darling Basin, Australia: Sediment provenance and palaeoclimate implications of fine scale chemical heterogeneity. *Appl. Geochemistry* **25**, 1221–1237.
- Mashiotta T. A., Lea D. W. and Spero H. J. (1999) Glacial–interglacial changes in Subantarctic sea surface temperature and $\delta^{18}\text{O}$ -water using foraminiferal Mg. *Earth Planet. Sci. Lett.* **170**, 417–432.
- Mazaud A., Michel E., Dewilde F. and Turon J. L. (2010) Variations of the Antarctic Circumpolar Current intensity during the past 500 ka. *Geochemistry, Geophys.*

Geosystems **11**.

- McCave I. N., Manighetti B. and Robinson S. G. (1995) Sortable silt and fine sediment size/composition slicing: Parameters for palaeocurrent speed and palaeoceanography. *Paleoceanography* **10**, 593–610.
- McCave I. N. and Hall I. R. (2006) Size sorting in marine muds: Processes, pitfalls, and prospects for paleoflow-speed proxies. *Geochemistry, Geophys. Geosystems* **7**.
- McCave I. N., Crowhurst S. J., Kuhn G., Hillenbrand C. D. and Meredith M. P. (2014) Minimal change in antarctic circumpolar current flow speed between the last glacial and holocene. *Nat. Geosci.* **7**, 113–116.
- McGowan H. A., Kamber B., McTainsh G. H. and Marx S. K. (2005) High resolution provenancing of long travelled dust deposited on the Southern Alps, New Zealand. *Geomorphology* **69**, 208–221.
- McGowan H. and Clark A. (2008) Identification of dust transport pathways from Lake Eyre, Australia using Hysplit. *Atmos. Environ.* **42**, 6915–6925.
- McTainsh G. H. (1989) Quaternary aeolian dust processes and sediments in the Australian region. *Quat. Sci. Rev.* **8**, 235–253.
- Méheust M., Fahl K. and Stein R. (2013) Variability in modern sea surface temperature, sea ice and terrigenous input in the sub-polar North Pacific and Bering Sea: Reconstruction from biomarker data. *Org. Geochem.* **57**, 54–64.
- Meijers A. J. S. (2014) The Southern Ocean in the Coupled Model Intercomparison Project phase 5. *Philos. Trans. R. Soc. A Math. Phys. Eng. Sci.* **372**.
- Meredith M. P., Woodworth P. L., Chereskin T. K., Marshall D. P., Allison L. C., Bigg G. R., Donohue K., Heywood K. J., Hughes C. W., Hibbert A., Hogg A. M., Johnson H. L., Jullion L., King B. A., Leach H., Lenn Y., Maqueda M. A. M., Munday D. R., Garabato A. C. N., Provost C., Sallée J. and Sprintall J. (2011) Sustained monitoring of the Southern Ocean at the Drake Passage: Past achievements and future priorities. *Rev. Geophys.* **49**.
- Meyer I., Davies G. R. and Stuut J. B. W. (2011) Grain size control on Sr-Nd isotope provenance studies and impact on paleoclimate reconstructions: An example from deep-sea sediments offshore NW Africa. *Geochemistry, Geophys. Geosystems* **12**.
- Molina-Kescher M., Frank M. and Hathorne E. C. (2014) Nd and Sr isotope compositions of different phases of surface sediments in the South Pacific: Extraction of seawater signatures, boundary exchange, and detrital/dust provenance. *Geochemistry, Geophys. Geosystems* **15**, 3502–3520.
- Mollenhauer G., Basse A., Kim J.-H., Damsté J. S. S. and Fischer G. (2015) A four-year record

- of $U_{37}^{K'}$ and TEX₈₆-derived sea surface temperature estimates from sinking particles in the filamentous upwelling region off Cape Blanc, Mauritania. *Deep Sea Res. Part I Oceanogr. Res. Pap.* **97**, 67–79.
- Müller G. (1967) *Methods in Sedimentary Petrology*. Schweizerbart'sche Verlagsbuchhandlung, Stuttgart.
- Müller P. J., Kirst G., Ruhland G., von Storch I. and Rosell-Melé A. (1998) Calibration of the alkenone paleotemperature index $U_{37}^{K'}$ based on core-tops from the eastern South Atlantic and the global ocean (60°N–60°S). *Geochim. Cosmochim. Acta* **62**, 1757–1772.
- Munksgaard N. C., Lim K. and Parry D. L. (2003) Rare earth elements as provenance indicators in North Australian estuarine and coastal marine sediments. *Estuar. Coast. Shelf Sci.* **57**, 399–409.
- Muratli J. M., Chase Z., Mix A. C. and McManus J. (2009) Increased glacial-age ventilation of the Chilean margin by Antarctic Intermediate Water. *Nat. Geosci.* **3**, 23–26.
- Murray A. E., Preston C. M., Massana R., Taylor L. T., Blakis A., Wu K. and Delong E. F. (1998) Seasonal and spatial variability of bacterial and archaeal assemblages in the coastal waters near Anvers Island, Antarctica. *Appl. Environ. Microbiol.* **64**, 2585–2595.
- Neff P. D. and Bertler N. A. N. (2015) Trajectory modeling of modern dust transport to the Southern Ocean and Antarctica. *J. Geophys. Res. Atmos.* **120**, 9303–9322.
- Nelson C. S., Hendy I. L., Neil H. L., Hendy C. H. and Weaver P. P. E. (2000) Last glacial jetting of cold waters through the Subtropical Convergence zone in the Southwest Pacific off eastern New Zealand, and some geological implications. *Palaeogeogr. Palaeoclimatol. Palaeoecol.* **156**, 103–121.
- Noble T. L., Piotrowski A. M., Robinson L. F., McManus J. F., Hillenbrand C. D. and Bory A. J. M. (2012) Greater supply of Patagonian-sourced detritus and transport by the ACC to the Atlantic sector of the Southern Ocean during the last glacial period. *Earth Planet. Sci. Lett.* **317–318**, 374–385.
- Nodder S. D. and Northcote L. C. (2001) Episodic particulate fluxes at southern temperate mid-latitudes (42–45°S) in the Subtropical Front region, east of New Zealand. *Deep Sea Res. Part I Oceanogr. Res. Pap.* **48**, 833–864.
- Norte F. A., Ulke A. G., Simonelli S. C. and Viale M. (2008) The severe zonda wind event of 11 July 2006 east of the Andes Cordillera (Argentina): a case study using the BRAMS model. *Meteorol. Atmos. Phys.* **102**, 1–14.
- Okrusch M. and Matthes S. (2005) Einführung in die Geochemie. In *Mineralogie: Eine*

- Einführung in die spezielle Mineralogie, Petrologie und Lagerstättenkunde* Springer. pp. 447–475.
- Olbers D., Gouretsky V., Seiß G. and Schröter J. (1992) *The Hydrographic Atlas of the Southern Ocean*.
- Orsi A. H., Nowlin W. D. and Whithworth T. (1993) On the circulation and stratification of the Weddell Gyre. *Deep. Res. Part I Oceanogr. Res. Pap.* **40**, 169–203.
- Orsi A. H., Whitworth T. and Nowlin W. D. (1995) On the meridional extent and fronts of the Antarctic Circumpolar Current. *Deep. Res.* **42**, 641–673.
- Paul M., Bridgestock L., Rehkämper M., van DeFlierdt T. and Weiss D. (2015) High-precision measurements of seawater Pb isotope compositions by double spike thermal ionization mass spectrometry. *Anal. Chim. Acta* **863**, 59–69.
- Pearson A. and Ingalls A. E. (2013) Assessing the Use of Archaeal Lipids as Marine Environmental Proxies. *Annu. Rev. Earth Planet. Sci.* **41**, 359–384.
- Pelejero C., Calvo E., Barrows T. T., Logan G. A. and Deckker P. De (2006) South Tasman Sea alkenone palaeothermometry over the last four glacial/interglacial cycles. *Mar. Geol.* **230**, 73–86.
- Peterse F., Kim J.-H., Schouten S., Kristensen D. K., Koç N. and Damsté J. S. S. (2009) Constraints on the application of the MBT/CBT palaeothermometer at high latitude environments (Svalbard, Norway). *Org. Geochem.* **40**, 692–699.
- Pin C. and Zalduegui J. S. (1997) Sequential separation of light rare-earth elements, thorium and uranium by miniaturized extraction chromatography: Application to isotopic analyses of silicate rocks. *Anal. Chim. Acta* **339**, 79–89.
- Piper D. Z. (1974) Rare earth elements in the sediment cycle: A summary. *Chem. Geol.* **14**, 285–304.
- Prahl F. G. and Wakeham S. G. (1987) Calibration of unsaturation patterns in long-chain ketone compositions for palaeotemperature assessment. *Nature* **330**, 367.
- Prahl F. G., Rontani J.-F., Zabeti N., Walinsky S. E. and Sparrow M. A. (2010) Systematic pattern in U_{37}^K -Temperature residuals for surface sediments from high latitude and other oceanographic settings. *Geochim. Cosmochim. Acta* **74**, 131–143.
- Prospero J. M., Ginoux P., Torres O., Nicholson S. E. and Gill T. E. (2002) Environmental characterization of global sources of atmospheric soil dust identified with the NIMBUS 7 Total Ozone Mapping Spectrometer (TOMS) absorbing aerosol product. *Rev. Geophys.* **40**, 1–31.

- Qin W., Carlson L. T., Armbrust E. V., Devol A. H., Moffett J. W., Stahl D. A. and Ingalls A. E. (2015) Confounding effects of oxygen and temperature on the TEX₈₆ signature of marine Thaumarchaeota. *Proc. Natl. Acad. Sci.* **112**, 10979–10984.
- Raeside J. D. (1964) Loess Deposits of the South Island, New Zealand, and Soils Formed on them. *New Zeal. J. Geol. Geophys.* **7**, 811–838.
- Rebesco M., Larter R. D., Camerlenghi A. and Barker P. F. (1996) Giant sediment drifts on the continental rise west of the Antarctic Peninsula. *Geo-Marine Lett.* **16**, 65–75.
- Reeder M. J., Smith R. K., Deslandes R., Tapper N. J. and Mills G. A. (2000) Subtropical fronts observed during the 1996 Central Australian Fronts Experiment. *Aust. Meteorol. Mag.* **49**, 181–200.
- Reid J. L. (1986) On the total geostrophic circulation of the South Pacific Ocean: Flow patterns, tracers and transports. *Prog. Ocean.* **16**, 1–61.
- Reimer P. J., Bard E., Bayliss A., Beck J. W., Blackwell P. G., Ramsey C. B., Buck C. E., Cheng H., Edwards R. L., Friedrich M., Grootes P. M., Guilderson T. P., Haflidason H., Hajdas I., Hatté C., Heaton T. J., Hoffmann D. L., Hogg A. G., Hughen K. A., Kaiser K. F., Kromer B., Manning S. W., Niu M., Reimer R. W., Richards D. A., Scott E. M., Southon J. R., Staff R. A., Turney C. S. M. and van der Plicht J. (2013) IntCal13 and Marine13 Radiocarbon Age Calibration Curves 0–50,000 Years cal BP. *Radiocarbon* **55**, 1869–1887.
- Renault A., Provost C., Sennéchaël N., Barré N. and Kartavtseff A. (2011) Two full-depth velocity sections in the Drake Passage in 2006—Transport estimates. *Deep. Res. Part II Top. Stud. Oceanogr.* **58**, 2572–2591.
- Revel-Rolland M., De Deckker P., Delmonte B., Hesse P., Magee J., Basile-Doelsch I., Grousset F. and Bosch D. (2006) Eastern Australia: A possible source of dust in East Antarctica interglacial ice. *Earth Planet. Sci. Lett.* **249**, 1–13.
- Rojas M., Moreno P., Kageyama M., Crucifix M., Hewitt C., Abe-Ouchi A., Ohgaito R., Brady E. C. and Hope P. (2009) The Southern Westerlies during the last glacial maximum in PMIP2 simulations. *Clim. Dyn.* **32**, 525–548.
- Ronge T. A., Tiedemann R., Lamy F., Köhler P., Alloway B. V., De Pol-Holz R., Pahnke K., Southon J. and Wacker L. (2016) Radiocarbon constraints on the extent and evolution of the South Pacific glacial carbon pool. *Nat. Commun.* **7**, 1–11.
- Rontani J.-F., Beker B. and Volkman J. K. (2004) Long-chain alkenones and related compounds in the benthic haptophyte *Chrysotila lamellosa* Anand HAP 17. *Phytochemistry* **65**, 117–126.

- Rontani J.-F., Harji R., Guasco S., Prahel F. G., Volkman J. K., Bhosle N. B. and Bonin P. (2008) Degradation of alkenones by aerobic heterotrophic bacteria: Selective or not? *Org. Geochem.* **39**, 34–51.
- Rosell-Melé A., Bard E., Emeis K. -C., Grimalt J. O., Müller P., Schneider R., Bouloubassi I., Epstein B., Fahl K., Fluegge A., Freeman K., Goñi M., Güntner U., Hartz D., Hellebust S., Herbert T., Ikehara M., Ishiwatari R., Kawamura K., Kenig F., de Leeuw J., Lehman S., Mejanelle L., Ohkouchi N., Pancost R. D., Pelejero C., Prahel F., Quinn J., Rontani J. - F., Rostek F., Rullkötter J., Sachs J., Blanz T., Sawada K., Schulz-Bull D., Sikes E., Sonzogni C., Ternois Y., Versteegh G., Volkman J. K. and Wakeham S. (2001) Precision of the current methods to measure the alkenone proxy U_{37}^K and absolute alkenone abundance in sediments: Results of an interlaboratory comparison study. *Geochemistry, Geophys. Geosystems* **2**.
- Saavedra-Pellitero M., Baumann K.-H., Flores J.-A. and Gersonde R. (2014) Biogeographic distribution of living coccolithophores in the Pacific sector of the Southern Ocean. *Mar. Micropaleontol.* **109**, 1–20.
- Sassen K., DeMott P. J., Prospero J. M. and Poellot M. R. (2003) Saharan dust storms and indirect aerosol effects on clouds: CRYSTAL-FACE results. *Geophys. Res. Lett.* **30**, 1–4.
- Schlitzer R. (2015) Ocean Data View. <http://odv.awi.de>.
- Schouten S., Hopmans E. C., Schefuß E. and Damsté J. S. S. (2002) Distributional variations in marine crenarchaeotal membrane lipids: a new tool for reconstructing ancient sea water temperatures? *Earth Planet. Sci. Lett.* **204**, 265–274.
- Schouten S., Hopmans E. C., van der Meer J., Mets A., Bard E., Bianchi T. S., Diefendorf A., Escala M., Freeman K. H., Furukawa Y., Huguet C., Ingalls A., Ménot-Combes G., Nederbragt A. J., Oba M., Pearson A., Pearson E. J., Rosell-Melé A., Schaeffer P., Shah S. R., Shanahan T. M., Smith R. W., Smittenberg R., Talbot H. M., Uchida M., Mooy B. A. S. Van, Yamamoto M., Zhang Z. and Damsté J. S. S. (2009) An interlaboratory study of TEX₈₆ and BIT analysis using high-performance liquid chromatography-mass spectrometry. *Geochemistry, Geophys. Geosystems* **10**.
- Schouten S., Hopmans E. C. and Damsté J. S. S. (2013a) The organic geochemistry of glycerol dialkyl glycerol tetraether lipids: A review. *Org. Geochem.* **54**, 19–61.
- Schouten S., Hopmans E. C., Rosell-Melé A., Pearson A., Adam P., Bauersachs T., Bard E., Bernasconi S. M., Bianchi T. S., Brocks J. J., Carlson L. T., Castañeda I. S., Derenne S., Selver A. D., Dutta K., Eglinton T., Fosse C., Galy V., Grice K., Hinrichs K., Huang Y.,

- Huguet A., Huguet C., Hurley S., Ingalls A., Jia G., Keely B., Knappy C., Kondo M., Krishnan S., Lincoln S., Lipp J., Mangelsdorf K., Martínez-García A., Ménot G., Mets A., Mollenhauer G., Ohkouchi N., Ossebaar J., Pagani M., Pancost R. D., Pearson E. J., Peterse F., Reichart G., Schaeffer P., Schmitt G., Schwark L., Shah S. R., Smith R. W., Smittenberg R. H., Summons R. E., Takano Y., Talbot H. M., Taylor K. W. R., Tarozo R., Uchida M., Dongen B. E., Mooy B. A. S., Wang J., Warren C., Weijers J. W. H., Werne J. P., Woltering M., Xie S., Yamamoto M., Yang H., Zhang C. L., Zhang Y., Zhao M. and Damsté J. S. S. (2013b) An interlaboratory study of TEX₈₆ and BIT analysis of sediments, extracts, and standard mixtures. *Geochemistry, Geophys. Geosystems* **14**, 5263–5285.
- Shoenfelt E.M., Winckler G., Lamy F., Anderson R.F. and Bostick B.C. (submitted) Highly bioavailable dust-borne iron delivered to the Southern Ocean during glacial periods.
- Shiroya K., Yokoyama Y., Obrochta S., Harada N., Miyairi Y. and Matsuzaki H. (2013) Melting history of the Patagonian Ice Sheet during Termination I inferred from marine sediments. *Geochem. J.* **47**, 107–117.
- Siani G., Michel E., De Pol-Holz R., DeVries T., Lamy F., Carel M., Isguder G., Dewilde F. and Laurantou A. (2013) Carbon isotope records reveal precise timing of enhanced Southern Ocean upwelling during the last deglaciation. *Nat. Commun.* **4**, 2758.
- Sigman D. M. and Boyle E. A. (2000) Glacial/Interglacial Variations In Atmospheric Carbon Dioxide. *Nature* **407**, 859–869.
- Sigman D. M., Hain M. P. and Haug G. H. (2010) The polar ocean and glacial cycles in atmospheric CO₂ concentration. *Nature* **466**, 47–55.
- Sikes E. L., Volkman J. K., Robertson L. G. and Pichon J.-J. (1997) Alkenones and alkenes in surface waters and sediments of the Southern Ocean: Implications for paleotemperature estimation in polar regions. *Geochim. Cosmochim. Acta* **61**, 1495–1505.
- Sime L. C., Kohfeld K. E., Quéré C. Le, Wolff E. W., de Boer A. M., Graham R. M. and Bopp L. (2013) Southern Hemisphere westerly wind changes during the Last Glacial Maximum: model-data comparison. *Quat. Sci. Rev.* **64**, 104–120.
- Simoneit B. R. T. (1977) Organic matter in eolian dusts over the Atlantic Ocean. *Mar. Chem.* **5**, 443–464.
- Damasté J. S.S., Rijpstra W. I. C., Hopmans E. C., Weijers J. W. H., Foesel B. U., Overmann J. and Dedysh S.N. (2011) 13,16-Dimethyl octacosanedioic acid (iso-diabolic acid), a common membrane-spanning lipid of Acidobacteria subdivisions 1 and 3. *Appl. Environ. Microbiol.* **77**, 4147–54.

- Skinner L. C., Fallon S., Waelbroeck C., Michel E. and Barker S. (2010) Ventilation of the Deep Southern Ocean and Deglacial CO₂ Rise. *Science*. **328**, 1147 LP-1151.
- Smetacek V., Klaas C., Strass V. H., Assmy P., Montresor M., Cisewski B., Savoye N., Webb A., D'Ovidio F., Arrieta J. M., Bathmann U., Bellerby R., Berg G. M., Croot P., Gonzalez S., Henjes J., Herndl G. J., Hoffmann L. J., Leach H., Losch M., Mills M. M., Neill C., Peeken I., Röttgers R., Sachs O., Sauter E., Schmidt M. M., Schwarz J., Terbrüggen A. and Wolf-Gladrow D. (2012) Deep carbon export from a Southern Ocean iron-fertilized diatom bloom. *Nature* **487**, 313.
- Smith R. O., Vennell R., Bostock H. C. and Williams M. J. M. (2013) Interaction of the subtropical front with topography around southern New Zealand. *Deep Sea Res. Part I Oceanogr. Res. Pap.* **76**, 13–26.
- Sokolov S. and Rintoul S. R. (2009) Circumpolar structure and distribution of the antarctic circumpolar current fronts: 1. Mean98 circumpolar paths. *J. Geophys. Res. Ocean.* **114**, 1–19.
- Sow M., Alfaro S. C., Rajot J. L. and Marticorena B. (2009) Size resolved dust emission fluxes measured in Niger during 3 dust storms of the AMMA experiment. *Atmos. Chem. Phys.* **9**, 3881–3891.
- Struve T., Van De Flierdt T., Robinson L. F., Bradtmiller L. I., Hines S. K., Adkins J. F., Lambelet M., Crocket K. C., Kreissig K., Coles B. and Auro M. E. (2016) Neodymium isotope analyses after combined extraction of actinide and lanthanide elements from seawater and deep-sea coral aragonite. *Geochemistry, Geophys. Geosystems* **17**, 232–240.
- Stuut J.-B. W. and Prins M. A. (2014) The significance of particle size of long-range transported mineral dust. *Past Glob. Chang.*, 70–71.
- Sugden D. E., McCulloch R. D., Bory A. J.-M. and Hein A. S. (2009) Influence of Patagonian glaciers on Antarctic dust deposition during the last glacial period. *Nat. Geosci* **2**, 281–285.
- Sutton P. J. H. (2003) The Southland Current: A subantarctic current. *New Zeal. J. Mar. Freshw. Res.* **37**, 645–652.
- Talley L. D., Pickard G. L., Emery W. J. and Swift J. H. (2011) Southern Ocean. In *Descriptive Physical Oceanography: An Introduction* Elsevier Ltd. pp. 437–472.
- Talley L. D. (2013) Closure of the global overturning circulation through the Indian, Pacific, and Southern Oceans: Schematics and transport. *Oceanography* **26**, 80–97.
- Tanaka T., Togashi S., Kamioka H., Amakawa H., Kagami H., Hamamoto T., Yuhara M., Orihashi Y., Yoneda S., Shimizu H., Kunimaru T., Takahashi K., Yanagi T., Nakano T.,

- Fujimaki H., Shinjo R., Asahara Y., Tanimizu M. and Dragusanu C. (2000) JNdi-1: a neodymium isotopic reference in consistency with LaJolla neodymium. *Chem. Geol.* **168**, 279–281.
- Taylor S. R. and McLennan S. M. (1995) The geochemical evolution of the continental crust. *Rev. Geophys.* **33**, 241–265.
- Taylor R. N., Ishizuka O., Michalik A., Milton J. A. and Croudace I. W. (2015) Evaluating the precision of Pb isotope measurement by mass spectrometry. *J. Anal. At. Spectrom.* **30**, 198–213.
- Tegen I. and Fung I. (1994) Modeling of mineral dust in the atmosphere: Sources, transport, and optical thickness. *J. Geophys. Res.* **99**, 22897–22914.
- Thirlwall M. F. (1991) Long-term reproducibility of multicollector Sr and Nd isotope ratio analysis. *Chem. Geol. Isot. Geosci. Sect.* **94**, 85–104.
- Thomson J., Colley S., Anderson R., Cook G. T., MacKenzie A. B. and Harkness D. D. (1993) Holocene sediment fluxes in the northeast Atlantic from ²³⁰Th excess and radiocarbon measurements. *Paleoceanography* **8**, 631–650.
- Thornalley D. J. R., Blaschek M., Davies F. J., Praetorius S., Oppo D. W., McManus J. F., Hall I. R., Kleiven H., Renssen H. and McCave I. N. (2013) Long-term variations in Iceland–Scotland overflow strength during the Holocene. *Clim. Past* **9**, 2073–2084.
- Tiedemann R. (2012) FS Sonne Fahrtbericht / Cruise Report SO213. Alfred Wegener Institute, Bremerhaven.
- Tierney J. E. and Tingley M. P. (2014) A Bayesian, spatially-varying calibration model for the TEX86 proxy. *Geochim. Cosmochim. Acta* **127**, 83–106.
- Toggweiler J. R., Russell J. L. and Carson S. R. (2006) Midlatitude westerlies, atmospheric CO₂, and climate change during the ice ages. *Paleoceanography* **21**.
- Tournadre J., Girard-Ardhuin F. and Legrésy B. (2012) Antarctic icebergs distributions, 2002–2010. *J. Geophys. Res. C Ocean.* **117**, 2002–2010.
- Tsoar H. and Pye K. (1987) Dust transport and the question of desert loess formation. *Sedimentology* **34**, 139–153.
- Ullermann J., Lamy F., Ninnemann U., Lembke-Jene L., Gersonde R. and Tiedemann R. (2016) Pacific-Atlantic Circumpolar Deep Water coupling during the last 500 ka. *Paleoceanography* **31**, 639–650.
- Vallelonga P., Gabrielli P., Balliana E., Wegner A., Delmonte B., Turetta C., Burton G., Vanhaecke F., Rosman K. J. R., Hong S., Boutron C. F., Cescon P. and Barbante C. (2010) Lead isotopic compositions in the EPICA Dome C ice core and Southern Hemisphere

- Potential Source Areas. *Quat. Sci. Rev.* **29**, 247–255.
- Veres D., Bazin L., Landais A., Toyé Mahamadou Kele H., Lemieux-Dudon B., Parrenin F., Martinerie P., Blayo E., Blunier T., Capron E., Chappellaz J., Rasmussen S. O., Severi M., Svensson A., Vinther B. and Wolff E. W. (2013) The Antarctic ice core chronology (AICC2012): An optimized multi-parameter and multi-site dating approach for the last 120 thousand years. *Clim. Past* **9**, 1733–1748.
- Versteegh G. J. M., Riegman R., de Leeuw J. W. and Jansen J. H. F. (2001) U_{37}^K values for *Isochrysis galbana* as a function of culture temperature, light intensity and nutrient concentrations. *Org. Geochem.* **32**, 785–794.
- Völker C. and Köhler P. (2013) Responses of ocean circulation and carbon cycle to changes in the position of the Southern Hemisphere westerlies at Last Glacial Maximum. *Paleoceanography* **28**, 726–739.
- Warren A., Chappell A., Todd M. C., Bristow C., Drake N., Engelstaedter S., Martins V., M'bayayel S. and Washington R. (2007) Dust-raising in the dustiest place on earth. *Geomorphology* **92**, 25–37.
- Weaver P. P. E., Carter L. and Neil H. L. (1998) Response of surface water masses and circulation to Late Quaternary climate change east of New Zealand. *Paleoceanography* **13**, 70–83.
- Weijers J. W. H., Schouten S., Spaargaren O. C. and Damsté J. S. S. (2006) Occurrence and distribution of tetraether membrane lipids in soils: Implications for the use of the TEX₈₆ proxy and the BIT index. *Org. Geochem.* **37**, 1680–1693.
- Weis D., Kieffer B., Maerschalk C., Barling J., de Jong J., Williams G. A., Hanano D., Pretorius W., Mattielli N., Scoates J. S., Goolaerts A., Friedman R. M. and Mahoney J. B. (2006) High-precision isotopic characterization of USGS reference materials by TIMS and MC-ICP-MS. *Geochemistry, Geophys. Geosystems* **7**.
- Well R. and Roether W. (2003) Neon distribution in South Atlantic and South Pacific waters. *Deep Sea Res. Part I Oceanogr. Res. Pap.* **50**, 721–735.
- Wengler M., Lamy F., Struve T., Borunda A., Böning P., Geibert W., Kuhn G., Pahnke K., Roberts J., Tiedemann R. and Winckler G. (under review at *Geochimica et Cosmochimica Acta*) A geochemical approach to reconstruct modern South Pacific dust fluxes and potential dust source areas.
- Winckler G., Anderson R. F., Fleisher M. Q., McGee D. and Mahowald N. (2008) Covariant glacial-interglacial dust fluxes in the equatorial Pacific and Antarctica. *Science*. **320**, 93–

96.

- Yamamoto M., Shimamoto A., Fukuhara T., Tanaka Y. and Ishizaka J. (2012) Glycerol dialkyl glycerol tetraethers and TEX₈₆ index in sinking particles in the western North Pacific. *Org. Geochem.* **53**, 52–62.
- Yokoyama T., Makishima A. and Nakamura E. (1999) Evaluation of the coprecipitation of incompatible trace elements with fluoride during silicate rock dissolution by acid digestion. *Chem. Geol.* **157**, 175–187.
- Zhang Y. G., Zhang C. L., Liu X.-L., Li L., Hinrichs K.-U. and Noakes J. E. (2011) Methane Index: A tetraether archaeal lipid biomarker indicator for detecting the instability of marine gas hydrates. *Earth Planet. Sci. Lett.* **307**, 525–534.
- Zhao T. L., Gong S. L., Zhang X. Y. and McKendry I. G. (2003) Modeled size-segregated wet and dry deposition budgets of soil dust aerosol during ACE-Asia 2001: Implications for trans-Pacific transport. *J. Geophys. Res. Atmos.* **108**.
- Zhu C., Weijers J. W. H., Wagner T., Pan J.-M., Chen J.-F. and Pancost R. D. (2011) Sources and distributions of tetraether lipids in surface sediments across a large river-dominated continental margin. *Org. Geochem.* **42**, 376–386.

Data handling

The data presented in the first (chapter 3), the second (chapter 4), the third (chapter 5) and the fourth (chapter 6) manuscript are archived in the PANGAEA-database and are available at:

Chapter 3: <https://doi.pangaea.de/10.1594/PANGAEA.890082>

Chapter 4: <https://doi.pangaea.de/10.1594/PANGAEA.890081>

Chapter 5: <https://doi.org/10.1594/PANGAEA.860666>

Chapter 6: <https://doi.org/10.1594/PANGAEA.848152>